UC Santa Barbara
UC Santa Barbara Electronic Theses and Dissertations

Title
Growth and Strain of Hybrid Perovskite Films: Impacts on Stability and Light Emission

Permalink
https://escholarship.org/uc/item/276683p4

Author
Kennard, Rhys M

Publication Date
2021

Peer reviewed|Thesis/dissertation

eScholarship.org Powered by the California Digital Library
University of California

University of California, Santa Barbara

Growth and Strain of Hybrid Perovskite Films:
Impacts on Stability and Light Emission

A dissertation submitted in partial satisfaction of the requirements for the degree

Doctor of Philosophy

in

Materials

By

Rhys Marie Kennard

Committee in charge:

Professor Michael L. Chabinyc, Chair

Professor Ram Seshadri

Professor Jon A. Schuller

Professor Kunal Mukherjee, Stanford University

June 2021

The dissertation of Rhys Marie Kennard is approved.

Professor Kunal Mukherjee

Professor Jon A. Schuller

Professor Ram Seshadri

Professor Michael L. Chabinyc, Chair

June 2021

Growth and Strain of Hybrid Perovskite Films:

Impacts on Stability and Light Emission

Copyright © 2021

By

Rhys Marie Kennard

ACKNOWLEDGMENTS

The work produced in this dissertation would not have been possible without the support of many people. First, I would like to thank Prof. Michael Chabinyc for being a great advisor, for the many opportunities and very interesting projects at UC Santa Barbara, as well as for teaching me strong scientific skills, writing skills, for having lots of patience. Next, I would like to thank Prof. Ram Seshadri and Dr. Clayton Dahlman, who have been excellent mentors at UCSB. I would not have been as productive without the many skills learned from both of you, as well as the regular advice you gave me. Thank you additionally to Ram for playing a strong role in helping me find a postdoctoral job after my PhD and for teaching me how to make figures, and to Clay for being a very supportive friend. In addition, I would like to thank my undergraduate and Master's advisor, Prof. Michael Sailor, who did an excellent job giving me opportunities and preparing me for graduate school; these factors played a big role in my acceptance to UCSB.

I have been fortunate to work with many excellent collaborators: Prof. Kunal Mukherjee, who spent much time helping with the analysis of the interdiffusion work; Dr. Ryan Decrescent, who has been an excellent optics collaborator and who also taught me optics; Prof. Jon Schuller, for great optics discussions; Prof. Anton Van der Ven, who has always been available for questions; Prof. Manjunatha Reddy, who has been a great NMR collaborator, as well as many others: the students and postdocs in the Chabinyc group, Schuller group, Seshadri group, Kanatzidis group, and Salleo group.

Finally, I would like to thank my parents, family and friends, for all of their support and for the excellent times had.

VITA OF RHYS MARIE KENNARD

EDUCATION

Ph.D., Materials, UC Santa Barbara	**Expected June 2021**
M.S. Materials Chemistry, UC San Diego	**August 2016**
B.S. Chemical Physics, UC San Diego, *magna cum laude*	**June 2015**

PUBLICATIONS (*reverse chronological order*)

1. Dahlman, C.J., **Kennard, R.M.**, Paluch, P., Venkatesan, N.R., Chabinyc, M.L. and Reddy, M. G. N., Dynamic Motion of Organic Spacer Cations in Ruddlesden-Popper Lead Iodide Perovskites Probed by Solid-State NMR Spectroscopy. *Chem. Mater.*, **2021**, *33*, 2, 642–656.
2. **Kennard, R.M.**, Dahlman, C.J., DeCrescent, R.A., Schuller, J.A., Mukherjee, K., Seshadri, R. and Chabinyc, M.L., Ferroelastic Hysteresis in Thin Films of Methylammonium Lead Iodide. *Chem. Mater.*, **2020**, *33*, 298-309.
3. Dahlman, C.J., Venkatesan, N.R., Corona, P.T., **Kennard, R.M.**, Mao, L., Smith, N.C., Zhang, J., Seshadri, R., Helgeson, M.E. and Chabinyc, M.L., Structural Evolution of Layered Hybrid Lead Iodide Perovskites in Colloidal Dispersions. *ACS nano*, **2020**, *14*, 11294-11308.
4. DeCrescent, R.A., Du, X., **Kennard, R.M.**, Venkatesan, N.R., Dahlman, C.J., Chabinyc, M.L. and Schuller, J.A., Even-Parity Self-Trapped Excitons Lead to Magnetic Dipole Radiation in Two-Dimensional Lead Halide Perovskites. *ACS nano*, **2020**,*14*, 8958-8968.
5. DeCrescent, R.A., Venkatesan, N.R., Dahlman, C.J., **Kennard, R.M.**, Zhang, X., Li, W., Du, X., Chabinyc, M.L., Zia, R. and Schuller, J.A., Bright magnetic dipole radiation from two-dimensional lead-halide perovskites. *Sci. Adv.*, **2020**, *6*, eaay4900.
6. Mao, L., Teicher, S.M., Stoumpos, C.C., **Kennard, R.M.**, DeCrescent, R.A., Wu, G., Schuller, J.A., Chabinyc, M.L., Cheetham, A.K. and Seshadri, R., Chemical and structural diversity of hybrid layered double perovskite halides. *J. Am. Chem. Soc.*, **2019**, *141*, 19099-19109.
7. Mao, L., **Kennard, R.M.**, Traore, B., Ke, W., Katan, C., Even, J., Chabinyc, M.L., Stoumpos, C.C. and Kanatzidis, M.G., Seven-layered 2D hybrid lead iodide perovskites. *Chem*, **2019**, *5*, 2593-2604
8. DeCrescent, R.A., Venkatesan, N.R., Dahlman, C.J., **Kennard, R.M.**, Chabinyc, M.L. and Schuller, J.A., Optical constants and effective-medium origins of large optical anisotropies in layered hybrid organic/inorganic perovskites. *ACS nano*, **2019**, *13*, 10745-10753.

9. Dahlman, C.J., DeCrescent, R.A., Venkatesan, N.R., **Kennard, R.M.**, Wu, G., Everest, M.A., Schuller, J.A. and Chabinyc, M.L., Controlling Solvate Intermediate Growth for Phase-Pure Organic Lead Iodide Ruddlesden-Popper $(C_4H_9NH_3)_2CH_3NH_3)_{n-1}Pb_nI_{3n+1}$ Perovskite Thin Films. *Chem. Mater.*, **2019**, *31*, 5832-5844.
10. **Kennard, R.M.**, Dahlman, C.J., Nakayama, H., DeCrescent, R.A., Schuller, J.A., Seshadri, R., Mukherjee, K. and Chabinyc, M.L., Phase Stability and Diffusion in Lateral Heterostructures of Methyl Ammonium Lead Halide Perovskites. *ACS Appl. Mater. Interfaces*, **2019**, *11*, 25313-25321.
11. Venkatesan, N.R., **Kennard, R.M.**, DeCrescent, R.A., Nakayama, H., Dahlman, C.J., Perry, E.E., Schuller, J.A. and Chabinyc, M.L., Phase intergrowth and structural defects in organic metal halide Ruddlesden–Popper thin films. *Chem. Mater.*, **2018**, *30*, 8615-8623.
12. Wang, J., Lee, G.Y., **Kennard, R.M.**, Barillaro, G., Bisiewicz, R.H., Cortez Lemus, N.A., Cao, X.C., Anglin, E.J., Park, J.S., Potocny, A., Bernhard, D., Li, J., and Sailor, M.J., Engineering the properties of polymer photonic crystals with mesoporous silicon templates. *Chem. Mater.*, **2017**, *29*, 1263-1272.
13. Wang, J., Joo, J., **Kennard, R.M.**, Lee, S.W. and Sailor, M.J., Thermolytic Grafting of Polystyrene to Porous Silicon. *Chem. Mater.*, **2016**, *28*, 79-89.
14. Li, X., Gu, M., Hu, S., **Kennard, R.M.**, Yan, P., Chen, X., Wang, C., Sailor, M.J., Zhang, J.G. and Liu, J., Mesoporous silicon sponge as an anti-pulverization structure for high-performance lithium-ion battery anodes. *Nat. Commun.*, **2014**, *5*, 1-7.

AWARDS/HONORS

- National Defense Science and Engineering Graduate (NDSEG) Fellowship *(5-10 % acceptance rate)*, covers graduate expenses **August 2017 - June 2021**
- 2020 Fall Virtual MRS Excellent Poster Award
- Undergraduate awards: *Magna cum laude* UC San Diego, 2015 Selma and Robert Silagi Award in Undergraduate Excellence, 2015 Joseph E. Mayer award for undergraduate research in Chemistry, Revelle College Honors, Provost Honors (2011-15, 11/12 quarters)

CONFERENCE PRESENTATIONS

- HOPV Meeting **2021**, "What happens when we bend $MAPbI_3$? Insights on sub-grain structures and stability", virtual talk
- MRS Fall Meeting **2020**, "Ferroelastic Hysteresis in $MAPbI_3$ Films", virtual poster 2-min video here
- NanoGE Fall Meeting **2020**, "Ferroelastic Hysteresis in $MAPbI_3$ Films", virtual poster (see above link)

- NDSEG Fellow's conference August **2019**, "Phase Stability and Diffusion in Lateral Heterostructures of Lead Halide Perovskites", poster presentation
- MRS Spring Meeting **2019**, "Phase Stability and Diffusion in Lateral Heterostructures of Methyl Ammonium Lead Halides", oral presentation

TEACHING/SERVICE/LEADERSHIP

- Mentoring undergraduate and incoming graduate students (Chabinyc group); **2019 - 2021**
  Designed and supervised projects, taught presentation skills
- Beyond Academia 2018 conference co-organizer, UCSB; **Summer 2017 - March 2018**
  Fundraising and helping putting together panels of non-academics
- Teaching assistant, Materials 101, UCSB; **Winter 2017**
- Teaching assistant, Physical Chemistry laboratory (upper division), UCSD; **Spring 2016**

ABSTRACT

Growth and Strain of Hybrid Perovskite Films: Impacts on Stability and Light Emission

by

Rhys Marie Kennard

Hybrid halide perovskites (HHPs) are being commercialized as solar cells and are being investigated for use in a wide variety of other optoelectronic devices. The most efficient solar cells rely on alloys of the cubic perovskite AMX_3 structure, such as $(CS.FA,MA)Pb(I,Br)_3$, where FA and MA stand for formamidinium and methylammonium. HHPs have incredibly versatile structure and consequently, emission color, making them attractive for light emitting diodes or lasers. In addition to the AMX_3 structure, HHPs can be made as two-dimensional (2D) materials, whereby large bulky organic cations separate M-X (metal-halide) semiconducting sheets. Tuning the thickness of the M-X layer changes the color of the exciton emission, and thus much effort has been devoted to making optoelectronic devices from 2D perovskites. Generally, HHP-based devices rely on polycrystalline thin films, which poses challenges: polycrystalline thin films contain grain boundaries, exhibit film strain, and are prone to forming undesired crystalline phases.

Here, the fundamental structural, ionic and optical properties of HHP thin films are investigated. The first section is dedicated to understanding how film strains, such as those imparted by commercial fabrication procedures, may change sub-grain structure and cause degradation of the HHP. The second section examines phase stability and halide interdiffusion in mixed-halide 3D alloys. The third and fourth sections report phase-pure 2D film fabrication, and examine how strain and residual solvent can turn off certain emission features intrinsic to the 2D phase in question. These results help extend the utility of HHPs for optoelectronic devices by providing design rules for how to grow films with targeted structural and optoelectronic properties.

TABLE OF CONTENTS

Chapter 1: Introduction

1.1 Structural diversity: HHPs for a plethora of applications

Hybrid halide perovskites (HHP) are currently being commercialized as solar cell absorbers and are attractive for a variety of other optoelectronic applications, such as light emitting devices or photodetectors. [1–5] HHP are solution processable, which means they can be fabricated at low temperature, thus circumventing energy-intensive processes needed to fabricate traditional semiconductor-based devices. [1,2] The power conversion efficiency of HHP-based solar cells rivals that of solar cells made with polycrystalline silicon. [6] In addition, the emission color of HHPs can be tuned by changing the crystal structure, making HHPs attractive for light emission [3,4]

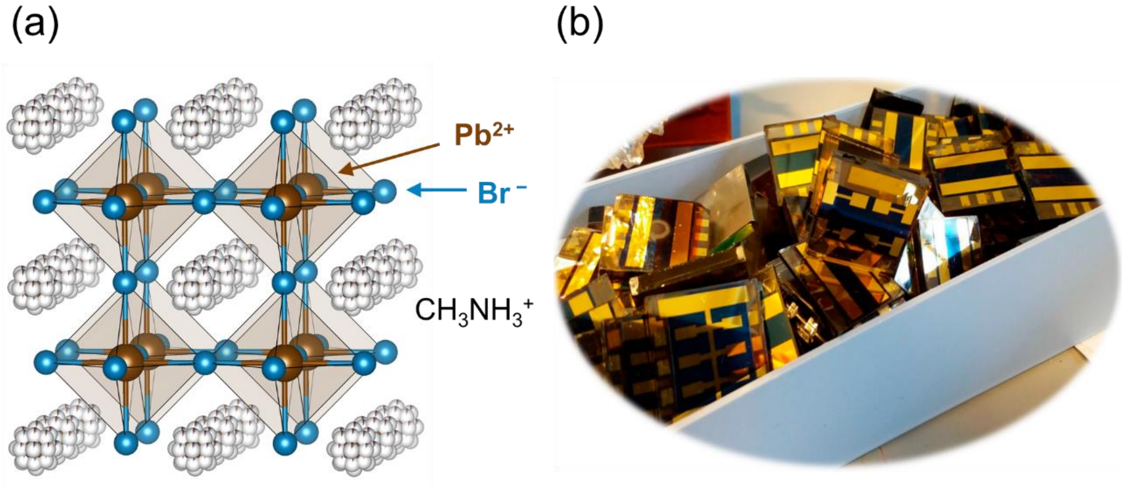

Figure 1.1. (a) Cubic AMX_3 structure of HHPs. Shown here is the cubic phase of methylammonium lead bromide $MAPbBr_3$, generated using a reported crystallographic information file (cif). [7] The methylammonium cation is disordered at room temperature. (b) Photograph of solar cell devices using HHPs as the absorbance layer. [6] (b) Reprinted (adapted) with permission from (*Chem. Mater.* **2018**, *30*, 13, 4193–4201). Copyright (2018) American Chemical Society.

HHPs have basic structure AMX_3, where A is a small cation, M is a metal, and X is a halide (**Figure 1.1**). Typically, methylammonium (MA), formamidinium (FA) or cesium are used as A-site cations, Pb or Sn are used as the metal, and I, Br or Cl are used as the halides. [2,6,8] Alloying the different ions is a common route to obtain specific optoelectronic properties. For example, alloying the halides to form $AM(Cl,Br)_3$ or $AM(Br,I)_3$ changes the bandgap and emission color, which is attractive for light emission. [9] **Figure 1.2** shows emission from $CsPbX_3$ nanocrystals. Films of such nanocrystals are efficient light emitters, with quantum yields up to 90%. [9] In addition, the highest solar cell efficiencies have been achieved by mixing the halides (typically ≈ 90% I and 10 % Br) and the A-site cations (Cs/FA/MA). [6] Pb is typically preferred over Sn for solar applications, as Sn-based devices suffer from poorer photoconversion efficiency in solar cells, from poorer film quality and from degradation from Sn^{2+} to Sn^{4+}. [6,10] However, Pb-Sn alloys are being investigated as an alternative to using Pb alone, due to concerns regarding the toxicity of Pb. [11]

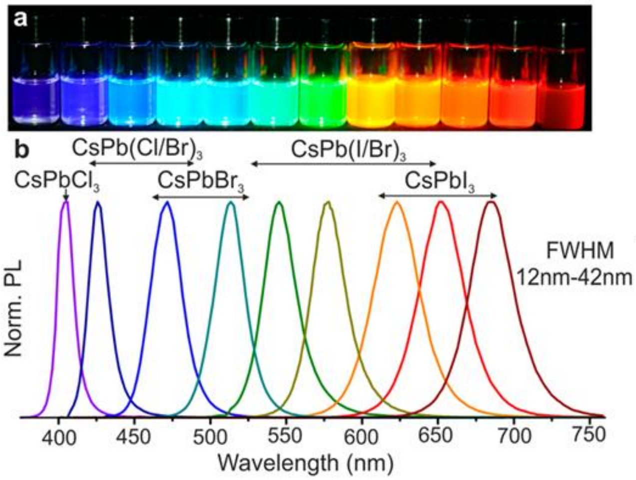

Figure 1.2. (a) Photograph of $CsPbX_3$ nanocrystals in solution under UV illumination. (b) Photoluminescence emission spectra of these nanocrystals. [9] Reprinted (adapted) with permission from (*Nano Lett.* **2015**, *15*, 3692–3696); https://pubs.acs.org/doi/10.1021/nl5048779. Copyright (2015) American Chemical Society. Further permissions related to the material excerpted should be directed to the ACS.

While HHP exhibit huge structural versatility, there are bounds on which ions can/cannot form a 3D perovskite phase (e.g., cubic, tetragonal, orthorhombic). The tolerance factor, t dictates whether or not ions can form a 3D perovskite phase, as well as which type of phase will be formed: [12]

$$t = \frac{r_A + r_X}{\sqrt{2}(r_M + r_X)}$$

Where t is the tolerance factor, and r_A, r_M and r_X are the radii of the ions in the AMX_3 structure. For alloys, average radii of the ions in the different sites can be used. Additional factors, such as globularity, are sometimes needed to account for different shapes of the A-site cations. [13] The tolerance factor is typically 0.8-1 for most three-dimensional (3D) perovskite structures (e.g. tetragonal, cubic). [14]

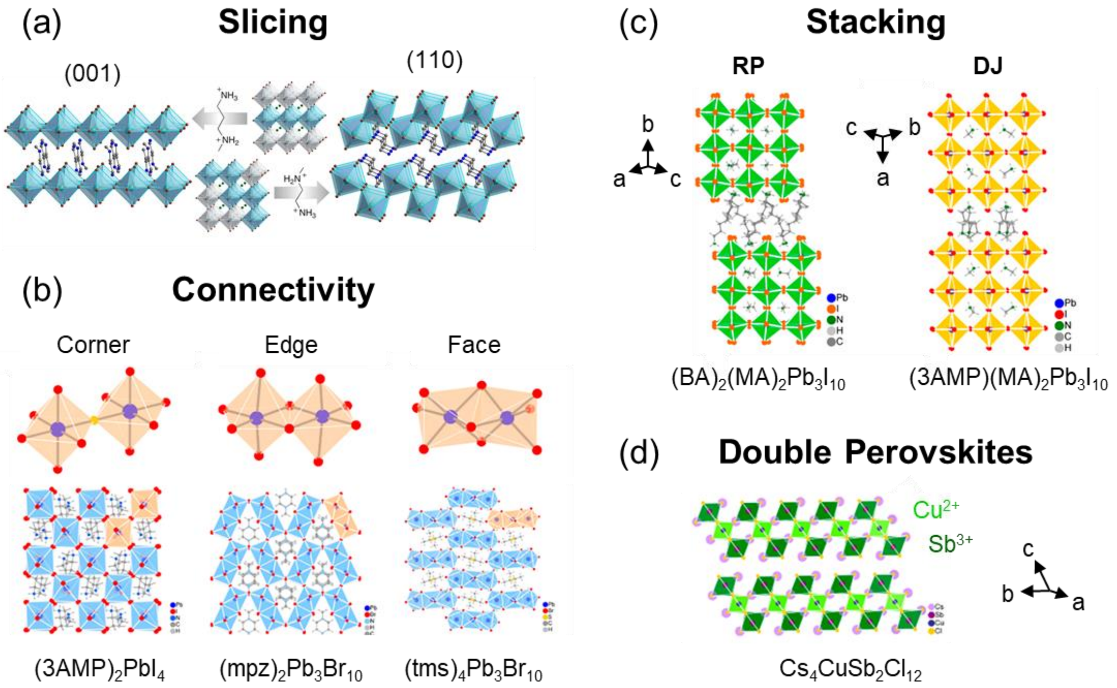

Figure 1.3. Types of 2D hybrid perovskites (non-exhaustive list) with different (a) slicing, (b) octahedral connectivity, (c) stacking, and (d) metal ion ordering (double perovskites). [8,15] (a) Reprinted (adapted) with permission from (*J. Am. Chem. Soc.* **2014**, *136*, 5, 1718–1721). Copyright (2014) American Chemical Society. (b)-(d) Reprinted (adapted) with permission from (*J. Am. Chem. Soc.* **2019**, *141*, 3, 1171–1190). Copyright (2018) American Chemical Society.

Another common perovskite structural type is the two-dimensional (2D) perovskite. 2D perovskites have semiconducting sheets of M-X octahedra that are separated by large, typically organic cations that are too big to go in the A-site of a 3D perovskite. 2D perovskites are attractive because they exhibit enhanced stability in ambient over their 3D counterparts when used in photovoltaic devices. [16] Changing the number *n* of M-X octahedra that sit between the spacer cations, as well as changing the chemistry of the spacer, provides an additional way to change the absorption/emission energies. [8,17] 2D perovskites also exhibit a variety of fascinating and/or unusual optoelectronic properties such as magnetic dipole transitions, [18,19] self-trapped exciton emission, [20–26] and ferroelectricity. [27]

Due to the wide variety of spacer cations available, there is enormous versatility in structures available to 2D perovskites. [8,20] 2D perovskites can be thought of as "slices" of 3D perovskites along various planes, such as the (001) plane or the (110) plane: **Figure 1.3.a** shows the resulting "(001)" and "(110)" 2D phases, [20] and **Figure 1.3.d** shows a "(111)" phase ($Cs_4CuSb_2Cl_{12}$). [8] The connectivity of the 2D sheets can be changed, from corner-sharing, to edge-sharing, to face-sharing (**Figure 1.3.b**). [8] The stacking of (001) phases can also change (**Figure 1.3.c**). [8] In Ruddlesden-Popper (RP) phases, the octahedra on the upper M-X layer are shifted by half an octahedron from the M-X layer below are called. In contrast, for Dion-Jacobson phases, the octahedra on the top and bottom M-X layers align. 2D perovskites that have several different ions in the metal site, which arrange themselves in an ordered manner, are called "double perovskites" (**Figure 1.3.d**).

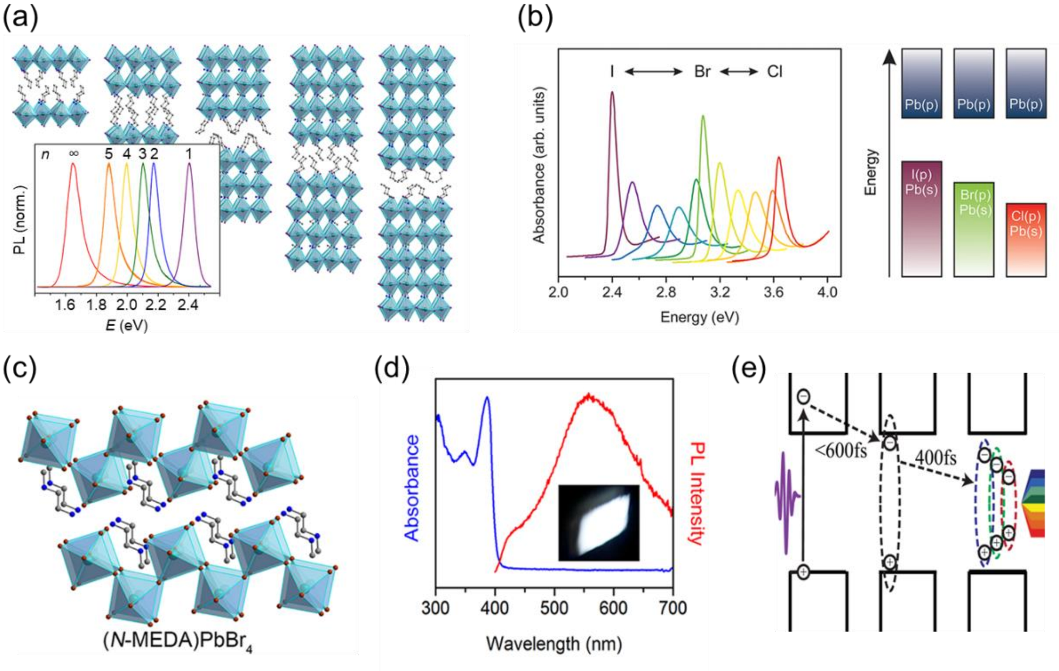

Figure 1.4. Examples of excitonic tunability in 2D perovskites. (a) Emission from members of the (BA)$_2$(MA)$_{n-1}$Pb$_n$I$_{3n+1}$ RP family, for $n = 1$ through 5 and MAPbI$_3$ ($n = \infty$). [20] (b) Absorbance of mixed-halide 2D perovskites with schematic block band diagrams. [20] (c) Corrugated 2D perovskite that exhibits self-trapped exciton (STE) emission, which is shown in (d). [15,20] (e) Schematic mechanism of STE emission. [15] (a)-(c) Reprinted (adapted) with permission from (*Chem. Rev.* **2019**, *119*, 5, 3104–3139). Copyright (2019) American Chemical Society. (d) Reprinted (adapted) with permission from (*J. Am. Chem. Soc.* **2014**, *136*, 5, 1718–1721). Copyright (2014) American Chemical Society. (e) Reprinted (adapted) with permission from (*J. Phys. Chem. Lett.* **2016**, *7*, 2258–2263). Copyright (2016) American Chemical Society.

The structural versatility of 2D perovskites provides additional knobs with which to tune the optoelectronic properties of HHPs. For example, the bandgap and optical emission can be changed by changing the number n of M-X octahedra in sheets of the Ruddlesden-Popper family, which has basic structure (A')$_2$(A)$_{n-1}$M$_n$X$_{3n+1}$, where A' is the spacer cation and A is the A-site cation. Because 2D perovskites exhibit both dielectric and quantum confinement, emission is typically excitonic. [28] **Figure 1.4.a** shows how the energy of the free exciton emission changes with n in the (BA)$_2$(MA)$_{n-1}$Pb$_n$I$_{3n+1}$ RP family. [20] The $n = \infty$ phase is the 3D perovskite MAPbI$_3$. The emission color can further be tuned by switching the halides in the 2D phases from I to Br to Cl, as shown in **Figure 1.4.b.** [20]

Changing the chemistry of the spacer can also change the dielectric confinement, which can change carrier mobility. [29] Introducing distortions to the M-X octahedral bond lengths and angles favors formation of self-trapped excitons (STEs), which broadens the emission until white (**Figure 1.4.c**). [15,20–26] A variety of mechanisms have been proposed to explain the mechanism of self-trapping, including coupling to phonons, [19] polarons, [30] or enhancement of the self-trapping by metal vacancies. [25]

1.2 Methods for growing hybrid perovskites

Novel compositions of HHPs are typically prepared as bulk crystals, while devices typically employ films. We will first review some common bulk crystal preparation methods, before reviewing film preparation methods. Many bulk crystals are prepared via precipitation from aqueous acid: the precursor salts are dissolved in the acid, the mixture is heated and stirred, and bulk crystals precipitate during cooling (**Figure 1.5.a**). [22,31] Different bulk crystals prepared in this manner can be alloyed via mixing with a mortar and pestle, followed by annealing. [22] Alternate methods for preparing bulk crystals involve preparation from organic solvent. Precursors are sometimes less soluble in organic solvent at elevated temperatures; this can be exploited to grow large crystals of 3D phases. [32] This process, called "inverse temperature crystallization", is shown in **Figure 1.5.b**. Diffusion of antisolvent into the precursor solution can also precipitate bulk crystals (**Figure 1.5.c**). [33] This process can be exploited to grow large, uniformly-oriented bulk crystals on substrates, which is particularly useful for optical studies, as crystallite orientation can sometimes control the optical emission. [19] Crystals grown directly oriented on substrates are then easier to exfoliate into flakes, for optical studies in which thin materials are needed. [19]

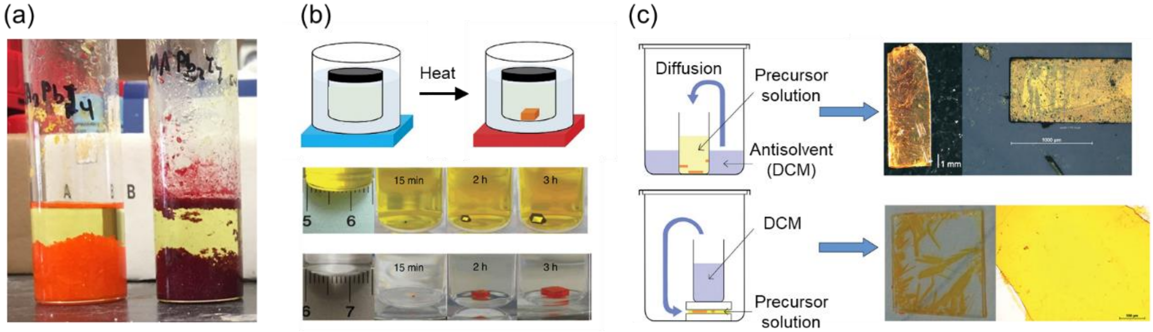

Figure 1.5. Growth methods for HHP bulk crystals. (a) Vials of 2D perovskites grown via precipitation from aqueous acid. [31] (b) Inverse temperature crystallization procedure for $MAPbI_3$ (top vials) and $MAPbBr_3$ (bottom vials). [32] (c) Antisolvent crystallization method for crystals grown either in solution or attached to a substrate[19].[33] (a) Reprinted (adapted) with permission from (*Chem. Mater.* **2016**, *28*, 2852–2867). https://pubs.acs.org/doi/10.1021/acs.chemmater.6b00847 Copyright (2016) American Chemical Society. Further permissions related to the material excerpted should be directed to the ACS. (b) is from an open-access article. (c) Republished with permission of the Royal Society of Chemistry, from Fast growth of monocrystalline thin films of 2D layered hybrid perovskite, Ferdinand Lédée, Gaëlle Trippé-Allard, Hiba Diab, Pierre Audebert, Damien Garrot, Jean-Sébastien Lauret, Emmanuelle Deleporte, 19, 19, 2017; permission conveyed through Copyright Clearance Center, Inc.

While bulk crystals are useful for discovering new compositions, optoelectronic devices typically use HHPs in film form. The most commonly-used method to grow HHP films on an academic laboratory scale is spin-casting shown in **Figure 1.6.** [6] Precursor salts, typically PbX_2, A'X and/or AX, are first dissolved in a polar solvent such as dimethylformamide (DMF) or dimethyl sulfoxide (DMSO). A few microliters of the solution are dropped onto a pre-cleaned substrate, which is then spun to spread the solution into a thin layer. Antisolvent, such as chlorobenzene or toluene, is sometimes dropped on before the end of the spinning, to drive solvent removal and enhance perovskite crystallization. The film is then annealed to finish removing solvent and obtain crystalline perovskite phases. The entire procedure is usually carried out in inert environment (i.e., glove box) to prevent degradation from air. Spin-casting is thus a very simple fabrication procedure, particularly in comparison to cleanroom processing. Film thickness and gain size are readily tunable by changing the spin speed and/or the concentration of precursor ions. The spin-casting procedure can impart wrinkling stresses, and the annealing procedure can cause thermal stress, due to thermal expansion mismatch between the perovskite and the substrate. Thermal stress can sometimes be used to stabilize cubic phases, but in other cases accelerates degradation back to the precursors.

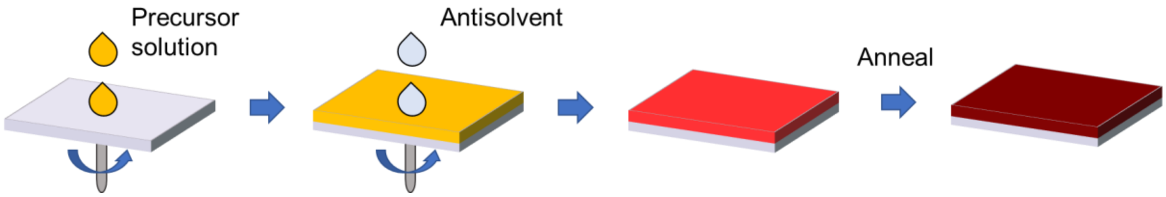

Figure 1.6. Typical steps in the spin-casting procedure for film casting: the precursor solution contain dissolved PbX_2 and AX salts is placed on a cleaned substrate, which is then spun. Antisolvent (e.g. toluene, chlorobenzene) is the dropped to aid crystallization. The film is then annealed.

Commercial methods for film fabrication also rely on solution casting, but sometimes require methods compatible with roll-to-roll processing, if that is the large-scale production method selected. Roll-to-roll processing is highly attractive as a manufacturing method, as it enables significant cost reduction over more traditional manufacturing methods. [34] To this end, a number of solution casting methodologies for HHPs have been developed, and include blade coating, slot-die coating, spray coating, inkjet printing and screen printing. [5] These all involve the perovskite "ink" (precursor ions dissolved in organic solvent) being fed onto a flexible substrate and spread or patterned by a nozzle, blade, patterned screen, etc. An alternate method involves deposition from vapor, which circumvents the need to use environmentally unfriendly solvents and can more easily yield thinner films (50 nm) than the solution-based techniques described above. However, vapor deposition is slower and requires more sophisticated equipment than solution deposition. [5]

1.3 Challenges for growing films of 3D phases

A great challenge for HHP devices has been to improve their environmental stability. HHPs can readily degrade in ambient back to their precursors, although the rate of degradation greatly depends on the composition selected. $MAPbI_3$, the prototypical 3D perovskite, is very sensitive to air, water, or UV light. [35] Thermal strain coming from thermal expansion mismatch between the substrate and the HHP has been shown to accelerate degradation. [36] Sn, while attractive as a replacement for Pb, can readily oxidize at film interfaces. [11] The stability in ambient can be improved by adding larger cations to the lattice, [37] by fabricating 2D/3D heterostructures, [16] or by encapsulating the HHP-based device. [38]

Improvements must also be made to the phase stability of HHPs. Mixed I-Br 3D alloys with higher Br content reversibly separate into I-rich and Br-rich phases under light exposure. [39] Reducing the crystallite size is necessary to prevent such phase separation, [40] making nanocrystals attractive for the red-green emission region. Furthermore, while alloy compositions such $(Cs,FA,MA)Pb(I,Br)_3$ yield the best solar cell power conversion efficiencies, [6] the long-term phase stability of such alloys is unclear. [41] Care is therefore required when assessing the viability of novel perovskite compositions for use in devices.

In addition, while the power conversion efficiency of HHP-based solar cells rivals that of Si, [6,41] a greater understanding of defects in films is required in order to further improve device performance. Strain heterogeneity in films has been correlated with enhanced carrier trapping, [42] so an improved understanding of film strain and of methodologies to control film strain are needed. In addition, grain boundaries can serve as hole traps, but the exact nature of trap clusters remains unclear. [41] Interfaces with electrodes introduce additional non-radiative recombination processes, which then limit the open circuit voltage and the fill factor of HHP-based solar cells. To mitigate these effects, various coatings can be applied to the top and bottom interfaces of the HHP layer; however, much remains to be understood regarding the mechanisms of passivation and how to further improve defect passivation. [41]

Thus, while 3D HHPs have demonstrated outstanding solar cell performance, limitations to their stability and the prominent roles played by defects motivate exploration of other forms of HHPs. To this end, 2D perovskite phases have received considerable attention. However, different challenges arise when trying to grow 2D films, as will be discussed in the next section.

1.4 Challenges for growing films of 2D phases

One challenge associated with growing films of 2D perovskite phases is that the emission from the film does not always match the emission of the corresponding bulk crystals (**Figure 1.7.a-b**). This is particularly noticeable for Ruddlesden-Popper phases (RPs), which are commonly studied as materials for solar cells and light emitting devices. The main advantages of using RP phases over 3D phases are that RPs are more stable in ambient [16] and do not exhibit rapid phase separation in the red-green spectral region like 3D phases do. [39] However, spin-cast films of 2D phases often exhibit emission corresponding to the associated 3D phase, instead of to that of the targeted 2D phase. For example, films RP phases, which have crystal structure $(A')_2(A)_{n-1}M_nX_{3n+1}$, often have emission corresponding to $n = \infty$ (AMX_3) instead of to that of the targeted $n = 3, 4$, etc.[43,44] This is particularly a problem for $n = 3$ and above; in contrast, $n = 1$ rarely form other phases in films, as there is no A-site cation to form other phases with. The ability to easily cast the 2D phase of choice as a film is crucial for deploying 2D perovskites in optoelectronic devices.

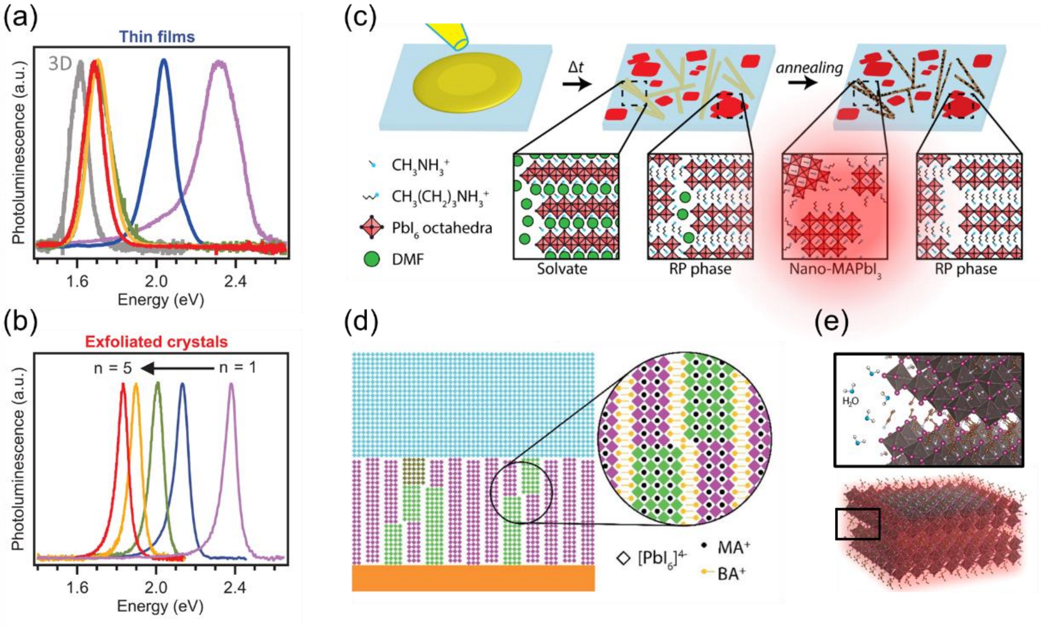

Figure 1.7. Challenges encountered when growing films of 2D perovskite phases. Emission from films (a) does not always match emission from bulk crystals (b) of $(BA)_2(MA)_{n-1}Pb_nI_{3n+1}$.[45] Emission from the 3D phase $MAPbI_3$ is labelled in gray. (c) Solvate complexes in $(BA)_2(MA)_{n-1}Pb_nI_{3n+1}$ precipitate after annealing into nano-$MAPbI_3$.[43] (d) Nanostructure of "2D" films: 2D and 3D phases are separated, and phases of various n are present. A stacking fault defect is shown in the inset.[46] (e) Formation of red-emitting edge states formed by exposure to moisture.[47] (a) and (b) Republished with permission of the American Association for the Advancement of Science, from Extremely efficient internal exciton dissociation through edge states in layered 2D perovskites, J.-C. Blancon, H. Tsai, W. Nie, C. C. Stoumpos, L. Pedesseau, C. Katan, M. Kepenekian, C. M. M. Soe, K. Appavoo, M. Y. Sfeir, S. Tretiak, P. M. Ajayan, M. G. Kanatzidis, J. Even, J. J. Crochet, A. D. Mohite, 355, 6331, 2017; permission conveyed through Copyright Clearance Center, Inc. (c) Reprinted (adapted) with permission from (*Chem. Mater.* **2019**, *31*, 15, 5832–5844). Copyright (2019) American Chemical Society. (d) Republished with permission of the Royal Society of Chemistry, from Direct assessment of structural order and evidence for stacking faults in layered hybrid perovskite films from X-ray scattering measurements, Wen Liang Tan, Yi-Bing Cheng and Christopher R. McNeill, 8, 25, 2020; permission conveyed through Copyright Clearance Center, Inc. (e) Reprinted (adapted) with permission from (*ACS Nano* **2019**, *13*, 2, 1635–1644). Copyright (2019) American Chemical Society.

Many reasons have been put forth to explain the off-target emission; three are highlighted here. The first is competing reactions: the AX, PbX_2 and A'X precursors complex with the solvent in different ways, resulting in the formation of a variety of intermediate phases during crystallization (**Figure 1.7.c**). [43,44] After solvent removal during the annealing step, some of these phases become nanoscale 3D phases, such as $MAPbI_3$. [43] Charge carriers then migrate to the 3D phase, which has lowest bandgap. This funneling has been exploited to produce light emitting diodes with high efficiency, [48] but removes tunability of light emission color in films. Stacking fault defects, shown in **Figure 1.7.d**, explain intergrowth of different n phases within a same grain. The Ruddlesden-Popper spacer area turns into a stacking fault defect when, instead of separating two sheets of $n = 3$ (for example), the spacer area separates one sheet of $n = 2$ and one of $n = 4$. [46,49] Thus, the overall stoichiometry of $n = 3$ is retained, but the nanostructure is not that of $n = 3$. A third main contributor to the emission shift is moisture: as shown in **Figure 1.7.e**, whereby insertion of water molecules between the semiconducting sheets can result in formation of red-emitting compounds that are localized at the edge of the crystal. [47] Thus, preventing formation of off-target 2D phases or 3D phases is key to obtaining films of 2D phases with desired emission.

A secondary challenge associated with 2D perovskite film growth is controlling the orientation of the semiconducting A-Pb-X sheets. The average sheet orientation of RP phases is known to change with n, being fully parallel to the substrate for $n = 1$ and increasingly perpendicular for larger n. [44,50] Changing these growth patterns can be challenging, but some degree of control is needed, as the semiconducting sheets need to be homogeneously aligned between the device electrodes in such a way that carrier transport is maximized.

A large number of solutions have been proposed for overcoming the challenges of phase control and orientation; a particularly effective one is highlighted here. Recent work replaced the A'X precursor salt with A'-acetate. [51] The resulting films exhibited emission from the target *n* 2D phases. However, one drawback of the acetate method is the need to synthesize the A'-acetate precursor, but this drawback might be overcome if the A'-acetate precursor becomes commercially available, as has been the case with many novel halide perovskite precursors. In addition to making films whose emission matched that of the targeted 2D phases, the authors also showed that the crystal structure of the films matched that of the bulk crystals. A key method for doing so is to check that the signature peaks for 2D phases are present: for the Ruddlesden-Popper family, these peaks are the $(0k0)$ peaks that arise from stacking of the 2D semiconducting sheets. In the next section, we will discuss a common method for verifying the presence and orientation of the 2D semiconducting sheets.

1.5 GIWAXS Characterization of thin films

Grazing Wide-Angle X-Ray Scattering (GIWAXS) is commonly used in the HHP field to extract a wealth of information regarding phase composition, crystallite orientation, and strain. GIWAXS is also used in other fields, such as polymers, batteries, or catalysis, to extract similar information. **REFs** In GIWAXS, X-Rays hit the sample at grazing incidence (typically under 2° - **Figure 1.8.a**) and are scattered onto a 2D detector (**Figure 1.8.b**). Planes parallel to the substrate scatter along q_Z; and planes perpendicular to the substrate scatter along q_{XY} (**Figure 1.8.c**). The ability to probe q_{XY} and other off-specular regions (i.e. anything other than- q_{Z}) provides invaluable information not typically accessible using lab diffractometers, which only probe q_{Z}. Due to geometric factors, a portion of q_{Z} is missing in GIWAXS; this “missing wedge” is shown in black in **Figure 1.8.b**. GIWAXS is typically performed at synchrotron beamlines, enabling much more sensitive detection and much faster acquisition times than laboratory-scale diffractometers. The rapid and sensitive acquisition enables *in-situ* or *in-operando* experiments to be performed that would be difficult or impossible with laboratory-scale instruments. Peak shifts and peak broadening can further provide information about strain or disorder in the lattice. For GIWAXS characterization of 2D HHPs specifically, particular care needs to be made to verify that the (0*k*0) peaks of the desired phase are present. These peaks correspond to Pb-Br sheet stacking, and become weak or absent when RP phases of different *n* are intergrown (**Figure 1.7.d**). In phase-pure films, like that shown in **Figure 1.8.b** or elsewhere reported, the (0*k*0) peaks appear strongly.

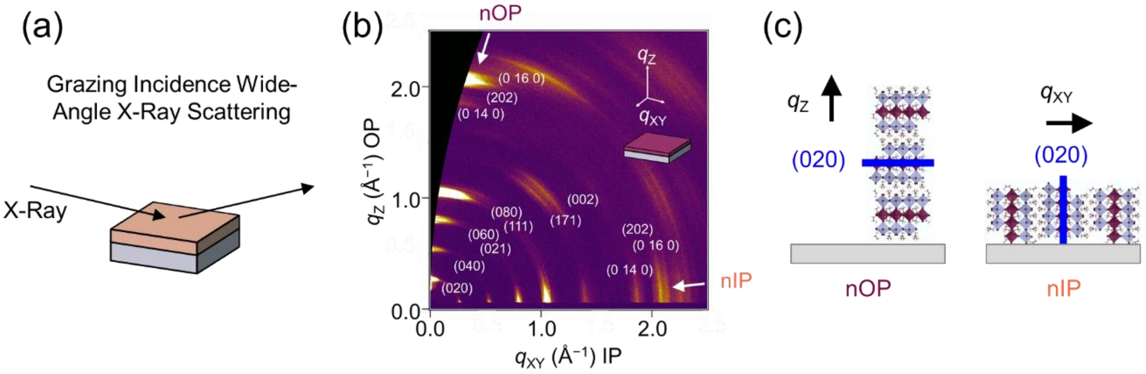

Figure 1.8. Grazing Incidence Wide-Angle Scattering (a) experiment, (b) example of pattern and (c) crystallite orientations corresponding to the pattern in (b). (See Chapter 4). Reproduced in part with permission from ACS Journals, submitted for publication. Unpublished work copyright 2021 American Chemical Society.

1.6 Outlook

Understanding degradation, phase behavior, and growth in HHP films is crucial for deployment of HHPs in optoelectronic devices. The first part of this thesis is dedicated to understanding film degradation mechanisms that may occur specifically during roll-to-roll processes. The second part explores phase stability and halide interdiffusion in mixed-halide 3D HHP phases. The third and fourth sections present methods for obtaining phase-pure n = 3 RP films and assess the roles of film strain and residual solvent in changing the emission properties of the resulting films. The results presented here enhance our understanding of fundamental properties of HHP films and extend the utility of HHPs for optoelectronic devices.

1.7 References

(1) Kojima, A.; Teshima, K.; Shirai, Y.; Miyasaka, T. Organometal Halide Perovskites as Visible-Light Sensitizers for Photovoltaic Cells. *J. Am. Chem. Soc.* **2009**, *131* (17), 6050–6051.

(2) Berry, J.; Buonassisi, T.; Egger, D. A.; Hodes, G.; Kronik, L.; Loo, Y. L.; Lubomirsky, I.; Marder, S. R.; Mastai, Y.; Miller, J. S.; et al. Hybrid Organic-Inorganic Perovskites (HOIPs): Opportunities and Challenges. *Adv. Mater.* **2015**, *27* (35), 5102–5112.

(3) Quan, L. N.; García de Arquer, F. P.; Sabatini, R. P.; Sargent, E. H. Perovskites for Light Emission. *Adv. Mater.* **2018**, *30* (45).

(4) Qi, X.; Zhang, Y.; Ou, Q.; Ha, S. T.; Qiu, C. W.; Zhang, H.; Cheng, Y. B.; Xiong, Q.; Bao, Q. Photonics and Optoelectronics of 2D Metal-Halide Perovskites. *Small* **2018**, *14* (31), 1–16.

(5) Li, Z.; Klein, T. R.; Kim, D. H.; Yang, M.; Berry, J. J.; Van Hest, M. F. A. M.; Zhu, K. Scalable Fabrication of Perovskite Solar Cells. *Nat. Rev. Mater.* **2018**, *3*, 1–20.

(6) Saliba, M.; Correa-Baena, J. P.; Wolff, C. M.; Stolterfoht, M.; Phung, N.; Albrecht, S.; Neher, D.; Abate, A. How to Make over 20% Efficient Perovskite Solar Cells in Regular (n-i-p) and Inverted (p-i-n) Architectures. *Chem. Mater.* **2018**, *30* (13), 4193–4201.

(7) Jaffe, A.; Lin, Y.; Beavers, C. M.; Voss, J.; Mao, W. L.; Karunadasa, H. I. High-Pressure Single-Crystal Structures of 3D Lead-Halide Hybrid Perovskites and Pressure Effects on Their Electronic and Optical Properties. *ACS Cent. Sci.* **2016**, *2*, 201–209.

(8) Mao, L.; Stoumpos, C. C.; Kanatzidis, M. G. Two-Dimensional Hybrid Halide Perovskites: Principles and Promises. *J. Am. Chem. Soc.* **2019**, *141* (3), 1171–1190.

(9) Protesescu, L.; Yakunin, S.; Bodnarchuk, M. I.; Krieg, F.; Caputo, R.; Hendon, C. H.; Yang, R. X.; Walsh, A.; Kovalenko, M. V. Nanocrystals of Cesium Lead Halide Perovskites (CsPbX3, X = Cl, Br, and I): Novel Optoelectronic Materials Showing Bright Emission with Wide Color Gamut. *Nano Lett.* **2015**, *15* (6), 3692–3696.

(10) Aftab, A.; Ahmad, M. I. A Review of Stability and Progress in Tin Halide Perovskite Solar Cell. *Sol. Energy* **2021**, *216* (January), 26–47.

(11) Mundt, L. E.; Tong, J.; Palmstrom, A. F.; Dunfield, S. P.; Zhu, K.; Berry, J. J.; Schelhas, L. T.; Ratcliff, E. L. Surface-Activated Corrosion in Tin-Lead Halide Perovskite Solar Cells. *ACS Energy Lett.* **2020**, *5* (11), 3344–3351.

(12) Goldschmidt, V. V. Die Gesetze Der Krystallochemie. *Naturwissenschaften* **1926**, *14*, 477–485.

(13) Gholipour, S.; Ali, A. M.; Correa-Baena, J. P.; Turren-Cruz, S. H.; Tajabadi, F.; Tress, W.; Taghavinia, N.; Grätzel, M.; Abate, A.; De Angelis, F.; et al. Globularity-Selected Large Molecules for a New Generation of Multication Perovskites. *Adv. Mater.* **2017**, *29* (38), 1–9.

(14) Burger, S.; Ehrenreich, M. G.; Kieslich, G. Tolerance Factors of Hybrid Organic-Inorganic Perovskites: Recent Improvements and Current State of Research. *J. Mater. Chem. A* **2018**, *6* (44), 21785–21793.

(15) Dohner, E. R.; Hoke, E. T.; Karunadasa, H. I. Self-Assembly of Broadband White-Light Emitters. *J. Am. Chem. Soc.* **2014**, *136* (5), 1718–1721.

(16) Grancini, G.; Roldán-Carmona, C.; Zimmermann, I.; Mosconi, E.; Lee, X.; Martineau, D.; Narbey, S.; Oswald, F.; De Angelis, F.; Graetzel, M.; et al. One-Year Stable Perovskite Solar Cells by 2D/3D Interface Engineering. *Nat. Commun.* **2017**, *8*, 1–8.

(17) Li, X.; Hoffman, J. M.; Kanatzidis, M. G. The 2D Halide Perovskite Rulebook: How the Spacer Influences Everything from the Structure to Optoelectronic Device Efficiency. *Chem. Rev.* **2021**.

(18) DeCrescent, R. A.; Venkatesan, N. R.; Dahlman, C. J.; Kennard, R. M.; Zhang, X.; Li, W.; Du, X.; Chabinyc, M. L.; Zia, R.; Schuller, J. A. Bright Magnetic Dipole Radiation from Two-Dimensional Lead-Halide Perovskites. *Sci. Adv.* **2020**, No. February, 1–11.

(19) Decrescent, R. A.; Du, X.; Kennard, R. M.; Venkatesan, N. R.; Dahlman, C. J.; Chabinyc, M. L.; Schuller, J. A. Even-Parity Self-Trapped Excitons Lead to Magnetic Dipole Radiation in Two-Dimensional Lead Halide Perovskites. *ACS Nano* **2020**, *14* (7), 8958–8968.

(20) Smith, M. D.; Connor, B. A.; Karunadasa, H. I. Tuning the Luminescence of Layered Halide Perovskites. *Chem. Rev.* **2019**, *119* (5), 3104–3139.

(21) Ma, Z.; Li, F.; Sui, L.; Shi, Y.; Fu, R.; Yuan, K.; Xiao, G.; Zou, B. Tunable Color Temperatures and Emission Enhancement in 1D Halide Perovskites under High Pressure. *Adv. Opt. Mater.* **2020**, *8* (18), 1–7.

(22) Mao, L.; Wu, Y.; Stoumpos, C. C.; Traore, B.; Katan, C.; Even, J.; Wasielewski, M. R.; Kanatzidis, M. G. Tunable White-Light Emission in Single-Cation-Templated Three-Layered 2D Perovskites (CH3CH2NH3)4Pb3Br10-XClx. *J. Am. Chem. Soc.* **2017**, *139* (34), 11956–11963.

(23) Luo, B.; Guo, Y.; Li, X.; Xiao, Y.; Huang, X.; Zhang, J. Z. Efficient Trap-Mediated Mn2+ Dopant Emission in Two Dimensional Single-Layered Perovskite (CH3CH2NH3)2PbBr4. *J. Phys. Chem. C* **2019**, *123* (23), 14239–14245.

(24) Smith, M. D.; Jaffe, A.; Dohner, E. R.; Lindenberg, A. M.; Karunadasa, H. I. Structural Origins of Broadband Emission from Layered Pb-Br Hybrid Perovskites. *Chem. Sci.* **2017**, *8* (6), 4497–4504.

(25) Cortecchia, D.; Neutzner, S.; Kandada, A. R. S.; Mosconi, E.; Meggiolaro, D.; De Angelis, F.; Soci, C.; Petrozza, A. Broadband Emission in Two-Dimensional Hybrid Perovskites: The Role of Structural Deformation. *J. Am. Chem. Soc.* **2017**, *139* (1), 39–42.

(26) Hu, T.; Smith, M. D.; Dohner, E. R.; Sher, M. J.; Wu, X.; Trinh, M. T.; Fisher, A.; Corbett, J.; Zhu, X. Y.; Karunadasa, H. I.; et al. Mechanism for Broadband White-Light Emission from Two-Dimensional (110) Hybrid Perovskites. *J. Phys. Chem. Lett.* **2016**, *7* (12), 2258–2263.

(27) Li, L.; Shang, X.; Wang, S.; Dong, N.; Ji, C.; Chen, X.; Zhao, S.; Wang, J.; Sun, Z.; Hong, M.; et al. Bilayered Hybrid Perovskite Ferroelectric with Giant Two-Photon Absorption. *J. Am. Chem. Soc.* **2018**, *140* (22), 6806–6809.

(28) Blancon, J. C.; Stier, A. V.; Tsai, H.; Nie, W.; Stoumpos, C. C.; Traoré, B.; Pedesseau, L.; Kepenekian, M.; Katsutani, F.; Noe, G. T.; et al. Scaling Law for Excitons in 2D Perovskite Quantum Wells. *Nat. Commun.* **2018**, *9* (1), 1–10.

(29) Venkatesan, N. R.; Mahdi, A.; Barraza, B.; Wu, G.; Chabinyc, M. L.; Seshadri, R. Enhanced Yield-Mobility Products in Hybrid Halide Ruddlesden-Popper Compounds with Aromatic Ammonium Spacers. *Dalt. Trans.* **2019**, *48* (37), 14019–14026.

(30) Cortecchia, D.; Yin, J.; Bruno, A.; Lo, S. Z. A.; Gurzadyan, G. G.; Mhaisalkar, S.; Brédas, J. L.; Soci, C. Polaron Self-Localization in White-Light Emitting Hybrid Perovskites. *J. Mater. Chem. C* **2017**, *5* (11), 2771–2780.

(31) Stoumpos, C. C.; Cao, D. H.; Clark, D. J.; Young, J.; Rondinelli, J. M.; Jang, J. I.; Hupp, J. T.; Kanatzidis, M. G. Ruddlesden-Popper Hybrid Lead Iodide Perovskite 2D Homologous Semiconductors. *Chem. Mater.* **2016**, *28* (8), 2852–2867.

(32) Saidaminov, M. I.; Abdelhady, A. L.; Murali, B.; Alarousu, E.; Burlakov, V. M.; Peng, W.; Dursun, I.; Wang, L.; He, Y.; Maculan, G.; et al. High-Quality Bulk Hybrid Perovskite Single Crystals within Minutes by Inverse Temperature Crystallization. *Nat. Commun.* **2015**, *6* (May), 7586.

(33) Lédée, F.; Trippé-Allard, G.; Diab, H.; Audebert, P.; Garrot, D.; Lauret, J. S.; Deleporte, E. Fast Growth of Monocrystalline Thin Films of 2D Layered Hybrid Perovskite. *CrystEngComm* **2017**, *19* (19), 2598–2602.

(34) Goswami, D.; Munera, J. C.; Pal, A.; Sadri, B.; Scarpetti, C. L. P. G.; Martinez, R. V.; Martinez, R. V. Roll-to-Roll Nanoforming of Metals Using Laser-Induced Superplasticity. *Nano Lett.* **2018**, *18* (6), 3616–3622.

(35) Ava, T. T.; Al Mamun, A.; Marsillac, S.; Namkoong, G. A Review: Thermal Stability of Methylammonium Lead Halide Based Perovskite Solar Cells. *Appl. Sci.* **2019**, *9* (1).

(36) Rolston, N.; Bush, K. A.; Printz, A. D.; Gold-Parker, A.; Ding, Y.; Toney, M. F.; McGehee, M. D.; Dauskardt, R. H. Engineering Stress in Perovskite Solar Cells to Improve Stability. *Adv. Energy Mater.* **2018**, *8* (29), 1–7.

(37) Ke, W.; Spanopoulos, I.; Tu, Q.; Hadar, I.; Li, X.; Shekhawat, G. S.; Dravid, V. P.; Kanatzidis, M. G. Ethylenediammonium-Based “Hollow” Pb/Sn Perovskites with Ideal Band Gap Yield Solar Cells with Higher Efficiency and Stability. *J. Am. Chem. Soc.* **2019**, *141* (21), 8627–8637.

(38) Weerasinghe, H. C.; Dkhissi, Y.; Scully, A. D.; Caruso, R. A.; Cheng, Y. B. Encapsulation for Improving the Lifetime of Flexible Perovskite Solar Cells. *Nano Energy* **2015**, *18*, 118–125.

(39) Hoke, E. T.; Slotcavage, D. J.; Dohner, E. R.; Bowring, A. R.; Karunadasa, H. I.; Mcgehee, M. D. Reversible Photo-Induced Trap Formation in Mixed- Halide Hybrid Perovskites for Photovoltaics. *Chem. Sci.* **2015**, *6* (613).

(40) Gualdrón-Reyes, A. F.; Yoon, S. J.; Barea, E. M.; Agouram, S.; Muñoz-Sanjosé, V.; Meléndez, Á. M.; Niño-Gómez, M. E.; Mora-Seró, I. Controlling the Phase Segregation in Mixed Halide Perovskites through Nanocrystal Size. *ACS Energy Lett.* **2019**, *4* (1), 54–62.

(41) Perini, C. A. R.; Doherty, T. A. S.; Stranks, S. D.; Correa-Baena, J.-P.; Hoye, R. L. Z. Pressing Challenges in Halide Perovksite Photovoltaics - From the Atomic to Module Level. *Joule* **2021**, *5*, 1–7.

(42) Jones, T. W.; Osherov, A.; Alsari, M.; Sponseller, M.; Duck, B. C.; Jung, Y. K.; Settens, C.; Niroui, F.; Brenes, R.; Stan, C. V.; et al. Lattice Strain Causes Non-Radiative Losses in Halide Perovskites. *Energy Environ. Sci.* **2019**, *12* (2), 596–606.

(43) Dahlman, C. J.; Decrescent, R. A.; Venkatesan, N. R.; Kennard, R. M.; Wu, G.; Everest, M. A.; Schuller, J. A.; Chabinyc, M. L. Controlling Solvate Intermediate Growth for Phase-Pure Organic Lead Iodide Ruddlesden-Popper (C4H9NH3)2(CH3NH3)n-1Pb NI3 N+1 Perovskite Thin Films. *Chem. Mater.* **2019**, *31* (15), 5832–5844.

(44) Quintero-Bermudez, R.; Gold-Parker, A.; Proppe, A. H.; Munir, R.; Yang, Z.; Kelley, S. O.; Amassian, A.; Toney, M. F.; Sargent, E. H. Compositional and Orientational Control in Metal Halide Perovskites of Reduced Dimensionality. *Nat. Mater.* **2018**, *17* (10), 900–907.

(45) Blancon, J. C.; Tsai, H.; Nie, W.; Stoumpos, C. C.; Pedesseau, L.; Katan, C.; Kepenekian, M.; Soe, C. M. M.; Appavoo, K.; Sfeir, M. Y.; et al. Extremely Efficient Internal Exciton Dissociation through Edge States in Layered 2D Perovskites. *Science* **2017**, *355* (6331), 1288–1292.

(46) Tan, W. L.; Cheng, Y. B.; McNeill, C. R. Direct Assessment of Structural Order and Evidence for Stacking Faults in Layered Hybrid Perovskite Films from X-Ray Scattering Measurements. *J. Mater. Chem. A* **2020**, *8* (25), 12790–12798.

(47) Shi, E.; Deng, S.; Yuan, B.; Gao, Y.; Akriti; Yuan, L.; Davis, C. S.; Zemlyanov, D.; Yu, Y.; Huang, L.; et al. Extrinsic and Dynamic Edge States of Two-Dimensional Lead Halide Perovskites. *ACS Nano* **2019**, *13* (2), 1635–1644.

(48) Yuan, M.; Quan, L. N.; Comin, R.; Walters, G.; Sabatini, R.; Voznyy, O.; Hoogland, S.; Zhao, Y.; Beauregard, E. M.; Kanjanaboos, P.; et al. Perovskite Energy Funnels for Efficient Light-Emitting Diodes. *Nat. Nanotechnol.* **2016**, *11* (10), 872–877.

(49) Tilley, R. J. D. An Electron Microscope Study of Perovskite-Related Oxides in the SrTiO System. *J. Solid State Chem.* **1977**, *21* (4), 293–301.

(50) Venkatesan, N. R.; Labram, J. G.; Chabinyc, M. L. Charge-Carrier Dynamics and Crystalline Texture of Layered Ruddlesden-Popper Hybrid Lead Iodide Perovskite Thin Films. *ACS Energy Lett.* **2018**, *3* (2), 380–386.

(51) Liang, C.; Gu, H.; Xia, Y.; Wang, Z.; Liu, X.; Xia, J.; Zuo, S.; Hu, Y.; Gao, X.; Hui, W.; et al. Two-Dimensional Ruddlesden–Popper Layered Perovskite Solar Cells Based on Phase-Pure Thin Films. *Nat. Energy* **2020**.

Chapter 2:

Structural Consequences of Repeated Bending: Ferroelastic Hysteresis in $MAPbI_3$ Films

2.1 Introduction

Hybrid halide perovskites of type $APbX_3$ have emerged as materials for solar cells and are attractive for a variety of other thin film electronic devices.[1–6] The highest power conversion efficiencies in solar cells have been achieved using compositional derivatives of tetragonal methylammonium lead iodide ($MAPbI_3$), by alloying MA^+ with Cs^+ and/or FA^+, or by alloying I^- with Br^-, to form $(Cs,FA,MA)Pb(Br,I)_3$.[1] Alloying of halides and introduction of large cations further provides a facile way to tune the band gap, making halide perovskites attractive for light emitting diodes or lasing applications.[3,5–10] A key advantage of hybrid halide perovskites over conventional semiconductors is the ease with which perovskites can be coated via roll-to-roll processing to form electronic devices.[11] A thorough understanding of the structural consequences of repeated bending, i.e., repeated strain application, on perovskites is therefore crucial. To date, strain in

$MAPbI_3$ films has been shown to affect defect concentration[12] and related properties such as degradation rate,[13,14] the activation energy of ion migration,[13] and the photoluminescence lifetime.[15]

Tetragonal MAPbI3 is ferroelastic, which complicates how it responds to mechanical strain. Ferroelasticity involves the spontaneous formation of sub-grain domains of differing orientation, the relative proportion of which can be changed by applying stress.[16–19] This phenomenon is common in a variety of materials, such as zirconia[20] or oxide and fluoride perovskites,[21,22] and has been increasingly investigated in halide perovskites.[23–32] At elevated temperatures many $APbX_3$ materials have higher symmetry, but as the material cools the R_4^+ phonon mode condenses, inducing permanent out-of-phase tilting of the BX_6 octahedra and a spontaneous strain in the material.[33–37] The strain magnitude is lowered by transition to a lower symmetry phase, which in $MAPbI_3$ is the cubic $Pm\bar{3}m$ to tetragonal $I4/mcm$ transition.[16,17,37–42] Mechanical constraints such as surrounding grains encourage twin domain formation, thus ensuring that the original macroscopic dimensions are maintained. Such domains have previously been observed in $MAPbI_3$.[24,25,29–31] Compositional derivatives of $MAPbI_3$ that are thought to be cubic on the bulk scale (e.g., $(Cs,FA,MA)Pb(Br,I)_3$) also exhibit twinning on the nanoscale.[23] Although processing conditions may affect the types of domains formed, twinning is inherent to tetragonal $MAPbI_3$ and is therefore observed in films of this material.[30]

Applying stress to a ferroelastic induces ferroelastic hysteresis, which involves semi-reversibly changing the relative proportion of different domains (“domain switching”) by inducing movement of the walls separating them.[18] Recent work shows that that the walls between twin domains in $MAPbI_3$ slow carrier diffusion in single crystals without any external strain applied.[43] Despite the increased attention paid to ferroelasticity in hybrid perovskites,[23,27,28,43–49] much still remains unknown. For example, in other materials, domain walls nucleate point defects and facilitate diffusion of ionic species.[50–53] Understanding how twin walls move and are created and annihilated is therefore crucial to the successful development of flexible $MAPbI_3$-based devices.

Here, we analyze the ferroelastic hysteresis loop of $MAPbI_3$ and its impact on the stability of polycrystalline films. Strain heterogeneity in previous reports that was linked to increased defect content was here found to originate from specific twin domains. Cyclic strain tests of films revealed the approximate stresses at which ferroelastic hysteresis initiated (coercive stress) and saturated, as well as the ways in which the stress–strain curve changed. The coercive stress revealed the thermal stress needed to change the domain population, which was estimated for different substrates. Changes to domain sizes and proportions revealed changes to the number of domain walls and were correlated closely with enhanced degradation of $MAPbI_3$. This behavior was related to particular strain cycles and can help explain differences in ion migration, degradation, and photoluminescence lifetime behavior observed in literature.

2.2 Experimental section

Materials

Lead(II) iodide was purchased from Sigma-Aldrich (PbI_2, 99.999% purity, trace metal basis) Methylammonium iodide (CH_3NH_3I, ≥99% purity) was purchased from Dyseol. N,N-dimethylformamide (DMF, 99.8%, anhydrous), dimethyl sulfoxide (DMSO,

≥99.9%, anhydrous), and chlorobenzene (99.8%, anhydrous) were purchased from Sigma-Aldrich and kept in a nitrogen glovebox.

Spin-Casting of Kapton-PEDOT: PSS-MAPbI$_3$-PMMA

Kapton sheets were cleaned via ultrasonication in isopropyl alcohol for 10 min. To stabilize the Kapton against further changes during heating, the cleaned sheets were carefully put between two aluminum plates and protected with very flat Al sheets, and the stack was heated at ≈350 °C for 2 h on a hot plate in a N_2-filled glovebox. Following this, the heat was turned off and the stack was allowed to cool naturally to room temperature. The pretreated Kapton sheets were then exposed to an oxygen plasma at ~300 mTorr for 10 min, with air as the oxygen source. To keep the Kapton flat during spin-casting, the Kapton sheets were gently placed onto a glass slide covered with a thin PDMS sheet (for information on making the PDMS sheet, see ref 7). For annealing, the Kapton sheets were then removed from the glass-PDMS support. Care was taken to not bend the Kapton sheets during any of these steps. PEDOT: PSS (≈300 μL) was spin-cast in air onto the treated Kapton substrates at 2000 rpm for 10 s. The Kapton-PEDOT: PSS stack was annealed at 130°C for 4 min. To ensure film smoothness, (1) Kapton substrates of at least 2 cm × 2 cm size were required, and (2) the PEDOT: PSS spin-casting and annealing procedures were repeated a second time, with the second annealing being 6 min. The samples were then transferred to a nitrogen-filled glovebox for MAPbI$_3$ and PMMA spin-casting. The precursor solution for MAPbI$_3$ was fabricated in a nitrogen-filled glovebox. PbI_2 and CH_3NH_3I were dissolved in 1 mL of DMF and 96 μL of DMSO to make a 1 M solution, and the mixture was stirred overnight under mild heating (60 °C). The solution was then spin-cast onto the Kapton-PEDOT: PSS at 1000 rpm for 10 s and then

4000 rpm for 30 s. When 8 s passed after the spin turned to 4000 rpm, 0.2 mL of anhydrous chlorobenzene was dropped on the substrate (23 s before the end of the coating). The films were then immediately annealed at 100°C for 10 min on a hot plate, again in a nitrogen-filled glovebox. All temperatures were verified with a thermocouple. PMMA was then cast onto Kapton-PEDOT: PSS-$MAPbI_3$ as a capping layer. A total of 60 µL of a 25 mg/mL solution of PMMA in toluene was spin-cast onto the stack at 2000 rpm for 30 s, and no further annealing treatment was performed.

GIWAXS Characterization

Grazing incidence wide-angle X-ray scattering (GIWAXS) experiments were performed on beamline 11-3 (12.7 keV, wiggler side-station) at the Stanford Synchrotron Radiation Lightsource (SSRL). The source-to-detector (two-dimensional Rayonix MX225 CCD) distances were calibrated using lanthanum hexaboride (LaB6). All raw images were geometrically corrected using Nika. Sections (cakeslices) of the 2D GIWAXS patterns at specific angles were selected and integrated to obtain 1D patterns. GIWAXS analysis was performed primarily on two cake slices: the first near-out-of-plane ("nOP", 18°–23°, Figure 1c) and the second near-in-plane ("nIP", 67°–72°). Both cake slices were chosen to be 18° from 0° and 90°. Due to the sample roughness and to avoid double diffraction issues, a large incidence angle (2°) was chosen, resulting in the entire $MAPbI_3$ film thickness being probed and the near-0° angles being cut off. Nevertheless, the parameters chosen enabled clear determination of near-in-plane vs near-out-of-plane twin orientations and of the strain magnitudes of the planes in each domain. All patterns were converted to d from q, and all peaks were fit to Pseudo-Voigt patterns using Igor, with Gaussian and Lorentzian contributions kept constant (Igor Multipeak "shape" factor of 1) across all peaks and samples. The *d*-spacings of the peaks in Figure 3a were then compared with measured *d*-spacings of $MAPbI_3$ single crystals at 300°K to assign the (220) vs (004) nature and to calculate the strain magnitude (see also discussion of Figures 3 and S3).

Other Characterizations

Scanning electron microscopy was performed using an FEI Nova Nano 650 FEG SEM operating at the 10–20 keV accelerating voltage with beam currents of 0.40–0.80 nA. For SEM measurements, the samples were sputter-coated with gold to prevent charging. No PMMA was cast on samples used for top-down measurements, to get accurate grain size measurements. Powder X-ray diffraction patterns were obtained using a Panalytical Empyrean powder diffractometer in reflection mode with a CuKα source, operating with an accelerating voltage of 45 kV and beam current of 40 mA.

2.3 Results and discussion

2.3.A. *Identifying Sets of Twin Domains Using GIWAXS*

We cast $MAPbI_3$ on polyimide (Kapton) and characterized the resulting films using Grazing Incidence Wide Angle X-ray Scattering (GIWAXS) (**Figure 2.1a**). PEDOT:PSS was cast to planarize the Kapton surface, and was selected because it is a widely-used hole transport layer in perovskite photovoltaic devices.[54,55] $MAPbI_3$ was then spin-cast following previously-described procedures (see **Experimental Section**),[7] with an antisolvent rinse and 100°C annealing steps.[1,56] Scanning Electron Microscopy (SEM) (**Figure 2.S1**) revealed that the $MAPbI_3$ film exhibited 200 ± 100 nm grain size and ≈ 400 nm thickness. PMMA was then cast on top of the $MAPbI_3$ to prevent degradation, [57] as subsequent experiments were largely performed in air. No X-ray scattering features of PbI_2 were observed (expected peak at $q \approx 0.9$ Å^{-1}; **Figure 2.1c**). The ring-like shape taken by the features in the 2D pattern (**Figure 2.1c**) indicates a distribution of orientations of $MAPbI_3$ crystallites, consistent with prior electron back scatter detection (EBSD) work on polycrystalline films.[58] To better understand correlations between these differing orientations and ferroelastic domains, small areas of the 2D GIWAXS patterns were integrated to form 1D patterns along two select orientations, near-in-plane (nIP) and near-out-of-plane (nOP) (**Figure 2.1c**). Details related to the analysis of the GIWAXS patterns are given in the **Experimental Section** and in **Figure 2.S2**. The large incidence angle (2°) was chosen so that the X-Rays penetrated the entire $MAPbI_3$ depth (calculated penetration depth 1000 nm; [59,60] **Figure 2.1a**); and observation of substrate peaks (**Figure 2.1c**) confirmed that the entire depth was probed. Because the GIWAXS beam area was several mm^2, the results below are representative of the bulk of the $MAPbI_3$ film.

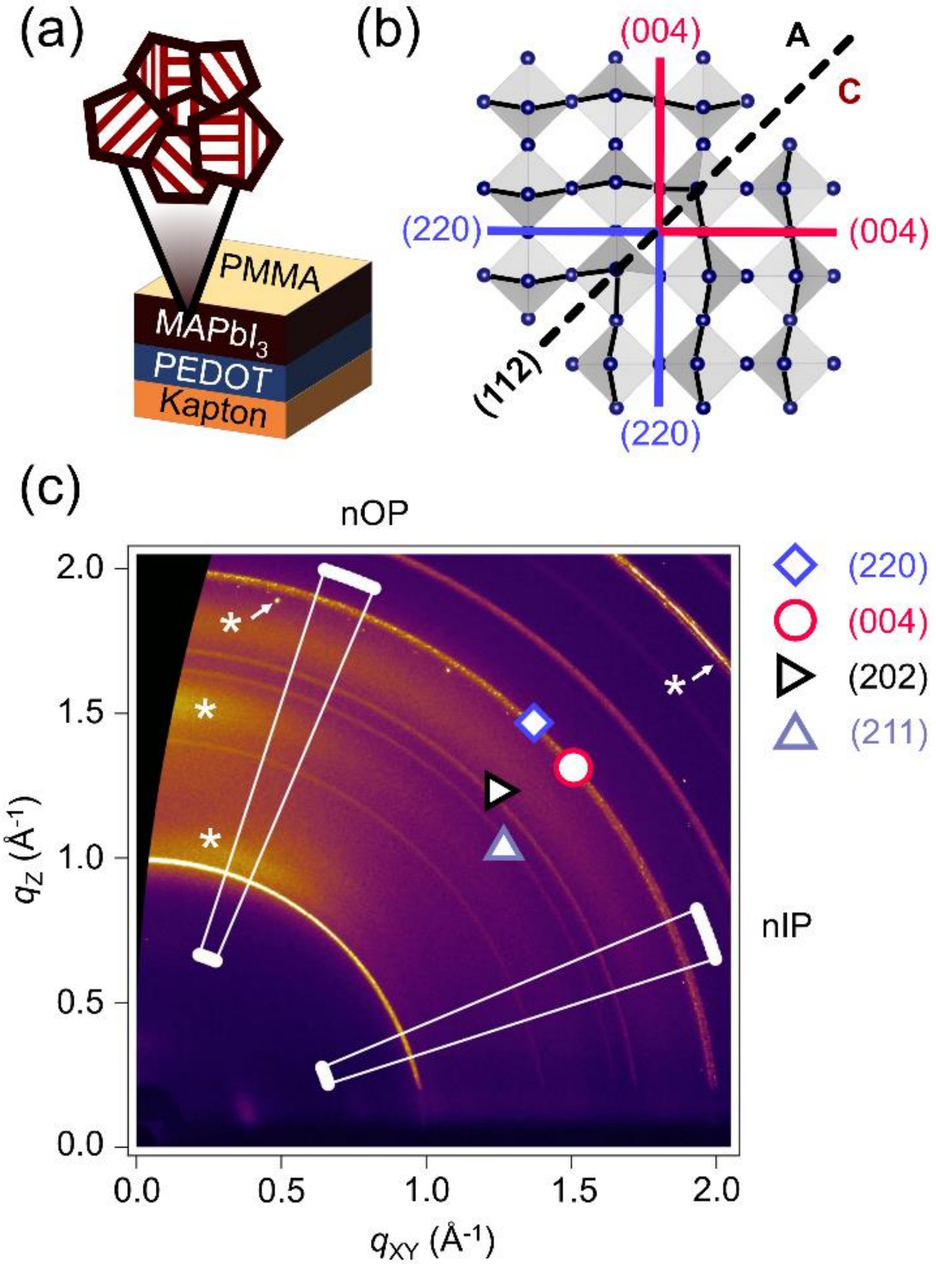

Figure 2.1. (a) Schematic of the samples as-prepared, with a Kapton substrate, a PEDOT: PSS planarization layer, $MAPbI_3$, and a PMMA encapsulation layer. GIWAXS X-Rays with incidence angle 2° penetrate roughly 1000 nm into the sample (throughout the whole $MAPbI_3$ film thickness), [59,60] over an area of several mm^2. (b) Twinning in $MAPbI_3$ grains, with crystallographic structure of two twin domains of $MAPbI_3$ following reference, [24] and with $MAPbI_3$ in the I4/*mcm* tetragonal phase.[24,37] The (220) and (004) planes are shown, as well as the (112) mirror plane (twin boundary/domain wall) separating the domains, and A and C twin types. (c) GIWAXS pattern of an as-cast $MAPbI_3$ film, showing the areas integrated for near-out-of-plane (nOP) analysis (18°-23°) and near-in-plane (nIP) analysis (67°-72°). The (220), (004), (202) and (211) rings are labelled. The asterisks correspond to substrate peaks (i.e. Kapton-PEDOT: PSS only; no $MAPbI_3$ or PMMA). Although appearing to overlap in this 2D pattern, the (220) and (004) peaks are distinguishable (see below).

The predominant twin domain structure and twin domain types observed by GIWAXS are shown in **Figure 2.1** and in **Figure 2.2**. At room temperature, $MAPbI_3$ is in the tetragonal I4/mcm phase,[37–42] with several ferroelastic domains cohabitating in the same grain (**Figure 2.1a-b**).[24,25,30] Previous Transmission Electron Microscopy (TEM) work[24] revealed that the (112) plane acts as a boundary between different domains (also called domain wall), and is also a mirror plane to these domains. Because we primarily saw ferroic *a* and *c* domain types (see below - **Figure 2.2**, **2.3**, **2.6**, **2.7**), we named the domains observed A and C.[61,62] To distinguish A vs. C, we used the scattering intensities and positions in reciprocal space of the (220) and (004) planes. The (220) nOP peak and associated (004) nIP peak revealed Domain A, while the (220) nIP peak and associated (004) nOP peak revealed Domain C (**Figure 2.1b**, **Figures 2.2-2.3**). However, the (220) and (004) planes have similar *d*-spacings in the 2D patterns (**Figure 2.1c**). For this reason, we additionally examined the evolution of the intensity of the (211) peak with respect to the (202) peak (see discussion of **Figure 2.S3**). Importantly, the analysis of the intensities of the (220) vs. (004) peaks also allowed us to extract the relative fraction of Domains A vs. C in the film, and how this proportion changed after bending.

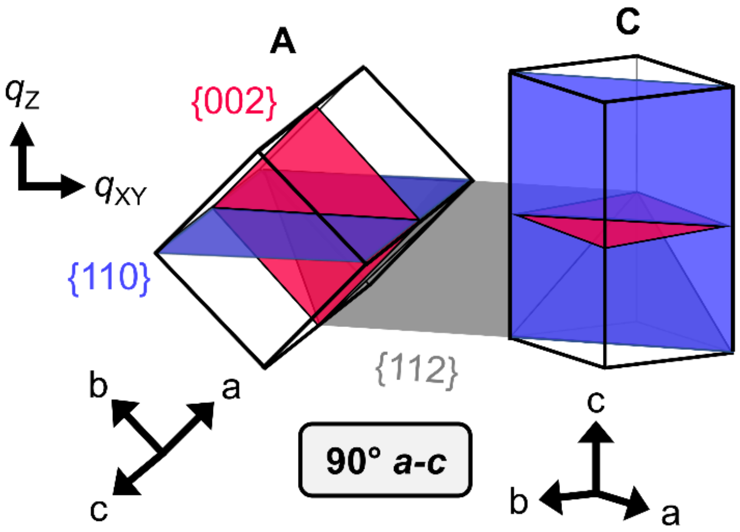

Figure 2.2. Summary schematic showing A and C domains, with preferential 90° *a*-*c* arrangement. [61,62]

Films that had not experienced mechanical deformation exhibited both A and C domain types (**Figure 2.3**). **Figure 2.3a** shows nOP and nIP patterns of an as-cast sample. The main nOP peak (near 3.14 Å) was assigned to a (220) plane, which is consistent with a higher intensity of the (211) peak appearing nOP (**Figure 2.3b**, see discussion of **Figure 2.S3**). This preference for the nOP orientation of the (220) plane is consistent with what is typically observed for $MAPbI_3$ films. [31] In the nIP pattern, the peak near 3.16 Å was considerably more intense than in the nOP direction, and the (211) peak was much weaker, indicating less scattering from the (220) peak in the nIP direction. We therefore assigned the nIP peak near 3.16 Å to be the (004) plane that corresponds to crystallites with (220) planes oriented nOP. Based on these two assignments, there is a considerable population of A-type domains in the film. Thus, the typically-observed strong presence of (220) in films [31] corresponds to Domain A.

Since $MAPbI_3$ is a ferroelastic, twin domains exhibit the same crystal structure, but in different orientations. Therefore, the strains of (220) planes in different twinned domains should be equal. The nIP peak near 3.14 Å was thus assigned to (220) and the nOP peak near 3.16 Å was thus likely (004). These two peak assignments reveal Domain C. The two populations identified here, Domains A and C, are consistent with the well-established 90° *a*-*c* configuration, hence our nomenclature for the domains (**Figure 2.2**).[61,62] Further analysis of the domains required correcting the intensities for structure factor (see **Appendix to Chapter 2**). We note that there were two other weaker peaks in this region, one near 3.12 Å and the other near 3.18 Å, with the latter being stronger in the nIP direction. The peak at 3.12 Å in particular appeared much more strongly after bending (**Figure 2.7a**). We thus appear to have two sets of twin domains: Twin Set 1 (TS1), that is dominant, with domains A:1 and C:1, and a smaller population of Twin Set 2 (TS2).

2.3.B. *Correlating Strain Heterogeneity with Ferroelastic Domains*

We analyzed the strain of all peaks, allowing the assignment of peaks to TS2 (**Figure 2.3a, 2.3d**). The structure of I4/*mcm* $MAPbI_3$ in single-crystal form has been extensively studied, with broad agreement regarding lattice parameters at various temperatures. [37–42] Here, we selected the unstrained *d*-spacings at 300°K from a neutron-diffraction study of $MAPbI_3$ single crystals, chosen due to the precision of the method. [37] Strain was calculated based on shift from these unstrained *d*-spacings. To ensure consistency, we took patterns of four film samples and calculated average *d*-spacings and *d*-spacing uncertainties. For TS1, the (220) peak (near 3.14 Å), hereafter called "(220):1", exhibited weak tensile strain (+ 0.08 ± 0.03 %). The (004) peak in TS1 (near 3.16 Å, "(004):1") exhibited compressive strain (− 0.37 ± 0.09 %). It is expected that the (220) and (004) planes of domains A and C for TS1 exhibit the same strain, as these domains should only differ in their orientation. For TS2, based on the improbability of having domains with strains ≥ 1.5 %, we assigned the peak near 3.12 Å to the (220) plane and the peak near 3.18 Å to the (004) plane. Thus, for TS2, we have compressive strain (− 0.39 ± 0.13 %) for (220):2, and large tensile strain (+ 0.8 ± 0.4 %) for (004):2. The relative intensities of (220):2 and (004):2 roughly follow those of (220):1 and (004):1, likely indicating A and C domain types for TS2 as well, called A:2 and C:2. The strains from the (220) peaks for both twin sets are approximately a third of the magnitudes of the strains of the (004) peaks, and opposite in sign, matching what is expected from Poisson's ratio of 0.33.[63] Thus, the strains identified are consistent with the film having two twin sets, each containing *a* and *c* type twin domains.

Importantly, we establish a correlation between the heterogeneity of strain in the films and the ferroelastic domains (**Figure 2.3d**). Sub-grain changes to strain and orientation were previously observed, but were not correlated with ferroelastic domains.[58] The *d*-spacings of the (220) peak were shown to vary by ≈ − 0.2 % within films, with the more compressed regions having higher defect densities.[12] Here, we show that variations in *d*-spacing in films correlate with different ferroelastic domains. Specifically, large compressive (220) strains originate from a different twin set. The large strains and small population of TS2 throughout the entire film thickness (**Figure 2.1a**) suggest that TS2 originates from unfavorable growth conditions such as rapid solvent removal, spatial constrains imposed by grain boundaries, and other factors. Because TS2 exhibits larger strains than TS1, it is more likely to appear in areas in which local strain is greater, such as near grain boundaries or at the substrate interface (**Figure 2.3d** and

2.7). The films are dense with few pinholes (**Figure 2.1a**) and it is possible that TS2 may help offset strain gradients within the film.

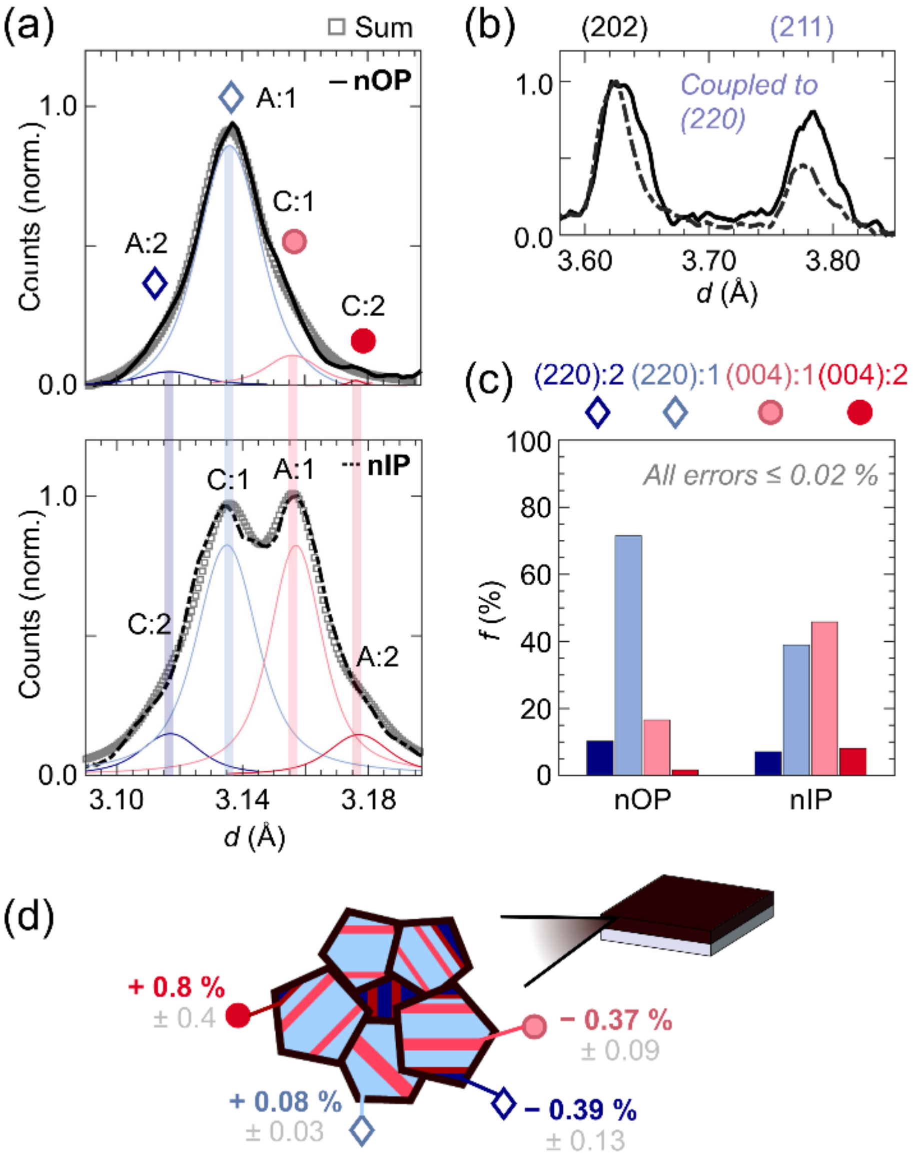

Figure 2.3. (a) GIWAXS near-out-of-plane (nOP) and near-in-plane (nIP) patterns of an as-cast $MAPbI_3$ film, with assignments to various (220) or (004) and twin domain type labelled. nOP and nIP patterns are normalized to highlight the relative contributions of different (220) and (004). Each fit is shown individually, as is the sum of the fit peaks. (b) (202)-(211) region of the nOP and nIP patterns (see **Figure 2.S3**), normalized with respect to the (202) for (211) intensity comparison. (c) Fraction *f* of the film exhibiting the different (220) and (004) orientations nOP and nIP for the patterns in (a). Average fractions for 4 samples are shown in **Figure 2.S4**. (d) Summary schematic of the sub-grain twinning microstructure identified here, with two possibilities for Twin Set 2 location (separate small grains and boundaries of grains that are predominantly Twin Set 1). Strains associated with the (220) and (004) peaks are listed (calculated from peak shifts from the single crystal structure at 300°K [37]) and were calculated from the average and standard deviation for 4 samples.

2.3.C. *Determining Volume Fractions of Ferroelastic Domains*

Next, we calculated the relative fraction *f* of each domain in the film (see **Appendix to Chapter 2**). The fractions for the patterns shown in **Figure 2.3a** are shown in **Figure 2.3c**, and the averaged fractions for four samples are shown in **Figure 2.S4**. We distinguish two fractions *f*, obtained respectively from the nOP and nIP patterns. The distinction is necessary, as nOP scattering detects most planes parallel to the substrate; however, nIP scattering can miss a significant number of planes perpendicular to the substrate (**Figure 2.S5**), in crystallites that otherwise have nOP planes visible. Thus, we extract volume fraction from the nOP patterns, and use the nIP patterns to qualitatively confirm our interpretations. The large incidence angle (2°) means the entire film thickness is considered (**Figure 2.1**).

From the nOP pattern (**Figure 2.3a**), ≈ 70 % of the film exhibits (220):1, with ≈ 20 % of the film exhibiting (004):1 and another ≈ 10 % exhibiting some combination of (220):2 and (004):2, with a greater amount of (220):2 (**Figure 2.3c**). This confirms the predominance of A-type domains. The results in **Figure 2.3** were also reproduced for 3 subsequent films, with between 80-100% of fractions *f* from the nOP patterns belonging to TS1, and the remaining 0-20 % being TS2 (**Figure 2.S4**). Analysis of nIP patterns revealed ≈ 45 % and ≈ 40 % for the (004):1 and (220):1 respectively, in agreement with both 80-100 % of the film being TS1, and with there being some invisible peaks nIP (**Figure .S5**). Some of the lack of agreement between nOP and nIP fractions could also originate from the grains being rotated in-plane with respect to each other. Another possibility is that we have some 90° *a-a* twinning, involving two A-type domains, where the domain wall belongs to the {112} family. This 90° *a-a* configuration is the structural equivalent of the 90° *a-c* configuration (**Figure 2.2**), but with a different orientation.[62] Prior work reported 90° *a-a* configuration for films cast directly on TEM grids,[24] rather than the predominant 90° *a-c* configuration observed here under different growth conditions. To circumvent questions of nIP plane invisibility vs. in-plane grain rotation vs. of 90° *a-c* / 90° *a-a* twinning type, we restrict quantitative analysis of fractions to the nOP patterns. Overall, the films are 80-100% TS1 and 0-20 % TS2, with a preference for 90° *a-c* twinning type (**Figure 2.2**, **2.3d**).

2.3.D. *Residual Stress in $MAPbI_3$ Films on Flexible Substrates*

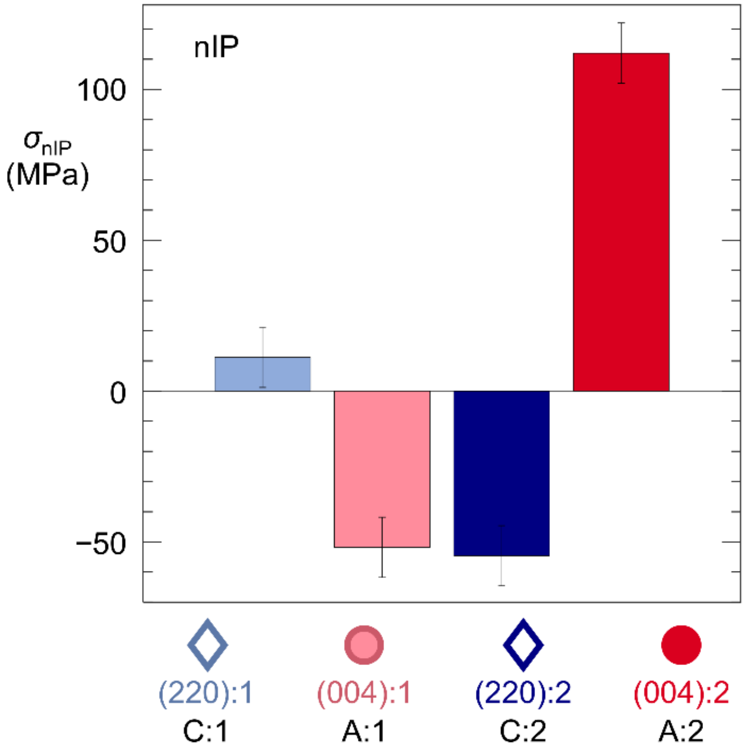

Figure 2.4. Conversion of the strains of (220):1, (004):1, (220):2 and (004):2 to stresses, with the corresponding nIP twin domains labelled. All error bars refer to the standard deviation from 4 samples.

Because the impacts of thermal stress from the substrate have garnered much interest, [13,14,64] we also quantified the nIP stresses of the four domains (**Figure 2.4**). We multiplied the strains identified for (220):1, (004):1, (220):2 and (004):2 (C:1, A:1, C:2

and A:2, nIP) by the Young's modulus for $MAPbI_3$ (14 GPa, chosen to be mid-range among reported values) and plotted these stresses in **Figure 2.4**. [63,65–67] Because the modulus is nearly directionally isotropic, [67] we multiplied the strains by the same modulus for (220) and (004) values to get the nIP stresses. These stresses were 11, − 52, − 55 and 112 (± 10) MPa for (220):1, (004):1, (220):2 and (004):2 respectively. As discussed above (**Figure 2.1a**), these are representative of the entire film depth. In prior work, switching from a silicon substrate with low thermal expansion coefficient or T.E.C. (0.26×10^{-5}/K) to a polycarbonate substrate with similar T.E.C. (6.5×10^{-5}/K) to those reported for $MAPbI_3$ ($4\text{-}16 \times 10^{-5}$/K) [68,69] was reported to greatly reduce the average residual in-plane stress, as measured via wafer curvature. [14] However, the contributions of individual twin domains to this stress were not elucidated. Here, we have a Kapton substrate (T.E.C. $3\text{-}11 \times 10^{-5}$/K) [70,71] and PEDOT: PSS planarization layer (T.E.C. 5×10^{-5}/K), [72] with similar T.E.C. to $MAPbI_3$ ($4\text{-}16 \times 10^{-5}$/K), [68,69] and a PMMA capping layer that also has similar T.E.C. ($5\text{-}10 \times 10^{-5}$/K). [73] Because $\text{T.E.C.}_{\text{Kapton/PEDOT: PSS}} \approx \text{T.E.C.}_{\text{Polycarbonate}}$ and because the films in prior work [14] were also processed at 100°C, we compared the individual domain stresses to the reported average stress of $MAPbI_3$ on polycarbonate (12 ± 2 MPa). With the exception of the (220):1, all of the individual domain stresses exhibited much larger magnitude than the average stress of $MAPbI_3$ on polycarbonate, with some exhibiting opposite sign. Notably, most individual domain stress magnitudes were of equal or larger magnitude to the average stress reported for $MAPbI_3$ on Si (54 ± 8 MPa). These results demonstrate that the residual stresses of individual twin domains in $MAPbI_3$ can be quite large even when using a substrate of similar T.E.C..

2.3.E. *Expected Ferroelastic Behavior upon Bending*

The ferroelastic hysteresis loop for $MAPbI_3$ has not yet been characterized in detail. Therefore, we analyzed structural changes caused by repeated bending, which is of interest for the behavior flexible devices. We will first describe expected ferroelastic behavior (**Figure 2.5**), then discuss the effects of repeated bending on film structure (**Figures 2.6**, **2.7**, **2.8**) and stability (**Figure 2.9**). We then relate our findings to existing literature on defect behavior in $MAPbI_3$, as domain walls have been found to nucleate vacancies and facilitate ion diffusion in other materials.[50–53]

Ferroelastic hysteresis involves non-linear, but to limited extent, reversible switching from one domain type to another; in our case, from domain A to domain C (**Figure 2.5a**). [18,74] This is accomplished by applying tensile strain (or stress) in q_X, which causes the domain wall to move, provided that the applied stress has some minimum magnitude corresponding to the coercive stress σ_C. Thus, the bond distances between the Pb^{2+} ions and the I^- ions change *at the domain wall, on the side of domain A*, such that eventually the octahedral tilting of domain C *at the domain wall* becomes more energetically favorable. [18] The domain wall thus advances through A and converts all the octahedral tilting to that of C. Correspondingly, the orientations of the (220) and (004) planes become that of C. If the material is under an opposite (compressive) stress in q_X, the octahedral tilting of A becomes again more favorable, so the domain wall moves back through C and A becomes bigger. Thus, while being somewhat reversible, the process is highly non-linear (**Figure 2.5b**), and the domain sizes after a full ferroelastic hysteresis loop may not be the same as they were initially. Saturation S (**Figure 2.4b**) is achieved when all possible switching to either A or C has occurred. Domain switching also imparts an inelastic strain ε_{i} on the material [20,21] that is retained after the applied strain is removed. This retention enabled us to indirectly analyze the ferroelastic hysteresis loop.

Ferroelastic hysteresis is one part of the stress-strain curve for ferroelastics. An idealized curve based on the literature for various oxide perovskites and zirconia is presented in **Figure 2.5c**. [20–22,75] Upon fabrication, a spontaneous strain ε_{S} exists in the material. At very low applied stresses (between point 1 and σ_{C}), there is an elastic-only regime, in which the domain walls do not move and bonds between atoms simply stretch or compress. At the coercive stress σ_{C}, ferroelastic hysteresis begins (**Figure 2.5b-2.5c**). In this regime, the types of strains acquired by the material are assigned differently from study to study; [20–22] but it is generally agreed that ferroelastic hysteresis imparts inelastic strains on the material, which for simplicity, we call the inelastic strain ε_{i}. The end of the ferroelastic hysteresis regime is marked by saturation *S*, at which point all possible domain switching has occurred. After this ferroelastic regime, a second mostly-elastic regime (until point 2) occurs, followed by the fully plastic regime (points 2-3) and fracture. For applied stresses below the fully plastic regime, the total strain in the material is $\varepsilon_{\mathrm{tot}} = \varepsilon_{\mathrm{Elastic}} + \varepsilon_{\mathrm{i}}$; where $\varepsilon_{\mathrm{Elastic}}$ is elastic strain and ε_{i} is the inelastic strain. Some ferroelastics exhibit large plastic regimes, [20] others less so, [21,22] indicated by two possible locations for fracture. Experiments on free-standing $\mathrm{MAPbI_3}$ films identified only a single mostly-linear elastic regime before fracture. [76] This indicates 1) that that the fully plastic regime is likely quite small and 2) that the slopes both quasi-elastic regimes and the ferroelastic hysteresis regime are likely quite similar. In **Figure 2.5c**, we have drawn them to be very different for clarity. For any stress larger than σ_{C}, if the applied stress is removed ("Unloading" in **Figure 2.5c**), the material does not go back to its initial state, due to the inelastic strain ε_i. Subsequent re-loading occurs much more closely to the Unloading (dashed) line in **Figure 2.5c** than to the original curve. In the following experiments, we focus particularly on the unloading/re-loading behavior to indirectly study the hysteresis loop.

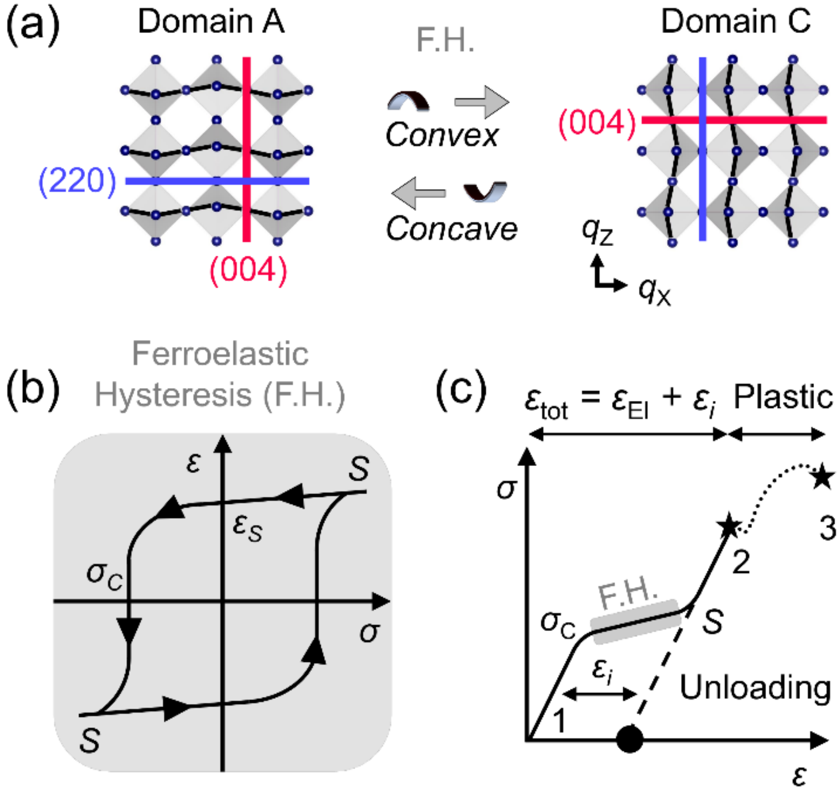

Figure 2.5. (a) Expected structural changes during ferroelastic hysteresis; tetragonal crystal structure from reference.[37] *Convex* bending applies tensile in-plane strain and *concave* bending applies compressive in-plane strain. (b) Ferroelastic hysteresis loop and (c) Idealized stress-strain curve for a ferroelastic based on prior work,[20–22] where ε_S, ε_i, ε_{tot}, $\varepsilon_{Elastic}$ are the spontaneous, inelastic, total and elastic strains respectively, *S* is the saturation point, and σ_C is the coercive stress. The stars indicate fracture point locations for different materials. GIWAXS patterns were collected after unloading the applied stress (black dot on the stress-strain curve).

The bending experiment is schematically shown in **Figure 2.S7**, and referenced in **Figure 2.5a.** The $MAPbI_3$ stack was repeatedly bent around cylinders and then released, with two different bending configurations used. Following the naming convention used in prior works, [13–15] *convex* bending ("outward" bending) involves having the Kapton substrate touch the cylinder, with $MAPbI_3$/PMMA on the outside, and *concave* bending (“inward” bending) involves having $MAPbI_3$/PMMA touch the cylinder with Kapton on the outside (**Figure 2.5**, **2.S7**). Thus, strain ε_X is applied along q_X, and strains ε_Y and ε_Z are induced in q_Y and q_Z, following the coordinate system of **Figure 2.S7**. Convex bending results in tensile ε_X (compressive ε_Y and ε_Z) and concave bending results in compressive ε_X (tensile ε_Y and ε_Z). Several bending diameters were selected and the applied strains $|\varepsilon_X|$ were calculated following the methodology outlined in the **Appendix to Chapter 2**.[63,65–67,77–79] Using Poisson’s ratio (0.33), [63] the induced strains $|\varepsilon_Z|$ in q_Z were then approximated (**Table 2.1**). We verified via SEM that applying these strains did not cause readily observable fracture of the films (**Figure 2.S8**). Prior to bending, the film was isotropic in-plane, as the small thermal expansion mismatch between the polymer substrate (T.E.C. 3-11 × 10^{-5}/K, [70,71]) and $MAPbI_3$ (T.E.C. 4-16 × 10^{-5}/K, [68,69]) induced a mild biaxial in-plane strain. We collected GIWAXS patterns immediately after the applied strain was relieved, i.e. after “Unloading” (**Figure 2.5**), and we call these post-bending samples “unbent”.

Diameter (mm)	$\mid \varepsilon_X \mid$ (%)	$\mid \varepsilon_Z \mid$ (%)
35	0.34	0.10
31	0.39	0.12
18	0.67	0.20
10	1.26	0.41
4.1	3.06	1.01

Table 1. List of diameters employed and the corresponding applied strains $|\varepsilon_X|$ and induced strains $|\varepsilon_Z|$ to the q_X and q_Z directions respectively.

2.2.F *Sweeping Through the Ferroelastic Hysteresis Loop by Bending.*

Bending with a diameter of 10 mm (**Figure 2.6**) induced clear signatures of ferroelastic hysteresis. **Figure 2.6a** shows the evolution of the nOP patterns of a film after up to 12 *convex* bending cycles around a 10 mm diameter. Following this, the film was bent *concavely* up to 12 times. After *convex* bending, the initial (220):1 intensity decreased, in favor of the (004):1 intensity increasing. Subsequent *concave* bending restored the (220):1 intensity. These observations were backed by quantitative analysis of the fractions for all peaks (**Figure 2.6b**) and by the decrease (*convex* bending) then increase (*concave* bending) of the (211) intensity (**Figure 2.S9**). Thus, A:1 domains were replaced by C:1 domains upon *convex* bending, and this process was generally reversed upon subsequent *concave* bending. However, the strong retention of (220):1 intensity (**Figure 2.6a**-2.**b**) suggests that the domain walls did not move very far. Some changes in (220) and (004) strains were observed after bending; however, the origins of these were not clear (see discussion of **Figure 2.S12**).

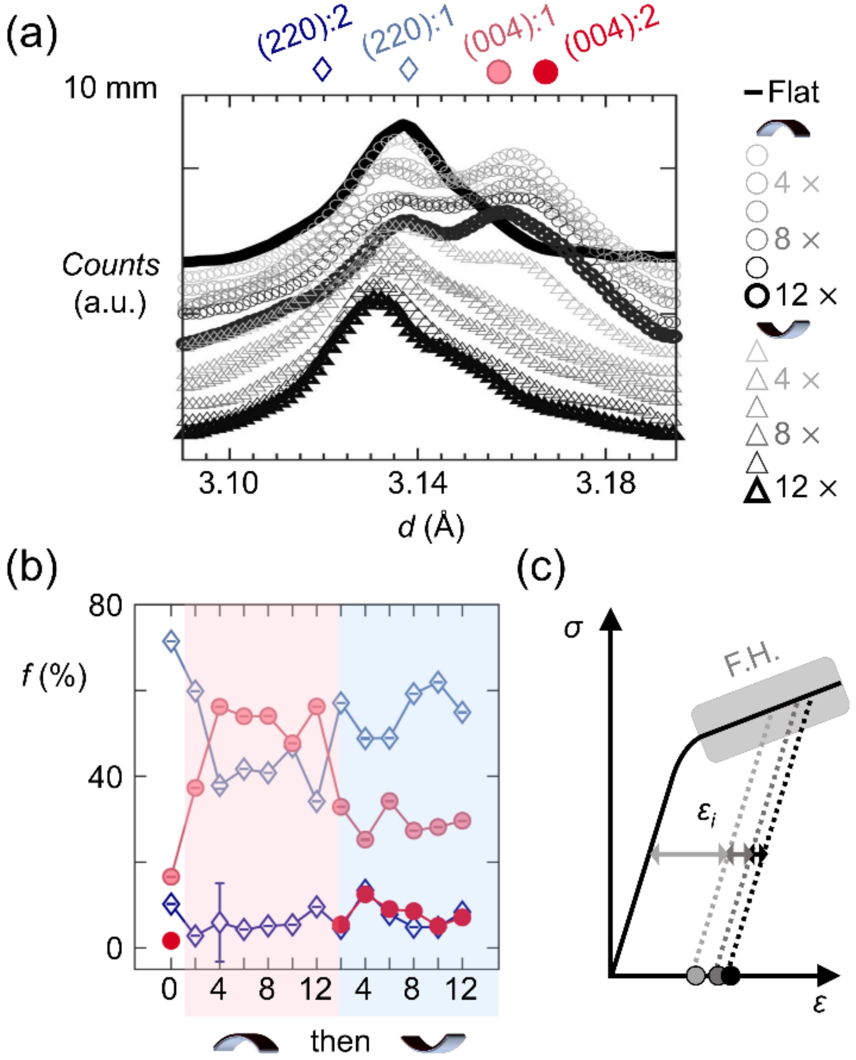

Figure 2.6. 10 mm bending experiment. (a) GIWAXS nOP patterns in the (004)-(220) region for the successive *convex* and *concave* bending around a 10 mm diameter. For the (220):1, (004):1, (220):2 and (004):2 peaks in these patterns, (b) corrected fractions *f* of the total scattered intensity in the peaks from (a). (c) Relationships between the observed domain switching and the stress-strain curve.

The changes observed can be correlated with the stress-strain curve, shown in **Figure 2.6c**. In cycles 4-12 for both *convex* and subsequent *concave* bending, the fractions plateaued at consistent values (**Figure 2.6b**), indicating that after cycle 4, the amount of A vs. C was stable. This suggests that during the first *convex* bending, $MAPbI_3$ followed the initial stress-strain curve, and the A:C domain ratio changed. When the applied stress was removed, the curve followed the unloading line (dashed). Subsequent re-loading and unloading occurred in a similar location to the first unloading line, leading to the plateau in the fraction of each domain. During subsequent *concave* bending, the domain walls moved closer to their original positions, and the unloading/reloading lines moved closer to the original curve.

We next applied larger strains to $MAPbI_3$ films. The bending experiment was repeated with a diameter of 4.1 mm ($|\varepsilon_X| = 3.06$ %; $|\varepsilon_Z| = 1.01$ %; **Figure 2.7**). Separately, we investigated the effects of *concave* bending only, without prior *convex* bending. The changes to the (220):1 and (004):1 peaks (**Figure 2.7a**) were more pronounced than for the 10 mm experiment, likely due to the larger applied strain (see also **Figure 2.S10**). Interestingly, the (220):2 appeared much more distinctly after *convex* then subsequent *concave* bending, suggesting some interaction between TS1 and TS2 (see discussion below).

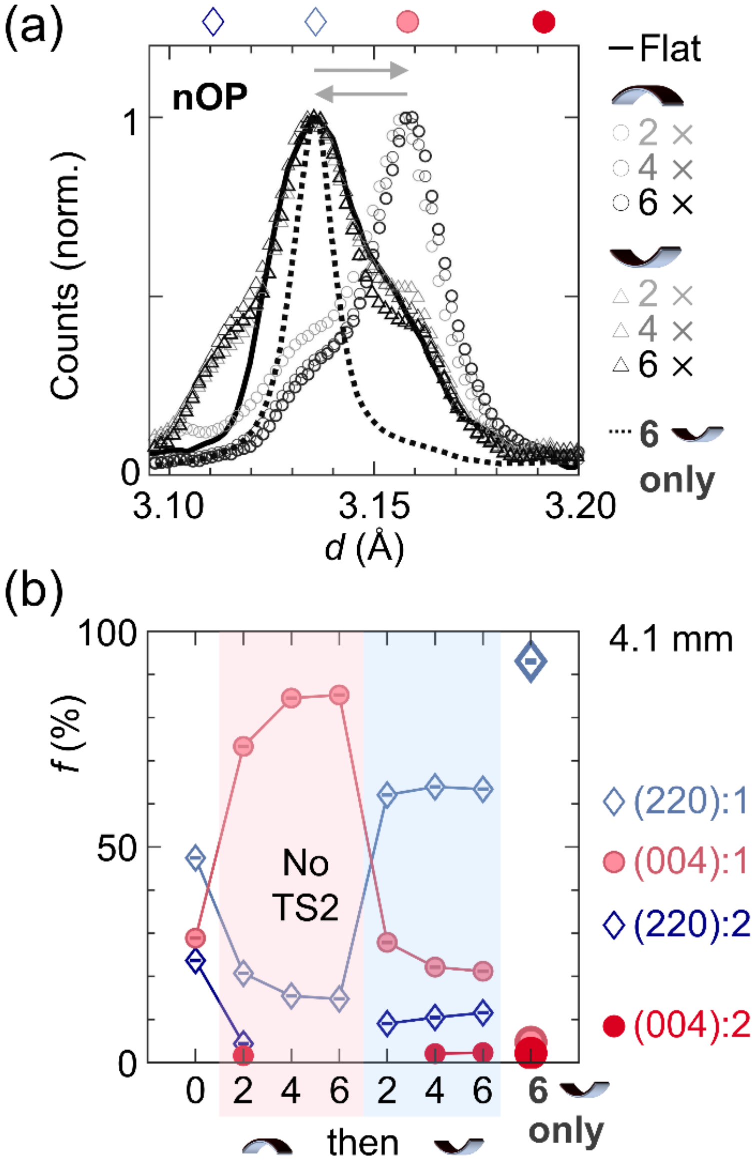

Figure 2.7. 4.1 mm bending experiment. (a) nOP patterns and (b) Corrected fractions of total scattered intensity *f* (uncertainties < 0.1 %) for nOP peaks in the (220)-(004) region, for 6 *convex* followed by 6 *concave* bending cycles, and 6 *concave* bending cycles only.

Saturation was nearly attained upon bending around a 4.1 mm diameter (**Figure 2.7a**). As-cast, the film exhibited the typical preference for A:1 ((220):1 nOP), with some C:1 ((004):1 nOP) and A:2 ((220):2 nOP). *Convex* bending increased the C:1 population to ≈ 85 % of the film, accompanied by a large decrease in the A:1 fraction and complete disappearance of A:2. No fracturing was observed **(Figure 2.S8**). This process was to some extent reversed with *concave* bending, with A:1 ((220):1) occupying ≈ 65 % of the total nOP population, which is still higher than the as-cast A:1 population (≈ 50 %). A:2 reappeared, much more distinctly, although at slightly lower fraction than for the as-cast sample. Strikingly, concave-only bending induced near-complete (95 %) A:1 population nOP, indicating near-complete saturation. These trends in the fractions suggest near-complete cycling through the hysteresis loop, and certainly to greater extents than for the 10 mm diameter.

2.3.G. *Removing Large Compressive Strains*

The evolution in fractions *f* for TS2 suggested interaction between TS1 and TS2 (**Figure 2.7**), and therefore, physical contact between them. TS2 disappeared after 4 *convex* cycles and reappeared very distinctly after subsequent *concave* bending. Because the entire film depth was probed (**Figure 2.1**), this suggests either the presence of a mobile domain wall between TS1 and TS2, or that small grains of TS2 only can be converted to the more favorable TS1 using very large applied strains ($|\varepsilon_X| \approx 3.06$ % here). In support of these interpretations, the compressively-strained A:2 disappeared completely after 6 *concave* cycles only (induced tensile $|\varepsilon_Z|$), in favor of A:1, which has mild tensile strain. Thus, the ratio of TS1: TS2 can be controlled by applying large strains.

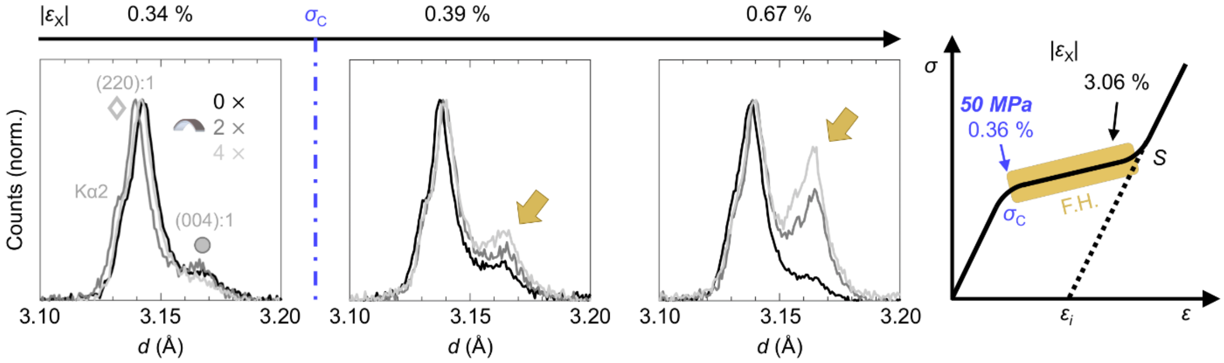

Figure 2.8. Determination of the coercive strain, from which the coercive stress σ_C was calculated. Powder XRD data for the 35 mm, 31 mm and 18 mm-diameter bending experiments, corresponding to applied $|\varepsilon_X|$ of ≈ 0.34 %, 0.39 % and 0.67 % respectively. The location of the coercive stress on the stress-strain curve is shown on the right. The yellow arrows show growth of the (004):1, indicative of ferroelastic hysteresis (F.H.).

Finally, we repeated the bending experiment with much larger diameters, to find the coercive stress (**Figure 2.8**). Because (004):1 grows into a peak that is very distinct from (220):1 (**Figure 2.6**, 2.7) we were able to use powder X-Ray diffraction (PXRD), rather than GIWAXS. Due impurities in the X-Ray wavelength (Cu-Kα2, tungsten and Cu-Kβ) resulting in extra peaks, and due to the low counts on the powder diffractometer, TS2 could not be resolved as easily; however, the onset of hysteresis was clearly identified using the TS1 peaks. The PXRD patterns of films bent convexly up to 4 × around diameters of 35 mm, 31 mm and 18 mm are shown in **Figure 2.8**, with applied strains $|\varepsilon_X|$ of ≈ 0.34 %, 0.39 % and 0.67 % respectively. The patterns shifted slightly and inconsistently in *d*-spacing after bending. This is likely caused by the lack of height alignment of the flexible films in PXRD, which is done in GIWAXS and necessary to obtain accurate *d*-spacings. Notably, the (004):1 did not grow when $|\varepsilon_X|$ ≈ 0.34 %, grew noticeably when $|\varepsilon_X|$ ≈ 0.39 %, and grew significantly when $|\varepsilon_X|$ ≈ 0.67 %. A control experiment was performed to confirm that these changes were not induced by the X-Ray beam (**Figure 2.S11**). Thus, the coercive strain is $|\varepsilon_X|$ ≈ 0.36 % Because the actual applied strain is in q_X, we take $|\varepsilon_X|$ to calculate the coercive stress. Using a modulus of 14 GPa, [63,65–67] the coercive stress for $MAPbI_3$ is thus $\sigma_C \approx 50$ MPa.

2.3.H. *Using Substrate Thermal Mismatch to Control Twin Population*

If an external stress source, such as thermal stress from the substrate or roll-to-roll printing setup, causes application of more than the coercive stress, |50| MPa in ε_X (**Figure 2.8**), it will modify the twin domain population. The stress σ_T imparted by thermal mismatch can be calculated using $\sigma_T = \frac{E_P}{1-\upsilon_P}(\alpha_S - \alpha_P)\Delta T$, [14] where E_P is the Young's modulus, υ_P is the Poisson's ratio, α_S and α_P are the T.E.C.s of the substrate and the perovskite and ΔT is the temperature gradient while cooling. Using the values discussed in the Residual Stress section, (E_P = 14 GPa, υ_P = 0.33, $\alpha_P \approx 5 \times 10^{-5}$/K and ΔT = 100°C – 20°C = – 80°C), a low T.E.C. substrate such as silicon ($\alpha_S = 0.26 \times 10^{-5}$/K) will induce ≈ 50 MPa on $MAPbI_3$ for a low annealing temperature of 70°C. A glass substrate with mid-range T.E.C. ($\alpha_S = 1 \times 10^{-5}$/K) will induce the coercive stress upon cooling from 80°C and finally, a substrate with a higher T.E.C. such as Kapton ($\alpha_S = 3 \times 10^{-5}$/K, chosen among the lower reporter T.E.Cs for Kapton) [70,71] will induce the coercive stress upon cooling from 140°C. These numbers will vary based on the E_P and T.E.C. selected for the calculation; however, it is clear that ferroelastic behavior should be quite different with substrates of differing T.E.C. Thus, it does seem that thermal mismatch can be used to tailor the ferroelastic domain population. However, this does not exclude interface interactions or other solution-casting phenomena [80] which may also greatly direct twin population. Further work is needed to decouple these effects.

2.3.H. *Domain Walls and Long-Term Stability*

We also examined the long-term stability of films with no bending, and either 6 *convex* cycles only or 6 *concave* cycles only around the 4.1 mm diameter (**Figure 2.9**). We stored these films for 7 months in ambient and in the dark, and then examined powder XRD patterns. Specifically, we looked for the appearance of the degradation product PbI_2 at $d \approx 7$ Å (**Figure 2.9a**) and for major changes in the proportions of A:1 vs. C:1 (**Figure 2.9b**). Due to low signal on the powder diffractometer, TS2 was not easily resolvable. Prior *convex* bending only correlated with a large amount of PbI_2, while no bending and *concave* bending only showed no PbI_2 (**Figure 2.9a**). In addition, the patterns in the (220)/(004) region (**Figure 2.9b**) were quite similar to those 7 months prior (**Figure 2.7a**), suggesting that the proportions of A:1 vs. C:1 changed negligibly over 7 months (**Figure 9b**). Thus, without external stimulus, the domain walls appear to be fairly immobile.

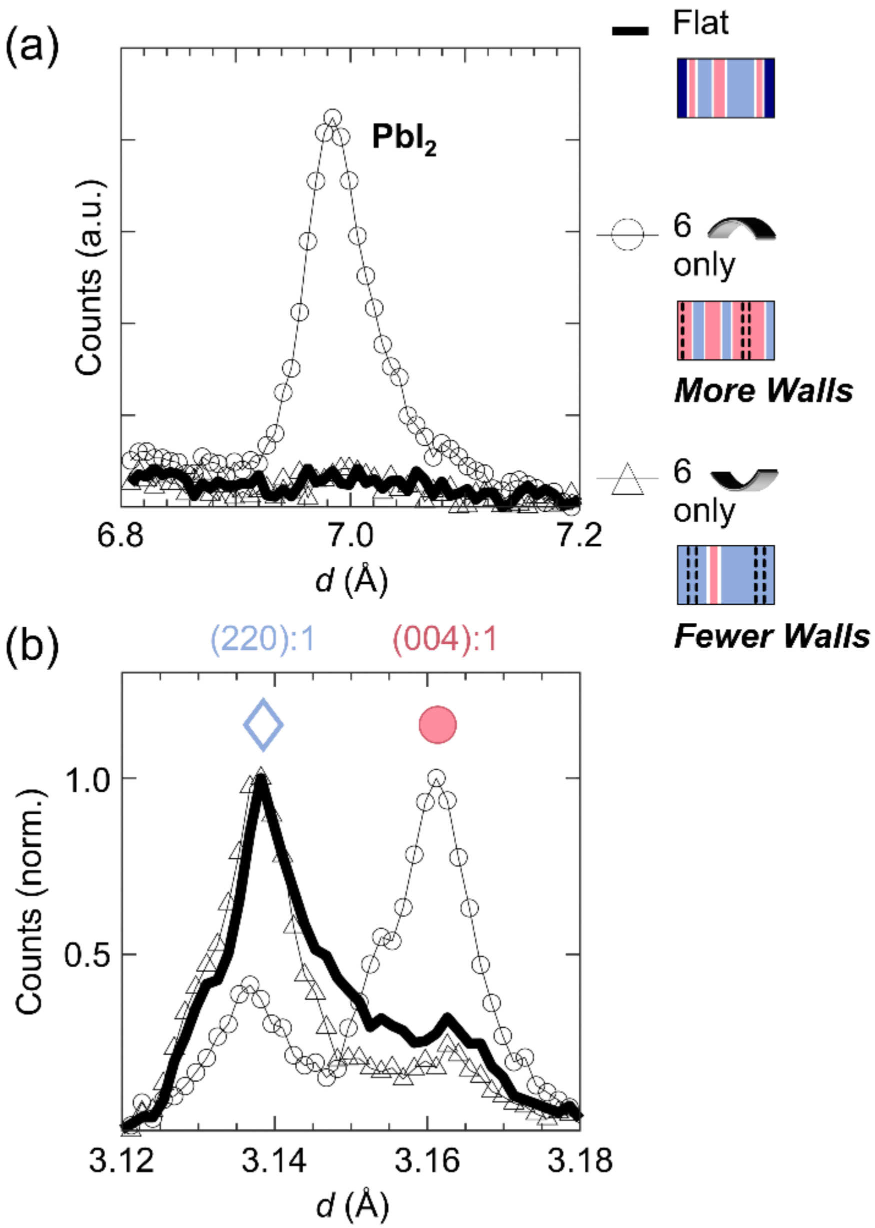

Figure 2.9. Powder XRD patterns of non-bent films (flat) and films previously bent *convexly* and *concavely* around a 4.1 mm diameter, after 7 months of storage in air, showing (a) the region in which the degradation product PbI$_2$ typically appears and (b) the (220)/(004) region. Schematics are shown of twin domain layout prior to storage (see **Figure 2.S13**), with the dashed lines indicating ghost walls.

We noticed an interesting correlation between these differences in degradation, and creation vs. annihilation of domain walls. Analysis of peak widths after bending (4.1 mm experiment – **Figure 2.S6** and **2.S13**) indicated wall creation during *convex* bending and annihilation during *concave* bending. This analysis (see discussion of **Figure 2.S6** and **2.S13**) is consistent with observations in literature from polarized optical microscopy of $MAPbI_3$.[30] Indeed, the as-cast films contained few C domains, so nucleation of new C domains might be necessary to accommodate all the applied strain during *convex* bending. In contrast, because *concave* bending favors the presence of A domains and because the as-cast films contained mostly A domains, existing A domains grew and merged into a few large domains without the need of domain nucleation. Thus, walls seemed to be created during *convex* bending, with more degradation occurring after bending in this configuration (**Figure 2.9**). In contrast, films with no changes in number of walls or annihilation of walls were stable.

More walls likely correlates with more degradation because walls encourage point defect presence. In other systems, walls are known to harbor a higher concentration of vacancies and to facilitate diffusion of vacancies/ionic species.[50–53] Domain walls can also nucleate point defects,[81] so the walls nucleated during *convex* bending may have also nucleated more point defects. However, walls may also have moved during *convex* bending. When they move, domain walls can leave behind some of the vacancies they contain, creating a "ghost line" of vacancies in the old wall location, also sometimes called "ghost wall".[50] This can create a "memory" of the wall,[82,83] which has been observed several times in $MAPbI_3$.[24,29] This memory could mean that wall movement or annihilation does not fully remove the point defects residing in the previous location of the wall. Here, we found that the films with likely wall nucleation (*convex* bending) showed PbI_2 formation; while the films for with wall annihilation or movement only (*concave* bending) showed no PbI_2 formation. Additionally, films for which no wall movement was imposed, also showed no PbI_2 formation. This result implies that additional point defects, created during the wall nucleation in *convex* bending, are responsible for the enhanced degradation. In contrast, wall movement, lack thereof, or annihilation do not nucleate new defects, so films with *concave* or no bending showed no bulk degradation.

2.3.I. ***Impact for Behavior of Optoelectronic Devices***

Wall creation during *convex* bending and wall annihilation during *concave* bending help explain prior defect-related results in $MAPbI_3$.[13–15] Prior studies found that films maintained under *convex* bending exhibited lower activation energy for vacancy-mediated ion migration[13] and more PbI_2 formation (i.e. degradation),[13,14] than flat films, suggesting higher defect content. Correspondingly, the photoluminescence lifetime of $MAPbI_3$ films decreased during *convex* bending in a different study,[15] suggesting more trap-mediated recombination. Our analyses (**Figures 2.7**, **2.9**, 2.**S13**) indicate that these behaviors originate from domain wall nucleation during *convex* bending. The opposite trends regarding degradation, ion migration, and photoluminescence lifetime were observed for *in-situ concave* bending, suggesting fewer point defects/ domain walls (**Figures 2.7**, **2.9**, 2.**S13**). Our results also indicate that repeated bending in one configuration (*convex* or *concave*) will likely not change the above-described behaviors much after the first few bending cycles (**Figure 2.6** and **Figure 2.7**). In addition, domain walls will not move without external stimulus (**Figure 2.9**). Subsequent bending in the opposite configuration (i.e. *concave* or *convex*) will change these defect behaviors to limited extents (**Figure 2.6** and **Figure 2.7**). To avoid such defect-related changes, the films should not be bent past the coercive stress (≈ 50 MPa, **Figure 2.8**), which is likely most relevant in the context of roll-to-roll processing $MAPbI_3$, or installing flexible modules. Thermal control over twin population may be employed using low-TEC substrates and mild temperatures (**Using Substrate Thermal Mismatch to Control the Population of Twins** section; **Figure 2.8**). A possible method for eliminating unfavorably-strained domains (compressive A:2 domains, **Figure 2.3**) and reducing the number of domain walls is to apply large out-of-plane tensile strain (**Figure 2.7**).

Changing the number of twin walls in films upon repeated bending may greatly impact carrier diffusion. Our findings reveal twin wall movement, and strongly suggest wall creation, annihilation, and the presence of "ghost walls" [24,29,50,82,83] in the sample after bending, which is a memory of the wall formed by the point defects the departed wall has left behind. Deep traps seem to nucleate along with twin walls *in films*, as evidenced by the decreased photoluminescence lifetime upon *convex* bending (i.e. enhanced trap-mediated recombination).[15] In apparent contrast, recent work on single crystals suggests that twin walls contain shallow traps that slow carrier diffusion, but do not induce trap-mediated recombination.[43–45] It is possible that single crystals contain fewer deep traps than films, and thus that twin walls impact carrier diffusion very differently in films vs. single crystals. It is also not clear to what extent twin walls carry their traps with them when they move or annihilate. "Ghost walls" may therefore greatly impact carrier transport in both films and single crystals. The impacts of repeated bending on shallow trapping and carrier diffusion requires further investigation, particularly in films.

We note that the detailed ferroelastic loop will also depend on factors such as the grain size. In oxide perovskites, grain size is known to affect domain/domain wall formation.[84] Here, we used films with grains of 200 ± 100 nm, but films used in devices can have grain sizes of up to several microns,[85] which may affect the types of twin domains formed and their strains. However, because $MAPbI_3$ is ferroelastic, the presence of twin domains is expected, regardless of processing conditions. We also probed the entire film thickness (**Figure 2.1a**), but different types of twins, in particular TS1 vs. TS2, may predominantly exist near different interfaces. Bringing the perovskite closer to the cubic phase via either temperature or composition should lower the spontaneous strain, and thus reduce the size of the hysteresis loop.[18,86] In addition, dislocations at interfaces are known to pin domain walls, thus preventing domain wall movement.[87,88] Complete understanding of defect behavior in $MAPbI_3$-based devices will therefore likely require investigations of how grain size, temperature, pinning, substrate interface interactions and other parameters affect the ferroelastic hysteresis loop of $MAPbI_3$.

2.4 Conclusions

In conclusion, we have examined ferroelastic twinning in polycrystalline thin films of $MAPbI_3$. Strain inhomogeneity in films originated from specific twin domains. We then characterized the ferroelastic hysteresis loop of $MAPbI_3$ and identified approximate values for the onset of the loop (coercive stress) and saturation. External stress sources, such as thermal stress from the substrate or roll-to-roll printing setups, must apply at least |50| MPa to modify the proportions of different twins, and the temperature at which this occurs is substrate-dependent. Cyclic strain tests revealed changes to the unloading/reloading line locations in the stress−strain curve. Domains from differently strained twin sets in the films are found to interact with each other and convert from one twin set type to another. Degradation of $MAPbI_3$ to PbI_2 was found to correlate with the presence of domain walls, with more domain walls (convex bending) favoring degradation and fewer domain walls (concave bending) favoring stability. These results help us to understand the structural processes related to defects in polycrystalline films of $MAPbI_3$ and the ionic and optoelectronic properties that they impact. We anticipate that the method presented above for characterizing the hysteresis loop will aid future studies of how strain and the hysteresis loop change under different device fabrication and operation conditions.

2.5 Acknowledgments, Permissions, and attributions

Experiments were supported by the U.S. Department of Energy, Office of Science, Basic Energy Sciences, under Award Number DE-SC-0012541. Support of optical characterization was provided by the U.S. Department of Energy (DOE), Office of Science, Basic Energy Sciences (BES), under Award Number DE-SC0019273. Use of the Stanford Synchrotron Radiation Lightsource, SLAC National Accelerator Laboratory, is supported by the U.S. Department of Energy, Office of Science, Office of Basic Energy Sciences under Contract No. DE-AC02-76SF00515. The research reported here also made use the shared facilities of the UCSB MRSEC (National Science Foundation DMR 1720256), a member of the Materials Research Facilities Network (www.mrfn.org). R.M.K. gratefully acknowledges the National Defense Science and Engineering Graduate fellowship for financial support. Reprinted (adapted) in full with permission from (*Chem. Mater.* **2021**, *33,* 1, 298–309), including section 2.7. Copyright (2021) American Chemical Society. https://doi.org/10.1021/acs.chemmater.0c03776

2.6 References

(1) Saliba, M.; Correa-Baena, J. P.; Wolff, C. M.; Stolterfoht, M.; Phung, N.; Albrecht, S.; Neher, D.; Abate, A. How to Make over 20% Efficient Perovskite Solar Cells in Regular (n-i-p) and Inverted (p-i-n) Architectures. *Chem. Mater.* **2018**, *30* (13), 4193-4201.

(2) National Renewable Energy Laboratory (NREL). Best Research Cell Efficiency Chart. https://www.nrel.gov/pv/cell-efficiency.html (accessed 2020-08-12).

(3) Mao, L.; Stoumpos, C. C.; Kanatzidis, M. G. Two-Dimensional Hybrid Halide Perovskites: Principles and Promises. *J. Am. Chem. Soc.* **2019**, *141* (3), 1171-1190.

(4) Zhang, T.; Yang, M.; Benson, E. E.; Li, Z.; Van De Lagemaat, J.; Luther, J. M.; Yan, Y.; Zhu, K.; Zhao, Y. A Facile Solvothermal Growth of Single Crystal Mixed Halide Perovskite $CH_3NH_3Pb(Br_{1-x}Cl_x)_3$. *Chem. Commun.* **2015**, *51* (37), 7820-7823.

(5) Kulkarni, S. A.; Baikie, T.; Boix, P. P.; Yantara, N.; Mathews, N.; Mhaisalkar, S. Band-Gap Tuning of Lead Halide Perovskites Using a Sequential Deposition Process. *J. Mater. Chem. A* **2014**, *2* (24), 9221-9225.

(6) Protesescu, L.; Yakunin, S.; Bodnarchuk, M. I.; Krieg, F.; Caputo, R.; Hendon, C. H.; Yang, R. X.; Walsh, A.; Kovalenko, M. V. Nanocrystals of Cesium Lead Halide Perovskites ($CsPbX_3$, X = Cl, Br, and I): Novel Optoelectronic Materials Showing Bright Emission with Wide Color Gamut. *Nano Lett.* **2015**, *15* (6), 3692-3696.

(7) Kennard, R. M.; Dahlman, C. J.; Nakayama, H.; Decrescent, R. A.; Schuller, J. A.; Seshadri, R.; Mukherjee, K.; Chabinyc, M. L. Phase Stability and Diffusion in Lateral Heterostructures of Methyl Ammonium Lead Halide Perovskites. *ACS Appl. Mater. Interfaces* **2019**, *11* (28), 25313-25321.

(8) Venkatesan, N. R.; Kennard, R. M.; DeCrescent, R. A.; Nakayama, H.; Dahlman, C. J.; Perry, E. E.; Schuller, J.; Chabinyc, M. L. Phase Intergrowth and Structural Defects in Organic Metal Halide Ruddlesden-Popper Thin Films. *Chem. Mater.* **2018**, *30*, 8615-8623.

(9) Venkatesan, N. R.; Mahdi, A.; Barraza, B.; Wu, G.; Chabinyc, M. L.; Seshadri, R. Enhanced Yield-Mobility Products in Hybrid Halide Ruddlesden-Popper Compounds with Aromatic Ammonium Spacers. *Dalt. Trans.* **2019**, *48* (37), 14019-14026.

(10) Stoumpos, C. C.; Cao, D. H.; Clark, D. J.; Young, J.; Rondinelli, J. M.; Jang, J. I.; Hupp, J. T.; Kanatzidis, M. G. Ruddlesden-Popper Hybrid Lead Iodide Perovskite 2D Homologous Semiconductors. *Chem. Mater.* **2016**, *28* (8), 2852-2867.

(11) Jung, Y. S.; Hwang, K.; Heo, Y. J.; Kim, J. E.; Vak, D.; Kim, D. Y. Progress in Scalable Coating and Roll-to-Roll Compatible Printing Processes of Perovskite Solar Cells toward Realization of Commercialization. *Adv. Opt. Mater.* **2018**, *6* (9), 1-30.

(12) Jones, T. W.; Osherov, A.; Alsari, M.; Sponseller, M.; Duck, B. C.; Jung, Y. K.; Settens, C.; Niroui, F.; Brenes, R.; Stan, C. V.; et al. Lattice Strain Causes Non-Radiative Losses in Halide Perovskites. *Energy Environ. Sci.* **2019**, *12* (2), 596-606.

(13) Zhao, J.; Deng, Y.; Wei, H.; Zheng, X.; Yu, Z.; Shao, Y.; Shield, J. E.; Huang, J. Strained Hybrid Perovskite Thin Films and Their Impact on the Intrinsic Stability of Perovskite Solar Cells. *Sci. Adv.* **2017**, *3* (11).

(14) Rolston, N.; Bush, K. A.; Printz, A. D.; Gold-Parker, A.; Ding, Y.; Toney, M. F.;

McGehee, M. D.; Dauskardt, R. H. Engineering Stress in Perovskite Solar Cells to Improve Stability. *Adv. Energy Mater.* **2018**, *8* (29), 1-7.

(15) Wang, C.; Ma, L.; Guo, D.; Zhao, X.; Zhou, Z.; Lin, D.; Zhang, F.; Zhao, W.; Zhang, J.; Nie, Z. Balanced Strain-Dependent Carrier Dynamics in Flexible Organic-Inorganic Hybrid Perovskites. *J. Mater. Chem. C* **2020**, *8* (10), 3374-3379.

(16) Aizu, K. Determination of the State Parameters and Formulation of Spontaneous Strain for Ferroelastics. *Journal of the Physical Society of Japan*. 1970, pp 706-716.

(17) Aizu, K. Possible Species of Ferromagnetic, Ferroelectric, and Ferroelastic Crystals. *Phys. Rev. B* **1970**, *2* (3), 754-772.

(18) Salje, E. K. H. Mesoscopic Twin Patterns in Ferroelastic and Co-Elastic Minerals. *Rev. Mineral. Geochemistry* **2000**, *39* (1), 65-84.

(19) Wadhawan, V. K. Ferroelasticity. *Bull. Mater. Sci.* **1984**, *6* (4), 733-753.

(20) Baither, D.; Bartsch, M.; Baufeld, B.; Tikhonovsky, A.; Foitzik, A.; Rühle, M.; Messerschmidt, U. Ferroelastic and Plastic Deformation of T′-Zirconia Single Crystals. *J. Am. Ceram. Soc.* **2004**, *84* (8), 1755-1762.

(21) Chen, Y.; Xu, J.; Xie, S.; Nie, R.; Yuan, J.; Wang, Q.; Zhu, J. Failure Mode, Ferroelastic Behavior and Toughening Effect of Bismuth Titanate Ferroelectric Ceramics under Uniaxial Compression Load. *Mater. Des.* **2018**, *152*, 54-64.

(22) Araki, W.; Malzbender, J. Ferroelastic Deformation of $La_{0.58}Sr_{0.4}Co_{0.2}Fe_{0.8}O_{3-\delta}$ under Uniaxial Compressive Loading. *J. Eur. Ceram. Soc.* **2013**, *33* (4), 805-812.

(23) Pham, H. T.; Duong, T.; Weber, K. J.; Wong-Leung, J. Insights into Twinning Formation in Cubic and Tetragonal Multi-Cation Mixed-Halide Perovskite. *ACS Mater. Lett.* **2020**, *2* (4), 415-424.

(24) Rothmann, M. U.; Li, W.; Zhu, Y.; Bach, U.; Spiccia, L.; Etheridge, J.; Cheng, Y. B. Direct Observation of Intrinsic Twin Domains in Tetragonal $CH_3NH_3PbI_3$. *Nat. Commun.* **2017**, *8*, 6-13.

(25) Hermes, I. M.; Bretschneider, S. A.; Bergmann, V. W.; Li, D.; Klasen, A.; Mars, J.; Tremel, W.; Laquai, F.; Butt, H. J.; Mezger, M.; et al. Ferroelastic Fingerprints in Methylammonium Lead Iodide Perovskite. *J. Phys. Chem. C* **2016**, *120* (10), 5724-5731.

(26) Wojciechowska, M.; Gagor, A.; Piecha-Bisiorek, A.; Jakubas, R.; Cizman, A.; Zaręba, J. K.; Nyk, M.; Zieliński, P.; Medycki, W.; Bil, A. Ferroelectricity and Ferroelasticity in Organic Inorganic Hybrid (Pyrrolidinium)$_3$[Sb_2Cl_9]. *Chem. Mater.* **2018**, *30* (14), 4597-4608.

(27) Huang, Y.; Yang, J.; Li, Z. J.; Qian, K.; Sao, F. High-Temperature Ferroelastic Phase Transition in a Perovskite-like Complex: $[Et_4N]_2[PbBr_3]_2$. *RSC Adv.* **2019**, *9* (18), 10364-10370.

(28) Chabin, M.; Gilletta, F. Experiment Investigation of the Ferroelastic Domain Structure in Cesium Lead Chloride in the Monoclinic Phase. *J. Appl. Crystallogr.* **1980**, *13* (6), 539-543.

(29) Huang, B.; Kong, G.; Esfahani, E. N.; Chen, S.; Li, Q.; Yu, J.; Xu, N.; Zhang, Y.; Xie, S.; Wen, H.; et al. Ferroic Domains Regulate Photocurrent in Single-Crystalline $CH_3NH_3PbI_3$ Films Self-Grown on FTO/TiO_2 Substrate. *npj Quantum Mater.* **2018**, *3* (1), 1-8.

(30) Strelcov, E.; Dong, Q.; Li, T.; Chae, J.; Shao, Y.; Deng, Y.; Gruverman, A.; Huang, J.; Centrone, A. $CH_3NH_3PbI_3$ Perovskites: Ferroelasticity Revealed. *Sci. Adv.* **2017**, *3*

(4), e1602165.

(31) Medjahed, A. A.; Dally, P.; Zhou, T.; Lemaitre, N.; Djurado, D.; Reiss, P.; Pouget, S. Unraveling the Formation Mechanism and Ferroelastic Behavior of $MAPbI_3$ Perovskite Thin Films Prepared in the Presence of Chloride . *Chem. Mater.* **2020**, *32* (8), 3346-3357.

(32) Wilson, J. N.; Frost, J. M.; Wallace, S. K.; Walsh, A. Dielectric and Ferroic Properties of Metal Halide Perovskites. *APL Mater.* **2019**, *7* (1), 010901.

(33) Minkiewicz, V. J.; Shirane, G. Soft Phonon Modes in $KMnF_3$. *J. Phys. Soc. Japan* **1969**, *26* (3), 674-680.

(34) Axe, J. D.; Shirane, G.; Müller, K. A. Zone-Boundary Phonon Instability in Cubic $LaAlO_3$. *Phys. Rev.* **1969**, *183* (3), 820-823.

(35) Shirane, G.; Yamada, Y. Lattice-Dynamical Study of the 110Â°K Phase Transition in $SrTiO_3$. *Phys. Rev.* **1969**, *177* (2), 858-863.

(36) Sakashita, H.; Ohama, N.; Okazaki, A. Thermal Expansion and Spontaneous Strain of $KMnF_3$ near the 186 K-Structural Phase Transition. *Phase Transitions* **1990**, *28* (1-4), 99-106.

(37) Whitfield, P. S.; Herron, N.; Guise, W. E.; Page, K.; Cheng, Y. Q.; Milas, I.; Crawford, M. K. Structures, Phase Transitions and Tricritical Behavior of the Hybrid Perovskite Methyl Ammonium Lead Iodide. *Sci. Rep.* **2016**, *6* (June), 1-16.

(38) Poglitsch, A.; Weber, D. Dynamic Disorder in Methylammoniumtrihalogenoplumbates (II) Observed by Millimeter-Wave Spectroscopy. *J. Chem. Phys.* **1987**, *87* (11), 6373-6378.

(39) Baikie, T.; Fang, Y.; Kadro, J. M.; Schreyer, M.; Wei, F.; Mhaisalkar, S. G.; Graetzel, M.; White, T. J. Synthesis and Crystal Chemistry of the Hybrid Perovskite $(CH_3NH_3)PbI_3$ for Solid-State Sensitised Solar Cell Applications. *J. Mater. Chem. A* **2013**, *1* (18), 5628-5641.

(40) Fang, H. H.; Raissa, R.; Abdu-Aguye, M.; Adjokatse, S.; Blake, G. R.; Even, J.; Loi, M. A. Photophysics of Organic-Inorganic Hybrid Lead Iodide Perovskite Single Crystals. *Adv. Funct. Mater.* **2015**, *25* (16), 2378-2385.

(41) Weller, M. T.; Weber, O. J.; Henry, P. F.; Di Pumpo, A. M.; Hansen, T. C. Complete Structure and Cation Orientation in the Perovskite Photovoltaic Methylammonium Lead Iodide between 100 and 352 K. *Chem. Commun.* **2015**, *51* (20), 4180-4183.

(42) Kawamura, Y.; Mashiyama, H.; Hasebe, K. Structural Study on Cubic-Tetragonal Transition of $CH_3NH_3PbI_3$. *J. Phys. Soc. Japan* **2002**, *71* (7), 1694-1697.

(43) Hermes, I. M.; Best, A.; Winkelmann, L.; Mars, J.; Vorpahl, S. M.; Mezger, M.; Collins, L.; Butt, H.-J.; Ginger, D. S.; Koynov, K.; et al. Anisotropic Carrier Diffusion in Single $MAPbI_3$ Grains Correlates to Their Twin Domains . *Energy Environ. Sci.* **2020**, *13*, 4168-4177.

(44) Shi, R.; Zhang, Z.; Fang, W. H.; Long, R. Ferroelastic Domains Drive Charge Separation and Suppress Electron-Hole Recombination in All-Inorganic Halide Perovskites: Time-Domain: Ab Initio Analysis. *Nanoscale Horizons* **2020**, *5* (4), 683-690.

(45) Warwick, A. R.; Íniguez, J.; Haynes, P. D.; Bristowe, N. C. First-Principles Study of Ferroelastic Twins in Halide Perovskites. *J. Phys. Chem. Lett.* **2019**, *10* (6), 1416-1421.

(46) Lim, A. R.; Jeong, S. Y. Twin Structure by 133Cs NMR in Ferroelastic $CsPbCl_3$ Crystal.

Solid State Commun. **1999**, *110* (3), 131-136.

(47) Bechtel, J. S.; Van Der Ven, A. Octahedral Tilting Instabilities in Inorganic Halide Perovskites. *Phys. Rev. Mater.* **2018**, *2* (2), 1-13.

(48) Bechtel, J. S.; Thomas, J. C.; Van Der Ven, A. Finite-Temperature Simulation of Anharmonicity and Octahedral Tilting Transitions in Halide Perovskites. *Phys. Rev. Mater.* **2019**, *3* (11), 1-10.

(49) Maughan, A. E.; Mozur, E. M.; Candia, A. M.; Neilson, J. R. Ferroelastic Phase Transition in Formamidinium Tin(IV) Iodide Driven by Organic-Inorganic Coupling. *Inorg. Chem.* **2020**, *59* (19), 14399-14406.

(50) He, X.; Li, S.; Ding, X.; Sun, J.; Selbach, S. M.; Salje, E. K. H. The Interaction between Vacancies and Twin Walls, Junctions, and Kinks, and Their Mechanical Properties in Ferroelastic Materials. *Acta Mater.* **2019**, *178*, 26-35.

(51) Farokhipoor, S.; Noheda, B. Local Conductivity and the Role of Vacancies around Twin Walls of (001)-$BiFeO_3$ Thin Films. *J. Appl. Phys.* **2012**, *112* (5).

(52) Aird, A.; Salje, E. K. H. Enhanced Reactivity of Domain Walls in WO_3 with Sodius. *Eur. Phys. J. B* **2000**, *15* (2), 205.

(53) Klie, R. F.; Ito, Y.; Stemmer, S.; Browning, N. D. Observation of Oxygen Vacancy Ordering and Segregation in Perovskite Oxides. *Ultramicroscopy* **2001**, *86* (3-4), 289-302.

(54) Reza, K. M.; Mabrouk, S.; Qiao, Q. A Review on Tailoring PEDOT:PSS Layer for Improved Performance of Perovskite Solar Cells. *Proc. Nat. Res. Soc.* **2018**, *2* (January).

(55) Sun, K.; Li, P.; Xia, Y.; Chang, J.; Ouyang, J. Transparent Conductive Oxide-Free Perovskite Solar Cells with PEDOT:PSS as Transparent Electrode. *ACS Appl. Mater. Interfaces* **2015**, *7* (28), 15314-15320.

(56) Chen, L. C.; Chen, C. C.; Chen, J. C.; Wu, C. G. Annealing Effects on High-Performance $CH_3NH_3PbI_3$ Perovskite Solar Cells Prepared by Solution-Process. *Sol. Energy* **2015**, *122*, 1047-1051.

(57) Ava, T. T.; Al Mamun, A.; Marsillac, S.; Namkoong, G. A Review: Thermal Stability of Methylammonium Lead Halide Based Perovskite Solar Cells. *Appl. Sci.* **2019**, *9* (1), 188.

(58) Jariwala, S.; Sun, H.; Adhyaksa, G. W. P.; Lof, A.; Muscarella, L. A.; Ehrler, B.; Garnett, E. C.; Ginger, D. S. Local Crystal Misorientation Influences Non-Radiative Recombination in Halide Perovskites. *Joule* **2019**, *3* (12), 3048-3060.

(59) Henke, B. L.; Gullikson, E. M.; Davis, J. C. X-Ray Interactions: Photoabsorption, Scattering, Transmission, and Reflection at E = 50-30, 000 EV, Z = 1-92. *Atomic Data and Nuclear Data Tables*. 1993, pp 181-342.

(60) GIXA Calculator for Penetration Depth (and Optical Properties) for X-rays https://gixa.ati.tuwien.ac.at/tools/penetrationdepth.xhtml (accessed Nov 9, 2020).

(61) Hu, Y. H.; Chan, H. M.; Wen, Z. X.; Harmer, M. P. Scanning Electron Microscopy and Transmission Electron Microscopy Study of Ferroelectric Domains in Doped $BaTiO_3$. *J. Am. Ceram. Soc.* **1986**, *69* (8), 594-602.

(62) Cheng, S. Y.; Ho, N. J.; Lu, H. Y. Transformation-Induced Twinning: The 90° and 180° Ferroelectric Domains in Tetragonal Barium Titanate. *J. Am. Ceram. Soc.* **2006**, *89* (7), 2177-2187.

(63) Feng, J. Mechanical Properties of Hybrid Organic-Inorganic $CH_3NH_3BX_3$ (B = Sn, Pb; X = Br, I) Perovskites for Solar Cell Absorbers. *APL Mater.* **2014**, *2* (8), 081801.
(64) Steele, J. A.; Jin, H.; Dovgaliuk, I.; Berger, R. F.; Braeckevelt, T.; Yuan, H.; Martin, C.; Solano, E.; Lejaeghere, K.; Rogge, S. M. J.; et al. Thermal Unequilibrium of Strained Black $CsPbI_3$ Thin Films. *Science (80-.).* **2019**, *365* (6454), 679-684.
(65) Spina, M.; Karimi, A.; Andreoni, W.; Pignedoli, C. A.; Náfrádi, B.; Forró, L.; Horváth, E. Mechanical Signatures of Degradation of the Photovoltaic Perovskite $CH_3NH_3PbI_3$ upon Water Vapor Exposure. *Appl. Phys. Lett.* **2017**, *110* (12). 121903.
(66) Rakita, Y.; Cohen, S. R.; Kedem, N. K.; Hodes, G.; Cahen, D. Mechanical Properties of $APbX_3$ (A = Cs or CH_3NH_3; X = I or Br) Perovskite Single Crystals. *MRS Commun.* **2015**, *5* (4), 623-629.
(67) Sun, S.; Fang, Y.; Kieslich, G.; White, T. J.; Cheetham, A. K. Mechanical Properties of Organic-Inorganic Halide Perovskites, $CH_3NH_3PbX_3$ (X = I, Br and Cl), by Nanoindentation. *J. Mater. Chem. A* **2015**, *3* (36), 18450-18455.
(68) Jacobsson, T. J.; Schwan, L. J.; Ottosson, M.; Hagfeldt, A.; Edvinsson, T. Determination of Thermal Expansion Coefficients and Locating the Temperature-Induced Phase Transition in Methylammonium Lead Perovskites Using X-Ray Diffraction. *Inorg. Chem.* **2015**, *54* (22), 10678-10685.
(69) Ramirez, C.; Yadavalli, S. K.; Garces, H. F.; Zhou, Y.; Padture, N. P. Thermo-Mechanical Behavior of Organic-Inorganic Halide Perovskites for Solar Cells. *Scr. Mater.* **2018**, *150*, 36-41.
(70) Elsner, G.; Kempf, J.; Bartha, J. W.; Wagner, H. H. Anisotropy of Thermal Expansion of Thin Polyimide Films. *Thin Solid Films* **1990**, *185*, 189-197.
(71) Polyimide (PI) Material Information, Thermal Properties http://www.goodfellow.com/E/Polyimide.html (accessed Jul 7, 2020).
(72) Music, D.; Elalfy, L. Tuneable Thermal Expansion of Poly (3,4-Ethylenedioxythiophene) Polystyrene Sulfonate. *J. Phys. Condens. Matter* **2019**, *31* (12), 125101.
(73) Tangram Technology Ltd. 2000. Polymer Data File: Polymethyl Methacrylate - PMMA (Acrylic). http://www.tangram.co.uk/TI-Polymer-PMMA.html (Last edited: 20/05/15; accessed 2020-08-20).
(74) Salje, E. K. *Phase Transitions in Ferroelastic and Co-Elastic Crystals,* Cambridge University Press, 1993, 1-12.
(75) Thomas, J. C.; Van Der Ven, A. Order Parameters for Symmetry-Breaking Structural Transitions: The Tetragonal-Monoclinic Transition in ZrO_2. *Phys. Rev. B* **2017**, *96* (13), 1-13.
(76) Ahn, S. M.; Jung, E. D.; Kim, S. H.; Kim, H.; Lee, S.; Song, M. H.; Kim, J. Y. Nanomechanical Approach for Flexibility of Organic-Inorganic Hybrid Perovskite Solar Cells. *Nano Lett.* **2019**, *19* (6), 3707-3715.
(77) Suo, Z.; Ma, E. Y.; Gleskova, H.; Wagner, S. Mechanics of Rollable and Foldable Film-on-Foil Electronics. *Appl. Phys. Lett.* **1999**, *74* (8), 1177-1179.
(78) Wang, Y.; Chen, Z.; Deschler, F.; Sun, X.; Lu, T. M.; Wertz, E. A.; Hu, J. M.; Shi, J. Epitaxial Halide Perovskite Lateral Double Heterostructure. *ACS Nano* **2017**, *11* (3), 3355-3364.
(79) Okuzaki, H.; Ishihara, M. Spinning and Characterization of Conducting Microfibers. *Macromol. Rapid Commun.* **2003**, *24* (3), 261-264.

(80) Bush, K. A.; Rolston, N.; Gold-Parker, A.; Manzoor, S.; Hausele, J.; Yu, Z. J.; Raiford, J. A.; Cheacharoen, R.; Holman, Z. C.; Toney, M. F.; et al. Controlling Thin-Film Stress and Wrinkling during Perovskite Film Formation. *ACS Energy Lett.* **2018**, *3* (6), 1225-1232.

(81) He, X.; Salje, E. K. H.; Ding, X.; Sun, J. Immobile Defects in Ferroelastic Walls: Wall Nucleation at Defect Sites. *Appl. Phys. Lett.* **2018**, *112* (9), 2-6.

(82) Salje, E. K. H.; Hayward, S. A.; Lee, W. T. Ferroelastic Phase Transitions: Structure and Microstructure. *Acta Crystallogr. Sect. A Found. Crystallogr.* **2005**, *61* (1), 3-18.

(83) Xu, H.; Heaney, P. J. Memory Effects of Domain Structures during Displacive Phase Transitions: A High-Temperature TEM Study of Quartz and Anorthite. *Am. Mineral.* **1997**, *82* (1-2), 99-108.

(84) Arlt, G. Twinning in Ferroelectric and Ferroelastic Ceramics: Stress Relief. *J. Mater. Sci.* **1990**, *25* (6), 2655-2666.

(85) DeQuilettes, D. W.; Vorpahl, S. M.; Stranks, S. D.; Nagaoka, H.; Eperon, G. E.; Ziffer, M. E.; Snaith, H. J.; Ginger, D. S. Impact of Microstructure on Local Carrier Lifetime in Perovskite Solar Cells. *Science (80-.).* **2015**, *348* (6235), 683-686.

(86) Yu, Y. S.; Jang, M. S.; Kim, H. J.; Cho, C. R. A Study on the Twin Domain of $Pb_3(PO_4)_2$ Ferroelastic Crystal. *Ferroelectrics* **1993**, *142* (1), 121-130.

(87) Chu, M. W.; Szafraniak, I.; Hesse, D.; Alexe, M.; Gösele, U. Elastic Coupling between 90° Twin Walls and Interfacial Dislocations in Epitaxial Ferroelectric Perovskites: A Quantitative High-Resolution Transmission Electron Microscopy Study. *Phys. Rev. B - Condens. Matter Mater. Phys.* **2005**, *72* (17), 1-5.

(88) Su, D.; Meng, Q.; Vaz, C. A. F.; Han, M. G.; Segal, Y.; Walker, F. J.; Sawicki, M.; Broadbridge, C.; Ahn, C. H. Origin of 90° Domain Wall Pinning in $Pb(Zr_{0.2}Ti_{0.8})O_3$ Heteroepitaxial Thin Films. *Appl. Phys. Lett.* **2011**, *99* (10), 8-11.

2.7 Appendix to Chapter 2

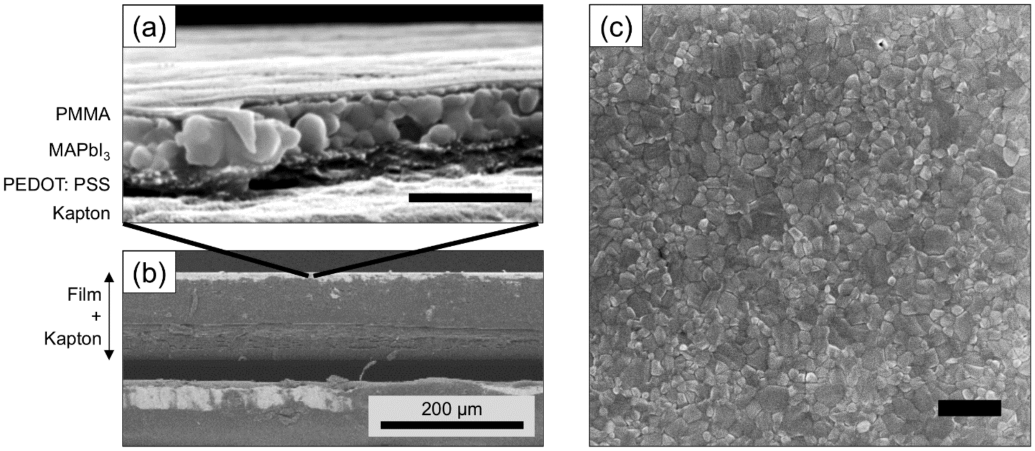

Figure 2.S1. SEM images of an as-cast film, showing (a) a cross-section of an as-cast film, (b) a lower-magnification cross-section showing the Kapton thickness and (c) a top-view image of an $MAPbI_3$ film on top of which no PMMA was cast. 19 keV accelerating voltage was used for (a) and (c) and 10 keV was used for (b). Scale bars in (a) and (c) are 1 µm.

The $MAPbI_3$ film measured here was 1-4 grains thick. Because the films were cast on plastic substrates, they did not break in half cleanly, so parallax issues were encountered when trying to determine thickness. The exact thicknesses were difficult to measure, but were approximately 400 nm for $MAPbI_3$, 200 nm for PEDOT: PSS and 50 nm for PMMA. To properly measure grain size without parallax issues, we measured a film from the top (**Figure 2.S1c**) that did not have PMMA. The average grain size was estimated from measurement of 100 grain widths to be 200 ± 100 nm.

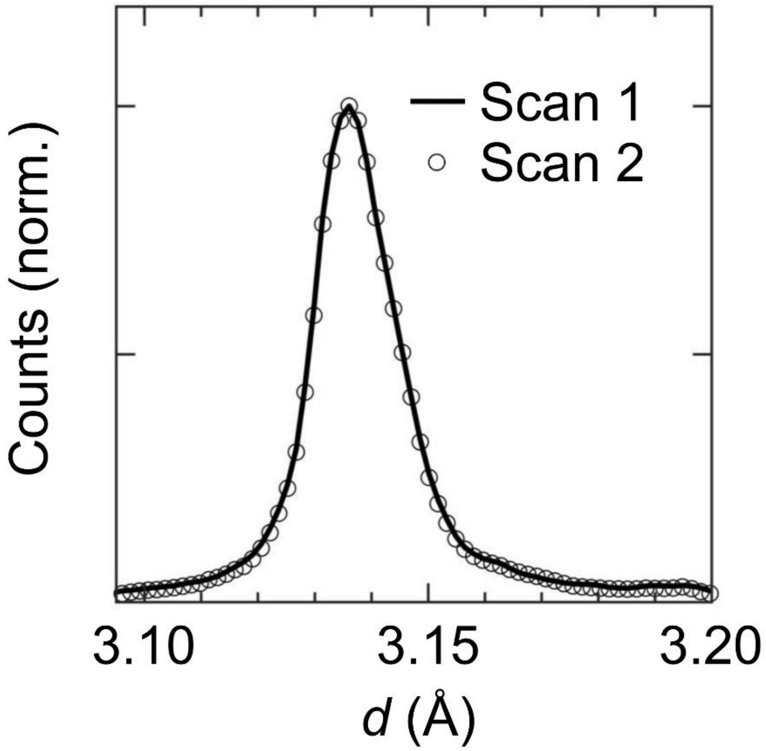

Figure 2.S2. GIWAXS nOP patterns of films bent *concavely* around a cylinder with 4.1 mm diameter. Scan 1 and Scan 2 indicate two consecutive scans of the same sample, showing lack of change and thus good stability under the beam.

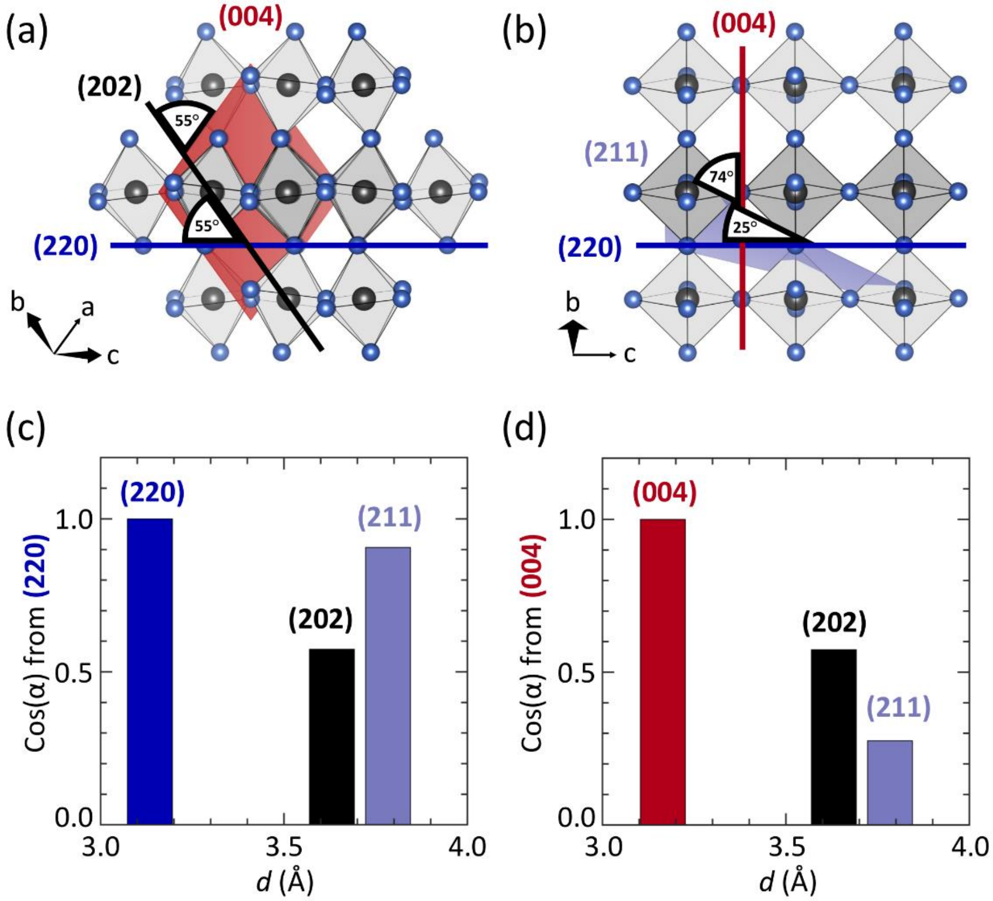

Figure 2.S3. Crystal structures of MAPbI$_3$ in the tetragonal I4/mcm phase [2] showing (a) the angles made between the (202) plane and the (220) and (004) planes and (b) the angles made between the (211) plane and the (220) and (004) planes. (c-d) Cosines of the angles in (a) and (b) respectively.

In order to properly assign GIWAXS peaks as (220) vs. (004), we tracked the intensity of the (211) peak with respect to its neighboring (202) peak. **Figures 2.S3a-b** show the angles that the (202) (**Figure 2.S3a**) and (211) (**Figure 2.S3b**) planes make with the (220) and (004) planes. Conveniently, the (202) plane is at equal angle from the (220) and (004), making normalization of the (211) with respect to the (202) useful for analysis (i.e. the (202) is a reference point and the (211) intensity will reveal (220) or (004) predominance). The cosines of the above-mentioned angles are shown in **Figure 2.S3c-d**. Because the (211) plane is nearly parallel to the (220), much stronger (211) intensity will be observed when the peak at *d* ≈ 3.1-3.2 Å is (220) (**Figure 2.S3c**). Correspondingly, because the (211) is nearly perpendicular to the (004), a weak (211) intensity with respect to the neighboring (202) peak likely indicates that the peak at *d* ≈ 3.1-3.2 Å is (004) (**Figure 2.S3d**). So, in nOP patterns, strong (211) correlates more with A domains and weak (211) correlates more with C domains. To further verify these assignments, we compared the nOP patterns with the nIP patterns, as a domain with (220) reflections out-of-plane should have corresponding (004) reflections in-plane (**Figure 2.3**).

Additional information regarding fraction *f*

To calculate *f*, the fitted peak intensities were corrected for structure factor, [3,4] and we used **Equation 2.1**:

$$f = 100 \times \frac{I_{Corr,peak\ of\ interest}}{I_{Corr,total}} \tag{2.1}$$

Where I_{Corr} is the corrected peak intensity.

f represents the fraction of the film having (220) or (004) reflections, in the nOP *or* the nIP patterns. Thus, it is important to correct the scattering intensities of (220) and (004) relative to each other. The intensities I_{hkl} of a peak (*hkl*) ((220) or (004)) were therefore corrected for structure factor F_{hkl}, using $I_{Corr} = (I_{\mathrm{hkl}})(F_{\mathrm{hkl}})^2$. [3] Conveniently, the (220) and (004) peaks were always within ≤ 0.1 Å of each other, and we calculated the *f*s for each *for the same nOP or nIP pattern*. Other correction factors [3] that might otherwise be necessary were therefore ignored, such as the Debye-Waller thermal correction or Lorentz/polarization factors. In addition, because each pattern probed specific domain orientations and not a powder sample, the multiplicity of all peaks should be 1. Thus, the corrected intensities were $I_{Corr} = (I_{\mathrm{hkl}})(F_{\mathrm{hkl}})^2$.

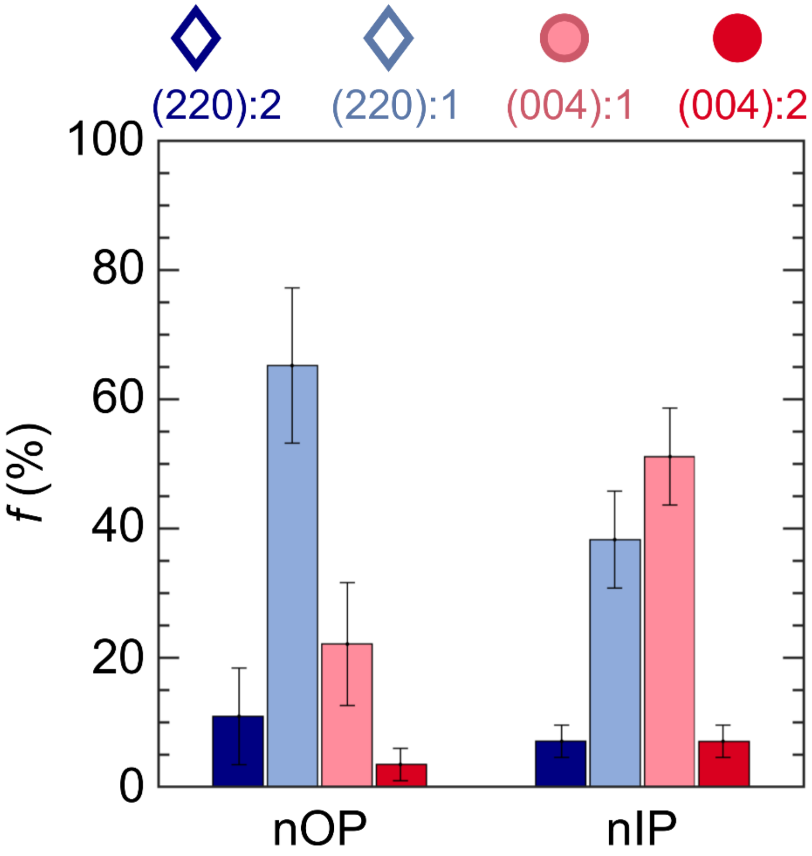

Figure 2.S4. Reproduction of **Figure 2.3c** for 4 samples, where the values are the average *f*s and the error bars represent the standard deviation of these values. The results reproduce those shown in **Figure 2.3**, albeit with larger uncertainty values.

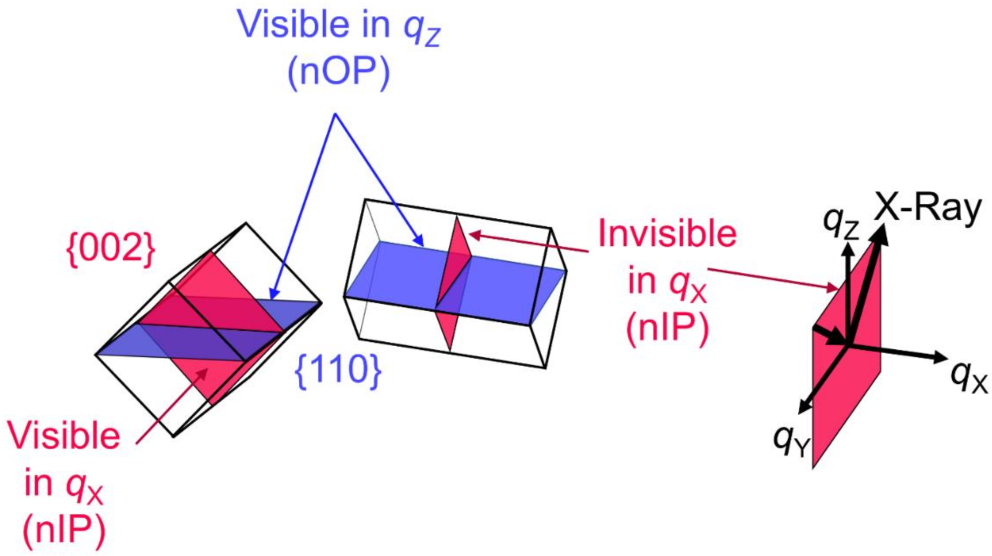

Figure 2.S5. A-type domains with all planes visible nOP but with only some planes visible nIP, depending on domain rotation. Two A-type domains with the orientation shown here, and with a domain wall between them belonging to {112}, would exhibit 90° *a*-*a* type twinning (also possible in this study).

Derivation of Equation for Minimum Domain Size D_{min}

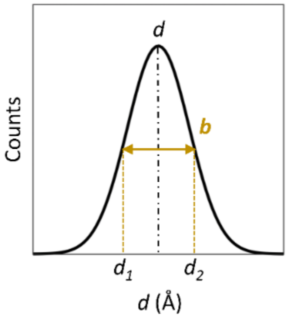

Figure 2.S6. Sample peak in real-space, showing a peak of center *d*, with breadth *b* spanning from d_1 to d_2.

Here, we extracted peak breadths to obtain domain size. Because we did this only for one peak, rather than over a series of peaks, the numbers reported in this study should be taken as the *minimum* domain size. We did not calculate size from a series of peaks because the (110) and (002) peaks significantly overlapped with each other and because the (330) and (006) peaks significantly overlapped with substrate peaks, so the (220) and (004) peaks were best for breadth calculations. For this reason, we caution that the following analysis provides estimates only, because the effects of strain are not decoupled from peak width, over multiple peaks. We do note, however, that the results of this analysis (number of walls increases or decreases) are consistent with prior microscopy observations. [5] We were also primarily concerned with *relative changes* to D_{min} upon application of stress, not with the absolute values of the numbers themselves.

Prior work modified the Scherrer equation for GIWAXS to obtain the following: [6]

$$D_{hkl} = \frac{2\pi K}{\Delta q_{hkl}}$$

Where D_{hlk} is the average domain size, K is an hkl-dependent constant [7] and Δq_{hkl} is the breadth of the Bragg reflection hkl in reciprocal space. However, because we analyzed all our data in real-space (d-spacings) and not in reciprocal space (q), we converted the above equation to real-space. Because $q = 2\pi/d$ and $\Delta q_{hkl} = q_1 - q_2$:

$$\Delta q_{hkl} = 2\pi\left(\frac{1}{d_1} - \frac{1}{d_2}\right) = 2\pi\left(\frac{d_2 - d_1}{d_1 d_2}\right) = 2\pi\left(\frac{b}{d_1 d_2}\right)$$

Where b is the breadth (area divided by intensity)[6] in real space, d is the center of the hkl peak, $d_1 = d - b/2$ and $d_2 = d + b/2$ (see **Figure 2.S6).** Thus,

$$\Delta q_{hkl} = 2\pi\left(\frac{b}{\left(d - {}^{b}\!/_{2}\right)\left(d + {}^{b}\!/_{2}\right)}\right) = 2\pi b\left(\frac{1}{d^2 - {}^{b^2}\!/_{4}}\right)$$

$$D_{min} = \frac{K}{b}\left(d^2 - {}^{b^2}\!/_{4}\right)$$

Where K is the Scherrer constant (≈ 1.0 for both (220) and (004)) [7], b is the breadth which in this case is the peak area divided by the peak intensity (uncorrected), and d is the d-spacing. Pseudo-Voigt fitting methodology was applied to all samples.

Calculation of Applied Strain Magnitudes

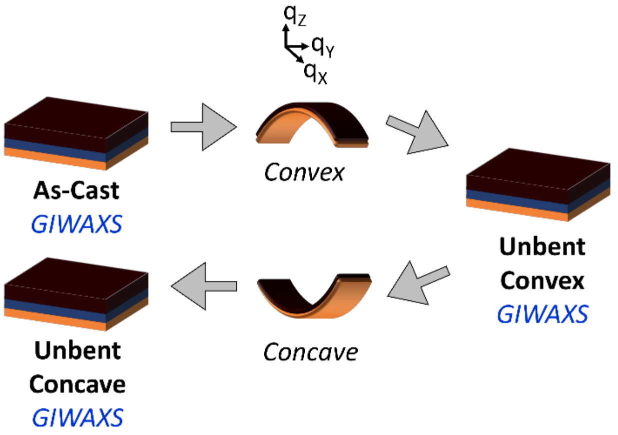

Figure S7. Bending experiment for convex and concave bending. GIWAXS patterns were taken after the applied strain was released.

Here we calculate the approximate magnitudes of the strains ε applied to $MAPbI_3$ films during bending (**Figure 2.S7**). To do so, we use the equation provided by Suo *et al.*:

8

$$\varepsilon_{top,\ qx} = \left(\frac{t_f + t_S}{2R}\right)\frac{(1 + 2\eta + \chi\eta^2)}{(1 + \eta)(1 + \chi\eta)}$$

In this equation, the "top" designates the top region of the Kapton-PEDOT: PSS-$MAPbI_3$-PMMA stack; thus, the area closest to $MAPbI_3$. "*qx*" designates the strain in the q_X direction; i.e. in-plane. R is the radius around which the film is bent (so $2R$ is the diameter), t_f is the film thickness, t_S is the substrate thickness, $\eta = t_f/t_S$ and χ is the ratio of elastic moduli Y, where $\chi = Y_f/Y_S$.

The Young's modulus of $MAPbI_3$ has been found to vary between 10 and 20 GPa (≈ 10, 12.8, 14, and 20 GPa); [9–12] so we take 14 GPa here as a mid-range value for approximation. The moduli of PEDOT: PSS is ≈ 2 GPa [13], that of PMMA is 3 GPa and that of Kapton is 2.5 GPa. Because the moduli of PEDOT: PSS and Kapton are not only very similar but also an order of magnitude lower than that of $MAPbI_3$, we can approximate the "substrate" as being composed of Kapton and PEDOT: PSS. In addition, because the modulus of PMMA is much lower than that of $MAPbI_3$ and because the PMMA layer is much thinner than the $MAPbI_3$ layer, we can approximate the "film" as being $MAPbI_3$ only. Thus, $\chi = Y_f/Y_S \approx Y_{\mathrm{MAPbI3}}/Y_{\mathrm{Kapton}} \approx$ (14 GPa) / (2.5 GPa) ≈ 5.6.

Next, from **Figure 2.S1**, we obtained the thickness of Kapton t_{Kapton} (125 000 nm), of PEDOT: PSS (≈ 200 nm), of $MAPbI_3$ (≈ 400 nm) and of PMMA (≈ 50 nm). Assuming again that the "substrate" is Kapton + PEDOT: PSS and that the "film" is $MAPbI_3$, $\eta = t_f/t_S$ ≈ (400 nm)/(125200 nm) ≈ 0.00319. Because $\eta \sim 10^{-3}$, $\varepsilon_{top,\ qx}$ is practically independent of both η and χ.[8] We can therefore approximate the applied strain in the q_X direction:

$$\varepsilon_X \approx \left(\frac{t_f + t_S}{2R}\right)$$

The ε_X obtained are listed in **Table 2.1**. Then, Poisson's ratio was used to calculate ε_Z.

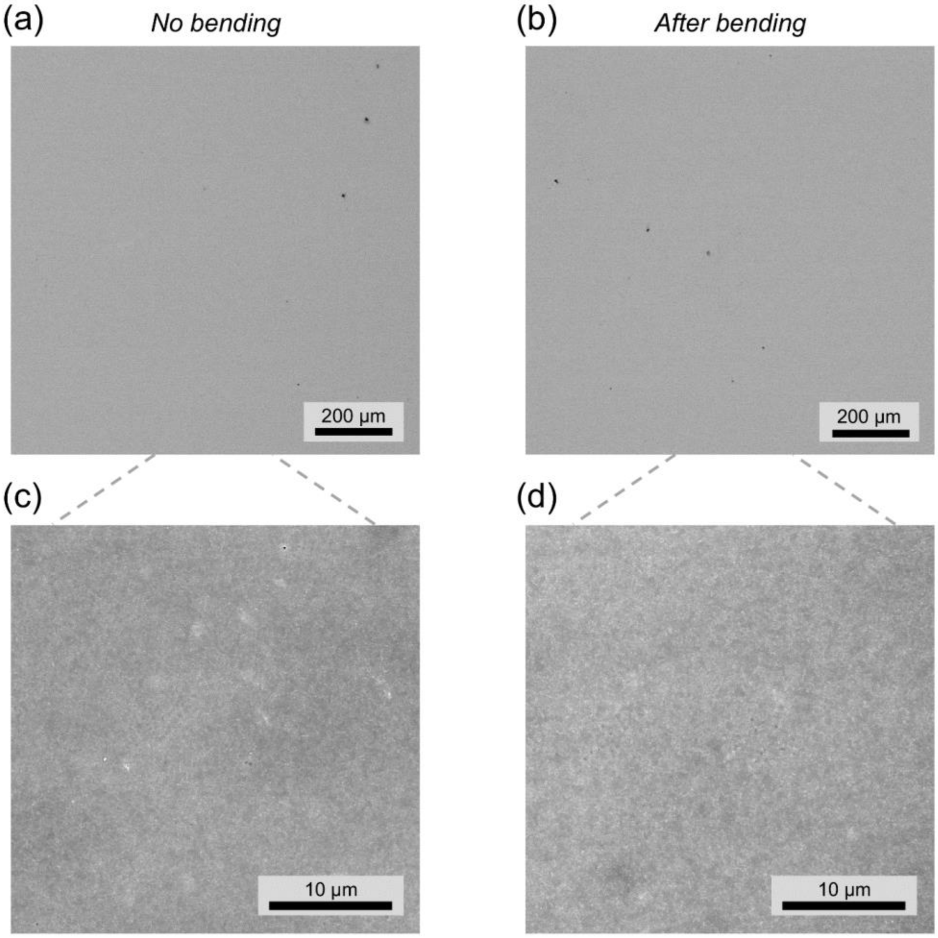

Figure 2.S8. SEM micrographs of films with no bending ((a), (c)) and after bending 2 times ((b), (d)) *convexly* around a diameter of 4.1 mm, with low and high magnifications. No cracks were observed here. (19 keV)

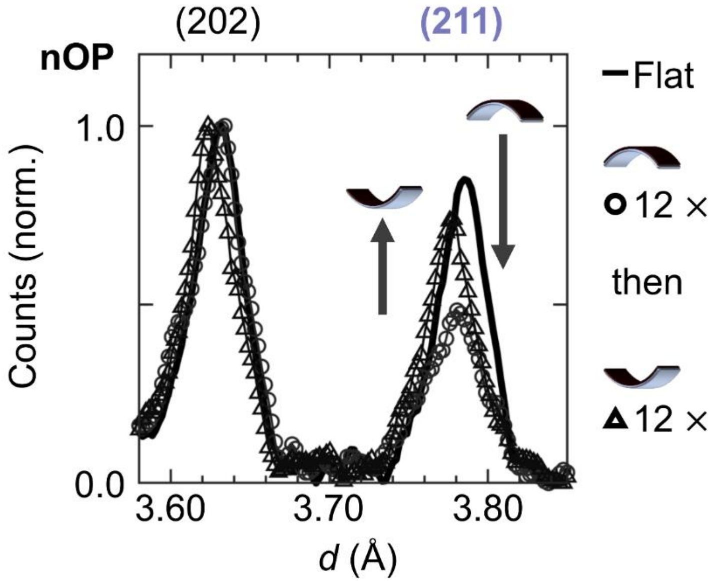

Figure 2.S9. (211)-(202) region of the nOP patterns in **Figure 2.6** (repeated bending around 10 mm diameter), showing the expected drop in (211) intensity as C replaces A after *convex* bending, with subsequent recovery of the (211) (and of A) after *concave* bending.

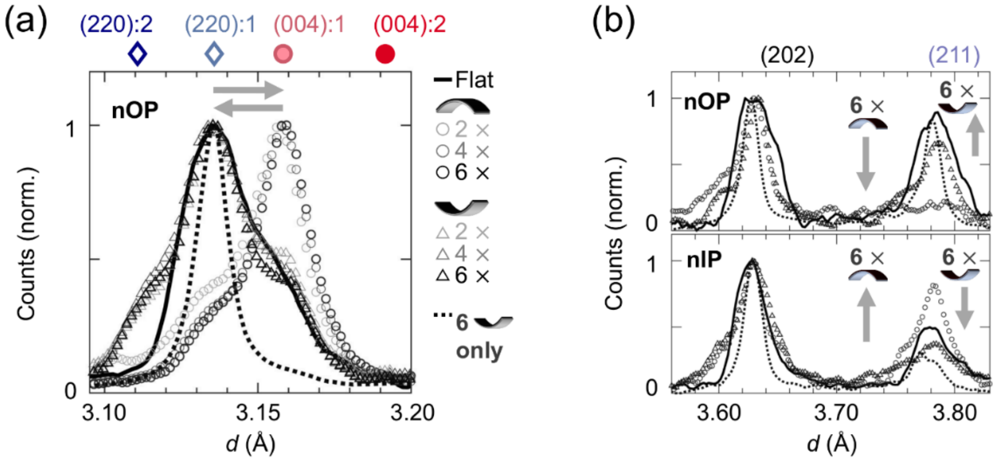

Figure 2.S10. (a) GIWAXS nOP patterns in the (004)-(220) region for the successive *convex* and *concave* bending around a 4.1 mm diameter, as listed. (b) (221)-(202) region of select GIWAXS nOP and nIP linecuts.

Convex bending resulted in very large growth of the (004):1, with the main as-cast (220):1 peak considerably decreasing (**Figure 2.7a**). Correspondingly, the (211) strongly increased nIP and decreased nOP (**Figure 2.S10b**). Subsequent *concave* bending resulted in an increase of the initial (220):1 peak, but with much (004):1 left over from the *convex* bending, and with a large and visible (220):2 shoulder. As expected, the (221) increased nOP and decreased nIP. Interestingly, when only *concave* bending was applied with no prior *convex* bending (called "*concave* bending only"), the (220):1 was practically the only peak observed, indicating mostly A:1. In this case, the (211) nIP is weaker than the (211) for the as-cast film, indicating more (004) nIP after 6 *concave* cycles only and therefore more (220) nOP. These striking changes are clear signs that much domain switching occurred during bending, with modifications made to the film being significantly retained when the applied strain was relieved.

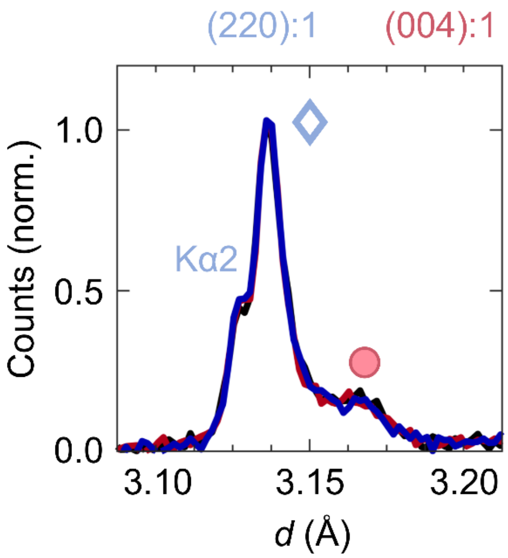

Figure 2.S11. Three sequential powder XRD patterns (black, then red, then blue) of an as-cast $MAPbI_3$ film in the (220)-(004) region, showing a lack of change, and thus, stability under the beam.

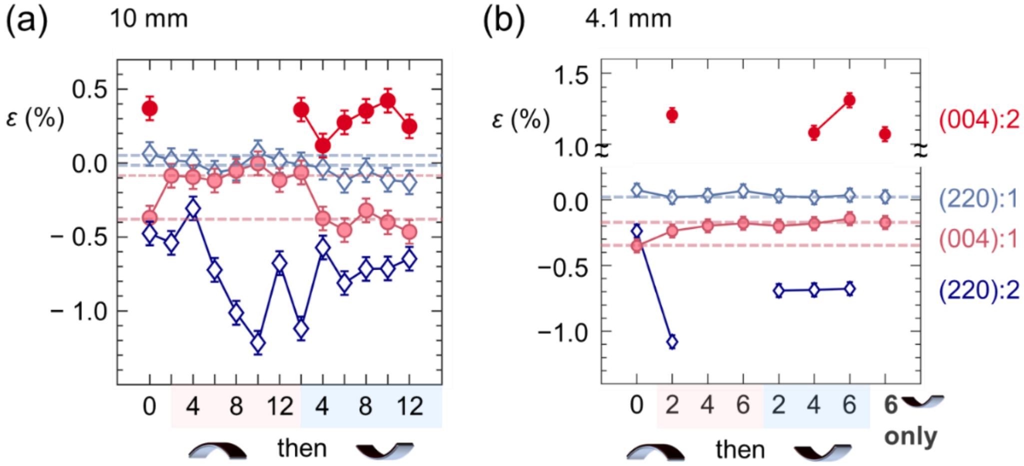

Figure 2.S12. Evolution of (220) and (004) strains after the (a) 10 mm bending cycles and (b) 4.1 mm bending cycles.

Some changes in strain for the (220) and (004) peaks were observed after bending. For the 10 mm experiment, these changes seemed to correlate with bending configuration (*convex* vs. *concave*). It is possible that inelastic strain was retained by the (220) and (004) planes of $MAPbI_3$ after the applied strain was released.

While extensive alignments and calibrations performed on multiple instruments enabled us to determine with certainty the strain values pre-bending (**Figure 2.3**), alignment difficulties encountered after bending made us hesitant to draw conclusions from the trends observed post-bending (**Figure 2.S12**). The strains measured in GIWAXS were fairly close to the resolution of both the height alignment performed during data collection, and the chi-*q* alignment performed during data processing (a further alignment that is done to correct any potential insufficient alignments during data collection). Good agreement for strains of the flat (pre-bent) samples measured via GIWAXS (**Figure 2.3**) and via lab XRD (on a variable-height stage) enabled us to conclude with confidence the values of the strains in **Figure 2.3**. Identification of different peaks post-bending was also obvious, such as the growth of the (004):1 peak in **Figures 2.6** or **2.8**. However, because the substrate was a very flexible polymer film, the precise locations of the different (220) and (004) peaks were less certain post-bending, even with all alignments, corrections, and various other measurement tricks (e.g. a very slightly sticky stage). For this reason, we included here the measured strains should the reader be curious, but do no extensively comment. We did not analyze the strain evolution of the (110)/(002) or (330)/(004) because the (110) and (002) peaks significantly overlapped with each other and the (330) and (006) peaks significantly overlapped with substrate peaks, so the (220) and (004) peaks were best for strain calculations.

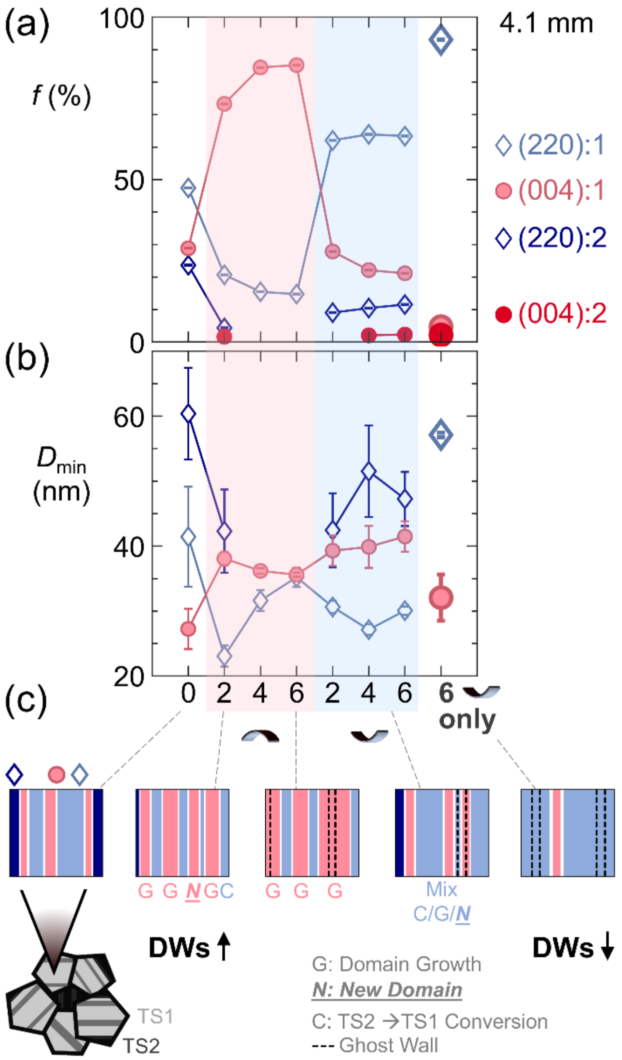

Figure 2.S13. 4.1 mm bending experiment. Corrected fractions of total scattered intensity *f* (uncertainties < 0.1 %) for nOP peaks in the (220)-(004) region. (b) changes in minimum domain size $D_{\min}$ for the (220):1, (004):1, (220):2 and (004):2 peaks of nOP patterns (see **Figure 2.7**). (c) Summary schematics of the processes occurring during the 4.1 mm diameter bending experiments, with the evolution in the number of domain walls (DWs) listed. TS stands for Twin Set. For clarity, only the prior locations of walls that disappeared are shown as ghosts, rather than the prior locations of *both* walls that moved and walls that disappeared.

Changing the Number of Domain Walls during Bending (4.1 mm).

We examined changes to the minimum domain size $D_{\min}$ for the 4.1 mm bending experiment (**Figure 2.7**) in more detail, to see if the walls only moved, or if walls were created/annihilated as well. We caution that this study provides estimations only, as the effects of strain are not decoupled from peak width, over multiple peaks; but the analysis below is consistent with prior microscopy work. [5] We focus on TS1, as the peaks in TS2 were quite weak. *Convex* bending induces more C, and *concave* bending induces more A (**Figures 2.5, 2.6** and **2.S13**), due to wall movement. Thus, if we only have wall movement, C domains should become bigger after *convex* bending and A domains should become bigger after *concave* bending. However, if new C domains nucleate during *convex* bending, the size of C should decrease. These trends should also apply to the *minimum* size $D_{\min}$, estimated using Scherrer broadening analysis (see above). Rapid growth of nucleated domains might mean that $D_{\min}$ of C decreases only slightly, as opposed to sharply decreasing. With respect to the minimum size specifically, if many C domains are annihilated during *concave* bending, the $D_{\min}$ of A domains will likely increase significantly. Such domain nucleation/annihilation is necessarily accompanied by an increase/decrease in the number of domain walls. In $MAPbI_3$ under applied stress, both domain nucleation and annihilation have been observed, so we know that large changes to the number of domain walls is possible. [5]

Changes in $D_{\min}$ revealed both wall movement and creation/annihilation (**Figure 2.S13b-c**). $D_{\min}$ of C:1 increased after 2 cycles of *convex* bending, and $D_{\min}$ of A:1 dropped. Thus, the walls moved through A:1s to increase the sizes of C:1s. This is reflected in the large increase in fraction of C:1 (**Figure 2.S13a**). The minimum size of C:1 then decreased (cycles 4-6) while fraction of C:1 continued to increase, suggesting C:1 nucleation upon further *convex* bending, and thus, more walls. Curiously, the $D_{\min}$ of A:1 concurrently increased. This suggests annihilation of the smallest A:1 domains as walls move from C:1s. The mixture of wall movement with wall creation/annihilation during *convex* bending/unbending is consistent with previous microscopy observations made on $MAPbI_3$ single crystals.[5] This process of wall movement/creation/annihilation appeared to be reversed with subsequent *concave* bending: D_{min} of A:1 decreased, suggesting A:1 nucleation. D_{min} of C:1 increased slightly but stayed within measurement uncertainty, suggesting slight C:1 annihilation. In the case of *concave* bending only (no prior *convex* bending), the minimum domain size of A:1 was 57.1 ± 0.4 nm, which is substantially larger than the range of as-cast domain sizes for A:1 (38 ± 4 nm, 4 samples). This result combined with the 95 % proportion of A:1 (**Figure 2.S13a**) suggests the microstructure shown in **Figure 2.S13c**, in which large A:1s are separated by very few C:1s, with very few domain walls total in the grain. Such a microstructure would result from progression of walls from A:1s through most C:1s such that many walls are annihilated, and large A:1s remain. Again, this behavior is consistent with observations of wall annihilation under *concave* bending in single crystals. [5] Thus, *convex* bending resulted in both wall creation and annihilation, while *concave* bending only seemed to favor annihilation.

REFERENCES

(1) Kennard, R. M.; Dahlman, C. J.; Nakayama, H.; Decrescent, R. A.; Schuller, J. A.; Seshadri, R.; Mukherjee, K.; Chabinyc, M. L. Phase Stability and Diffusion in Lateral Heterostructures of Methyl Ammonium Lead Halide Perovskites. *ACS Appl. Mater. Interfaces* **2019**, *11* (28), 25313-25321.

(2) Whitfield, P. S.; Herron, N.; Guise, W. E.; Page, K.; Cheng, Y. Q.; Milas, I.; Crawford, M. K. Structures, Phase Transitions and Tricritical Behavior of the Hybrid Perovskite Methyl Ammonium Lead Iodide. *Sci. Rep.* **2016**, *6* (June), 1-16.

(3) Birkholz, M.; Fewster, P. F.; Genzel, C. *Thin Film Analysis by X-Ray Scattering*; WILEY-VCH Verlag GmbH & Co. KGaA: Weinheim, Germany, 2006.

(4) Venkatesan, N. R.; Labram, J. G.; Chabinyc, M. L. Charge-Carrier Dynamics and Crystalline Texture of Layered Ruddlesden-Popper Hybrid Lead Iodide Perovskite Thin Films. *ACS Energy Lett.* **2018**, *3* (2), 380-386.

(5) Strelcov, E.; Dong, Q.; Li, T.; Chae, J.; Shao, Y.; Deng, Y.; Gruverman, A.; Huang, J.; Centrone, A. $CH_3NH_3PbI_3$ Perovskites: Ferroelasticity Revealed. *Sci. Adv.* **2017**, *3* (4), e1602165.

(6) Smilgies, D. M. Scherrer Grain-Size Analysis Adapted to Grazing-Incidence Scattering with Area Detectors. *J. Appl. Crystallogr.* **2009**, *42* (6), 1030-1034.

(7) WILSON, J. I. L. A. A. J. C. Seherrer after Sixty Years: A Survey and Some New Results in the Determination of Crystallite Size. *J. Appl. Crystallogr.* **1978**, *11*, 102-113.

(8) Suo, Z.; Ma, E. Y.; Gleskova, H.; Wagner, S. Mechanics of Rollable and Foldable Film-on-Foil Electronics. *Appl. Phys. Lett.* **1999**, *74* (8), 1177-1179.

(9) Sun, S.; Fang, Y.; Kieslich, G.; White, T. J.; Cheetham, A. K. Mechanical Properties of Organic-Inorganic Halide Perovskites, $CH_3NH_3PbX_3$ (X = I, Br and Cl), by Nanoindentation. *J. Mater. Chem. A* **2015**, *3* (36), 18450-18455.

(10) Rakita, Y.; Cohen, S. R.; Kedem, N. K.; Hodes, G.; Cahen, D. Mechanical Properties of $APbX_3$ (A = Cs or CH_3NH_3; X = I or Br) Perovskite Single Crystals. *MRS Commun.* **2015**, *5* (4), 623–629.

(11) Spina, M.; Karimi, A.; Andreoni, W.; Pignedoli, C. A.; Náfrádi, B.; Forró, L.; Horváth, E. Mechanical Signatures of Degradation of the Photovoltaic Perovskite $CH_3NH_3PbI_3$ upon Water Vapor Exposure. *Appl. Phys. Lett.* **2017**, *110* (12).

(12) Feng, J. Mechanical Properties of Hybrid Organic-Inorganic $CH_3NH_3BX_3$ (B = Sn, Pb; X = Br, I) Perovskites for Solar Cell Absorbers. *APL Mater.* **2014**, *2* (8).

(13) Okuzaki, H.; Ishihara, M. Spinning and Characterization of Conducting Microfibers. *Macromol. Rapid Commun.* **2003**, *24* (3), 261-264.

Chapter 3:

Phase Stability and Diffusion in Lateral Heterostructures of Methyl Ammonium Lead Halide Perovskites

3.1 Introduction

Hybrid halide perovskites have recently emerged as candidates for optoelectronic applications because they exhibit solar cell efficiencies similar to those of crystalline silicon,[1,2] are solution processable, and are made from inexpensive, earth-abundant materials.[3–6] Hybrid halide perovskites have an ABX_3 structure, where A is a cation (e.g. Cs^+, $CH_3NH_3^+$, $CH_5N_2^+$), B is a metal (e.g. Pb, Sn, Bi) and X is a halide. Mixed A-site cations and halides can be used to tune the optical gap and structure near room temperature; the resulting alloys have the highest power conversion efficiency in solar cells.[1,7–14] Films of nanocrystals of alloys are efficient light emitters, with quantum yields up to 90 %,[15] and have been explored for LED applications.[16] Despite the successes of alloys, halides can diffuse in hybrid perovskites, [17] which negatively impacts the performance of devices. Hysteresis in the current-voltage characteristics of solar cells is attributed to halide migration.[18,19] Mixed bromide-iodide perovskites can phase separate into I-rich and Br-rich domains upon light exposure,[20-31] leading to instabilities in the performance of Br-rich perovskite solar cells.[32-37] A thorough understanding of halide movement in mixed-halide perovskites is therefore desirable for future design of efficient devices.

While much progress has been made towards understanding the mechanisms and kinetics of light-induced phase separation,[20-31] the diffusion of halides in $MAPb(Br_xI_{1-x})_3$

without illumination is not as well understood. Many studies have focused on ion/vacancy movement in response to an electric field,[18,38-48] rather than on ion/vacancy movement down a concentration gradient.[29,49] Recent work has elucidated interdiffusion behavior of bromide and chloride in $CsPb(Br_xCl_{1-x})_3$ nanowires;[49,50] however, interdiffusion in Br-I systems has been less explored. Halide interdiffusion constants were previously extracted from $CsPbBr_3$-$MAPbI_3$ [49] and $PbBr_2$-$MAPbI_3$ [29] heterostructures, where distances travelled by the halides in a given time enabled calculation of the diffusion constant.[29,49] However, halide interdiffusion in $CsPbBr_3$-$MAPbI_3$ and $PbBr_2$-$MAPbI_3$ may differ from that in pure $MAPbX_3$ because of differences between the phase diagrams of the systems. Studies of Br-I interdiffusion in the $MAPb(Br_xI_{1-x})_3$ system are further complicated by the prediction of a miscibility gap,[51-52] where compositions within the gap phase-separate into I-rich and Br-rich regions, impeding halide interdiffusion down concentration gradients.

Here, we examine interdiffusion of halides in diffusion couples with varying composition of $MAPb(Br_xI_{1-x})_3$ at temperatures relevant to electronic devices. Using a halide substitution procedure, we fabricated lateral heterostructures of hybrid halide perovskite thin films and examined changes in the interfacial profiles upon exposure to heat and light. The stability of interfacial profiles confirmed that the interdiffusion coefficients D_i at temperatures relevant to device operation are low, and suggests that the $MAPb(Br_xI_{1-x})_3$ miscibility gap extends to higher temperatures and more Br-rich compositions than expected based on computational models. These results suggest compositions where it is possible to form heat-stable heterostructures of $MAPb(Br_xI_{1-x})_3$.

3.2 Experimental section

Materials

Lead (II) iodide was purchased from Sigma Aldrich (PbI_2 – 99.999% purity, trace metal basis) and from TCI chemicals (PbI_2 – 99.99% purity, trace metal basis). Methylammonium iodide (CH_3NH_3I, ≥ 99% purity) was purchased from Dyseol. Lead (II) bromide ($PbBr_2$ – 99.999% purity, trace metal basis) and methylammonium bromide (CH_3NH_3Br – 98% purity) were purchased from Sigma Aldrich. PolyDiMethylSiloxane (PDMS) was fabricated from a Sylgard 184 elastomer kit. N-N-dimethylformamide (DMF, 99.8%, anhydrous), dimethyl sulfoxide (DMSO, ≥ 99.9%, anhydrous), Chlorobenzene (99.8%, anhydrous) were purchased from Sigma Aldrich and kept in a nitrogen glove box. γ-butyl lactone (GLB, ≥ 99%) was purchase from Sigma Aldrich and stored in air. Bromine (Br_2, 99.5% purity) liquid was purchased from Alpha Aesar and stored in air. Quartz substrates (z-cut, seedless, 15 × 15 × 0.5 mm) were purchased from University Wafer. Polytriarylamine (PTAA), polyethylenimine (PEIE, 37% aqueous solution) were purchased from Sigma Aldrich and phenyl-C61-butyric acid methyl ester (PCBM, ≥ 99%) was purchased from Nano C.

Spin-casting of I-rich perovskites for heterostructures

Quartz substrates were ultrasonicated for 10 min in acetone and then for 10 min in isopropyl alcohol. The substrates were then exposed to oxygen plasma at ~300 mTorr for 10 min, with air as the oxygen source. Precursor solutions were fabricated in a nitrogen-filled glove box. PbI_2 and CH_3NH_3I were dissolved in 1 mL DMF and 96 μL DMSO to make a 1M solution, and the mixture was stirred for at least 30 min in a nitrogen-filled glove box. The same procedure was applied to precursors $PbBr_2$ and CH_3NH_3Br. The two solutions were then mixed in stoichiometric ratios necessary to obtain the desired perovskites (e.g. 3 parts I-solution and 7 parts Br-solution to obtain $MAPb(Br_{0.70}I_{0.30})_3$). The mixed solutions were then spin-cast onto the quartz substrates at 1000 rpm for 10 s then 4000 rpm for 30 s. When 8 s passed after the spin turned 4000 rpm, 0.2 mL of anhydrous chlorobenzene was dropped on the substrate. The films were transferred on a hotplate of 100 °C immediately, and thermally annealed for 10 min, again in a nitrogen-filled glove box. The temperature of the heat diffuser was verified with a thermocouple. This spin-coating procedure was used for all heterostructures except that of **Figure 3.S13** (see discussion of this figure below). The above-described preparation yielded 17% solar cell PCE for $MAPbI_3$ (see **Figure 3.S1**).

Solar cell device fabrication and characterization (Figure 3.S1)

Quartz substrates were cleaned and plasma-treated as described above. All procedures were performed in a nitrogen-filled glove box. A 2 mg/mL solution of PTAA in chlorobenzene was spin-cast on the substrates at 6000 rpm. The DMF solution containing $MAPbI_3$ precursors was then spin-cast as described above. A solution for the electron transport layer (30 mg/mL PCBM in chlorobenzene) was spin-cast on the $MAPbI_3$ layer at 1000 rpm. 0.02 wt.% PEIE in isopropyl alcohol was then spin-cast at 6000 rpm. The devices were finally capped with Ag (80 nm) by vacuum deposition. The *J*–*V* characteristics were measured at 1 sun illumination (AM 1.5G, 100mW/cm^2) in a N_2-filled glovebox with a solar simulator equipped with a Xenon lamp (Newport), a Keithley 2602 Source Meter and a calibrated silicon reference cell (**Figure 3.S1**). The voltage was ramped from 1.50 V to –0.50 V then back to 1.50 V with 0.01 V step and 0.03 s delay time. The power conversion efficiency (PCE) was calculated with the following equation:

PCE (%) = 100 × V_{OC} × J_{SC} × FF / P_{inc} from the open circuit voltage, V_{OC}, the short circuit current, J_{SC}, the fill factor FF and the incident powder P_{inc}.

Spin-casting of $MAPb(Br_xI_{1-x})_3$ thin films for lattice parameter calibration curve (Figure 3.S5c)

The procedure was identical to that described immediately above, with the following differences. PbI_2 and CH_3NH_3I were dissolved in DMF to make an 0.55 M solution (same procedure for $PbBr_2$ and CH_3NH_3Br), and the mixtures were stirred for >1 h at 60 ^oC in a nitrogen-filled glove box. The spin procedure was 2000 rpm for 1 min, with no antisolvent used. The films were annealed at 70 ^oC (verified with a thermocouple) for 5 min.

Fabrication of PDMS mask for heterostructures

Polydimethylsiloxane (PDMS) was fabricated by pouring 0.5 g of Sylgard 184 silicone elastomer base into an aluminum boat and adding 0.12 g of curing agent. The base and curing agent were stirred using a disposable plastic spatula until visible formation of many bubbles. The boat was then set on a flat surface, to ensure even spreading. After the last bubble disappeared, the cup was placed on a hot plate at 53 ^oC (as determined by thermocouple) for 10 min. The PDMS was poked with a needle to ensure no liquid remained and cut with a razor blade for use as a mask. The top surface (exposed to air) of the PDMS was contacted with the perovskite, as it was flatter than the bottom surface (that had been in contact with the bottom of the boat). Care was taken not to press the PDMS layer onto the perovskite, as this led to partial removal of the perovskite by the PDMS.

Vapor substitution to fabricate heterostructures

Briefly, a previously-reported vapor substitution setup was reproduced, with the following differences. [1] All nitrogen gas lines were purged for 5 min. 1.25 mL of liquid bromine was poured into a 50mL round-bottomed flask and allowed to equilibrate for ~ 2 min. The bromine gas stream was combined with a second nitrogen stream, leading to a second 50mL round-bottomed flask (the sample chamber). The masked thin films were dropped into the chamber (Br_2 concentration ≈ 0.48 atm) and kept there for ~1 min. The PDMS mask was then carefully removed from the heterostructure.

Interdiffusion experiments

Prior to heating, we spin-coated a thin layer of polystyrene on top of the heterostructures, both to prevent desorption of methylammonium, enabling lengthy and high-temperature experiments, and to minimize diffusion along the perovskite surface. The heterostructures were heated for extended times (up to 360 min.) on a hot plate with a heat diffuser in a nitrogen-filled glove box. The heat diffuser was encased in aluminum foil to ensure that the samples were kept in the dark, as light may affect halide transport. At particular time points, the heterostructures were transported from the hot plate (in the glove box) to the optical microscope for analysis. The time from hot plate to microscope was < 5 min. The heterostructures were then transported back to the glove box, and put on the hot plate again. The total time off the hot plate at each time point was < 10 min.

Characterization and Equipment

Optical microscopy images were acquired using an Olympus BH-2 microscope in transmission mode. X-Ray Diffraction patterns were acquired using an Empyrean Powder Diffractometer with a step size of 0.01313°, with a Cu-Kα source, operating with an accelerating voltage of 45 kV and beam current of 40 mA, with samples rotated at 4 revolutions/min to improve signal-to-noise ratios. UV-Vis spectra were acquired using a Shimadzu UV3600 UV-Nir-NIR Spectrometer with a step of 1 nm, in ambient conditions. Scanning Electron Microscopy/Energy Dispersive X-Ray data was acquired using both an FEI XL30 Sirion FEG SEM and a ThermoFischer Apreo C LoVac FEG SEM with EDX detectors. 10keV was used in both SEMs so as to be able to detect iodine with an adequate signal-to-noise ratio via EDX. Confocal microscopy was performed on a Leica SP8 Laser Scanning Confocal microscope, with a laser excitation wavelength of 458 nm. Time-resolved PL were collected using an inverted microscope (Nikon Eclipse Ti-U) at 20x magnification. Samples were continuously excited by a 405nm laser (Thorlabs S1FC405) through a 20x objective, with power density ≈ 160 mW/cm^2 at the level of the sample, and PL was continuously collected with 1 s integration times through the same objective and was passed through the entrance slit of an imaging spectrometer (Princeton Instruments IsoPlane), spectrally separated by a 150 lines/mm grating, and collected with a CCD array (Princeton Instruments Pixis). A standard 405nm PL filter set (Semrock) was used for all PL measurements to remove excitation wavelengths from the collected signal.

Image integration to obtain interface profiles

To obtain interface profiles, optical and EDX microscopy images were integrated using FIJI/ImageJ software. The optical images were converted to grayscale by taking the average values of the red, green and blue pixels, giving each pixel equal weight. The entire image area was then selected and then collapsed (integrated) to a line using the "plot profile" function. This methodology was used (rather than obtaining simple linecuts of the images) in order to improve signal-to-noise ratios, which was particularly important for EDX-obtained interface profiles. Compositional verification of the optically-obtained interface profiles was performed using EDX, with $MAPbBr_3$ and $MAPbI_3$ baseline compositional verifications performed in regions far from the interface.

3.3 Results and Discussion

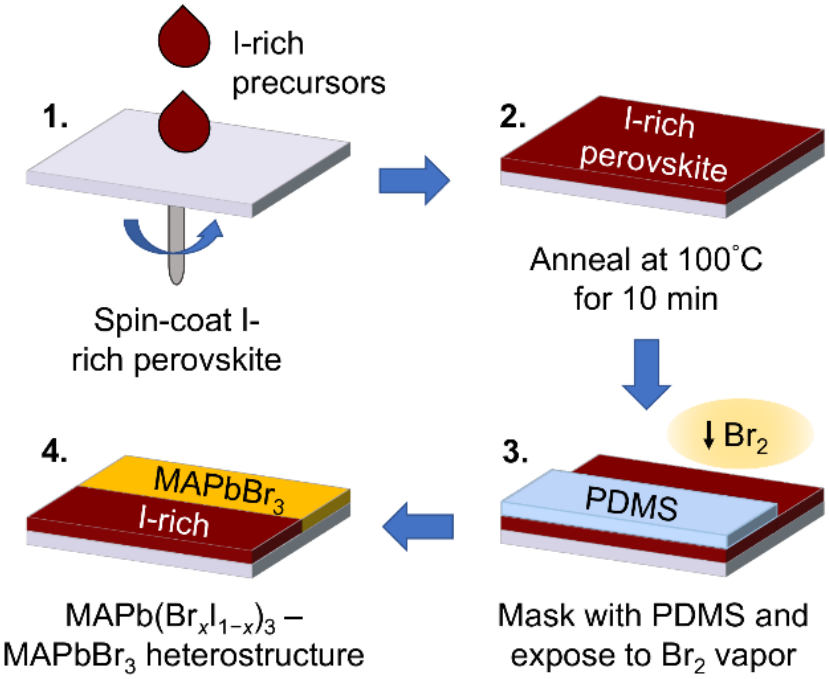

Figure 3.1. Fabrication procedure for perovskite-perovskite heterostructures.

To fabricate a diffusion couple comprising a lateral heterostructure of two compositions of $MAPb(Br_xI_{1-x})_3$, we used a two-step process. First, we spin-coated an I-rich perovskite thin film and then we used a halide exchange reaction to form the heterostructure.[53] We sought a methodology that would reflect the crystallinity and microstructure of thin films typically used in devices. Other heterostructures or halide gradients have been formed by processes including solution exchange,[54] placement of microplates on top of nanowires,[49] activation of phase separation/domain merging in single crystal nanowires using light,[25] electron-beam lithographic patterning of nanowires,[55] and contacting nanowires with single crystals.[56] While lithographic patterning enables fabrication of very sharp patterns, developers and electron beams may cause sample damage and/or introduce vacancies in the hybrid halide perovskites.[57] Modification of the halide composition using precursors in solvent may also impact the crystallinity of the substituted layer due to recrystallization. We therefore selected substitution by reaction with a vapor of Br_2 to ensure that the I-rich and Br-rich perovskites had similar morphology and grain size,[53] which is desirable for interdiffusion studies. As with many substitution procedures, the number of vacancies in the Br_2-exposed side may change relative to that on the masked side, which could change the rates of interdiffusion in these two areas relative to other methods.

The procedure to form lateral heterostructures is shown in **Figure 3.1**. Iodine-rich perovskites were spin-coated onto quartz substrates. We chose an I-rich perovskite spin-coating procedure that yields 17% solar cell efficiency for $MAPbI_3$, before any halide substitution (**Figure 3.S1**). A ≈ 450 μm-thick PDMS conformal mask was then laid on top of the thin film of $MAPb(Br_xI_{1-x})_3$, thus covering half of the 1.5 cm × 1.5 cm × 300 nm thin film. The masked film was exposed to bromine vapor (≈ 0.48 atm) in a nitrogen environment. The PDMS acted as a barrier to the bromine vapor and the exposed areas were allowed to react fully with the vapor, yielding $MAPbBr_3$. Consistent with previous reports,[53] the reaction was complete within one minute, indicating rapid reaction of Br_2 with $MAPbI_3$. The PDMS was then peeled off, leaving behind a lateral heterostructure of

$MAPb(Br_xI_{1-x})_3$|$MAPbBr_3$. We focused on heterostructures with three compositions: $MAPbI_3$|$MAPbBr_3$, $MAPb(Br_{0.12}I_{0.88})_3$|$MAPbBr_3$, and $MAPb(Br_{0.70}I_{0.30})_3$|$MAPbBr_3$. These are hereafter referred to as x_{Br} = 0|1, x_{Br} = 0.12|1, and x_{Br} = 0.70|1 heterostructures respectively. We chose to examine the response of iodine-containing phases x_{Br} = 0.12 and x_{Br} = 0.70, in addition to that of x_{Br} = 0, because these are at the approximate locations of the binodal lines at room-temperature predicted by calculations using density functional theory.[51]

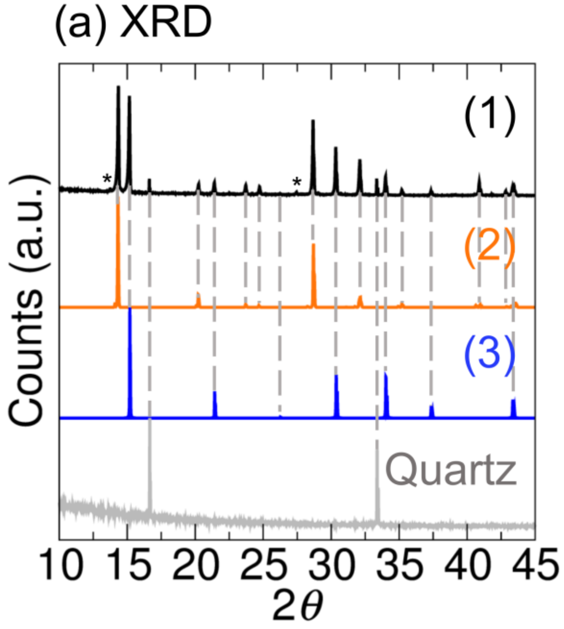

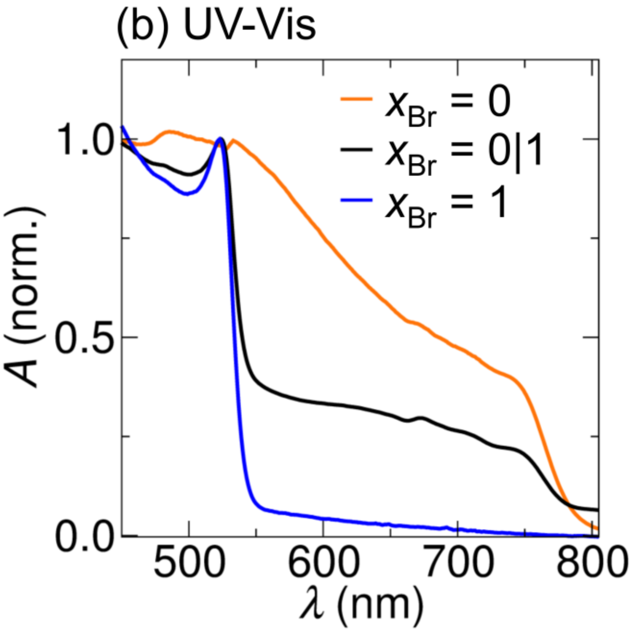

Figure 3.2. (a) XRD patterns of the $MAPbI_3$-$MAPbBr_3$ heterostructure (x_{Br} = 0|1 - black trace (1)), of simulated $MAPbI_3$ (orange trace (2)), of simulated $MAPbBr_3$ (blue trace (3)), and the quartz substrate (gray trace). Simulations were performed using the *I4/mcm* structure of $MAPbI_3$ [58] and using the *Pm-3m* structure of $MAPbBr_3$.[26] The dotted gray lines are guides for the eye, and the black * indicate additional peaks arising from Tungsten (1.4764 Å) and CuKβ (1.3926 Å) contamination in the X-Ray source. (b) UV-Vis spectra of the $MAPbI_3$-$MAPbBr_3$ heterostructure, of spin-cast $MAPbI_3$ and of spin-cast $MAPbBr_3$.

The conformal mask and substitution by Br_2 vapor led to complete exchange of the halide along with an interfacial region (70 - 100 microns wide) of mixed composition;

examination of changes along this interfacial region in response to heat was used to analyze phase behavior in MAPb(Br_xI_{1-x})$_3$, as will be discussed later. Formation of the desired heterostructures was confirmed via X-Ray Diffraction (XRD), UV-Vis spectroscopy (**Figure 3.2**), Scanning Electron Microscopy (SEM – **Figure 3.3**) combined with Energy-Dispersive X-ray analysis (EDX – **Figures 3.*S2*, 3.*S3* and 3.*S4***) and confocal microscopy (**Figures 3.3** and **3.S5**). XRD of the entire film of an $x_{Br} = 0|1$ heterostructure displayed peaks corresponding to both $MAPbI_3$ and $MAPbBr_3$, indicating full replacement of the iodine with bromine (**Figure 3.2a**). Similarly, the UV-Vis spectrum of an $x_{Br} = 0|1$ heterostructure displayed increased absorption at the onsets of the $MAPbI_3$ and $MAPbBr_3$ bandgaps (**Figure 3.2b**). XRD and UV-Vis characterization for the $x_{Br} = 0.12|1$ and $x_{Br} = 0.70|1$ heterostructures also confirmed formation of the desired phases (**Figure 3.S6**). Plan view SEM of $x_{Br} = 0|1$ revealed the local structure of the interfacial region (**Figure 3.3a**). The films comprised ≈ 300 nm grains contained in large, continuous domains, which is favorable for examining halide diffusion across large areas. The change in contrast in domains along the interface indicated that halide substation occurred in the middle of the domains (**Figure 3.3a**). Top-view and cross-sectional EDX (**Figures 3.4**, **3.*S2*, 3.*S3*, and 3.*S4***) confirmed the locations of Br and I, and thus of $x_{Br} = 0$ and $x_{Br} = 1$. No iodine was observed above noise level in the $x_{Br} = 1$ region, again suggesting complete removal of iodine from this area. Intermediate x_{Br} compositions along the interface were assigned based on halide content relative to the EDX- and optically-determined $x_{Br} = 0$ and $x_{Br} = 1$ compositions for $x_{Br} = 0|1$. Similar analysis was performed to determine macroscopic interfacial composition in the $x_{Br} = 0.12|1$ and $x_{Br} = 0.70|1$ heterostructures. EDX baseline compositions were obtained far from the interface (data not shown) to confirm lack of bromine in $x_{Br} = 0$ and lack of iodine in $x_{Br} = 1$ (**Figures 3.4, 3.6** and **3.S3**). The interface width was determined to be ≈100 μm (**Figures 3.4** and **3.S3**) via both EDX, optical microscopy, and confocal laser scanning microscopy (**Figures 3.3b-d** and **3.S5**). We attribute the width of the interfacial region to our fabrication procedure in which Br_2 vapor permeates PDMS at the edge of the mask (**Figure 3.S7**); and note that in a system with a miscibility gap, which is predicted for the $MAPb(Br_xI_{1-x})_3$ system,[51] a sharp interface would be expected with an impermeable mask.

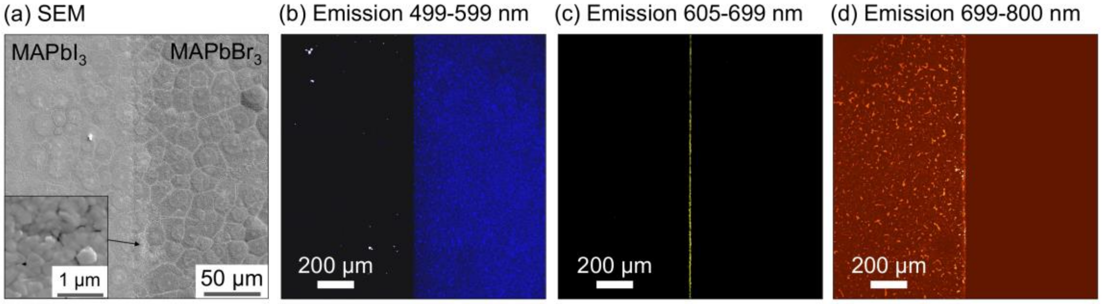

Figure 3.3. Plan view SEM of an MAPbI3-$MAPbBr_3$ heterostructure before heating (a). The inset in is a high-magnification view of the area indicated by the arrow. Confocal scanning luminescence emission map at three windows of emission, 499 - 599 nm (b), 605 - 699 nm (c), and 699 - 800 nm(d), each labelled with false color, of an $MAPbI_3$-$MAPbBr_3$ heterostructure before heating, with excitation wavelength 458 nm.

We examined the phase stability of the heterostructures upon heating without light exposure, at temperatures relevant for thin film devices (see **Experimental Section**). Operating temperatures are typically under 70°C for solar cells[59] and lamination or curing temperatures for solar cell encapsulants can exceed 100°C.[60,61] The miscibility gap for $MAPb(Br_xI_{1-x})_3$ calculated by DFT extends to 70°C,[51] leading to the expectation that halides will not diffuse down concentration gradients below this temperature. We therefore selected 100°C because it is within the window of temperatures encountered under practical conditions for devices and can test the expected miscibility of the halide ions, at a temperature that will not be too damaging to the perovskite layer.[62] Prior to heating, we spin-coated a thin layer of polystyrene on top of the heterostructure, both to prevent desorption of methylammonium, enabling lengthy and high-temperature experiments, and to minimize diffusion along the perovskite surface. The heterostructures were heated for extended times (up to 360 min.) on a hot plate with a heat diffuser in a nitrogen-filled glove box. Lack of degradation and change in grain structure after heating were confirmed via XRD and top-view SEM (**Figures 3.S8 and 3.S9**). The heat diffuser was encased in aluminum foil to ensure that the samples were kept in the dark, as light may affect halide transport. After heating, the compositional profiles at the heterostructure interface were analyzed via optical microscopy in transmission mode and via EDX (**Figure 3.4**). At each time point, the samples were quickly removed from the hot plate/heat diffuser in the glove box for optical microscopy analysis and were placed again on the heat diffuser afterwards. The total time off the hot plate, at each time point, was kept under 10 min. This method ensured rapid quenching of any halide migration, which would be visible via change in local bandgap. Using optical microscopy to obtain interface profiles enabled repeated analysis of the same location on each heterostructure at each time point, enabling very rapid analysis of the interface profiles at specific times. Optical microscopy also circumvented potential electron beam-induced sample damage (and corresponding changes in vacancy concentration) that may have occurred during EDX analysis. Interface profiles were subsequently analyzed after heating via EDX to confirm the composition.

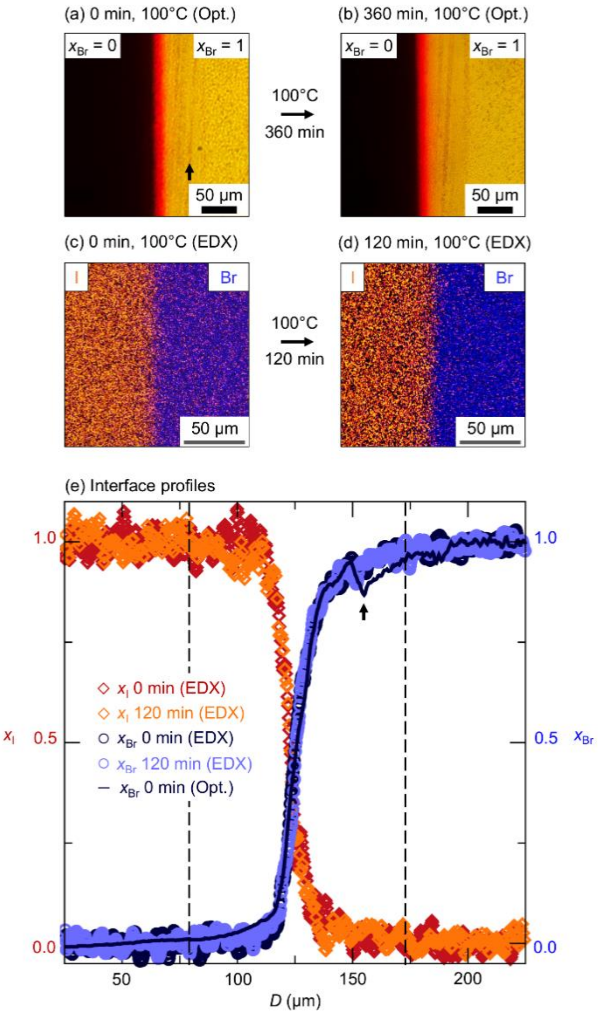

Figure 3.4. Optical microscopy images (transmission mode) of the same x_{Br} =0|1 heterostructure before (a) and after (b) heating at 100°C for 360 min, obtained via illumination with white light. (c, d) EDX maps of I and Br in separate x_{Br} =0|1 heterostructures before (c) and after (d) heating at 100°C for 120 min. (e) Interface profiles (halide fraction vs. distance *D*) of the heterostructures in (a)-(d), showing overlap of the optical microscopy and EDX-determined x_{Br} traces. x_I represents the halide fraction of I obtained from the EDX images (c) and (d) (orange circles). x_{Br} represents the halide fraction of Br obtained from the EDX images (c) and (d) (blue circles) and from the optical microscopy image (a) (blue line). The dashed lines indicate the interface width. The black arrow in (a) and (e) denotes residual PDMS on the heterostructure surface (**Figure 3.S7**), resulting in a dip in optical intensity near ≈ 150 μm.

We verified that optical microscopy provided comparable interfacial profiles to EDX, enabling a measurement of the interface profiles in a quasi-real-time and non-destructive manner (**Figure 3.4**). The interface profiles of x_{Br} = 0|1 obtained before and after heating, using both optical microscopy and EDX, are shown in **Figure 3.4**. Because the bandgap of $MAPbBr_3$ is ≈ 540 nm and that of $MAPbI_3$ is ≈ 775 nm (**Figure 3.2b**), when the heterostructures were illuminated with white light, the $MAPbI_3$, the $MAPbBr_3$ and the intermediate mixed-halide regions exhibited very different transmission behavior (**Figure 3.4a/b**) and thus very different contrast. The dark color in **Figure 3.4a/b** is $MAPbI_3$, the yellow is $MAPbBr_3$, and the pink is the intermediate region. The images were converted to grayscale by taking the average values of the red, green and blue pixels, giving each pixel equal weight. We then integrated the images to obtain interface profiles, with the darker and lighter areas corresponding to $MAPbI_3$ and $MAPbBr_3$ respectively (**Figure 3.4e** and **Appendix to Chapter 3**). Interface profiles obtained from EDX overlapped well with those obtained via optical microscopy (**Figure 3.4e**), confirming the validity of the optical method. The optical microscopy and EDX interfacial profiles differ at a position of ≈ 150 μm along the interface (black arrows in **Figure 3.4a/e**), which we attribute to residual PDMS on the sample (**Figure 3.S7**). We assume the EDX trace is more accurate in this region. We subsequently applied the optical method to x_{Br} = 0.70|1 and x_{Br} = 0.12|1 heterostructures (**Figures 3.7** and **3.S10**), again confirming compositions using EDX.

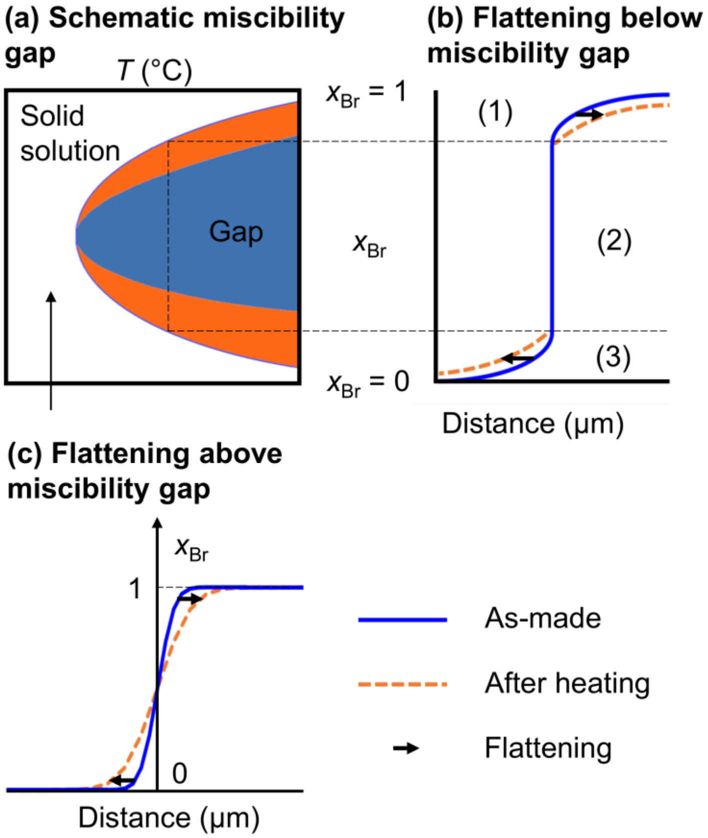

Figure 3.5. (a) Predicted miscibility gap for the MAPb(Br_xI_{1-x})$_3$ system following a regular solution model (from DFT [51]), with expected interface profile behavior (b) when heated to below the gap for a two-phase binary system and (c) when heated to above the gap, for a single-phase binary system.[63] Sections (1) and (3) refer to the Br-rich and I-rich halide miscible regions outside the miscibility gap, and section (2) refers to the halide-immiscible region within the gap. The blue and orange regions designate predicted binodal and spinodal areas of the miscibility gap.

The expected changes in the interface profiles upon exposure to heat strongly depend on whether or not the heterostructure is heated to below or above the miscibility gap. [63,64] **Figure 3.5** depicts a schematic miscibility gap for the MAPb(Br_xI_{1-x})$_3$ system, with approximate interfacial profile shapes before and after heating shown if the heterostructure is kept at temperatures within the miscibility gap (**Figure 3.5b**) or is heated to above the miscibility gap (**Figure 3.5c**). For simplicity, the tetragonal-cubic phase transition in the I-rich region is not shown. Within the schematic gap (**Figure 3.5a** - shaded area), halides are expected to phase separate into I-rich and Br-rich phases. The shape of the interface profile is thus not expected to change for composition regions of the interfacial profile that are contained within the miscibility gap (**Figure 3.5b** – section (2)). However, outside of the miscibility gap, halides can still intermix, which should change the shape of the profile away from the interface (**Figure 3.5b** – sections (1) and (3)). Due to mass balance as halides move from one side to the other, the interface should shift also slightly in location (**Figure 3.5b**).[63,64] In contrast, should the heterostructures be heated to above the miscibility gap (**Figure 3.5c**), halides should be free to intermix across the entire interfacial profile. Br and I should thus diffuse down their respective concentration gradients, resulting in apparent flattening of the entire interfacial profile, as shown in **Figure 3.5c**. This flattening would be most apparent near the edges of the interface (Br-rich and I-rich regions), and least apparent near the mid-point, where the composition stays constant.

Before discussing the response of the interfacial profiles to heat, we first analyzed the behavior of the interfacial profiles upon formation. Although XRD and other characterizations indicated clear presence $x_{\mathrm{Br}} = 0$ and $x_{\mathrm{Br}} = 1$ in the heterostructure (**Figures 3.2** and **3.4**), no XRD peaks corresponding to intermediate compositions were identified (**Figure 3.2 and 3.S6**), as the interfacial region is a small percentage of the overall area in the incident beam. Given the presence of the gap,[25,51] one might expect the interface to be composed of crystallites with stoichiometries corresponding to the I-rich and Br-rich binodal lines. When averaged, mixtures of different amounts of these crystallites would then yield the apparently-smooth composition profiles of **Figures 3.4** and **3.6**. In agreement with this, a $MAPbI_3$ film exposed to Br_2 vapor for only 5 seconds (as opposed to 60s required for full bromination) exhibited highly uneven bromination, in the sense that exposure to Br_2 vapor induced formation of pockets of Br-rich regions, rather than the even, gradual composition change that would be expected if the compositions were miscible (**Figure 3.S11**). However, emission corresponding to intermediate mixed-halide compositions (605 - 699 nm, or $0.3 < x_{Br} < 0.7$; see discussion of **Figure 3.S5**) was observed in the interfacial region via scanning confocal microscopy (**Figures 3.2b** and **3.S5**), where sample exposure times are on the order of microseconds, indicating some retention of the $0.3 < x_{Br} < 0.7$ compositions. Prolonged exposure to above-bandgap light (405 nm, or 3.06 eV) induced a red-shifting photoluminescence emission at 730 nm (1.7 eV) that also became more intense over time, which is characteristic of light-induced phase separation into I-rich and Br-rich regions[20] (**Figure 3.S12**), and suggests that some intermediate compositions were present initially. Given all these observations, it is likely that upon formation, the interface was composed of some metastable intermediate compositions, as well as of some phase separated nanoscale I-rich and Br-rich regions (**Figures 3.2b** and **3.S5**).

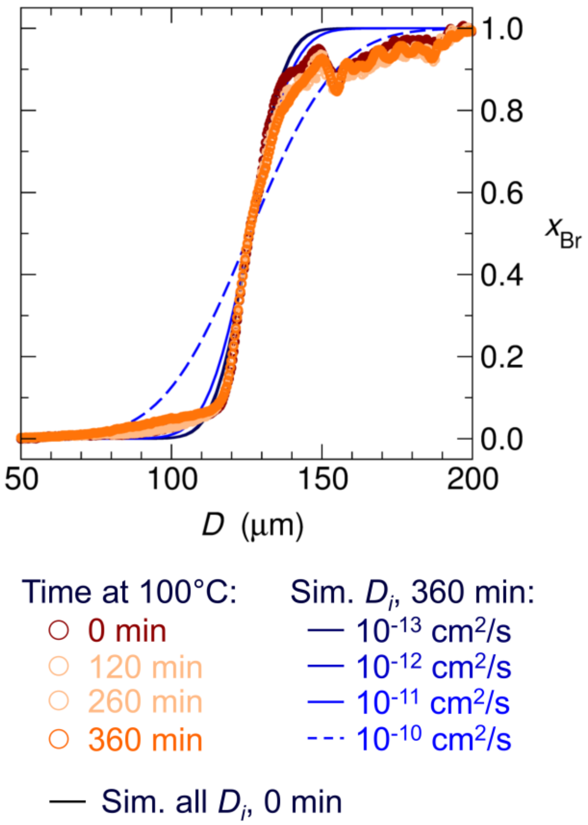

Figure 3.6. Compositional profiles of an x_{Br} =0|1 heterostructure obtained using optical microscopy after 0 min, 120 min, 260 min and 360 min of heating at 100°C. Profiles from Fick's second law with different interdiffusion coefficients D_i were calculated as described in **Section 3.S9**.

We then examined the effects of heating on the interfacial profiles. All heterostructures studied exhibited little interfacial profile flattening upon heat exposure (**Figures 3.6, 3.7, 3.S10** and **3.S15**). Slight changes in composition near x_{Br} = 0.8 and x_{Br} = 0.1 were observed in x_{Br} =0|1 after heating at 100°C for 360 min (**Figure 3.6**); however, overall, the interfacial profiles changed very little. The profiles do not follow Fickian behavior described by **Figure 3.5c**, i.e. what would be expected from a solid solution (see **Figure 3.S13**). Calculations of how the diffusion profile should change according to Fick's law (see **Section 3.S9** of the **Appendix to Chapter 3**) with interdiffusion coefficients D_i of different magnitudes were overlaid with the interfacial profiles for comparison

(**Figure 3.6**). Although there is some uncertainty of the profile derived from microscopy at higher values of x_{Br}, D_i cannot be larger than ~ 10^{-11} cm^2/s at 100° C based on examination of the profile on both sides of the interface. The profiles of the x_{Br} =0.12|1 and x_{Br} =0.70|1 heterostructures were also unchanged upon heating at 100°C for 260 min by microscopy and EDX (**Figures 3.7** and **3.*S*10, 3.*S*14**). We thus take $D_i \leq 10^{-11}$ cm^2/s as an upper bound of the interdiffusion coefficient for MAPb(Br$_x$I$_{1-x}$)$_3$ at 100°C. Such a value is consistent with D_i obtained at lower temperatures and in different systems, namely 3 × 10^{-12} cm^2/s at 50°C using PbBr$_2$ as a Br-source for a PbBr$_2$-MAPbI$_3$ heterostructure[29] and ~1 × 10^{-12} cm^2/s at room temperature for a CsPbBr$_3$-MAPbI$_3$ heterostructure.[49] However, the poor fit to this model suggests an alternative explanation.

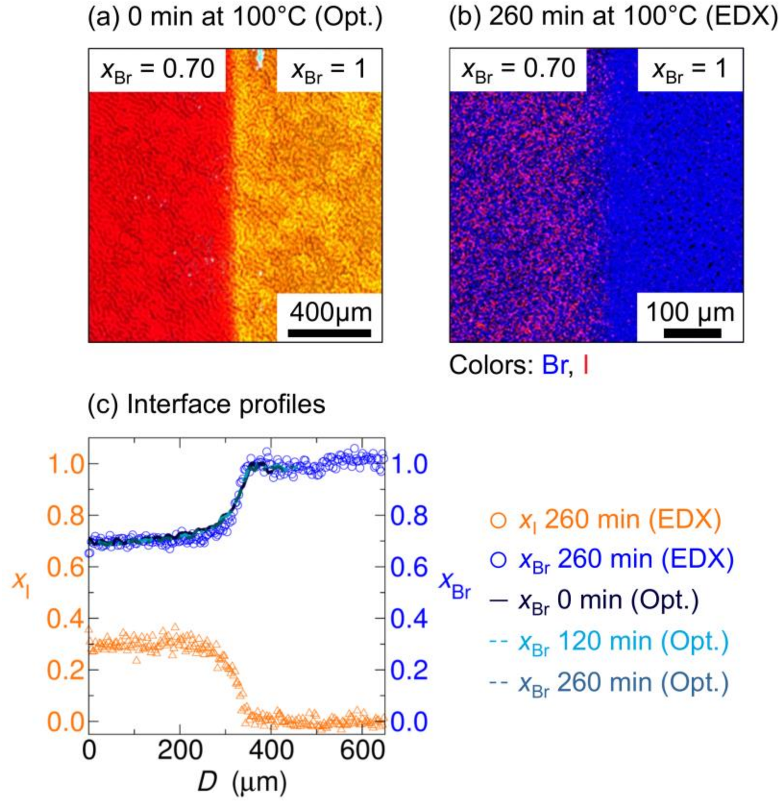

Figure 3.7. (a) Optical microscopy image of an x_{Br} = 0.70|1 heterostructure before heating. (b) EDX mapping of I and Br in the same x_{Br} = 0.70|1 heterostructure (in the same location) after heating at 100°C

for 260 min. (c) Interface profiles (halide fraction vs. distance *D*) of the same x_{Br} = 0.70|1 heterostructure upon heating to 100°C for varying amounts of time. x_{I} represents the halide fraction of I obtained from the EDX image (b) (orange circles). x_{Br} represents the halide fraction of Br obtained from the EDX image (b) (blue circles) as well as from the optical microscopy image (a) (black line). Additional interface profiles obtained via optical microscopy are included (dashed blue lines).

The lack of flattening of the interfacial region may indicate slow interdiffusion, but if the miscibility gap extends to higher temperatures than predicted then we would expect different behavior than that of **Figure 3.5c**. The changes in the interface profile at 100°C were slight and only at the edges of the interface profiles (**Figure 3.6**), much like the interfacial profiles depicted in **Figure 3.5b**. No large changes were observed in x_{Br} = 0.12|1 and in x_{Br} = 0.70|1 heterostructures upon heating at 100°C for 260 min (**Figures 3.7** and **3.*S*10**). The interfacial profiles were all set to overlap at x_{Br} = 0.5 during analysis and we do not have a marker to track changes in the interfacial profile shifted in location as in **Figure 3.5b**. We also examined a x_{Br} = 0|1 formed using another route to for the initial $\mathrm{MAPbI_3}$ layer and found similar behavior (**Figure 3.S15**). Overall, these results suggest a miscibility gap extending to above 100°C and well into the Br-rich region.

(a) x_{Br} = 0|1, 8 months at RT

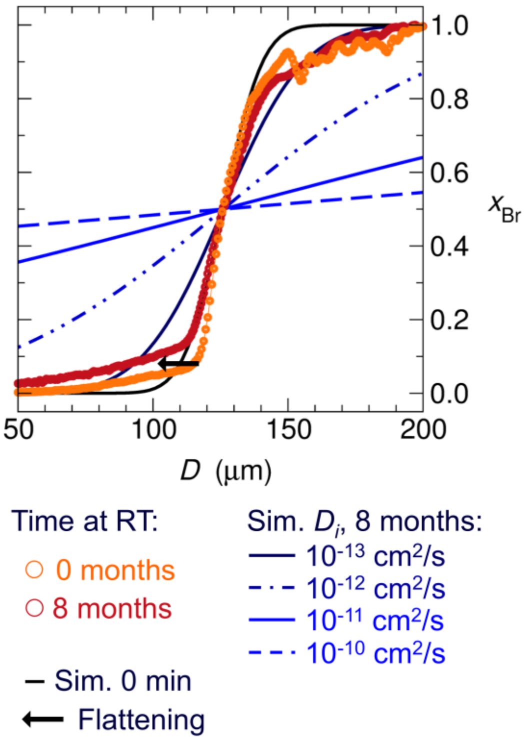

(b) x_{Br} = 0.7|1, 9 months at RT

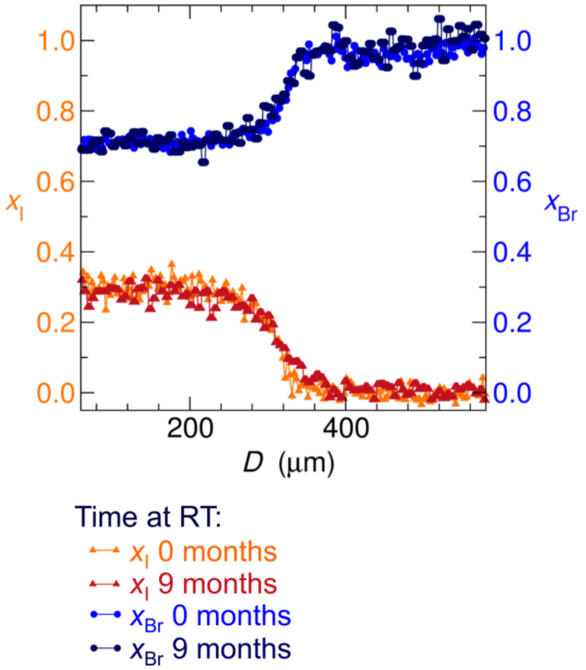

Figure 3.8. Effects of 8-9 months of storage at room temperature on the interfacial profiles of (a) x_{Br} = 0|1 and (b) x_{Br} = 0.70|1, with overlapping simulations of Fick's law with different D_i and interfacial profile flattening (black arrow).

To rule out the possibility of slow interdiffusion at room temperature, we then examined the response of interfacial profiles to long-term storage (8-9 months), to determine the composition bounds of the miscibility gap at room temperature. All encapsulated heterostructures (x_{Br} =0|1, x_{Br} =0.12|1 and x_{Br} =0.70|1) were stored at room temperature in ambient for 8 to 9 months, after which the interfacial profiles were again obtained via a combination of optical microscopy and EDX (**Figures 3.8**, **3.S10** and **3.S16**). We show the profiles expected for simple diffusion in the absence of a miscibility gap for a range of interdiffusion constants. Even for values as low as ~10^{-13} cm^2/s at this timescale we would expect a substantial change in the profile on both sides of the midpoint which is not observed. A noticeable change towards higher concentration of iodide was observed in the composition region from $0 < x_{Br} < 0.2$ in x_{Br} =0|1 stored for 8 months, consistent with the presence of a solid solution region from $0 < x_{Br} < 0.2$ **(Figure 3.8a)**.[20,51,65] Based on the distance that the composition shifted (≈ 20 μm), D_i in this region would be ≈ 10^{-13} cm^2/s, which is lower than the D_i estimated in the I-rich region of a $CsPbBr_3$-$MAPbI_3$ heterostructure at room temperature.[49] In contrast, little change was observed in the composition region $0.2 < x_{Br} < 1.0$ in x_{Br} =0|1 **(Figure 3.8a)**, consistent with the presence of a miscibility gap for $0.2 < x_{Br} < 1.0$. The behavior of the profile, particularly the region near $x_{Br} \approx 0.2$, is consistent with the presence of a miscibility gap (**Figure 3.5b**), in general agreement with the predicted phase diagram by DFT. To further probe the extent of the gap into the Br-rich region, we compared the interfacial profiles of x_{Br} =0.70|1 before and after 9 months of storage, via EDX. No flattening was observed, suggesting that the miscibility gap extends to very near $x_{Br} = 1$ at room temperature (**Figure 3.9**), which is much further into the Br-rich region than predicted by theory.[51] Extension of the gap to $x_{Br} \approx 1$ may explain why mixed Br-I hybrid of very high Br-content (e.g. $x_{Br} = 0.9$) have been observed to undergo light-induced phase separation.[20] Because we cannot access longer times for interdiffusion at elevated temperatures, we cannot completely rule out that diffusion is simply slow which limits our ability to set the temperature for the miscibility gap. Such very slow interdiffusion would be consistent with the slower re-mixing of halides in the dark, after light-induced phase separation, the latter of which is typically a rapid process. [20,21] **Figure 3.9** shows three possibilities constrained by the magnitude of the interdiffusion constant.

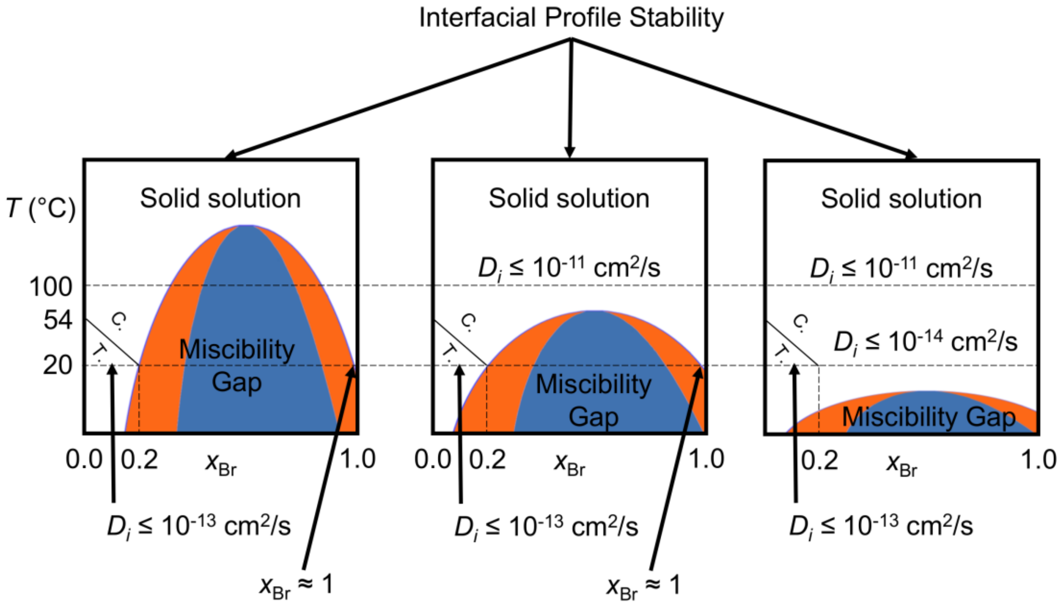

Figure 3.9. Summary of results, with three possible explanations for the obtained data, and with the Br-rich binodal line at room temperature near $x_{Br} = 1$. Schematic phase diagrams for the $MAPb(Br_xI_{1-x})_3$ system, modified from reference,[51] should the miscibility gap either extend to above 100°C or extend to below 100°C, with the obtained upper bounds for D_i at room temperature and 100°C. C. and T. refer to cubic (*Pm-3m*) [26] and tetragonal (*I4/mcm*)[58] phases respectively, with phase transition temperatures for the $x_{Br} = 0.0$ and $x_{Br} = 0.2$ compositions reported from references.[33,66] The blue and orange regions designate binodal and spinodal areas of the miscibility gap, respectively.

Finally, we examined the response of an $x_{Br} = 0|1$ heterostructure to light (**Figure 3.10**). Light-induced spinodal decomposition has been observed in single-crystal nanowires of $MAPb(Br_xI_{1-x})_3$, where halides diffused up the concentration gradient.[25] We would thus not expect interface profile flattening when exposing an x_{Br} = 0|1 heterostructure to light, but rather the formation of I-rich and Br-rich regions along the interface. Consistent with these expectations, prolonged exposure of the interface region to above-bandgap light (3.06 eV) at ≈ 0.14 Suns (≈ 14 mW/cm^2) induced the growing and red-shifting photoluminescence emission at 1.7 eV characteristic of light-induced phase separation into I-rich and Br-rich regions (**Figure 3.S12**).[20] Previous works also reported that the I-rich domains formed during spinodal decomposition are sub-100 nm[20,23] in polycrystalline $MAPb(Br_xI_{1-x})_3$, which is below the resolution of our experiment. We tested the response of the interfacial profiles of an x_{Br} = 0|1 heterostructure to light by exposing the whole heterostructure to 1 Sun (AM 1.5G, 100 mW/cm^2) of light for 360 min (**Figure 3.10**) at room temperature. In agreement with expectations, the interfacial profile of x_{Br} = 0|1 did not change after light exposure, providing additional confirmation that light does not activate long-range halide transport in mixed-halide perovskite thin films.

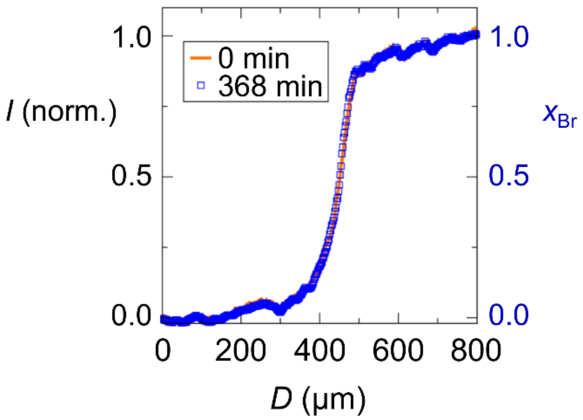

Figure 3.10. Integrated interfacial profiles of an x_{Br} = 0|1 heterostructure before and after exposure to 1 Sun for 368 min, with corresponding x_{Br} axis shown on the right.

3.4 Conclusions

In conclusion, we have examined interdiffusion in planar heterostructures of $MAPb(Br_xI_{1-x})_3$ films. These structures did not undergo simple interdiffusion that would be expected for a miscible system, but were more consistent with the presence of a miscibility gap at 100 °C. We also determined the upper bound of the bromide-iodide interdiffusion coefficient ($D_i \leq 10^{-11}$ cm^2/s) in spin-coated $MAPb(Br_xI_{1-x})_3$ films at 100°C. Long term study of the interface indicates that the binodal line at room temperature extends to higher fractional composition of bromine than predicted by theory, but is in reasonable agreement at high iodide composition. Improvement of our understanding of the phase diagram of $MAPb(Br_xI_{1-x})_3$ will help to explain the origin of light-induced phase separation observed in very Br-rich mixed halide perovskites.

3.5 Acknowledgments, Permissions, and attributions

The research reported was funded by the Department of Energy Basic Energy Science Award No. DE-SC-0012541, and Award No.# DE-SC0019273. R.M.K. gratefully acknowledges the National Defense Science and Engineering Graduate fellowship for financial support. The work was performed using the shared facilities of the UCSB MRSEC (NSF DMR 1720256), a member of the Materials Research Facilities Network (www.mrfn.org), and of the NRI-MCDB Microscopy Facility (the Resonant Scanning Confocal supported by the NSF MRI grant DBI-1625770). Reprinted (adapted) in full with permission from (*ACS Appl. Mater. Interfaces* **2019**, *11*, 28, 25313–25321), including section 3.7. Copyright (2019) American Chemical Society. https://doi.org/10.1021/acsami.9b06069

3.6 References

(1) Yang, W. S.; Park, B.-W.; Jung, E. H.; Jeon, N. J. Iodide Management in Formamidinium-Lead-Halide - Based Perovskite Layers for Efficient Solar Cells. *Science (80).* **2017**, *356* (6345), 1376 - 1379.

(2) Blakers, A.; Zin, N.; McIntosh, K. R.; Fong, K. High Efficiency Silicon Solar Cells. *Energy Procedia* **2013**, *33*, 1 - 10.

(3) Kojima, A.; Teshima, K.; Shirai, Y.; Miyasaka, T. Organometal Halide Perovskites as Visible - Light Sensitizers for Photovoltaic Cells. *J Am Chem Soc* **2009**, *131* (October), 6050 - 6051.

(4) Stoumpos, C. C.; Malliakas, C. D.; Kanatzidis, M. G. Semiconducting Tin and Lead Iodide Perovskites with Organic Cations: Phase Transitions, High Mobilities, and near-Infrared Photoluminescent Properties. *Inorg. Chem.* **2013**, *52* (15), 9019 - 9038.

(5) Lee, M. M.; Teuscher, J.; Miyasaka, T.; Murakami, T. N.; Snaith, H. J. Efficient Hybrid Solar Cells Based on Meso-Superstructured Organometal Halide Perovskites. *Science (80).* **2012**, *338* (November), 1209 - 1214.

(6) Berry, J.; Buonassisi, T.; Egger, D. A.; Hodes, G.; Kronik, L.; Loo, Y. L.; Lubomirsky, I.; Marder, S. R.; Mastai, Y.; Miller, J. S.; Mitzi, D. B.; Paz, Y.; Rappe, A. M.; Riess, I.; Rybtchinski, B.; Stafsudd, O.; Stevanovic, V.; Toney, M. F.; Zitoun, D.; Kahn, A.; Ginley, D.; Cahen, D.Hybrid Organic-Inorganic Perovskites (HOIPs): Opportunities and Challenges. *Adv. Mater.* **2015**, *27* (35), 5102 - 5112.

(7) Zhao, D.; Wang, C.; Song, Z.; Yu, Y.; Chen, C.; Zhao, X.; Zhu, K.; Yan, Y. Four-Terminal All-Perovskite Tandem Solar Cells Achieving Power Conversion Efficiencies Exceeding 23%. *ACS Energy Lett.* **2018**, *3* (2), 305 - 306.

(8) Saliba, M.; Matsui, T.; Seo, J. Y.; Domanski, K.; Correa-Baena, J. P.; Nazeeruddin, M. K.; Zakeeruddin, S. M.; Tress, W.; Abate, A.; Hagfeldt, A.; Grätzel, M. Cesium-Containing Triple Cation Perovskite Solar Cells: Improved Stability, Reproducibility and High Efficiency. *Energy Environ. Sci.* **2016**, *9* (6), 1989 - 1997.

(9) Yi, C.; Luo, J.; Meloni, S.; Boziki, A.; Ashari-Astani, N.; Grätzel, C.; Zakeeruddin, S. M.; Röthlisberger, U.; Grätzel, M. Entropic Stabilization of Mixed A-Cation ABX_3 Metal Halide Perovskites for High Performance Perovskite Solar Cells. *Energy Environ. Sci.* **2016**, *9* (2), 656 - 662.

(10) McMeekin, D. P.; Sadoughi, G.; Rehman, W.; Eperon, G. E.; Saliba, M.; Horantner, M. T.; Haghighirad, A.; Sakai, N.; Korte, L.; Rech, B.; Johnston, M. B.; Herz, L. M.; Snaith, H. J. A Mixed-Cation Lead Mixed-Halide Perovskite Absorber for Tandem Solar Cells. *Science (80).* **2016**, *351* (6269), 151 - 155.

(11) Jeon, N. J.; Noh, J. H.; Yang, W. S.; Kim, Y. C.; Ryu, S.; Seo, J.; Seok, S. Il. Compositional Engineering of Perovskite Materials for High-Performance Solar Cells. *Nature* **2015**, *517* (7535), 476 - 480.

(12) Ono, L. K.; Juarez-Perez, E. J.; Qi, Y. Progress on perovskite materials and solar cells with mixed cations and halide anions. *ACS Appl. Mater. Interfaces* **2017**, *9* (36), 30197-30246.

(13) Zhang, Y.; Grancini, G.; Feng, Y.; Asiri, A. M.; Nazeeruddin, M. K. Optimization of Stable Quasi-Cubic $FA_xMA_{1-x}PbI_3$ Perovskite Structure for Solar Cells with

Efficiency beyond 20%. *ACS Energy Lett.*, **2017**, *2*(4), 802-806.

(14) Dai, J.;, Fu, Y.; Manger, L. H.; Rea, M. T.; Hwang, L.; Goldsmith, R. H.; Jin, S. Carrier Decay Properties of Mixed Cation Formamidinium–Methylammonium Lead Iodide Perovskite $[HC(NH_2)_2]_{1-x}[CH_3NH_3]_xPbI_3$ Nanorods. *J. Phys. Chem. Lett.*, **2016**, *7* (24), 5036-5043.

(15) Protesescu, L.; Yakunin, S.; Bodnarchuk, M. I.; Krieg, F.; Caputo, R.; Hendon, C. H.; Yang, R. X.; Walsh, A.; Kovalenko, M. V. Nanocrystals of Cesium Lead Halide Perovskites ($CsPbX_3$, X = Cl, Br, and I): Novel Optoelectronic Materials Showing Bright Emission with Wide Color Gamut. *Nano Lett.* **2015**, *15* (6), 3692–3696.

(16) Song, J.; Li, J.; Li, X.; Xu, L.; Dong, Y.; Zeng, H. Quantum Dot Light-Emitting Diodes Based on Inorganic Perovskite Cesium Lead Halides ($CsPbX_3$). *Adv. Mater.* **2015**, *27* (44), 7162 - 7167.

(17) Walsh, A.; Stranks, S. D. Taking control of ion transport in halide perovskite solar cells. *ACS Energy Lett.*, **2018**, *3* (8), 1983-1990.

(18) Azpiroz, J. M.; Mosconi, E.; Bisquert, J.; De Angelis, F. Defect Migration in Methylammonium Lead Iodide and Its Role in Perovskite Solar Cell Operation. *Energy Environ. Sci.* **2015**, *8* (7), 2118 - 2127.

(19) Snaith, H. J.; Abate, A.; Ball, J. M.; Eperon, G. E.; Leijtens, T.; Noel, N. K.; Stranks, S. D.; Wang, J. T. W.; Wojciechowski, K.; Zhang, W. Anomalous Hysteresis in Perovskite Solar Cells. *J. Phys. Chem. Lett.* **2014**, *5* (9), 1511 - 1515.

(20) Hoke, E. T.; Slotcavage, D. J.; Dohner, E. R.; Bowring, A. R.; Karunadasa, H. I.; Mcgehee, M. D. Reversible Photo-Induced Trap Formation in Mixed- Halide Hybrid Perovskites for Photovoltaics. *Chem. Sci.* **2015**, *6*, 613-317.

21) Draguta, S.; Sharia, O.; Yoon, S. J.; Brennan, M. C.; Morozov, Y. V.; Manser, J. M.; Kamat, P. V.; Schneider, W. F.; Kuno, M. Rationalizing the Light-Induced Phase Separation of Mixed Halide Organic-Inorganic Perovskites. *Nat. Commun.* **2017**, *8* (1).

(22) Barker, A. J.; Sadhanala, A.; Deschler, F.; Gandini, M.; Senanayak, S. P.; Pearce, P. M.; Mosconi, E.; Pearson, A. J.; Wu, Y.; Ram Srimath Kandada, A.; Leijtens, T; De Angelis, F.; Dutton, S. E.; Petrozza, A.; Friend, R. H. Defect-Assisted Photoinduced Halide Segregation in Mixed-Halide Perovskite Thin Films. *ACS Energy Lett.* **2017**, *2*, 1416–1424.

(23) Bischak, C. G.; Hetherington, C. L.; Wu, H.; Aloni, S.; Ogletree, D. F.; Limmer, D. T.; Ginsberg, N. S. Origin of Reversible Photo-Induced Phase Separation in Hybrid Perovskites. *Nano Lett.* **2017**, *17*, 1028 - 1033.

(24) Yoon, S. J.; Kuno, M.; Kamat, P. V. Shift Happens. How Halide Ion Defects Influence Photoinduced Segregation in Mixed Halide Perovskites. *ACS Energy Lett.* **2017**, *2*, 1507 - 1514.

(25) Wang, Y.; Chen, Z.; Deschler, F.; Sun, X.; Lu, T. M.; Wertz, E. A.; Hu, J. M.; Shi, J. Epitaxial Halide Perovskite Lateral Double Heterostructure. *ACS Nano* **2017**, *11* (3), 3355 - 3364.

(26) Jaffe, A.; Lin, Y.; Beavers, C. M.; Voss, J.; Mao, W. L.; Karunadasa, H. I. High-Pressure Single-Crystal Structures of 3D Lead-Halide Hybrid Perovskites and Pressure Effects on Their Electronic and Optical Properties. *ACS Cent. Sci.* **2016**, *2*, 201 - 209.

(27) Marongiu, D.; Chang, X.; Sarritzu, V.; Sestu, N.; Pau, R.; Geddo Lehmann, A.; Mattoni, A.; Quochi, F.; Saba, M.; Mura, A.; Bongiovanni, G. Self-Assembled Lead Halide

Perovskite Nanocrystals in a Perovskite Matrix. *ACS Energy Lett.* **2017**, *2* (4), 769 - 775.

(28) Yang, X.; Yan, X.; Wang, W.; Zhu, X.; Li, H.; Ma, W.; Sheng, C. X. Light Induced Metastable Modification of Optical Properties in $CH_3NH_3PbI_{3-x}Br_x$ Perovskite Films: Two-Step Mechanism. *Org. Electron. physics, Mater. Appl.* **2016**, *34*, 79 - 83.

(29) Xing, J.; Wang, Q.; Dong, Q.; Yuan, Y.; Fang, Y.; Huang, J. Ultrafast Ion Migration in Hybrid Perovskite Polycrystalline Thin Films under Light and Suppression in Single Crystals. *Phys. Chem. Chem. Phys.* **2016**, *18* (44), 30484 - 30490.

(30) Yoon, S. J.; Draguta, S.; Manser, J. S.; Sharia, O.; Schneider, W. F.; Kuno, M.; Kamat, P. V. Tracking Iodide and Bromide Ion Segregation in Mixed Halide Lead Perovskites during Photoirradiation. *ACS Energy Lett.* **2016**, *1* (1), 290 - 296.

(31) Slotcavage, D. J.; Karunadasa, H. I.; McGehee, M. D. Light-Induced Phase Segregation in Halide-Perovskite Absorbers. *ACS Energy Lett.* **2016**, *1* (6), 1199 - 1205.

(32) Samu, G. F.; Janáky, C.; Kamat, P. V. A Victim of Halide Ion Segregation. How Light Soaking Affects Solar Cell Performance of Mixed Halide Lead Perovskites. *ACS Energy Lett.* **2017**, *2* (8), 1860 - 1861.

(33) Noh, J. H.; Im, S. H.; Heo, J. H.; Mandal, T. N.; Seok, S. Il. Chemical Management for Colorful, Efficient, and Stable Inorganic - Organic Hybrid Nanostructured Solar Cells. *Nano Lett.* **2013**, *13*, 1764 - 1769.

(34) Suarez, B.; Gonzalez-Pedro, V.; Ripolles, T. S.; Sanchez, R. S.; Otero, L.; Mora-Sero, I. Recombination Study of Combined Halides (Cl, Br, I) Perovskite Solar Cells. *J. Phys. Chem. Lett.* **2014**, *5* (10), 1628 - 1635.

(35) Kulkarni, S. A.; Baikie, T.; Boix, P. P.; Yantara, N.; Mathews, N.; Mhaisalkar, S. Band-Gap Tuning of Lead Halide Perovskites Using a Sequential Deposition Process. *J. Mater. Chem. A* **2014**, *2* (24), 9221 - 9225.

(36) Eperon, G. E.; Stranks, S. D.; Menelaou, C.; Johnston, M. B.; Herz, L. M.; Snaith, H. J. Formamidinium Lead Trihalide: A Broadly Tunable Perovskite for Efficient Planar Heterojunction Solar Cells. *Energy Environ. Sci.* **2014**, *7* (3), 982 - 988.

(37) Balakrishna, R. G.; Kobosko, S. M.; Kamat, P. V. Mixed Halide Perovskite Solar Cells. Consequence of Iodide Treatment on Phase Segregation Recovery. *ACS Energy Lett.* **2018**, (3), 2267 - 2272.

(38) Meloni, S.; Moehl, T.; Tress, W.; Franckevičius, M.; Saliba, M.; Lee, Y. H.; Gao, P.; Nazeeruddin, M. K.; Zakeeruddin, S. M.; Rothlisberger, U.; Graetzel, M. Ionic Polarization-Induced Current - Voltage Hysteresis in $CH_3NH_3PbX_3$ Perovskite Solar Cells. *Nat. Commun.* **2016**, *7* (May 2015), 10334.

(39) Zhang, T.; Chen, H.; Bai, Y.; Xiao, S.; Zhu, L.; Hu, C.; Xue, Q.; Yang, S. Understanding the Relationship between Ion Migration and the Anomalous Hysteresis in High-Efficiency Perovskite Solar Cells: A Fresh Perspective from Halide Substitution. *Nano Energy* **2016**, *26*, 620 - 630.

(40) Eames, C.; Frost, J. M.; Barnes, P. R. F.; O'Regan, B. C.; Walsh, A.; Islam, M. S. Ionic Transport in Hybrid Lead Iodide Perovskite Solar Cells. *Nat. Commun.* **2015**, *6* (May), 7497.

(41) Hoque, M. N. F.; Islam, N.; Zhu, K.; Fan, Z. Hybrid Perovskite Phase Transition and Its Ionic, Electrical and Optical Properties. *MRS Adv.* **2017**, *2* (53), 3077-3082.

(42) Haruyama, J.; Sodeyama, K.; Han, L.; Tateyama, Y. First-Principles Study of Ion Diffusion in Perovskite Solar Cell Sensitizers. *J. Am. Chem. Soc.* **2015**, *137* (32),

10048 - 10051.

(43) Li, D.; Wu, H.; Cheng, H. C.; Wang, G.; Huang, Y.; Duan, X. Electronic and Ionic Transport Dynamics in Organolead Halide Perovskites. *ACS Nano* **2016**, *10* (7), 6933 - 6941.

(44) Ming, W.; Chen, S.; Du, M. H. Chemical Instability Leads to Unusual Chemical-Potential-Independent Defect Formation and Diffusion in Perovskite Solar Cell Material $CH_3NH_3PbI_3$. *J. Mater. Chem. A* **2016**, *4* (43), 16975 - 16981.

(45) Zhao, Y.-C.; Zhou, W.-K.; Zhou, X.; Liu, K.-H.; Yu, D.-P.; Zhao, Q. Quantification of Light-Enhanced Ionic Transport in Lead Iodide Perovskite Thin Films and Its Solar Cell Applications. *Light Sci. Appl.* **2016**, *6* (5), 16243.

(46) Głowienka, D.; Miruszewski, T.; Szmytkowski, J. The Domination of Ionic Conductivity in Tetragonal Phase of the Organometal Halide Perovskite $CH_3NH_3PbI_{3-x}Cl_x$. *Solid State Sci.* **2018**, *82* (May), 19 - 23.

(47) Game, O. S.; Buchsbaum, G. J.; Zhou, Y.; Padture, N. P.; Kingon, A. I. Ions Matter: Description of the Anomalous Electronic Behavior in Methylammonium Lead Halide Perovskite Devices. *Adv. Funct. Mater.* **2017**, *27* (16), 1606584.

(48) Delugas, P.; Caddeo, C.; Filippetti, A.; Mattoni, A. Thermally Activated Point Defect Diffusion in Methylammonium Lead Trihalide: Anisotropic and Ultrahigh Mobility of Iodine. *J. Phys. Chem. Lett.* **2016**, *7* (13), 2356 - 2361.

(49) Pan, D.; Fu, Y.; Chen, J.; Czech, K. J.; Wright, J. C.; Jin, S. Visualization and Studies of Ion-Diffusion Kinetics in Cesium Lead Bromide Perovskite Nanowires. *Nano Lett.* **2018**, *18* (3), 1807 - 1813.

(50) Lai, M.; Obliger, A.; Lu, D.; Kley, C. S.; Bischak, C. G.; Kong, Q.; Lei, T. Intrinsic Anion Diffusivity in Lead Halide Perovskites Is Facilitated by a Soft Lattice. **2018**, *115* (47), 2 - 7.

(51) Brivio, F.; Caetano, C.; Walsh, A. Thermodynamic Origin of Photoinstability in the $CH_3NH_3Pb(I_{1-x}Br_x)_3$ Hybrid Halide Perovskite Alloy. *J. Phys. Chem. Lett.* **2016**, *7*, 1083 - 1087.

(52) Bechtel, J. S.; Van Der Ven, A. First-Principles Thermodynamics Study of Phase Stability in Inorganic Halide Perovskite Solid Solutions. *Phys. Rev. Mater. 2* **2018**, *045401*, 1 - 7.

(53) Solis-Ibarra, D.; Smith, I. C.; Karunadasa, H. I. Post-Synthetic Halide Conversion and Selective Halogen Capture in Hybrid Perovskites. *Chem. Sci.* **2015**, *6* (7), 4054 - 4059.

(54) Shewmon, N. T.; Yu, H.; Constantinou, I.; Klump, E.; So, F. Formation of Perovskite Heterostructures by Ion Exchange. *ACS Appl. Mater. Interfaces* **2016**, *8* (48), 33273 - 33279.

(55) Dou, L.; Lai, M.; Kley, C. S.; Yang, Y.; Bischak, C. G.; Zhang, D.; Eaton, S. W.; Ginsberg, N. S.; Yang, P. Spatially Resolved Multicolor $CsPbX_3$ Nanowire Heterojunctions via Anion Exchange. *Proc. Natl. Acad. Sci.* **2017**, 201703860.

(56) Tian, W.; Leng, J.; Zhao, C.; Jin, S. Long-Distance Charge Carrier Funneling in Perovskite Nanowires Enabled by Built-in Halide Gradient. *J. Am. Chem. Soc.* **2017**, *139* (2), 579 - 582.

(57) Rothmann, M. U.; Li, W.; Zhu, Y.; Liu, A.; Ku, Z.; Bach, U.; Etheridge, J.; Cheng, Y. Structural and Chemical Changes to $CH_3NH_3PbI_3$ Induced by Electron and Gallium Ion Beams. *Adv. Mater.* **2018**, *30* (25), 1800629.

(58) Yamada, Y.; Yamada, T.; Phuong, L. Q.; Maruyama, N.; Nishimura, H.; Wakamiya, A.; Murata, Y.; Kanemitsu, Y. Dynamic Optical Properties of $CH_3NH_3PbI_3$ Single Crystals As Revealed by One - and Two - Photon Excited Photoluminescence Measurements. *J. Am. Chem. Soc.* **2015**, *137* (33), 10456 - 10459.
(59) Khanna, S.; Sundaram, S.; Reddy, K. S.; Mallick, T. K. Performance Analysis of Perovskite and Dye-Sensitized Solar Cells under Varying Operating Conditions and Comparison with Monocrystalline Silicon Cell. *Appl. Therm. Eng.* **2017**, *127*, 559 - 565.
(60) Xue, H.; Ruan, W.; Zhang, M.; Rong, M. Fast Curing Ethylene Vinyl Acetate Films with Dual Curing Agent towards Application as Encapsulation Materials for Photovoltaic Modules. **2014**, *8* (2), 116 - 122.
(61) Drabczyk, K.; Panek, P. A Comparative Study of EVA with and without Thermal History for Different Lamination Process Parameters. *Mater. Sci. Eng. B* **2012**, *177* (15), 1378 - 1383.
(62) Baranwal, A. K.; Kanaya, S.; Peiris, T. A. N.; Mizuta, G.; Nishina, T.; Kanda, H.; Miyasaka, T.; Segawa, H.; Ito, S. 100°C Thermal Stability of Printable Perovskite Solar Cells Using Porous Carbon Counter Electrodes. *ChemSusChem* **2016**, *9* (18), 2604 - 2608.
(63) Shewmon, P. G. *Diffusion in Solids.*; Springer, 2016; Vol. 36.
(64) Balluffi, R. W.; Allen, S. J.; Carter, C. W. *Kinetics of Materials*; John Wiley & Sons: Hoboken, NJ, 2005.
(65) Nandi, P.; Giri, C.; Swain, D.; Manju, U.; Mahanti, S. D. B.; Topwal, D. Temperature Dependent Photo-Induced Reversible Phase Separation in Mixed Halide Perovskite. *ACS Appl. Energy Mater.* **2018**, *1*, 3807 - 3814.
(66) Onada-Yamamur, N.; Matsuo, T.; Suga, H. Calorimetric and IR Spectroscopic Studies of Phase Transitions in Methylammonium Trihalogenoplumbates (II). *J. Phys. Chem. Solids* **1990**, *51* (12), 1383 - 1395.

3.7 Appendix to Chapter 3

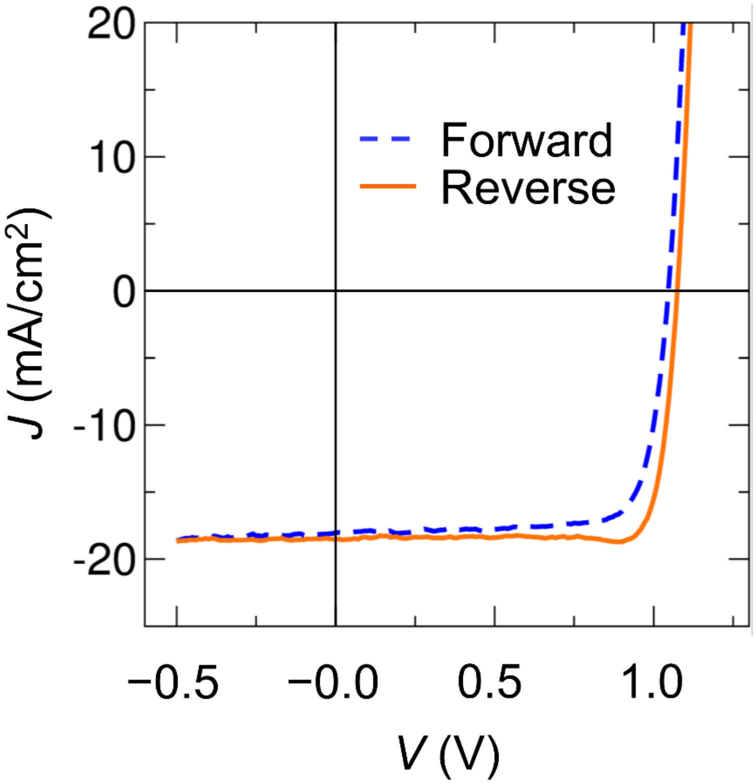

Figure 3.S1. Current-Voltage (*J*-*V*) curve for a solar cell made from $MAPbI_3$ with an ITO/PTAA/MAPbI3/PEIE/Ag device structure with V_{oc}=1.07 V, J_{sc} = 18.5 mA/cm^2, FF=0.86 and power conversion efficiency of 17.6% under 1 Sun simulated solar illumination, in forward and reverse bias.

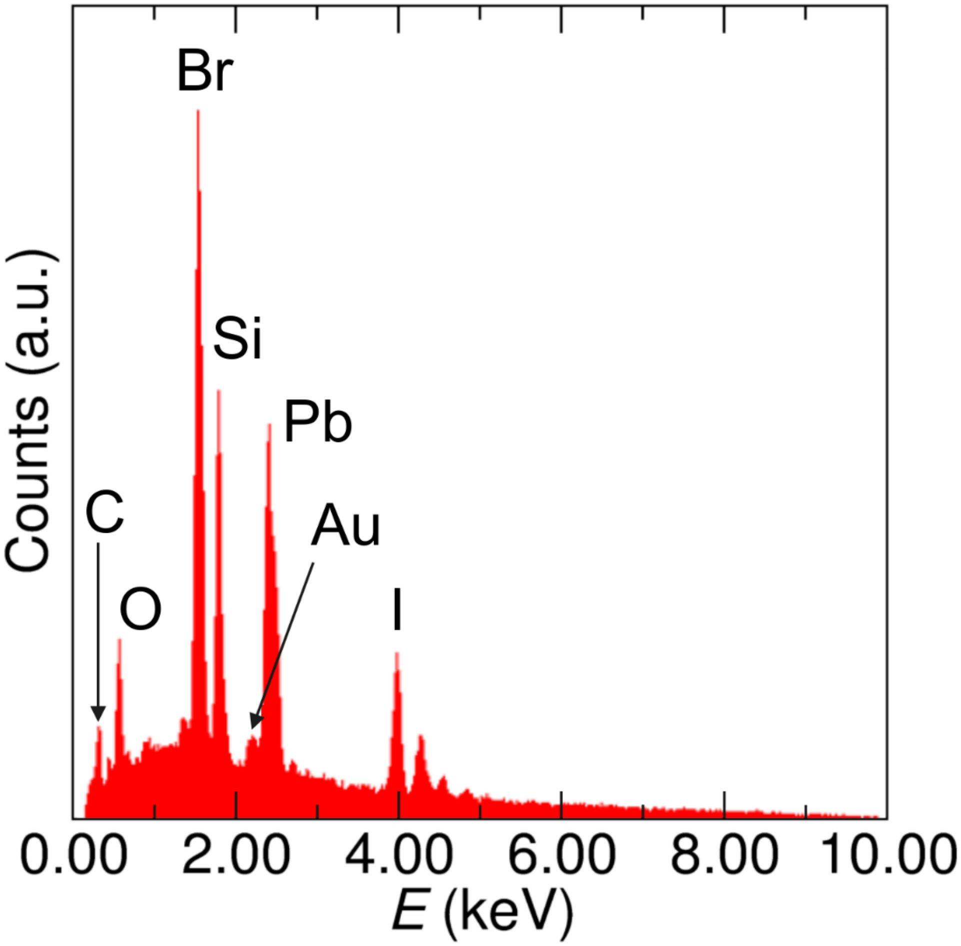

Figure 3.S2. EDX spectrum of the gold-coated x_{Br} =0|1 heterostructure in **Figure 3.3a** (fabricated on a quartz substrate).

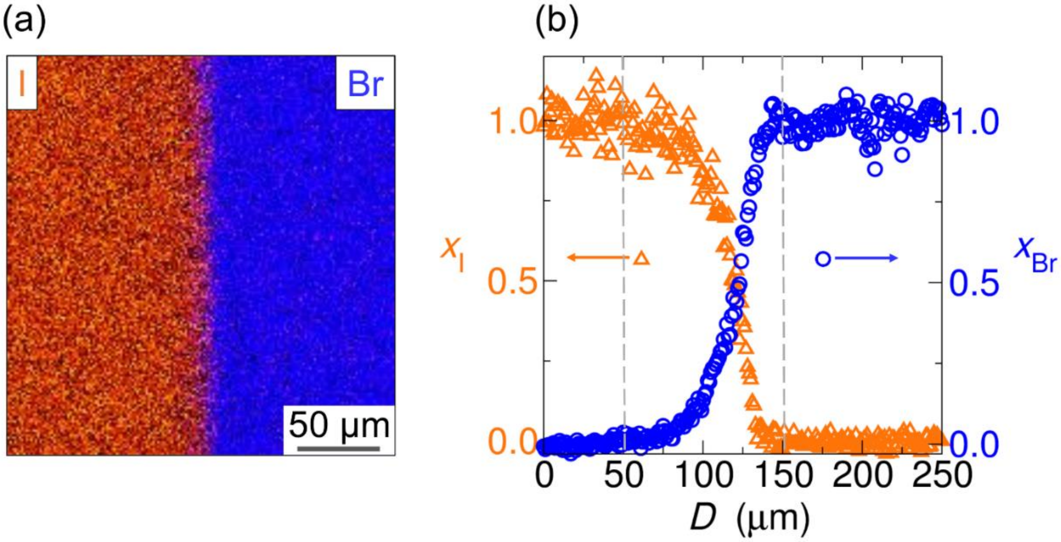

Figure 3.S3. Overlayed EDX iodine and bromine maps (a) and integrated EDX interface profiles (b) of the x_{Br} =0|1 heterostructure shown in **Figure 3.3a** where x_{Br} and x_I represent the halide fractions of Br and I respectively.

The x_{Br} = 0, x_{Br}=1, x_I = 0, and x_I = 1 compositions far from the interface were assigned by taking EDX baseline compositions were obtained far from the interface (data not shown) to confirm lack of iodine in $MAPbBr_3$ regions and lack of bromine in $MAPbI_3$ regions. Compositions far from the interface were separately confirmed via XRD and UV-Vis (**Figures 3.2** and **3.S6**). The halide interface profiles of **Figure 3.S3** are thus compositionally representative.

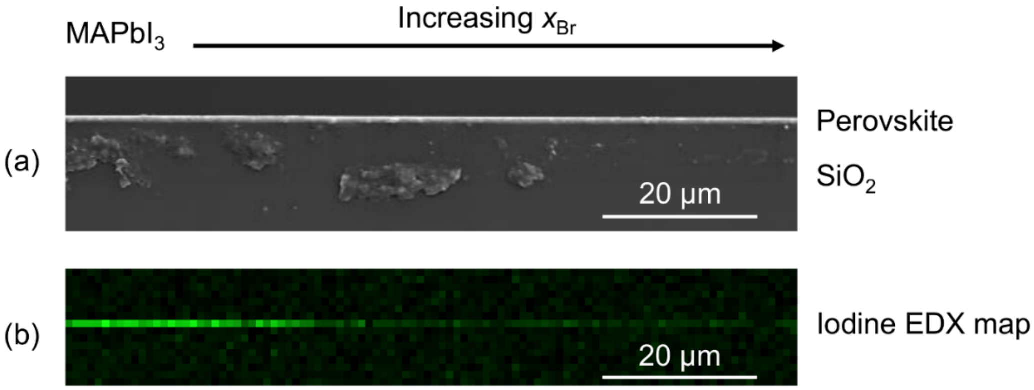

Figure 3.S4. (a) Cross-sectional SEM and (b) corresponding iodine EDX map of a $MAPbI_3$-$MAPbBr_3$ heterostructure before heating.

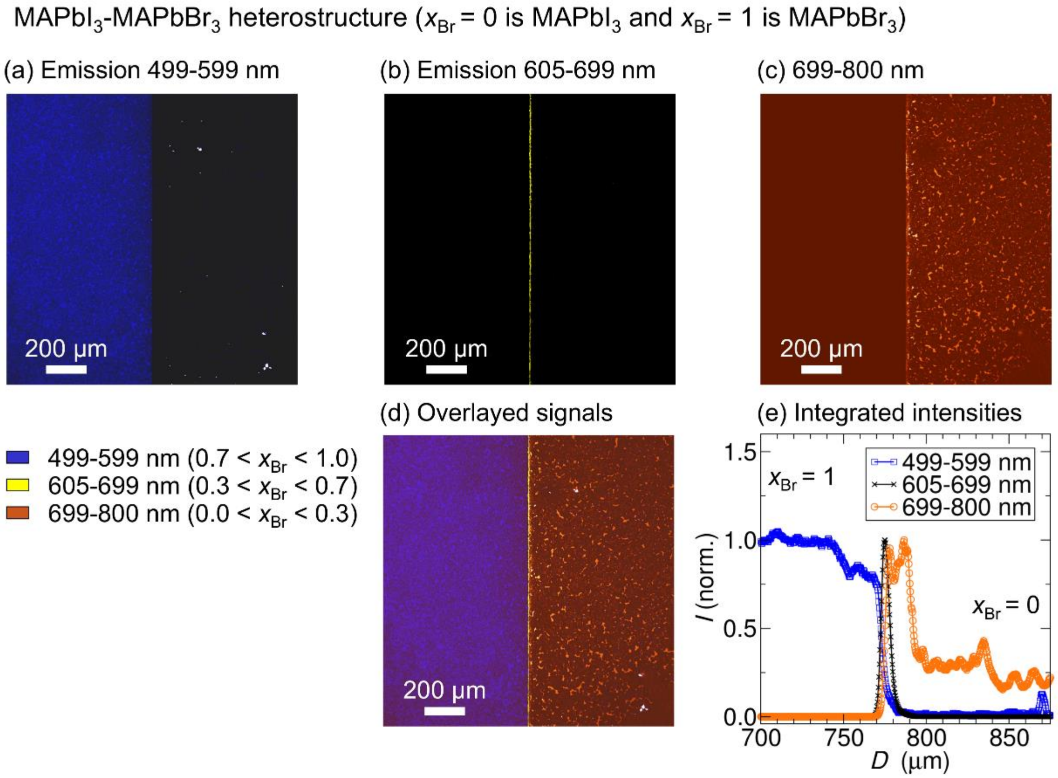

Figure 3.S5. Confocal microscopy image of an $x_{\mathrm{Br}} = 0|1$ heterostructure, for an excitation wavelength of 458 nm. Images (a)-(d) represent emission between (a) 499-599 nm, (b) 605-699 nm, (c) 699-800 nm and (d) is an overlay of these emission signals. x_{Br} composition assignments were made using reference [2]. (e) Represents the integrated intensities of each emission (normalized).

Emission between 499 nm and 599 nm includes emission from $x_{\mathrm{Br}} = 1$ (at ~540 nm) as well as from some Br-rich phases ($0.7 < x_{\mathrm{Br}} < 1.0$), based on previously-published work.[2] The 699-800 nm emission channel covers $x_{\mathrm{Br}} = 0$ (at ~780 nm) as well as some I-rich phases ($0.0 < x_{\mathrm{Br}} < 0.3$). Correspondingly, the 605-699 nm emission channel covers intermediate mixed-halide phases not included in the other two emission channels ($0.3 < x_{\mathrm{Br}} < 0.7$). Observation of 605-699 nm emission indicates emission from mixed-halide compositions ($0.3 < x_{\mathrm{Br}} < 0.7$) under light exposure at 458 nm, which is expected given the short exposure times in scanning confocal microscopy (~ microsecond). This approximate composition assignment is in agreement with composition assignment from optical microscopy and EDX (**Figures 3.4e** and **3.6**), as emission from the 605-699 nm channel spans a width of ≈ 10 μm, corresponding to the interface width for $0.3 < x_{\mathrm{Br}} < 0.7$. Given the large width of emission peaks from $\mathrm{MAPb(Br}_x\mathrm{I}_{1-x})_3$, [2,3] the observed overlap between channels is not surprising. We therefore relied on EDX for exact composition determination (**Figures 3.4** and **3.S3**). The decrease in intensity near 800 μm in the 699-800 nm emission channel ($0.0 < x_{\mathrm{Br}} < 0.3$) likely stems from emission being cut off at 800 nm in this channel, which cuts off some of the MAPbI_3 emission (emission center wavelength 775 nm)[2] and other low x_{Br} emission.

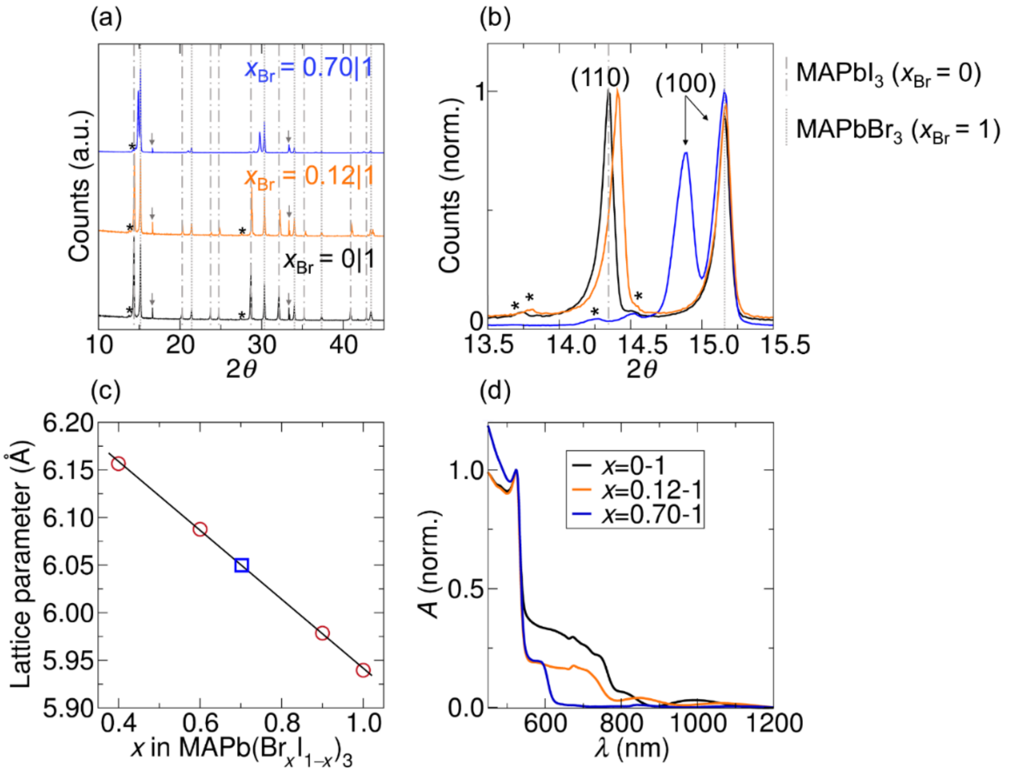

Figure 3.S6. (a, b) XRD patterns of x_{Br} = 0.7|1 and x_{Br} = 0.12|1 heterostructures after 260 min of heating, with for comparison x_{Br} = 0|1 before heating. The gray lines are a guide to the eye, with large dashes indicating MAPbI$_3$ (x_{Br} = 0) peaks and the small dashes indicating MAPbBr$_3$ (x_{Br} = 1) peaks. The downwards gray arrows in (a) designate peaks from the quartz substrate and the * indicate extra (110) and (100) peaks arising from Tungsten (1.4764 Å) and CuKβ (1.3926 Å) radiation contamination in the X-ray source. (c) Calibration curve made from the (100) XRD peaks of spin-coated MAPb(Br$_x$I$_{1-x}$)$_3$ thin films to verify the XRD x_{Br} = 0.70 (blue box) and x_{Br} = 1 assignments. (d) UV-Vis spectra of x_{Br} = 0.70|1 and x_{Br} = 0.12|1 heterostructures after heating to 100°C for 260 min and of x_{Br} = 0|1 before heating.

For all XRD pattern analyses, a z-height correction was applied to match the x_{Br} = 1 lattice parameter with the known lattice parameter of MAPbBr$_3$ from the reported CIF file. [4] The calibration curve in (c) matches that of previous works to within the step size of our instrument (2θ = 0.01313°). [2,5] The band onsets for MAPbI$_3$ and MAPbBr$_3$ are visible at ~795 nm and ~540 nm respectively, as well as the onsets for x_{Br} = 0.12 at ~775 nm and for x_{Br} = 0.7 at ~625 nm. Interference fringes become apparent at longer wavelengths.

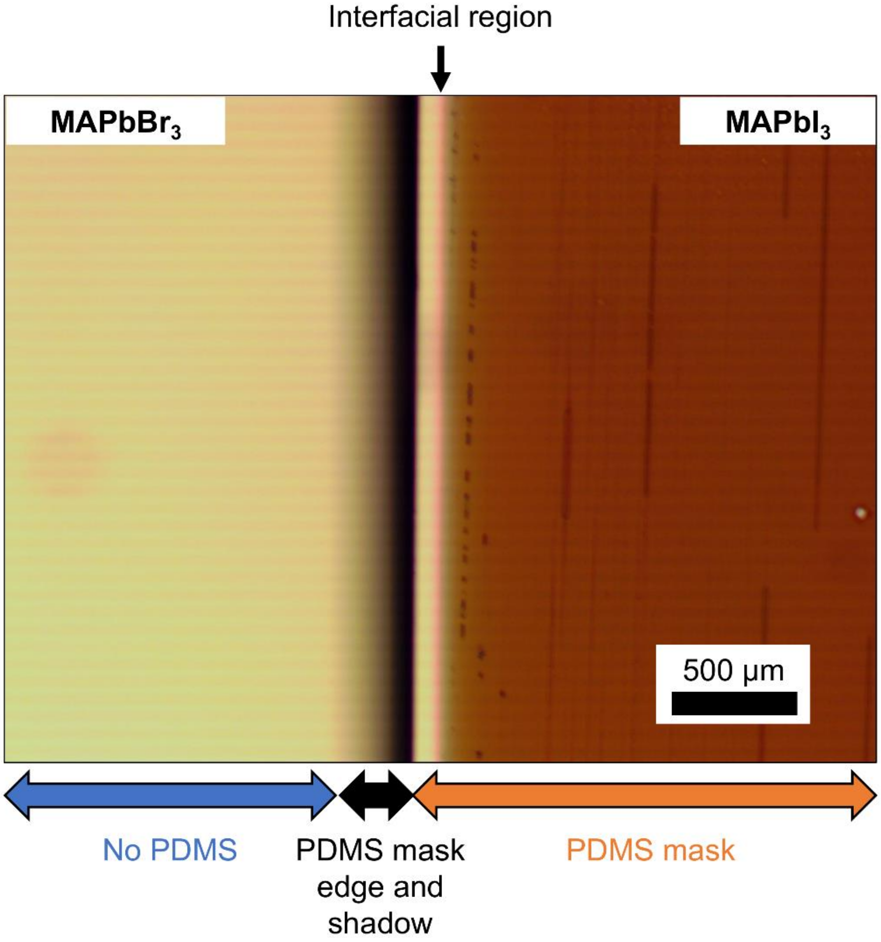

Figure 3.S7. Optical microscopy image of an MAPbBr$_3$-MAPbI$_3$ heterostructure with the PDMS mask still on the MAPbI$_3$ side.

Figure 3.S7 shows a MAPbBr$_3$-MAPbI$_3$ heterostructure, with the PDMS mask still on it. The thick black stripe indicates the location of the edge of the ≈ 450 μm mask, as well as the mask's shadow. The location of the PDMS mask to the left of the interfacial region indicates that Br$_2$ bled under the mask. The coincidence of the locations of the PDMS mask and of the optical artifact in **Figures 3.4/3.6** strongly suggests that the artifact arises due to residual PDMS on the film.

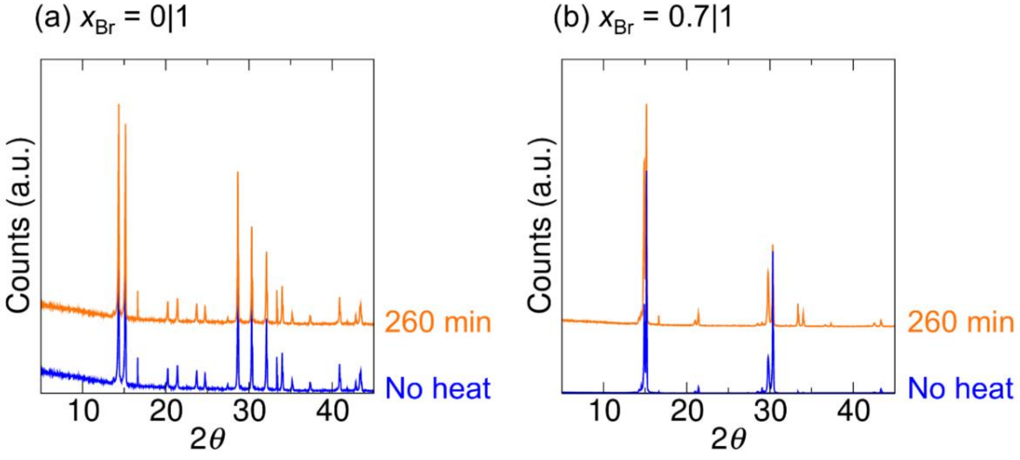

Figure 3.S8. XRD patterns of x_{Br} = 0|1 (a) and x_{Br} = 0.7|1 (b) before and after 260 min of heating, showing no change, and therefore little degradation. Notably, a PbI_2 peak at ≈ 12° does not appear after heating.

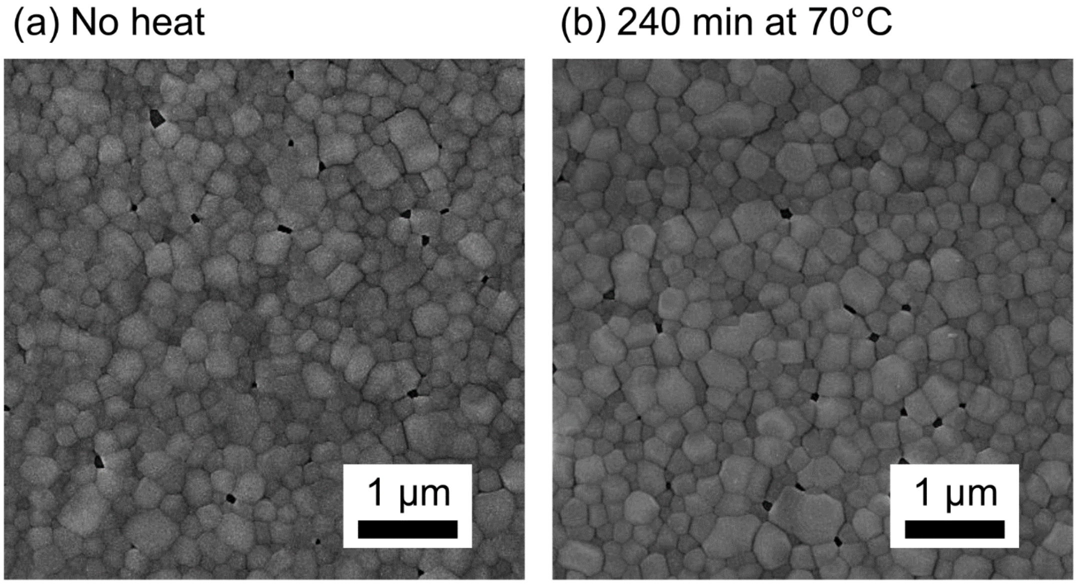

Figure 3.S9. Top-view SEM of two halves of the same fully-brominated film (a) without heating and (b) after heating at 70°C for 240 min.

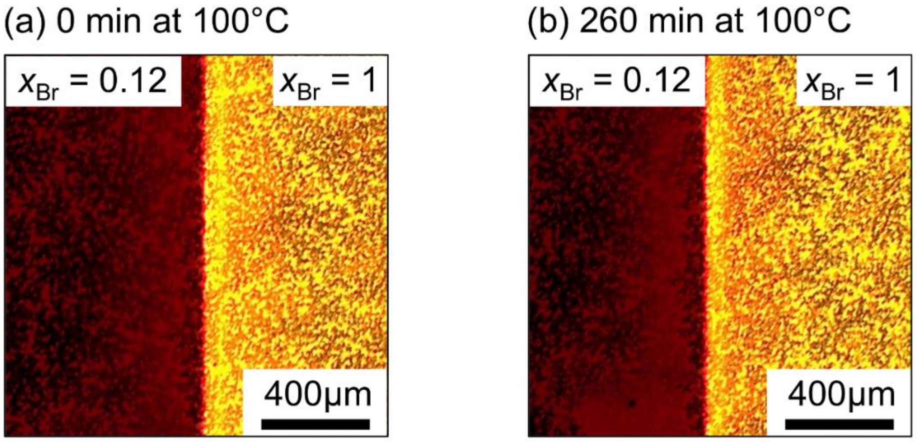
(a) 0 min at 100°C

(b) 260 min at 100°C

(c) Interface profiles

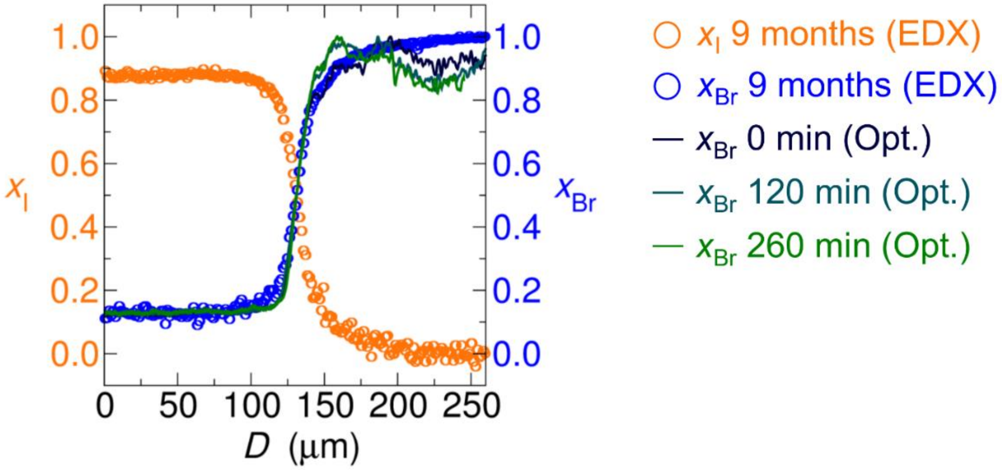

Figure 3.S10. Optical microscopy images of the same x_{Br}=0.12|1 heterostructure before (a) and after (b) heating at 100°C for 260 min, obtained via illumination with white light. (c) Interface profiles of the heterostructure after 0 min, 137 min and 260 min of heating at 100°C, and after storage at room temperature for 9 months. The deviations between optical microscopy and EDX at high x_{Br} are interpreted as noise.

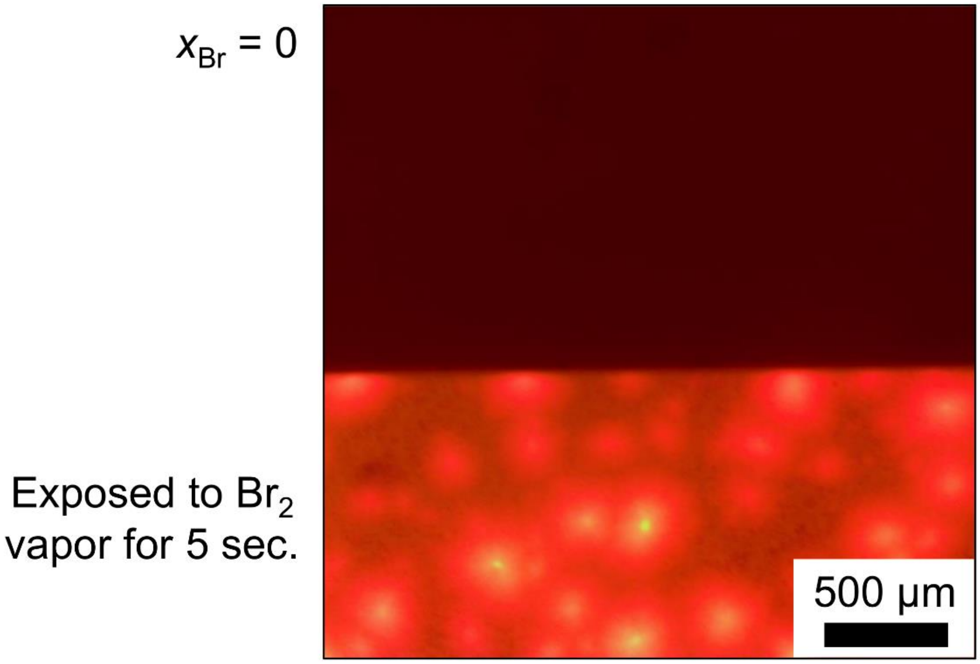

Figure 3.S11. Optical microscope image of a $MAPbI_3$ film ($x_{Br} = 0$) exposed on the bottom half to Br_2 vapor in an N_2 environment for 5 sec, demonstrating the unevenness of the bromination reaction.

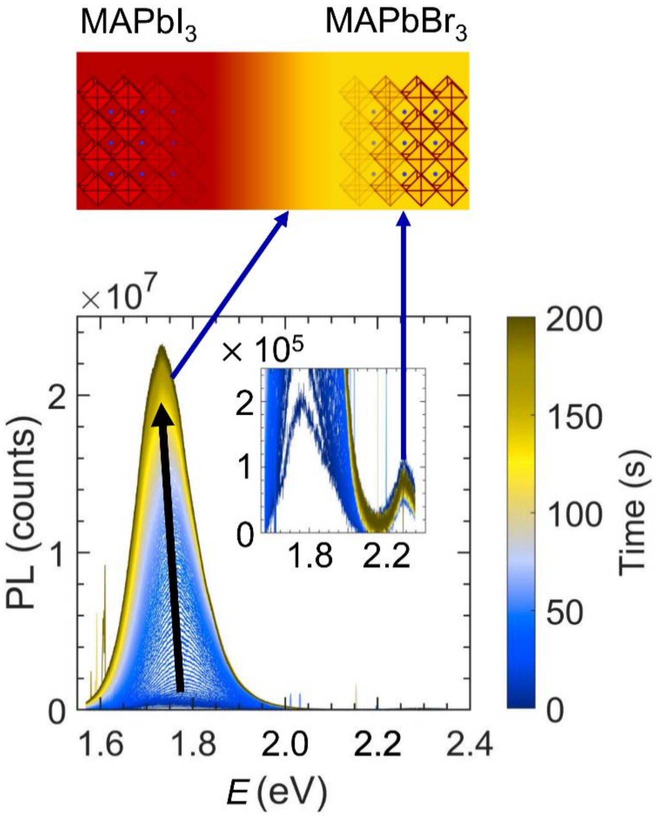

Figure 3.S12. Time-dependent photoluminescence spectra of localized regions (the interfacial and MAPbBr$_3$ regions) of an x_{Br} = 0|1 heterostructure under 405 nm excitation (continuous collections with 1 s integration times), with a power density ≈ 14 mW/cm^2 at the level of the sample.

The gradually increasing and red-shifting peak at ≈ 1.7 eV indicates light-induced phase separation in the mixed-halide interfacial region. [2] The gradual red-shift of the peak at ≈ 1.7 eV indicates formation of I-rich regions that increase in iodine content. The inset shows photoluminescence peaks at low intensity, with constant MAPbBr$_3$ emission visible at 2.3 eV.

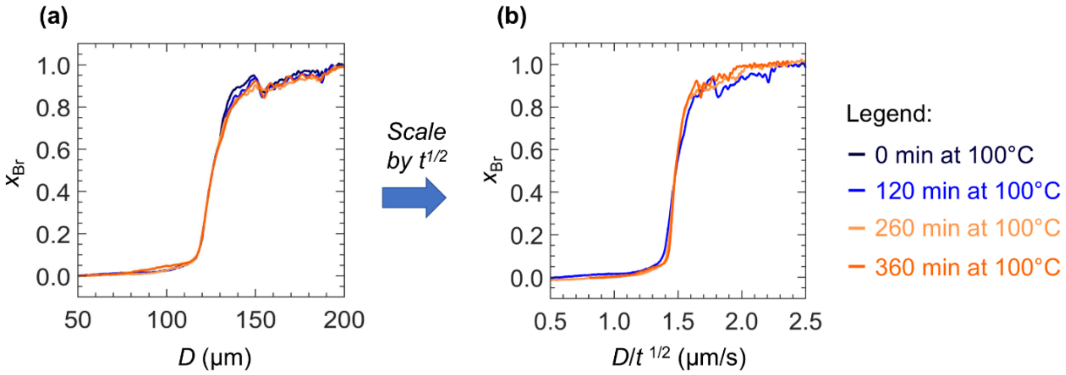

Figure 3.S13. Bromide fraction x_{Br} vs. distance (a), which was then normalized by the square root of time $t^{1/2}$ (i.e. the Boltzmann transformation) (b) for the optical microscopy-obtained traces of the x_{Br} = 0|1 heterostructure in **Figure 3.6.**

Dividing distance axis of the interface profiles by $t^{1/2}$, the square root of the time (120 min, 260 min, or 360 min at 100°C), resulted in lack of interface profile overlap. This confirmed that Fick's second law cannot be used to determine D_i, assuming a solid solution regime.

Section S9 – Simulations of Fick's Second Law

To approximate D_i, we used the error function solution for a diffusion couple (binary system) based on Fick's second law, for a solid solution regime: [6,7]

$$c(d,t) = \frac{c_R + c_L}{2} + \frac{c_R - c_L}{2}\, erf\left(\frac{d}{\sqrt{4D_i t}}\right) \qquad (1)$$

Where $c\ (d,\ t)$ is the concentration of a species having diffused a distance d after heating for a time t, c_R and c_L are the concentrations of that same species very far away from the interface (at infinity) on the right and left sides of the interface respectively, and D_i is the interdiffusion coefficient, which in this expression is constant with respect to composition.

Initial and boundary conditions

Equation (1) can be used as an approximation for concentration-dependent interdiffusion provided that the following boundary and initial conditions hold true: c_R and c_L are uniform compositions extending to quasi-infinity, and the initial shape of the diffusion couple is a step-wise function. [6-8] Because the as-fabricated heterostructures exhibited a wide interface rather than a step-wise shape, we made the following assumption. The initial (fictional) form of the interface profiles was a step function. After a time t_0, halides (fictionally) interdiffused, forming the wide interface that was initially observed upon fabrication (**Figures 3.4**, **3.6**, **3.7** and **3.S10**). For each D_i (10^{-10} - 10^{-13} cm^2/s), t_0 was adjusted, so that the simulated error function would overlap as best as possible with the interfacial profile of the $x_{\mathrm{Br}} = 0|1$ heterostructure upon fabrication (0 min of heating). Times heated (360 min) or stored at room temperature (8 months) were subsequently added to t_0 (i.e. $t + t_0$) to simulate the error function. For all $x_{Br} = 0|1$ simulations, $c_R = 1$ ($MAPbBr_3$) and $c_L = 0$ ($MAPbI_3$), and for all $x_{Br} = 0.70|1$ simulations, $c_R = 1$ ($MAPbBr_3$) and $c_L = 0.7$. Below is a summary of the simulation parameters used for equation (1).

Table 3.*S*1. Parameters for simulations of Fick's second law (equation 1)

Figure	**D_i (cm^2/s)**	**t_0 (s)**
4, S12 (100°C for 0 min and 260 / 360 min)	10^{-10}	4000
	10^{-11}	40000
	10^{-12}	400000
	10^{-13}	4000000
5 (Room temp. for 8 months)	10^{-10}	6500
	10^{-11}	65000
	10^{-12}	650000
	10^{-13}	6500000

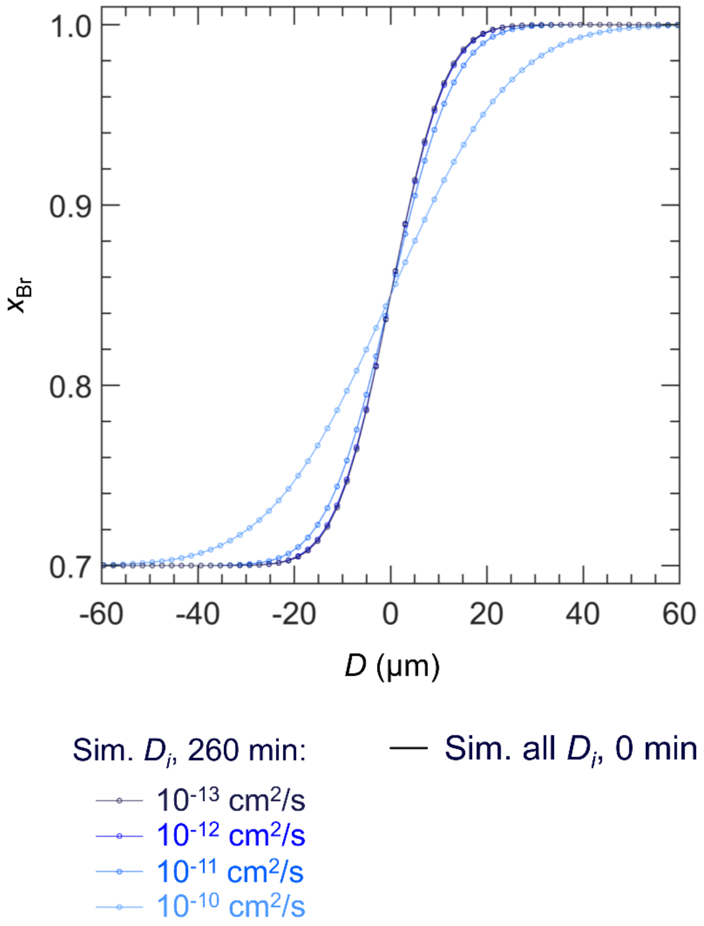

Figure 3.S14. Calculated interfacial profiles for x_{Br} =0.70|1, for 0 min and 260 min of heating, using the parameters of **Table 3.S1.**

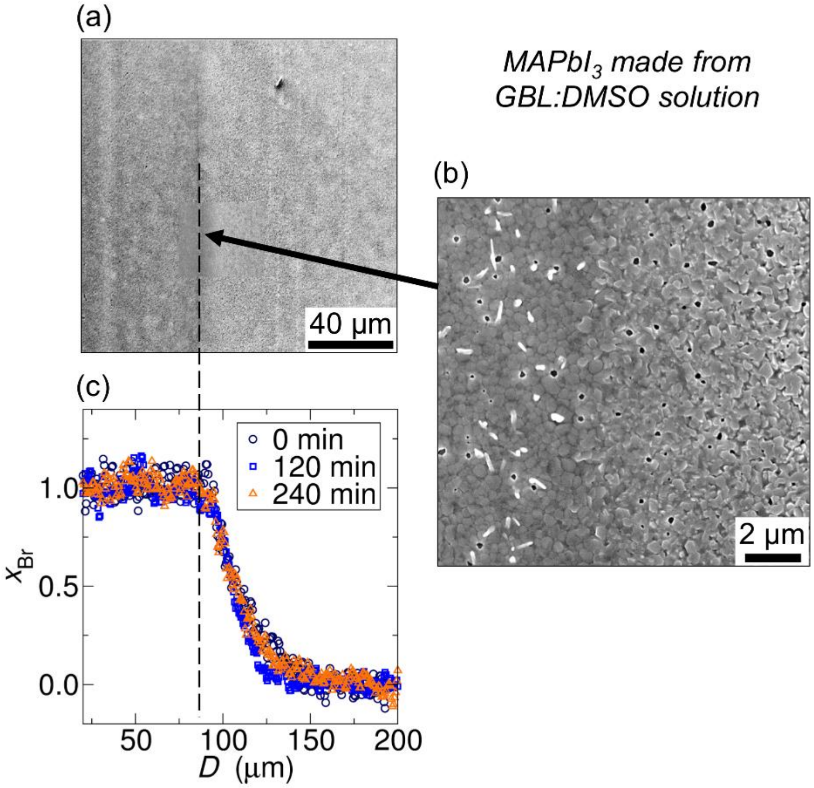

Figure 3.S15. SEM/EDX study of an x_{Br} = 0|1 heterostructure made from poorer-quality MAPbI$_3$ films. (a) Plan view SEM image of the x_{Br} = 0|1 heterostructure after heating at 70 °C for 120 min. (b) Higher-magnification image of the section of the interface indicated by the black arrow. (c) EDX-determined interface profiles of the heterostructure in (a) after heating at 70 °C for 0 min, 120 min, and 240 min, where the profiles were determined by fraction of halide x that is Br. The vertical dashed line indicates correspondence between the SEM image and the Br composition profile.

We examined whether changes in the interface profile were affected by the spin-coating process for MAPbI$_3$. The heterostructure in **Figure 3.S15** was fabricated as described above in all ways except the spin-casting of x_{Br} = 0 perovskite. Here, PbI$_2$ and CH$_3$NH$_3$I were dissolved in 300 µL DMSO and 700 µL γ-butyl lactone (GBL) to make a 1M solution, and the mixture was stirred for >1 h at 60°C in a nitrogen-filled glove box. The solution was then spin-cast onto quartz substrates using a two-step procedure: 1000 rpm for 10 s, with a 200 rpm/s acceleration then 5000 rpm for 20 s with a 1000 rpm/s acceleration. A few drops of chlorobenzene were dispensed onto the spinning substrate ~5 s prior to the end of the spin-coating procedure to aid crystallization. The thin films were then annealed on a hot plate with a heat diffuser at 34°C for 2 min, at 40°C for 2 min, at 50°C for 2 min, and at 70°C for 10 min (temperatures were verified with a thermocouple) again in a nitrogen-filled glove box. These films yielded 8% solar cell PCE (data not shown).

Consistent with our other heterostructure analyses, we observed little change in the interface profiles after heating (**Figure 3.S15a** and **Figure 3.S15c**). Here, the heterostructure was heated to 70°C rather than to 100°C. No interface profile flattening was observed via EDX after 240 min of heating. Because the linewidth of our EDX traces was ≈ 3 µm, we took this to be the maximum possible distance travelled by halides after 240 min. Using equation (1), we then obtained an interdiffusion coefficient $D_i \leq 10^{-13}$ cm^2/s at 70°C.

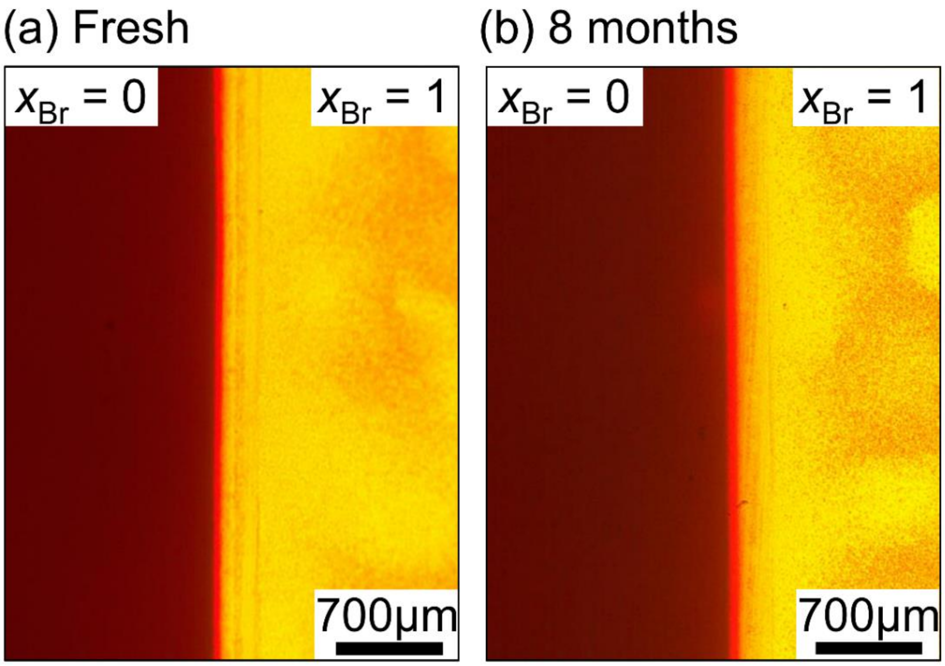

Figure 3.S16. Optical microscopy images of the $x_{Br} = 0|1$ heterostructure from **Figure 3.8**, before (a) and after (b) storage for 8 months. The strong retention of initial color indicates substantial retention of perovskite phases.

References

(1) Solis-Ibarra, D.; Smith, I. C.; Karunadasa, H. I. Post-Synthetic Halide Conversion and Selective Halogen Capture in Hybrid Perovskites. *Chem. Sci.* **2015**, *6* (7), 4054 - 4059.

(2) Hoke, E. T.; Slotcavage, D. J.; Dohner, E. R.; Bowring, A. R.; Karunadasa, H. I.; Mcgehee, M. D. Reversible Photo-Induced Trap Formation in Mixed- Halide Hybrid Perovskites for Photovoltaics. *Chem. Sci.* **2015**, *6* (613).

(3) Barker, A. J.; Sadhanala, A.; Deschler, F.; Gandini, M.; Senanayak, S. P.; Pearce, P. M.; Mosconi, E.; Pearson, A. J.; Wu, Y.; Ram Srimath Kandada, A.; Leijtens, T; De Angelis, F.; Dutton, S. E.; Petrozza, A.; Friend, R. H. Defect-Assisted Photoinduced Halide Segregation in Mixed-Halide Perovskite Thin Films. *ACS Energy Lett.* **2017**, *2*, 1416 - 1424.

(4) Jaffe, A.; Lin, Y.; Beavers, C. M.; Voss, J.; Mao, W. L.; Karunadasa, H. I. High-Pressure Single-Crystal Structures of 3D Lead-Halide Hybrid Perovskites and Pressure Effects on Their Electronic and Optical Properties. *ACS Cent. Sci.* **2016**, *2*, 201 - 209.

(5) Noh, J. H.; Im, S. H.; Heo, J. H.; Mandal, T. N.; Seok, S. Il. Chemical Management for Colorful, Efficient, and Stable Inorganic - Organic Hybrid Nanostructured Solar Cells. *Nano Lett.* **2013**, *13*, 1764 - 1769.

(6) Balluffi, R. W.; Allen, S. J.; Carter, C. W. *Kinetics of Materials*; John Wiley & Sons: Hoboken, NJ, 2005.

(7) Shewmon, P. G. *Diffusion in Solids.*; Springer, 2016; Vol. 36.

(8) Crank, J. *The Mathematics of Diffusion*, 2nd Ed.; Oxford University Press: Uxbridge, 1975.

Chapter 4:

Growth-Controlled Broad Emission in Phase-Pure Two-Dimensional Hybrid Perovskite Films

4.1 Introduction

Two-dimensional hybrid perovskites are attractive for optoelectronic applications such as solar cells and light-emitting devices because their optical emission can be changed by their structure. [1–5] Many 2D perovskites belong to the Ruddlesden-Popper (RP) family, which has a layered $(A')_2(A)_{n-1}B_nX_{3n+1}$ structure, where A' and A are cations, B is a divalent metal and X is a halide. [4–10] By changing the number n of B-X octahedral sheets that sit between large organic A' cations, the energies of the band gap and of the free exciton change, leading to tunable emission across the entire visible spectrum. Increasing distortions in B-X octahedral bond lengths and angles has been found to broaden the emission, with some compounds exhibiting white emission. [11–17] This broad emission has been proposed to originate from radiative recombination of self-trapped excitons (STEs). [11–15,17,18] The mechanisms of broad emission are under debate, however, and include different types of STEs, [17–19] coupling of STEs to specific point defects, [16] coupling of phonons to spacer cation stacking, [20] phonon replicas, [21] polaron self-localization, [22] extrinsic effects, [23,24] and shallow traps. [25]

Because perovskite optoelectronic devices typically comprise polycrystalline thin films, [3,26–31] much work has been devoted to understanding growth of RP phases in polycrystalline form. RP phases with narrow emission (i.e. free exciton emission) exhibit similar spectral features in single crystals and in phase-pure polycrystalline thin films. [9,32,33] Strain, which is typically present in films, [34–39] results in a small shift in the energy of the free exciton emission. [40] The growth conditions used to cast films of RP-phases can produce impurities, which are typically higher-*n* RP phases and 3D phases, that cause the emission to red-shift relative to that of the intended phase. [41–47] However, being able to tune the emission color RP-based LEDS or lasers requires the elimination of undesired higher-*n* RP phases and 3D phases. Recent work has identified routes to prevent impurity formation and grow 2D RPs with narrow emission, but there is less known about the growth of polycrystalline films of broad/white emitting perovskites. [4,32,33,42,45,48,49] In particular, the impacts of film fabrication characteristics, such as strain or casting kinetics, on the optical properties of broad-emitting 2D perovskites are not yet understood.

Here, we find that film growth can greatly affect the proportions of broad vs. narrow luminescence emitted by a solution-cast 2D phase. We found that using a single A/A'-site cation, ethylammonium, enables spin-casting of phase-pure films of lead bromide perovskites, and that the optimal size of this cation also prohibits off-target phase formation due to unfavorable tolerance factor and octahedral distortions. Strain that occurs in thin films favors high-energy, narrow emission, while slowing the growth kinetics and removing strains and enables recovery of broad, lower-energy emission. Lower-energy emission appears to be phonon-coupled, and can be attributed to self-trapped exciton emission or to phonon replicas.

4.2 Experimental Methods

Materials

Lead bromide ($PbBr_2$, 99.999 %), ethylammonium bromide (EABr, ≥ 98 %), lead oxide (PbO, ≥ 99.0 %), N-N-dimethylformamide (DMF, 99.8%, anhydrous), poly (methyl methacrylate) (PMMA, MW 350000), and hydrobromic acid (HBr, ACS reagent, 48%) were purchased from Sigma Aldrich and used as received. Polished z-cut quartz substrates (15 × 15 × 0.5 mm) were purchased from University Wafer.

Film casting

Quartz substrates were cleaned via ultrasonication in isopropyl alcohol for 10 min and exposed to oxygen plasma at ≈ 300 mTorr for 10 min. All subsequent solution preparation and film fabrications were performed in a nitrogen-filled glove box. Precursor solutions for $(EA)_2(EA)_2Pb_3Br_{10}$ were fabricated by dissolving 0.375 mmol (47 mg) EABr and 0.25 mmol (92 mg) $PbBr_2$ (molar ratio of EA/Pb = 1.5) in 0.5 mL DMF, to make an 0.5 mM solution (based on Pb). To make other compositions ($(EA)_2PbBr_4$ and mixed-phase films), the ratio of EABr/ $PbBr_2$ was adjusted following **Figure S9**. The solutions were left stirring overnight at 60°C to ensure good dissolution. Films were spin-cast at 4000 rpm for 60 seconds without antisolvent rinse, and promptly annealed at 100°C (verified by thermocouple) on a hot plate with a heat diffuser. After the films cooled, 60 µL of a PMMA solution (75 mg PMMA/3mL toluene) was spin-cast on top of the films at 2000 rpm for 30 seconds. The films were stored in a nitrogen glove box until characterization. For SEM, PDS, and certain stability experiments, the same spin-casting procedures were employed, but PMMA was not cast on the films. Films for PDS were cast on separate amorphous quartz substates.

Growth of $(EA)_4Pb_3Br_{10}$ bulk crystals

$(EA)_2(EA)_2Pb_3Br_{10}$ crystals were grown similarly to the previously-published procedure. [1] Briefly, PbO and EABr (in 3:4 molar ratio) were dissolved in HBr, and the solution was heated. Large crystals of $(EA)_2(EA)_2Pb_3Br_{10}$ were formed upon cooling.

GIWAXS characterization.

Grazing Incidence Wide-Angle X-Ray Scattering (GIWAXS) experiments were performed on beamline 11-3 (12.7 keV, wiggler side-station) at the Stanford Synchrotron Radiation Lightsource (SSRL). The source-to-detector (two-dimensional Rayonix MX225 CCD) distances were calibrated using lanthanum hexaboride (LaB6). All raw images were geometrically corrected using Nika. Au nanoparticles (100 nm) drop-cast on quartz substrates were used to verify chi-q alignment post-processing. Sections (cakeslices) of the 2D GIWAXS patterns at specific angles were selected and integrated to obtain 1D patterns. The two cakeslices used were near-out-of-plane ("nOP", 3°-21°) and near-in-plane ("nIP", 70°-88°), both with a chi-q angle width of 18°. An incidence angle of 0.5° was chosen for the following reasons: (1) it is shallow enough to properly detect the nIP $(0k0)$ peaks (these were cut off when large incidence angles, such as 2°, were used) and (2) it is well above the critical angle. The critical angle was calculated to be near 0.17° using GIXA; [2] this value is slightly below the measured critical angles (0.2°-0.26°) of the BA-MA RP film series. [3] It is important to be far enough above the critical angle to avoid double diffraction, which may manifest in the nOP (but not nIP) peaks. [4] All peaks were fit to Pseudo-Voigt patterns using Igor, with Gaussian and Lorentzian contributions kept constant (Igor Multipeak "shape" factor of 1) across all peaks.

PDS characterization

Photothermal Deflection Spectroscopy (PDS) measurements were performed using a homebuilt instrument as previously described. [5] Briefly, monochromated light from either a 150 W Xenon or a 100 W halogen lamp is modulated at 0.5 Hz with a mechanical chopper and then split to be separately focused onto the sample and a pyroelectric detector. Degassed and filtered perfluorohexane (C6F14, 3M Fluorinert FC-72) is employed as the deflection medium. The deflection of a HeNe laser aligned perpendicularly to the pump beam to also be parallel and proximal to the sample surface is measured by a position-sensitive Si detector using a lock-in amplifier. Analysis and fitting was performed using MATLAB.). Absorbance peak positions are best determined from UV-Vis (**Figure 4.3a**), since the PDS signal is less accurate above 3 eV.

Other Characterizations

Powder X-Ray Diffraction patterns were obtained using a Panalytical Empyrean powder diffractometer in reflection mode with a Cu-Kα source, operating with an accelerating voltage of 45 kV and beam current of 40 mA. Au nanoparticles (100 nm) drop-cast on quartz substrates were used to calibrate peak positions for strain characterization. All peak locations were obtained by Pseudo-Voigt fits using Igor Pro 8.

Scanning Electron Microscopy was performed using an FEI Nova Nano 650 FEG SEM operating at 7-10 keV accelerating voltage with beam currents of 0.40-0.80 nA. For SEM measurements, the samples were sputter-coated with gold to prevent charging.

Absorbance spectra were extracted from transmission measurements made on a Shimadzu UV-2600 ultraviolet-visible spectrophotometer at room temperature and in ambient conditions.

Photoluminescence spectra were acquired using a Horiba FluoroMax 4 spectrometer calibrated with Milli-Q water. Photoluminescence spectra reported in in the main text were all collected using an angle of 75° between the excitation and emission port to reduce scattering. Some PL spectra in the SI were acquired using an angle of 25° for comparison, since the proportions of different features can be angle dependent. All measurements were performed with an excitation wavelength of 370 nm (3.35 eV) and a 400 nm long-pass filter was placed in front of the mission port to reduce scattering. Spectra were fit to Gaussians using Igor Pro 8.

Temperature-Dependent Photoluminescence measurements were performed using a home-build photoluminescence spectrometer. For the temperature control, the samples were placed into a LN2-cooled cold finger cryostat (Janice VPF-100) with Lakeshore 335 temperature controller. The PL was excited by an 80 MHz laser pulse train with wavelength of 370 nm (3.35 eV), the pulse energy was in sub 100 pJ range and the laser spot size diameter was about 100 μm. The UV laser light was produced by frequency doubling the output of Spectraphysics Tsunami Ti: Sapphire femtosecond laser oscillator with the fundamental wavelength of 740 nm in Coherent/Inrad optical harmonics generator. We verified that at the given laser energy density level there was no photoinduced damage to the sample. The PL emission was collected in near 90 degrees geometry by a system of lenses and focused on the input slit of a spectrometer (Acton Research SP500). The stray laser light was blocked by an interference long pass filter (Omega Filters) with cut on wavelength 380 nm. The spectra dispersed by the spectrometer were recorded by a charge- coupled device detector (Princeton Instruments PIXIS:400). The spectra collected were corrected for the instrument response by measuring the response of the setup to the light of a black body-like source (Ocean Optics LS-1) and calculating appropriate correction factors. Spectra were acquired at an angle of 45° between the excitation and emission port to avoid scattering from the laser beam. All spectra were fit to Gaussians using Igor Pro 8.

4.3 Results and Discussion

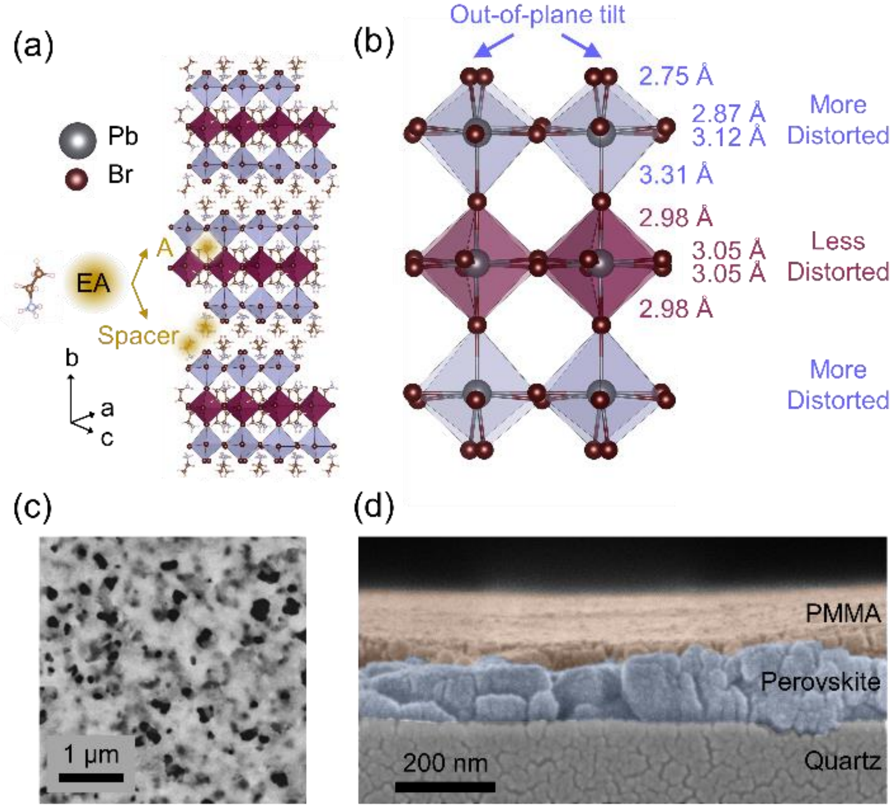

Figure 4.1. (a) Crystal structure of $(EA)_4Pb_3Br_{10}$ from reference [12] with (b) reported Pb-Br bond lengths and octahedral distortions. (c) Top-view and (d) cross-sectional SEM images of an $(EA)_4Pb_3Br_{10}$ film spin-cast on quartz. Films were capped with PMMA for most measurements, but not for top-view SEM, to better examine film morphology. The black color in the background of (c) is the substrate.

We aimed to understand relationships between growth and optical properties in polycrystalline thin films of RP phases that exhibit broad emission. One challenge encountered during RP film growth, for RPs with $n > 1$, is that the A-site and A'-site (spacer) cations segregate into different phases, resulting in highly-emissive 3D impurities. [45] To circumvent this challenge, we sought to study the film growth of RP phases in which A and A' are identical. We therefore selected the $(EA)_2(EA)_{n-1}Pb_nBr_{3n+1}$ family, where EA is ethylammonium. The structures of the n = 1 and n = 3 phases of this family have been determined from bulk crystals. [12,13] The n = 1 phase contains single sheets of Pb-Br octahedra separated by EA cations (**Figure 4.S1**). The structure of the n = 3 phase, $(EA)_4Pb_3Br_{10}$, is shown in **Figure 4.1**. [12] To accommodate the large size of EA in the A-site (274 pm), [50,51] the 3-layer inorganic sheet forms two substructures comprising highly-distorted outer octahedra and relatively undistorted inner octahedra (**Figure 4.1b**). The bond lengths of the outer, distorted octahedra show large variations (≈ 20 %), with the shortest at 2.75 Å and the longest at 3.31 Å, while those of the inner octahedra have less variation. The outer layers also exhibit significant out-of-plane tilting, contrary to the inner octahedra. The angle and bond length [11–17] distortions in the outer layers are thought to encourage formation of self-trapped excitons (STEs), which create broad, lower-energy photoluminescence emission. [12,16] Both the n = 1 and n = 3 phases of the $(EA)_2(EA)_{n-1}Pb_nBr_{3n+1}$ family exhibit pronounced narrow emission from free excitons, as well as broad emission at room temperature.[12,13] Thus, studying the properties of $(EA)_2(EA)_{n-1}Pb_nBr_{3n+1}$ films can reveal if strain and growth kinetics impact emission.

We first verified the phase composition of n = 3 and n = 1 $(EA)_2(EA)_{n-1}Pb_nBr_{3n+1}$ films before assessing how growth conditions impact emission. To prepare films of n = 3, we spin-cast precursor salts in nearly-stoichiometric proportions (see **Experimental Section**). A very small excess of EA was found to be necessary to growth the films, likely counteracting strong Pb-Br-DMF complexation. [52] Films were then capped with PMMA to prevent possible degradation. The as-cast n = 3 films exhibit ≤ 130 nm grain size and thickness and many pinholes (**Figure 4.1c-d**). Bulk crystals of n = 3 were also grown using literature methods and the crystal structure was verified (see Methods and **Figure 4.S2**).[12] We also prepared n = 1 films and confirmed their composition for comparison with the n = 3 films (**Figure 4.S1**).

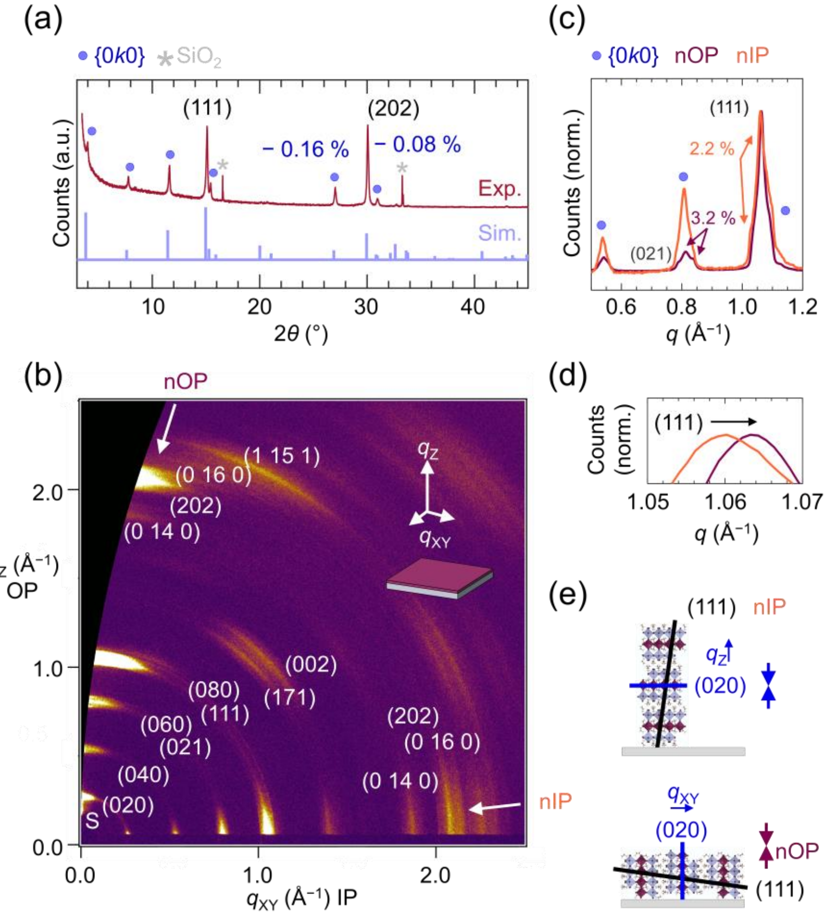

Figure 4.2. (a) XRD pattern of a spin-cast $(EA)_4Pb_3Br_{10}$ film, with % strain of peaks and a simulated (Sim.) powder pattern assuming no preferred crystallite orientation.[12] (b) Grazing Incidence Wide-Angle X-Ray Scattering (GIWAXS) pattern of a spin-cast $(EA)_4Pb_3Br_{10}$ film with indexed peaks and near-out-of-plane (nOP) and near-in-plane (nIP) regions indicated. S indicates spillover from the incident beam. (c) Integrated and normalized nOP and nIP patterns, with *relative* % strain of select peaks. (d) Inset of (c), showing a closer view of the (111) nOP and nIP peak positions. (e) Schematic of the two primary crystallite orientations identified from the GIWAXS pattern: one oriented with (0k0) in-plane (q_{XY} axis) and the other oriented with (0k0) out-of-plane (q_Z axis). Out-of-plane-oriented peaks have mild compressive strain and the (111) is more compressed than in the in-plane-oriented crystallites.

X-ray scattering from the as-prepared n = 3 films is consistent with the desired $(EA)_4Pb_3Br_{10}$ phase (**Figure 4.2**). The X-Ray diffraction (XRD) pattern of the n = 3 film is in good agreement with the simulated powder pattern of this material (**Figure 4.2a**). The $(0k0)$ and (111) features have approximately the relative intensities that would be expected from the XRD pattern expected from the single crystal structure. [12] The presence of the $(0k0)$ features suggests phase purity, since they appear strongly in phase-pure RP films [33] and in powders of target RP n phase. [9] In contrast, the $(0k0)$ are weakened relative to other peaks, or absent entirely, in mixed-phase films [42] due to stacking fault defects that result in intergrowth of different n within a single grain. [42,43] Grazing Incidence Wide-Angle X-Ray Scattering (GIWAXS) patterns of the films were collected to probe off-specular diffraction (**Figure 4.2b**). All observed peaks are indexed to features of $(EA)_4Pb_3Br_{10}$ (**Figure 4.*S*3**) with the only missing peaks predicted to have very small intensity. GIWAXS confirms that there is a distribution of orientations of crystallites in the films (**Figure 4.2b**). In particular, the presence of $(0k0)$ and (111) *only* near q_{XY} and q_Z, but not in between, reveals that the Pb-Br octahedral sheets prefer to grow either parallel or perpendicular to the substate (**Figure 4.2c-d**). Further analysis reveals a slight preference for the crystallites growing with Pb-Br octahedra growing perpendicular to the substrate (**Figure 4.*S*3**). Thus, the $(EA)_4Pb_3Br_{10}$ films appear phase-pure and textured based on X-ray scattering.

X-ray scattering also reveals that the grains in the n = 3 films exhibit strain. Based on the peak shifts seem in XRD (see **Experimental Section**), the film is compressively strained (by under 0.3 %) in the out-of-plane direction (**Figure 4.2a**). This mild strain is consistent with prior reports of the spin-coating [35] and/or annealing [34] procedures imparting mild biaxial stress in hybrid organic metal halides. To examine strain in greater detail, sections of the GIWAXS pattern were integrated near-out-of-plane (nOP) and near-in-plane (nIP) (see **Figure 4.S4** for definition of these areas), and normalized for clarity. The position of the (111) nOP is shifted into compression, in agreement with the mild compression observed in XRD, and is additionally more compressed than the (111) nIP (**Figure 4.2a/c/d**). The difference in strain between the (111) nOP and (111) nIP shows that the mild biaxial strain affects out-of-plane vs. in-plane oriented crystallites differently (**Figure 4.2d**). In addition, small peaks are identified near the main ($0k0$) and (111) peaks for the nOP and nIP patterns (**Figure 4.2d** and **Figure 4.S4**), and are assigned to strained ($0k0$) and (111) features. From peak fits, these weaker peaks had 2-3 % strain relative to their respective main ($0k0$) and (111) peaks. Overall, the films exhibit mild biaxial strain that differently affects in-plane vs. out-of-plane oriented crystallites, with small populations of highly-strained crystallites.

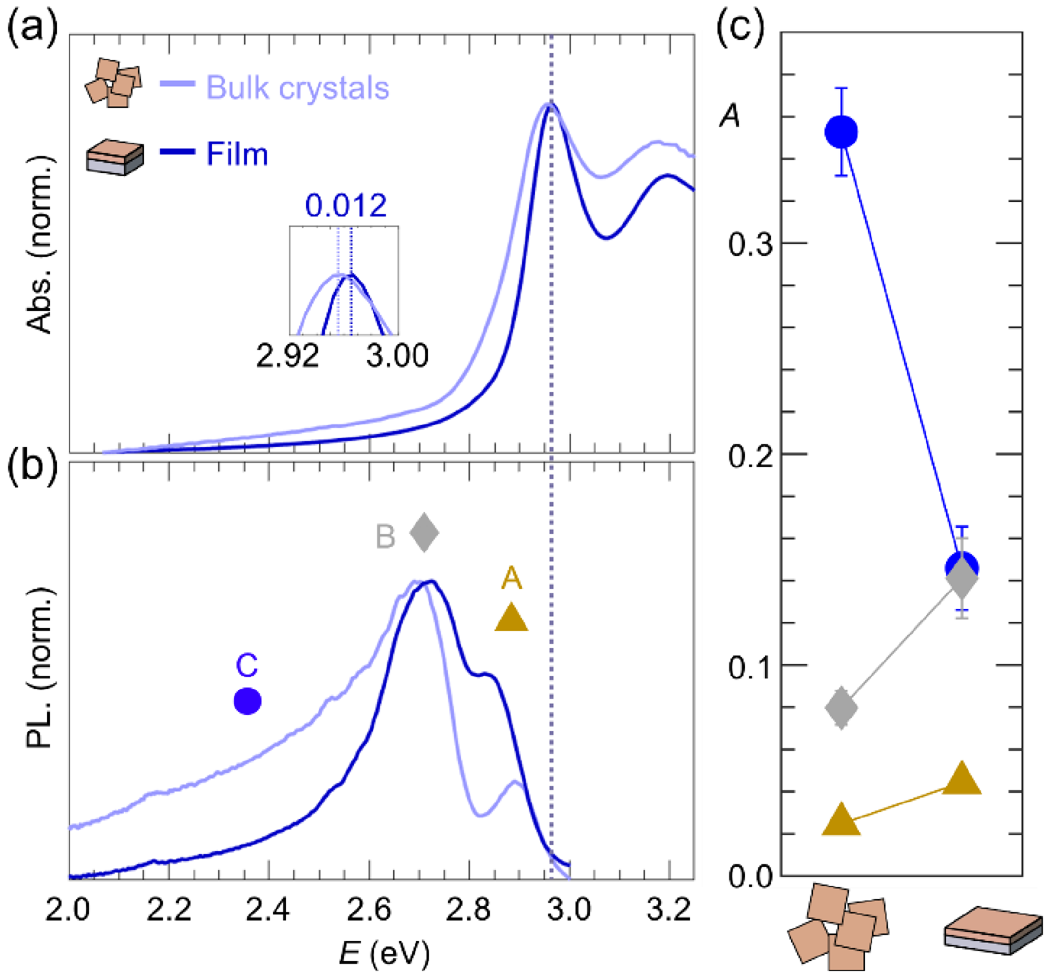

Figure 4.3. (a) Absorbance and (b) Photoluminescence emission (excitaiton 3.35 eV) of bulk crystals and spin-cast films of $(EA)_4Pb_3Br_{10}$. The inset in (a) shows the energy difference between the $n = 3$ main exciton absorbance peak of the bulk crystals and film. The dashed line connecting (a) and (b) is a guide to the eye. Emission peaks are labelled A, B and C. (c) Gaussian area of features A, B, and C (see **Figure 4.S5** for fits).

The optical properties of polycrystalline films and bulk crystals of $(EA)_4Pb_3Br_{10}$ show features of only $n = 3$. The UV-Vis absorbance spectrum of polycrystalline thin films is well-matched with that of the bulk crystals (**Figure 4.3a**), and both are comparable to the bulk crystal spectrum previously reported. [12] The absorbance spectra of the bulk crystals and film exhibit a sharp increase near the main $n = 3$ excitonic feature at ≈ 3.0 eV (**Figure 4.3a**). In contrast, thin films of $n = 3$ RP phases that also contain off-target n or 3D impurities frequently show absorbance spectra that have large sub-gap slopes and poorly-visible $n = 3$ excitonic features. [42,45,53] In addition, the 2.9 eV onset of emission is close in energy to the absorbance onset for both films and crystals (dashed line in **Figure 4.3**), which is a sign of phase purity (**Figure 4.3b**). If lower band-gap phases were present, even in small concentrations, we would expect emission from excitations funneled to these phases, as observed in mixed-phase $(BA)_2(MA)_{n-1}Pb_nI_{3n+1}$ RP films. [42,45] Three primary features are observed in the emission in both bulk crystals and films: a high-energy excitonic feature near 2.9 eV (peak A), one near 2.7 eV (peak B), and broad emission below 2.7 eV (peak C - for spectra in nm, see **Figure 4.S6** [54]). No other emissive features are detected. Thus, the optical properties of the films are those of the $n = 3$ phase.

The proportions of the different $n = 3$ emission peaks change considerably from bulk crystals to films (**Figure 4.3b**). To better assess these changes, we fit the normalized emission spectra (**Figure 4.S5**) and examined the areas of peaks A, B and C (**Figure 4.3c**). The integrated area of the free exciton at 2.9 eV (peak A) does not change much from bulk crystals to films. However, the area of B (2.7 eV) increased slightly in films, which is the opposite of what is seen from self-absorption, as peaks from self-absorption become weaker in thinner perovskites. [55] Notably, the broad, low-energy tail, C, decreases sharply in area from bulk crystals to polycrystalline films. Broad, low-energy peaks such as C, that are far in energy from the free exciton, are commonly attributed to self-trapped excitons, [11–17] and not to self-absorption. [55] To further understand C, we excited bulk crystals below-gap (2.75 eV), and observed no emission (**Figure 4.S7**). Thus, C does not come from impurities or extrinsic effects, [23] and $(EA)_4Pb_3Br_{10}$ must be excited above-gap for the low-energy emission (peak C) to appear, which is again consistent with attributions of peak C to self-trapped excitons. [11–18] We then confirmed that the changes in relative areas of A, B and C were not due to measurement conditions (see **Figure 4.S8**), since the proportions of emissive features in 2D materials can sometimes vary with collection angle. [18] In all cases, the bulk *n* = 3 crystals exhibit more low-energy tail emission (peak C) than the polycrystalline films. We also notice that the EA *n* = 1 films contain the same emission features as bulk *n* = 1 crystals, but proportionally less low-energy, broad emission than that reported for the bulk *n* = 1 crystals (**Figure 4.S1**). [13] Thus, the target-*n* emission seems to be preserved in films for both *n* = 3 and *n* = 1, but with large changes to the proportions of emissive species.

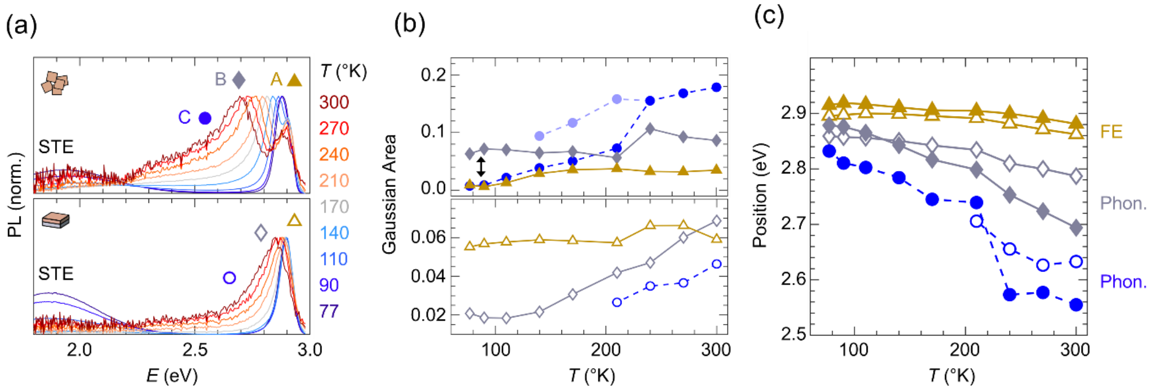

Figure 4.4. Effects of cooling on photoluminescence emission. (a) Temperature-dependent photoluminescence emission of bulk crystals (top panel) and film (bottom panel) of $(EA)_4Pb_3Br_{10}$, with pulsed excitation at 3.35 eV (see **Experimental Section**). A self-trapped exciton (STE) peak appears below 110°K near 1.9 eV. (b) Evolution of integrated area of peaks A, B and C with temperature for bulk crystals (top panel) and a film (bottom panel). The black arrow indicates strong overlap between peaks A and B at low temperatures in the bulk crystals, making decoupling A and B uncertain at low temperatures (for fits and additional discussion of fits, see **Figure 4.S9**). C is a broad feature that appears to split into 2 peaks (lighter and darker blue) below 200 K (c) Evolution of peak position with temperature for peaks A, B and C in the bulk crystals and films. FE stands for free exciton and Phon. for phonon-coupled.

Temperature-dependent emission reveals several types of emissive features, which allows us to understand the changes in emission proportions in films (**Figure 4.4**). Conventional STEs observed in perovskites increase in intensity with cooling; this is attributed to less de-trapping back to the free exciton state at lower temperatures. [14,17] This type of STE appears below 110 K in both bulk crystals and films, near 1.9 eV. The behavior of B and C contrasts strongly with this 1.9 eV feature. The normalized emission spectra with cooling of bulk crystals and films are shown in **Figure 4.4a** with peak area (**Figure 4.4b**) and peak position (**Figure 4.4c)** and fits in **Figure 4.S9**. The B and C features blue-shift strongly with cooling, and C seems to disappear at low temperatures. The fits for feature C are less certain due to its breadth; however, the disappearance of C with cooling is obvious. It is possible that B and C blue-shift so strongly with cooling that they overlap with themselves or with peak A, as highlighted by the black arrow in **Figure 4.4b** (see also **Figure 4.S9**). The large blue-shift/disappearance of B and C with cooling is consistent with coupling to phonons. Similar blue-shifts have been previously observed in $(A')_2PbI_4$, [18,21] as well as in lithium niobate. [56] In particular, the energy shifts with cooling of C (277 meV in the crystals) and B (184 meV in the crystals; 72 meV in the film) are on the order of the blue-shift observed for $(A')_2PbI_4$ over a similar temperature differential (120 meV). [18] The strongly blue-shifting feature of $(A')_2PbI_4$ has been assigned to both an STE with specific phonon-coupling behavior [18] and to a phonon replica; [21] both are possibilities for B and C. This large blue-shift/disappearance with cooling of B and C contrasts with the behavior of extrinsic features, [23] polaron self-localization, [22] convolutions of a bright exciton with a localized state, [25] or shallow traps, [25] as these have different behavior with cooling. The blue-shifts of B and C are larger (>10x) than shifts expected from self-absorption. [55] In addition, the free exciton (peak A) exhibits a much smaller shift with cooling (34 meV and 33 meV in crystals/films respectively), consistent with previously-reported free exciton behavior. [18] Overall, the behavior of B and C is most consistent with phonon-mediated processes, such as STEs or phonon replicas.

Strain likely causes the differences in the proportions of A, B and C in bulk crystals and polycrystalline films (**Figures 4.2, 4.3, 4.4**). Film strain observed in the $(EA)_4Pb_3Br_{10}$ films by X-ray scattering (**Figure 4.2**) is likely the origin of the small blue-shift (by 0.012 eV) of the main free exciton in the film compared to in bulk crystals (**Figure 4.3a**). Similar shifts (≈ 0.013 eV) in free exciton energy were observed in other 2D perovskites upon application of ≈ 1 % strain.[40] Strain can also affect the lower-energy emission: prior work on bulk crystals of $(BA)_2PbBr_4$ found that microstrain, caused by differing stacking of spacer cations in the bulk region, can enhance the phonon-coupled, lower-energy emission. [20] Given the assignment that B and C are phonon-coupled and the crystallites are strained (**Figure 4.2**), it is likely that changes to the emission intensities of B and C are linked to these strains. The effects of thickness are not as easily decoupled, as preparing thinner samples involves either spin-casting or mechanical exfoliation, and both of these involve strain [35] of some sort (exfoliation involves manually applying pressure in order to separate the semiconducting sheets). We also exfoliated bulk crystals of $(EA)_4Pb_3Br_{10}$; the results are consistent with different strain changing the relative proportions of B and C (**Figure 4.S10**). Strain has also been found to turn the emission from STEs off or on, depending on whether strain decreases or increases Pb-Br octahedral distortions in 1-D or 0-D hybrid halide perovskite-like free-standing crystals. [11,58] In particular, when strain decreased the octahedral distortions, [11] the free exciton emission (narrow and higher energy) proportionally increased at the expense of the STE emission. Here, we find that the films contain strain that varied between 0.1 % and 3 % (**Figure 2**), which is on the order of the deformation that were found to decrease STE emission in free-standing, micron-sized crystals under pressure [11] (see additional discussion in the **Appendix to Chapter 4** [59,60]). The changes in emission intensity of B and C from bulk crystals to polycrystalline films thus likely stem from film strain, which can affect both spacer cation stacking and octahedral distortions.

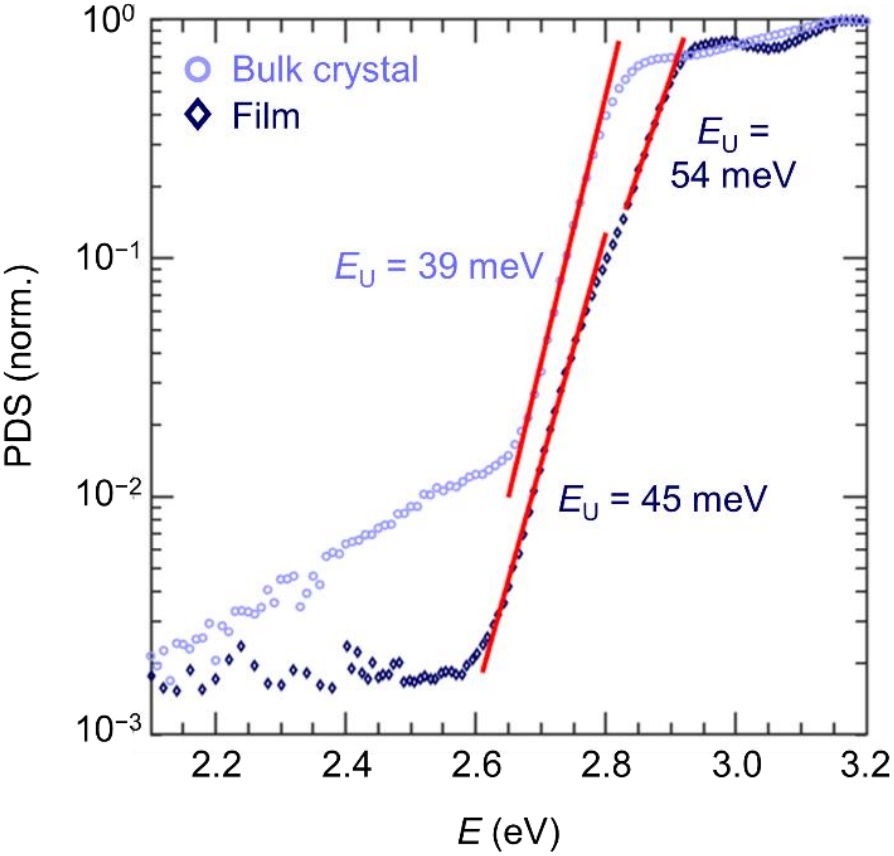

Figure 4.5. PDS spectra of a bulk crystal and film of $(EA)_4Pb_3Br_{10}$, showing fits of different absorption onsets (see **Appendix to Chapter 4**) and the extracted Urbach energies E_U. More detail in the 2.6 eV-3.0 eV region, as well as goodness of fits, are shown in **Figure 4.S11**.

Photothermal Deflection Spectroscopy (PDS) was then used to examine more subtle optical changes caused by switching from bulk crystal to polycrystalline films (**Figure 4.5**). PDS enabled highly sensitive measurement of the absorption onsets throughout the ≈ 130 nm film (see **Experimental Section**). The slight blue-shift of the film PDS absorbance with respect to that of bulk crystal is consistent with the UV-Vis measurement of **Figure 4.3a** (see also **Experimental Section**). The lack of any PDS absorbance feature in the film below the main onset is further indication of *n* = 3 phase purity in the films. In contrast, nominally *n* = 3 films with mixed-phase composition exhibited low-energy absorbance features that were indexed to higher-*n* Ruddlesden-Popper phases. [45] The bulk crystal of $(EA)_4Pb_3Br_{10}$ exhibits a tail at low energy, but this tail is non-emissive when excited directly (**Figure 4.S7**), so we rule out emissive impurities or extrinsic effects [23] as the source of the tail. We fit portions of the PDS spectra (see **Experimental Section**) to extract the Urbach energies E_U, representing the degree of disorder in electronic states near the absorption edge (see also **Figure 4.S11**).

Differences in onset between the film and bulk crystal can be attributed to strain (**Figure 4.5**). While the bulk crystal only exhibits one absorbance onset with an Urbach energy E_U of 39 meV, the film exhibits two onsets that can be fit with different E_U of 45 meV and 54 meV. GIWAXS reveals populations of crystallites with two different strain states (**Figure 4.2**). The two absorbance onsets, with their two distinct Urbach energies, likely correspond to these two states because of the sensitivity of free excitons to strain. [40] The increase in Urbach energies from the crystal (39 meV) to the film (45 and 54 meV) also likely originates from strain. In addition, the weak, sub-gap absorbance in the bulk crystal below 2.6 eV is likely connected to the larger amount of broad, lower-energy emission from C present in the bulk crystals. Direct excitation near the absorbance tail does not lead to emission (**Figure 4.S7**), ruling out emissive impurities as the source of the tail. However, it is clear that making $(EA)_4Pb_3Br_{10}$ as a film prevents formation of this tail. Thus, strain has two effects – it can increase the electronic disorder of the free excitons present, and likely hinders formation of states likely connected to broad emission. These results suggest the importance of controlling strain during growth of thin films for modifying the photoluminescence.

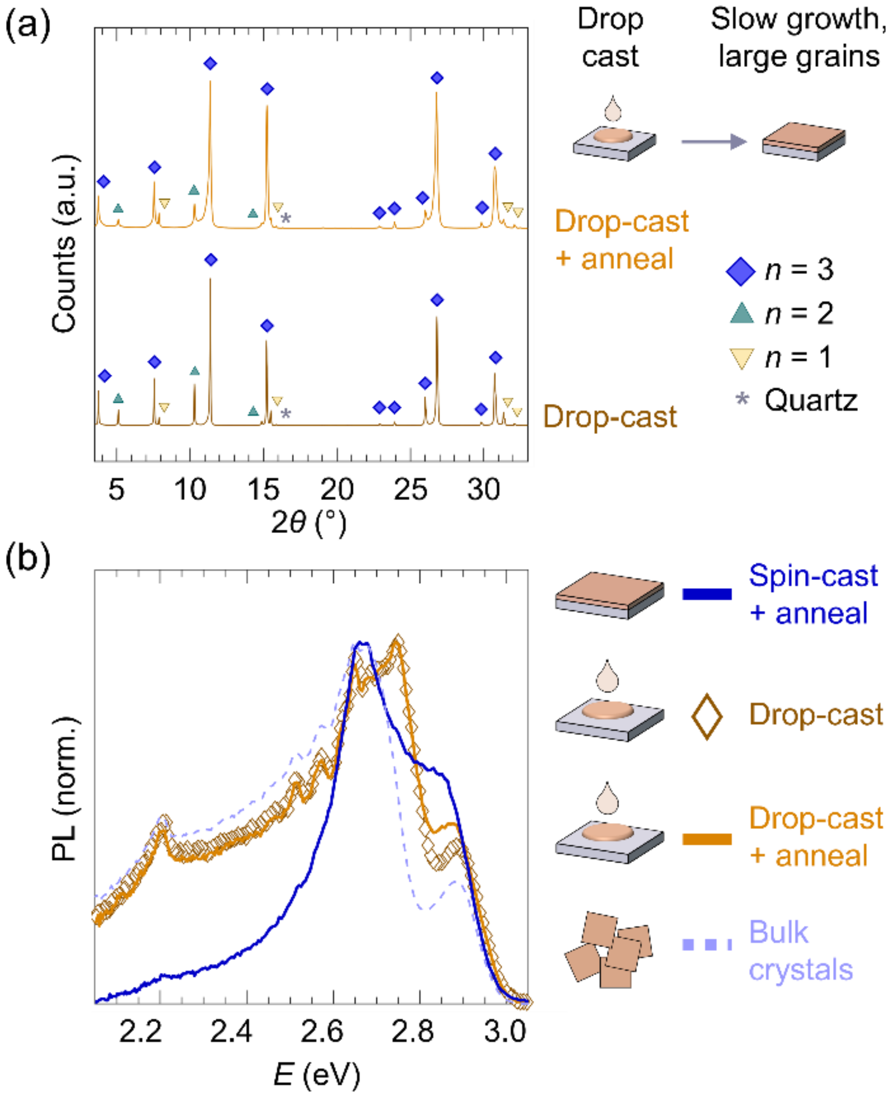

Figure 4.6. (a) XRD patterns of films made by drop-casting the *n* = 3 precursor solution, with/without annealing. The *n* = 3 and *n* = 1 peaks were assigned from reported structures [12,13] and the *n* = 2 peaks were assigned based on analogy from other RPs. [61] (b) Photoluminescence emission of these films (3.94 eV excitation). The emission spectra of $(EA)_4Pb_3Br_{10}$ bulk crystals and spin-cast films are also shown.

Having examined the various ways in which sample thickness and film strain can impact the optical properties of $(EA)_4Pb_3Br_{10}$, we next sought ways to control the optical properties of films by controlling film growth. Film strains suggest that rapid spin-casting may not be the optimal growth method for controlling low-energy emission. Because film strains can originate from stresses acquired during spin-casting [35] and from thermal expansion mismatch between the material and substrate during annealing, [34] we tried to modify the deposition kinetics to avoid these two factors. We slowed the deposition kinetics by drop-casting the precursor solution and allowed the solvent to slowly evaporate (in N_2 atmosphere glove box for 1h). The samples were then, in some cases, annealed, and then capped with PMMA for protection (see **Experimental Section**). SEM images of the non-annealed and annealed films show large grains, ~20 μm-wide and ~3 μm-thick, without complete coverage of the substrate (**Figure 4.S12**). Thus, in the drop-cast films, the grains grow on the substrate with few spatial constrains from neighboring grains, in contrast to spin-cast films. The grains exhibit one crystal habit and are isotropic and homogeneous, suggesting that non-RP phases, such as solvates or other intermediates, do not form, in contrast to the behavior of other drop-cast 2D or 3D perovskites. [45,46,62] XRD patterns of drop-cast films, with and without annealing, are shown in **Figure 4.6a**. The drop-cast films contain in majority n = 3 and the position of the peaks do not indicate strain. Additionally, small amounts of n = 1 and additional features are present. Because only n = 1 and n = 3 single crystal structures have been reported, we attribute certain peaks to n = 2, by estimation of where the n = 2 peaks should be based on analogy with the $(BA)_2(MA)_{n-1}Pb_nX_{3n+1}$ RP peak locations. [9]

Slowing growth by drop-casting enables recovery of the broad emission. **Figure 4.6b** shows the photoluminescence of the drop-cast films overlaid with those of the spin-cast n = 3 film and of the n = 3 bulk crystals. The drop-cast films exhibit comparable low-energy emission (peaks B and C) to the bulk crystals. An extra feature is observed near 2.75 eV, possibly originating from the small amount of proposed $n = 2$ in the drop-cast films (see **Figure 4.6a**). However, the spectra of the drop-cast films closely resemble that of the $n = 3$ bulk crystals, indicating that most of the emission comes from $n = 3$. Since thick grains in the drop-cast $n = 3$ films grow slowly and with few spatial constrains from neighboring grains, such slow and unconstrained growth of thick grains seems necessary for retaining the lower-energy emission. The slow, drop-cast growth may also have changed cation stacking in a way that encourages broad emission. [20] Annealing the drop-cast films does not change the emission much, likely because the $n = 3$ phase formed before annealing, so the perovskite likely did not retain much thermal stress post-cooling, although this may depend on the thermal expansion coefficient of the substrate used. [34] Thus, deposition methods that reduce strain are likely to favor low-energy emission in films.

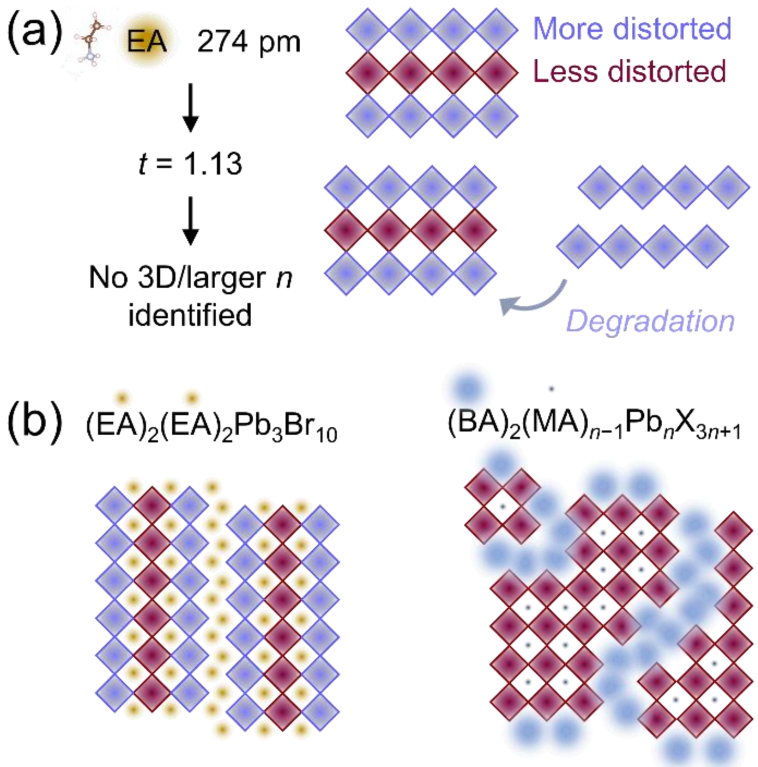

Scheme 4.1. Origins of phase purity in the $n = 3$ films. (a) Summary of findings of **Figures 4.2**, **4.3**, **4.6**, **4.S13** and **4.S14**, where t stands for the tolerance factor. (b) Illustration of how stacking fault defects lead to intergrowth of n in the $(BA)_2(MA)_{n-1}Pb_nX_{3n+1}$ RP series, and how in contrast, the EA RPs have a lack of different n phases available for intergrowth, resulting in $n = 3$ phase-purity.

Finally, we discuss why only n = 3 is observed in spin-cast films, rather than other phases in the $(EA)_2(EA)_{n-1}Pb_nBr_{3n+1}$ family, and why it is favorably formed (**Scheme 4.1**). The spin-casting procedures we used typically yield 2D-3D mixed-phase films unless particular care is taken, [33,42,43,45,46] so the formation of a phase-pure $n = 3$ film via spin-casting is notable. First, no experimental single crystal structure for a 3D $EAPbBr_3$ phase has been reported to our knowledge. Previous work that attempted to make films of 3D $EAPbBr_3$ found that a 2D phase formed instead, [63] and we believe that prior assignments to the $EAPbBr_3$ phase in nanocrystals may actually correspond to $(EA)_4Pb_3Br_{10}$ (see "Further Discussion on 2D and 3D Phases" in the **Appendix to Chapter 4**). [64] We also attempted to make $EAPbBr_3$ films (**Figure 4.S13** and **Scheme 4.1a**) and obtain non-emissive films with broad features in XRD. The absence of formation of a 3D perovskite phase of $EAPbBr_3$ is consistent with the tolerance factor for EA with Pb and Br prohibiting 3D phase formation (t = 1.13; see **Appendix to Chapter 4** for calculation). By itself, EA (274 pm) [50,51] is just small enough to fit in the A-site of 2D phases, since the 2D perovskites have less strict requirements for tolerance factor. [65,66] The n = 3 and n = 1 RP phases in the $(EA)_2(EA)_{n-1}Pb_nBr_{3n+1}$ family have been reported as single crystal structures, but there are no reports of phases with other n values. [12,13] The presence of a single EA cation in the A/A' sites also limits the number of competing precipitations. The phase purity observed in n = 3 and n = 1 films thus likely originates from lack of available other phases, due to the large size of EA and consequently unfavorable tolerance factor for impurity 3D or larger-n RP phases. This phase selectivity is in direct contrast to the behavior of the widely studied $(A')_2(A)_{n-1}Pb_n(I \text{ or } Br)_{3n+1}$ RPs families, where spin-casting leads to polycrystalline films with mixed RP and 3D phases unless particular care is taken to suppress their formation. [33,42,43,45,46] The tolerance factor of the 3D structures $MAPbI_3$ and $MAPbBr_3$ are 0.96 and 0.99 respectively, so a large variety of corner-sharing structures can form (**Scheme 4.1b**) leading to more ready formation of off-target RP and 3D phases. [42,43,45,46,67] The ability to grow phase pure polycrystalline films with EA shows that selecting A-site cations that are too large to form 3D phases, but are within sizes tolerable for layered structures, is a route to eliminating alternative phase formation.

The n = 3 phase forms preferentially over the n = 1 phase, likely due to specific patterns of Pb-Br octahedral distortions (**Scheme 4.1**). While the stoichiometry of the n = 3 precursor solution roughly matched $(EA)_4Pb_3Br_{10}$, a large excess of EA (nearly 2×) is needed to make thin films of n = 1 $(EA)_2PbBr_4$ (**Figure 4.S13**). Bulk crystal synthesis of *n* = 1 is also reported to require EA excess, [13] unlike bulk crystal synthesis of *n* = 3, which follows *n* = 3 stoichiometry. [12] Not only are *n* = 3 films much more stable to heat and the ambient than the *n* = 1, but the *n* = 1 films degrade to *n* = 3 (see discussion of **Figure 4.S14**). Thus, *n* = 3 is much more easily formed and stable than *n* = 1. This preference likely originates from the large size of EA (274 pm): [50,51] the *n* = 3 phase forms distorted/undistorted octahedral substructures within the Pb-Br sheets to accommodate this large size, and the less-distorted inner layer of the *n* = 3 likely stabilizes the 3-layer Pb-Br sheet. In contrast, the *n* = 1 contains only one highly-distorted octahedral layer (**Figure 4.S1**). The *n* = 1 can thus can form in a phase-pure manner but requires significant stoichiometric excess to form (**Figure 4.S13**) and readily transforms into the more stable *n* = 3 (**Figure 4.S14**). We hypothesize that the *n* = 2 structure, similarly to the *n* = 1, would only contain highly distorted octahedral sheets, and not have the inner stabilizing layer of the *n* = 3 phase. Thus, the optimal size of the EA cation, creating the inner stabilizing layer and preventing 3D formation, is instrumental to casting phase-pure *n* = 3 RP films. Tailoring the ratio of less: more-distorted layers with cations other than EA may be crucial for spin-casting phase-pure RP films with *n* ≠ 3.

4.4 Conclusions

Overall, we find that that strain can greatly affect the relative proportions of different luminescence features emitted by a solution-cast 2D phase. Film strain can suppress lower-energy, broad emission that is coupled to phonons, in favor of free exciton emission. Film strain also increases electronic disorder, and removes sub-gap absorbance features that are likely correlated with broad emission. Broad emission can be recovered by slowing the film growth and removing spin-casting strains. Growth methods that avoid rapid solvent removal, such as co-evaporation or blade coating, will likely prove more fruitful for retaining broad emission than spin-casting. In addition, the use of a single cation for both the A-site and spacer enables casting of phase-pure films. The large size of this cation prevents 3D impurities from forming due to unfavorable tolerance factor, and prevents off-target n from forming due to unfavorable octahedral distortions. These results further our understanding of how to control phase composition and emission in films, which extends the utility of 2D perovskites for light-emitting devices and may enable novel fabrication of perovskite-perovskite heterostructures, which are useful in a variety of devices.

4.5 Acknowledgments and Permissions

Growth and structural characterization were supported by the U.S. Department of Energy, Office of Science, Basic Energy Sciences, under Award Number DE-SC-0012541. Support of optical characterization was provided by the U.S. Department of Energy (DOE), Office of Science, Basic Energy Sciences (BES), under Award Number DE-SC0019273, as well as from Quantum Materials for Energy Efficient Neuromorphic Computing, an Energy Frontier Research Center funded by the U.S. Department of Energy (DOE), Office of Science, Basic Energy Sciences, (BES), under Award Number DE-SC0019273. Time-resolved spectroscopy capabilities were supported by DURIP ARO grant 66886LSRIP. Use of the Stanford Synchrotron Radiation Lightsource, SLAC National Accelerator Laboratory, is supported by the U.S. Department of Energy, Office of Science, Office of Basic Energy Sciences under Contract No. DE-AC02-76SF00515. The research reported here also made use the shared facilities of the UCSB MRSEC (National Science Foundation DMR 1720256), a member of the Materials Research Facilities Network (www.mrfn.org). R.M.K. gratefully acknowledges the National Defense Science and Engineering Graduate fellowship for financial support. Reproduced with permission from ACS Journals, submitted for publication. Unpublished work copyright 2021 American Chemical Society.

4.6 References

(1) Zhou, Y.; Chen, J.; Bakr, O. M.; Mohammed, O. F. Metal Halide Perovskites for X - Ray Imaging Scintillators and Detectors. *ACS Energy Lett.* **2021**, *6*, 739-768.

(2) Saparov, B.; Mitzi, D. B. Organic-Inorganic Perovskites: Structural Versatility for Functional Materials Design. *Chem. Rev.* **2016**, *116* (7), 4558-4596.

(3) Ge, C.; Xue, Y. Z. B.; Li, L.; Tang, B.; Hu, H. Recent Progress in 2D/3D Multidimensional Metal Halide Perovskites Solar Cells. *Front. Mater.* **2020**, *7*, 380.

(4) Li, X.; Hoffman, J. M.; Kanatzidis, M. G. The 2D Halide Perovskite Rulebook: How the Spacer Influences Everything from the Structure to Optoelectronic Device Efficiency. *Chem. Rev.* **2021**, *121*, 2230-2291.

(5) Smith, M. D.; Crace, E. J.; Jaffe, A.; Karunadasa, H. I. The Diversity of Layered Halide Perovskites. *Annu. Rev. Mater. Res.* **2018**, *48*, 111-136.

(6) Ruddlesden, S. N.; Popper, P. The Compound $Sr_3Ti_2O_7$ and Its Structure . *Acta Crystallogr.* **1958**, *11* (1), 54-55.

(7) Ruddlesden, S. N.; Popper, P. New Compounds of the K_2NIF_4 Type . *Acta Crystallogr.* **1957**, *10* (8), 538-539.

(8) Smith, I. C.; Hoke, E. T.; Solis-Ibarra, D.; McGehee, M. D.; Karunadasa, H. I. A Layered Hybrid Perovskite Solar-Cell Absorber with Enhanced Moisture Stability. *Angew. Chemie* **2014**, *126* (42), 11414-11417.

(9) Stoumpos, C. C.; Cao, D. H.; Clark, D. J.; Young, J.; Rondinelli, J. M.; Jang, J. I.; Hupp, J. T.; Kanatzidis, M. G. Ruddlesden-Popper Hybrid Lead Iodide Perovskite 2D Homologous Semiconductors. *Chem. Mater.* **2016**, *28* (8), 2852-2867.

(10) Mao, L.; Stoumpos, C. C.; Kanatzidis, M. G. Two-Dimensional Hybrid Halide Perovskites: Principles and Promises. *J. Am. Chem. Soc.* **2019**, *141* (3), 1171-1190.

(11) Ma, Z.; Li, F.; Sui, L.; Shi, Y.; Fu, R.; Yuan, K.; Xiao, G.; Zou, B. Tunable Color Temperatures and Emission Enhancement in 1D Halide Perovskites under High Pressure. *Adv. Opt. Mater.* **2020**, *8* (18), 1-7.

(12) Mao, L.; Wu, Y.; Stoumpos, C. C.; Traore, B.; Katan, C.; Even, J.; Wasielewski, M. R.; Kanatzidis, M. G. Tunable White-Light Emission in Single-Cation-Templated Three-Layered 2D Perovskites $(CH_3CH_2NH_3)_4Pb_3Br_{10-x}Cl_x$. *J. Am. Chem. Soc.* **2017**, *139*

(34), 11956-11963.

(13) Luo, B.; Guo, Y.; Li, X.; Xiao, Y.; Huang, X.; Zhang, J. Z. Efficient Trap-Mediated Mn^{2+} Dopant Emission in Two Dimensional Single-Layered Perovskite $(CH_3CH_2NH_3)_2PbBr_4$. *J. Phys. Chem. C* **2019**, *123* (23), 14239-14245.

(14) Smith, M. D.; Jaffe, A.; Dohner, E. R.; Lindenberg, A. M.; Karunadasa, H. I. Structural Origins of Broadband Emission from Layered Pb-Br Hybrid Perovskites. *Chem. Sci.* **2017**, *8* (6), 4497-4504.

(15) Smith, M. D.; Connor, B. A.; Karunadasa, H. I. Tuning the Luminescence of Layered Halide Perovskites. *Chem. Rev.* **2019**, *119* (5), 3104-3139.

(16) Cortecchia, D.; Neutzner, S.; Kandada, A. R. S.; Mosconi, E.; Meggiolaro, D.; De Angelis, F.; Soci, C.; Petrozza, A. Broadband Emission in Two-Dimensional Hybrid Perovskites: The Role of Structural Deformation. *J. Am. Chem. Soc.* **2017**, *139* (1), 39-42.

(17) Hu, T.; Smith, M. D.; Dohner, E. R.; Sher, M. J.; Wu, X.; Trinh, M. T.; Fisher, A.; Corbett, J.; Zhu, X. Y.; Karunadasa, H. I.; et al. Mechanism for Broadband White-Light Emission from Two-Dimensional (110) Hybrid Perovskites. *J. Phys. Chem. Lett.* **2016**, *7* (12), 2258-2263.

(18) Decrescent, R. A.; Du, X.; Kennard, R. M.; Venkatesan, N. R.; Dahlman, C. J.; Chabinyc, M. L.; Schuller, J. A. Even-Parity Self-Trapped Excitons Lead to Magnetic Dipole Radiation in Two-Dimensional Lead Halide Perovskites. *ACS Nano* **2020**, *14* (7), 8958-8968.

(19) DeCrescent, R. A.; Venkatesan, N. R.; Dahlman, C. J.; Kennard, R. M.; Zhang, X.; Li, W.; Du, X.; Chabinyc, M. L.; Zia, R.; Schuller, J. A. Bright Magnetic Dipole Radiation from Two-Dimensional Lead-Halide Perovskites. *Sci. Adv.* **2020**, *6*, 1-11.

(20) Du, Q.; Zhu, C.; Yin, Z.; Na, G.; Cheng, C.; Han, Y.; Liu, N.; Niu, X.; Zhou, H.; Chen, H.; et al. Stacking Effects on Electron-Phonon Coupling in Layered Hybrid Perovskites via Microstrain Manipulation. *ACS Nano* **2020**, *14* (5), 5806-5817.

(21) Moral, R. F.; Germino, J. C.; Bonato, L. G.; Almeida, D. B.; Therézio, E. M.; Atvars, T. D. Z.; Stranks, S. D.; Nome, R. A.; Nogueira, A. F. Influence of the Vibrational Modes from the Organic Moieties in 2D Lead Halides on Excitonic Recombination and Phase Transition. *Adv. Opt. Mater.* **2020**, *8* (24), 1-8.

(22) Cortecchia, D.; Yin, J.; Bruno, A.; Lo, S. Z. A.; Gurzadyan, G. G.; Mhaisalkar, S.; Brédas, J. L.; Soci, C. Polaron Self-Localization in White-Light Emitting Hybrid Perovskites. *J. Mater. Chem. C* **2017**, *5* (11), 2771-2780.

(23) Kahmann, S.; Tekelenburg, E. K.; Duim, H.; Kamminga, M. E.; Loi, M. A. Extrinsic Nature of the Broad Photoluminescence in Lead Iodide-Based Ruddlesden-Popper Perovskites. *Nat. Commun.* **2020**, *11* (1), 1-8.

(24) Yu, J.; Kong, J.; Hao, W.; Guo, X.; He, H.; Leow, W. R.; Liu, Z.; Cai, P.; Qian, G.; Li, S.; et al. Broadband Extrinsic Self-Trapped Exciton Emission in Sn-Doped 2D Lead-Halide Perovskites. *Adv. Mater.* **2019**, *31* (7), 1-9.

(25) Kahmann, S.; Duim, H.; Fang, H.; Adjokatse, S.; Medina, R.; Pitaro, M.; Plochocka, P.; Loi, A. Photophysics of Two-Dimensional Perovskites - Learning from Metal Halide Substitution. *Arxiv* **2021**, 1-22.

(26) Gharibzadeh, S.; Hossain, I. M.; Fassl, P.; Nejand, B. A.; Abzieher, T.; Schultes, M.; Ahlswede, E.; Jackson, P.; Powalla, M.; Schäfer, S.; et al. 2D/3D Heterostructure for Semitransparent Perovskite Solar Cells with Engineered Bandgap Enables

Efficiencies Exceeding 25% in Four-Terminal Tandems with Silicon and CIGS. *Adv. Funct. Mater.* **2020**, *30* (19), 1909919.

(27) Gharibzadeh, S.; Abdollahi Nejand, B.; Jakoby, M.; Abzieher, T.; Hauschild, D.; Moghadamzadeh, S.; Schwenzer, J. A.; Brenner, P.; Schmager, R.; Haghighirad, A. A.; et al. Record Open-Circuit Voltage Wide-Bandgap Perovskite Solar Cells Utilizing 2D/3D Perovskite Heterostructure. *Adv. Energy Mater.* **2019**, *9* (21), 1803699.

(28) Sutanto, A. A.; Szostak, R.; Drigo, N.; Queloz, V. I. E.; Marchezi, P. E.; Germino, J. C.; Tolentino, H. C. N.; Nazeeruddin, M. K.; Nogueira, A. F.; Grancini, G. In Situ Analysis Reveals the Role of 2D Perovskite in Preventing Thermal-Induced Degradation in 2D/3D Perovskite Interfaces. *Nano Lett.* **2020**, *20* (5), 3992-3998.

(29) Grancini, G.; Roldán-Carmona, C.; Zimmermann, I.; Mosconi, E.; Lee, X.; Martineau, D.; Narbey, S.; Oswald, F.; De Angelis, F.; Graetzel, M.; et al. One-Year Stable Perovskite Solar Cells by 2D/3D Interface Engineering. *Nat. Commun.* **2017**, *8*, 1-8.

(30) Schlipf, J.; Hu, Y.; Pratap, S.; Bießmann, L.; Hohn, N.; Porcar, L.; Bein, T.; Docampo, P.; Müller-Buschbaum, P. Shedding Light on the Moisture Stability of 3D/2D Hybrid Perovskite Heterojunction Thin Films. *ACS Appl. Energy Mater.* **2019**, *2* (2), 1011-1018.

(31) Yuan, M.; Quan, L. N.; Comin, R.; Walters, G.; Sabatini, R.; Voznyy, O.; Hoogland, S.; Zhao, Y.; Beauregard, E. M.; Kanjanaboos, P.; et al. Perovskite Energy Funnels for Efficient Light-Emitting Diodes. *Nat. Nanotechnol.* **2016**, *11* (10), 872-877.

(32) Li, T.; Zeidell, A. M.; Findik, G.; Dunlap-Shohl, W. A.; Euvrard, J.; Gundogdu, K.; Jurchescu, O. D.; Mitzi, D. B. Phase-Pure Hybrid Layered Lead Iodide Perovskite Films Based on a Two-Step Melt-Processing Approach. *Chem. Mater.* **2019**, *31* (11), 4267-4274.

(33) Liang, C.; Gu, H.; Xia, Y.; Wang, Z.; Liu, X.; Xia, J.; Zuo, S.; Hu, Y.; Gao, X.; Hui, W.; et al. Two-Dimensional Ruddlesden–Popper Layered Perovskite Solar Cells Based on Phase-Pure Thin Films. *Nat. Energy* **2020**, *6*, 38-4.

(34) Rolston, N.; Bush, K. A.; Printz, A. D.; Gold-Parker, A.; Ding, Y.; Toney, M. F.; McGehee, M. D.; Dauskardt, R. H. Engineering Stress in Perovskite Solar Cells to Improve Stability. *Adv. Energy Mater.* **2018**, *8* (29), 1-7.

(35) Bush, K. A.; Rolston, N.; Gold-Parker, A.; Manzoor, S.; Hausele, J.; Yu, Z. J.; Raiford, J. A.; Cheacharoen, R.; Holman, Z. C.; Toney, M. F.; et al. Controlling Thin-Film Stress and Wrinkling during Perovskite Film Formation. *ACS Energy Lett.* **2018**, *3* (6), 1225-1232.

(36) Kennard, R. M.; Dahlman, C. J.; DeCrescent, R. A.; Schuller, J. A.; Mukherjee, K.; Seshadri, R.; Chabinyc, M. L. Ferroelastic Hysteresis in Thin Films of Methylammonium Lead Iodide. *Chem. Mater.* **2021**, *33*, 298-309.

(37) Steele, J. A.; Jin, H.; Dovgaliuk, I.; Berger, R. F.; Braeckevelt, T.; Yuan, H.; Martin, C.; Solano, E.; Lejaeghere, K.; Rogge, S. M. J.; et al. Thermal Unequilibrium of Strained Black $CsPbI_3$ Thin Films. *Science* **2019**, *365(6454)*, 679-684.

(38) Zhu, C.; Niu, X.; Fu, Y.; Li, N.; Hu, C.; Chen, Y.; He, X.; Na, G.; Liu, P.; Zai, H.; et al. Strain Engineering in Perovskite Solar Cells and Its Impacts on Carrier Dynamics. *Nat. Commun.* **2019**, *10* (1), 1-11.

(39) Jones, T. W.; Osherov, A.; Alsari, M.; Sponseller, M.; Duck, B. C.; Jung, Y.-K.; Settens, C.; Niroui, F.; Brenes, R.; Stan, C. V.; et al. Lattice strain causes non-radiative losses in halide perovskites. *Energy & Environmental Science*, **2019**, *12(2*), 596-606.

(40) Tu, Q.; Spanopoulos, I.; Hao, S.; Wolverton, C.; Kanatzidis, M. G.; Shekhawat, G. S.; Dravid, V. P. Probing Strain-Induced Band Gap Modulation in 2D Hybrid Organic-Inorganic Perovskites. *ACS Energy Lett.* **2019**, *4* (3), 796-802.

(41) Zhou, M.; Fei, C.; Sarmiento, J. S.; Wang, H. Manipulating the Phase Distributions and Carrier Transfers in Hybrid Quasi-Two-Dimensional Perovskite Films. *Sol. RRL* **2019**, *3* (4), 1-9.

(42) Venkatesan, N. R.; Kennard, R. M.; DeCrescent, R. A.; Nakayama, H.; Dahlman, C. J.; Perry, E. E.; Schuller, J.; Chabinyc, M. L. Phase Intergrowth and Structural Defects in Organic Metal Halide Ruddlesden–Popper Thin Films. *Chem. Mater.* **2018**, *30*, 8615-8623.

(43) Tan, W. L.; Cheng, Y. B.; McNeill, C. R. Direct Assessment of Structural Order and Evidence for Stacking Faults in Layered Hybrid Perovskite Films from X-Ray Scattering Measurements. *J. Mater. Chem. A* **2020**, *8* (25), 12790-12798.

(44) Blancon, J. C.; Tsai, H.; Nie, W.; Stoumpos, C. C.; Pedesseau, L.; Katan, C.; Kepenekian, M.; Soe, C. M. M.; Appavoo, K.; Sfeir, M. Y.; et al. Extremely Efficient Internal Exciton Dissociation through Edge States in Layered 2D Perovskites. *Science* **2017**, *355* (6331), 1288-1292.

(45) Dahlman, C. J.; Decrescent, R. A.; Venkatesan, N. R.; Kennard, R. M.; Wu, G.; Everest, M. A.; Schuller, J. A.; Chabinyc, M. L. Controlling Solvate Intermediate Growth for Phase-Pure Organic Lead Iodide Ruddlesden-Popper $(C_4H_9NH_3)_2(CH_3NH_3)_{n-1}Pb_nI_{3n+1}$ Perovskite Thin Films. *Chem. Mater.* **2019**, *31* (15), 5832-5844.

(46) Quintero-Bermudez, R.; Gold-Parker, A.; Proppe, A. H.; Munir, R.; Yang, Z.; Kelley, S. O.; Amassian, A.; Toney, M. F.; Sargent, E. H. Compositional and Orientational Control in Metal Halide Perovskites of Reduced Dimensionality. *Nat. Mater.* **2018**, *17* (10), 900-907.

(47) Hoffman, J. M.; Strzalka, J.; Flanders, N. C.; Hadar, I.; Cuthriell, S. A.; Zhang, Q.; Schaller, R. D.; Dichtel, W. R.; Chen, L. X.; Kanatzidis, M. G. In Situ Grazing-Incidence Wide-Angle Scattering Reveals Mechanisms for Phase Distribution and Disorientation in 2D Halide Perovskite Films. *Adv. Mater.* **2020**, *32* (33), 1-8.

(48) Luo, S. Q.; Wang, J. F.; Yang, B.; Yuan, Y. B. Recent Advances in Controlling the Crystallization of Two-Dimensional Perovskites for Optoelectronic Device. *Front. Phys.* **2019**, *14* (5), 1-17.

(49) Shi, E.; Deng, S.; Yuan, B.; Gao, Y.; Akriti; Yuan, L.; Davis, C. S.; Zemlyanov, D.; Yu, Y.; Huang, L.; et al. Extrinsic and Dynamic Edge States of Two-Dimensional Lead Halide Perovskites. *ACS Nano* **2019**, *13* (2), 1635-1644.

(50) Kieslich, G.; Sun, S.; Cheetham, A. K. An Extended Tolerance Factor Approach for Organic-Inorganic Perovskites. *Chem. Sci.* **2015**, *6* (6), 3430-3433.

(51) Becker, M.; Klüner, T.; Wark, M. Formation of Hybrid ABX3 Perovskite Compounds for Solar Cell Application: First-Principles Calculations of Effective Ionic Radii and Determination of Tolerance Factors. *Dalt. Trans.* **2017**, *46* (11), 3500-3509.

(52) Yoon, S. J.; Stamplecoskie, K. G.; Kamat, P. V. How Lead Halide Complex Chemistry Dictates the Composition of Mixed Halide Perovskites. *J. Phys. Chem. Lett.* **2016**, *7* (7), 1368-1373.

(53) Venkatesan, N. R.; Labram, J. G.; Chabinyc, M. L. Charge-Carrier Dynamics and Crystalline Texture of Layered Ruddlesden-Popper Hybrid Lead Iodide Perovskite

Thin Films. *ACS Energy Lett.* **2018**, *3* (2), 380-386.

(54) Mooney, J.; Kambhampati, P. Get the Basics Right: Jacobian Conversion of Wavelength and Energy Scales for Quantitative Analysis of Emission Spectra. *J. Phys. Chem. Lett.* **2013**, *4* (19), 3316-3318.

(55) Schotz, K.; Abdelrahman, M. A.; Peng, W.; Seeberger, D.; Gujar, T. P.; Thelakkat, M.; Kohler, A.; Huettner, S.; Bakr, O. M.; Shankar, K.; et al. Double Peak Emission in Lead Halide Perovskites by Self-Absorption. *J. Mater. Chem. C* **2020**, *8*, 2289-2300.

(56) Messerschmidt, S.; Krampf, A.; Freytag, F.; Imlau, M.; Vittadello, L.; Bazzan, M.; Corradi, G. The Role of Self-Trapped Excitons in Polaronic Recombination Processes in Lithium Niobate. *J. Phys. Condens. Matter* **2019**, *31* (6), 065701.

(57) Sheikh, T.; Shinde, A.; Mahamuni, S.; Nag, A. Possible Dual Bandgap in $(C_4H_9NH_3)_2PbI_4$ 2D Layered Perovskite: Single-Crystal and Exfoliated Few-Layer. *ACS Energy Lett.* **2018**, *3* (12), 2940-2946.

(58) Li, Q.; Chen, Z.; Li, M.; Xu, B.; Han, J.; Luo, Z.; Tan, L.; Xia, Z.; Quan, Z. Pressure-Engineered Photoluminescence Tuning in Zero-Dimensional Lead Bromide Trimer Clusters. *Angew. Chemie - Int. Ed.* **2021**, *60* (5), 2583-2587.

(59) Tu, Q.; Spanopoulos, I.; Hao, S.; Wolverton, C.; Kanatzidis, M. G.; Shekhawat, G. S.; Dravid, V. P. Out-of-Plane Mechanical Properties of 2D Hybrid Organic-Inorganic Perovskites by Nanoindentation. *ACS Appl. Mater. Interfaces* **2018**, *10* (26), 22167-22173.

(60) Feng, J. Mechanical Properties of Hybrid Organic-Inorganic $CH_3NH_3BX_3$ (B = Sn, Pb; X = Br, I) Perovskites for Solar Cell Absorbers. *APL Mater.* **2014**, *2* (8), 081801.

(61) Stoumpos, C. C.; Cao, D. H.; Clark, D. J.; Young, J.; Rondinelli, J. M.; Jang, J. I.; Hupp, J. T.; Kanatzidis, M. G. Ruddlesden-Popper Hybrid Lead Iodide Perovskite 2D Homologous Semiconductors. *Chem. Mater.* **2016**, *28* (8), 2852–2867.

(62) Mao, W.; Zheng, J.; Zhang, Y.; Chesman, A. S. R.; Ou, Q.; Hicks, J.; Li, F.; Wang, Z.; Graystone, B.; Bell, T. D. M.; et al. Controlled Growth of Monocrystalline Organo-Lead Halide Perovskite and Its Application in Photonic Devices. *Angew. Chemie - Int. Ed.* **2017**, *56* (41), 12486-12491.

(63) Gholipour, S.; Ali, A. M.; Correa-Baena, J. P.; Turren-Cruz, S. H.; Tajabadi, F.; Tress, W.; Taghavinia, N.; Grätzel, M.; Abate, A.; De Angelis, F.; et al. Globularity-Selected Large Molecules for a New Generation of Multication Perovskites. *Adv. Mater.* **2017**, *29* (38), 1-9.

(64) Mittal, M.; Jana, A.; Sarkar, S.; Mahadevan, P.; Sapra, S. Size of the Organic Cation Tunes the Band Gap of Colloidal Organolead Bromide Perovskite Nanocrystals. *J. Phys. Chem. Lett.* **2016**, *7* (16), 3270-3277.

(65) Fu, Y.; Hautzinger, M. P.; Luo, Z.; Wang, F.; Pan, D.; Aristov, M. M.; Guzei, I. A.; Pan, A.; Zhu, X.; Jin, S. Incorporating Large A Cations into Lead Iodide Perovskite Cages: Relaxed Goldschmidt Tolerance Factor and Impact on Exciton-Phonon Interaction. *ACS Cent. Sci.* **2019**, *5* (8), 1377-1386.

(66) Goldschmidt, V. V. Die Gesetze Der Krystallochemie. *Naturwissenschaften* **1926**, *14*, 477-485.

(67) Yantara, N.; Bruno, A.; Iqbal, A.; Jamaludin, N. F.; Soci, C.; Mhaisalkar, S.; Mathews, N. Designing Efficient Energy Funneling Kinetics in Ruddlesden–Popper Perovskites for High-Performance Light-Emitting Diodes. *Adv. Mater.* **2018**, *30* (33), 1-7.

4.7 Appendix to Chapter 4

Calculation of Tolerance Factors

Tolerance factors *t* were calculated using ion sizes in [6,7] and using the equation: [8]

$$t = \frac{r_A + r_X}{\sqrt{2}(r_B + r_X)}$$

Where r_A, r_B and r_X are the ion radii of the ABX_3 structure. **Table 4.1** below shows the ion radii used in pm, and the resulting *t*s:

A (EA, MA)	**Pb**	**Br or I**	***t***
274 (EA)	98	196 (Br)	1.13
217 (MA)	98	196 (Br)	0.99
217 (MA)	103	220 (I)	0.96

Fitting the PDS Data

Following previous work, [9,10] the Urbach tails were fit according to:

$$PDS = A\ exp\left(\frac{E - E_G}{E_U}\right)$$

Where PDS is the PDS signal from **Figure 4.5**, where A is a prefactor, E_G is the bandgap and E_U is the Urbach energy.

Further Explanations regarding Strain

Prior work on 1-dimensional Pb-Br compounds found that the broad emission intensity sharply decreased with respect to the free exciton emission when 0.5 GPa of pressure (or stress) was applied. [11] The proposed mechanism for this was that under stress, the bond lengths and angles become closer to those of the ideal cubic $MAPbB_3$. [11] While the directional Young's modulus of $(EA)_2(EA)_2Pb_3Br_{10}$ is not known, we can estimate that it is between the values for $(BA)_2(MA)_2Pb_3Br_{10}$ and $MAPbBr_3$, or $4\ \mathrm{GPa} < E < 30\ \mathrm{GPa}$. [12,13] In terms of strain, these stress values correspond to $12.5\ \% > \varepsilon > 1.7\ \%$, using the simple stress-strain relationship $\sigma = E\varepsilon$. Although these values represent a broad, range, it is reasonable that the strain values measured in **Figure 4.2** could be big enough to cause emission changes.

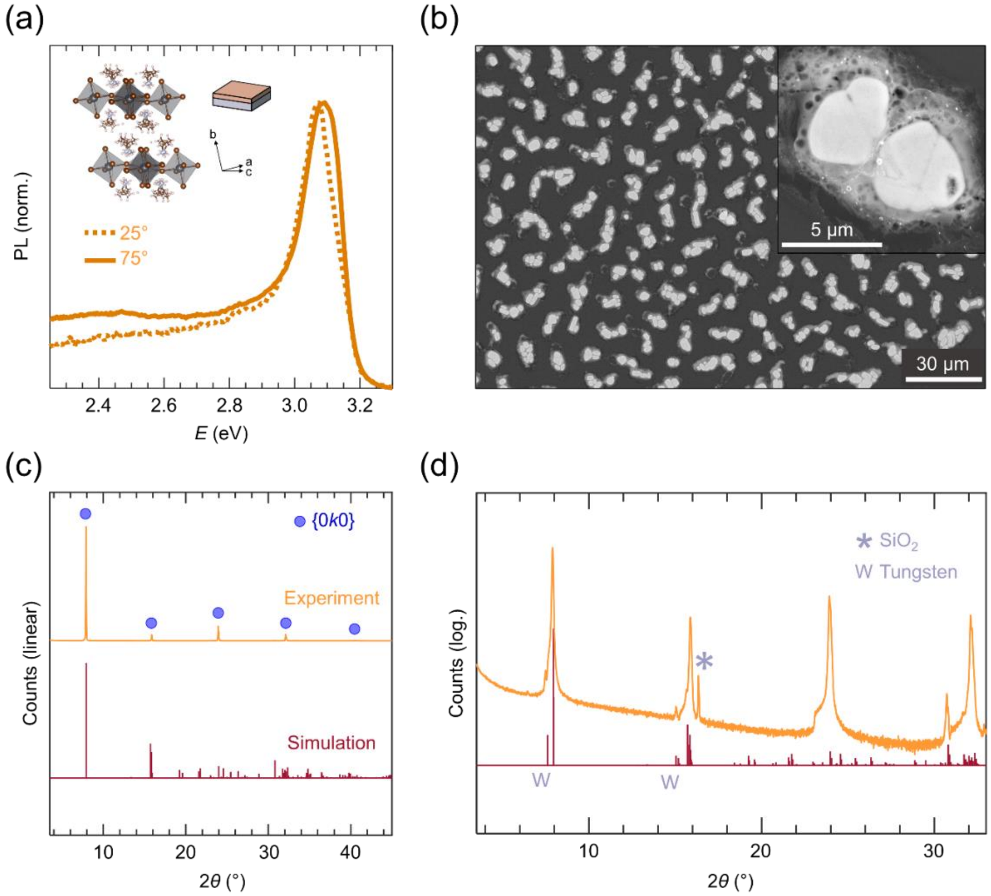

Figure 4.S1. Characterization of $(EA)_2PbBr_4$ (n = 1) films. (a) Photoluminescence emission (3.94 eV excitation) at 25- and 75-degree collection angles. (b) Scanning Electron Microscopy of an n = 1 film. XRD patterns plotted on (c) linear and (d) log scales. A simulated pattern of $(EA)_2PbBr_4$ assuming no preferred crystallite orientation, and based on the published structure, is shown as well. [14] The copper X-Ray source has tungsten contamination (1.4764 Å), resulting in occasional extra peaks. The simulation in (d) shows the extra peaks from Tungsten-X-Rays as well.

The films appear to be $(EA)_2PbBr_4$ from X-Ray characterization. The crystallites seem to orient with the long b axis normal to the substrate, as evidenced by the strong diffraction from $(0k0)$ peaks. The photoluminescence emission energies match well those of published crystals. [14] However, as with $(EA)_2(EA)_2Pb_3Br_{10}$, the broad emission is considerably weakened in favor of the free exciton emission. The large size of $(EA)_2PbBr_4$ suggests that grain size is not the only contributor to this emission change. Other potential factors (e.g., growth kinetics, strain) are discussed in the main text.

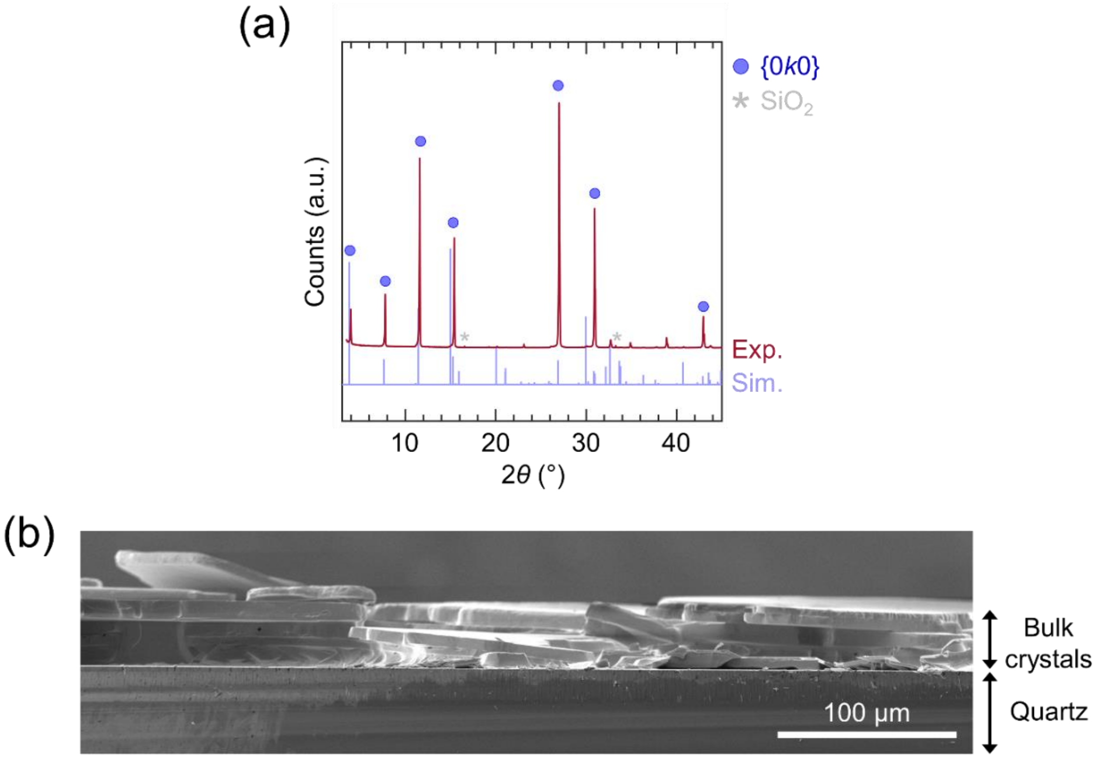

Figure 4.S2. (a) Experimental XRD pattern of bulk crystals of $(EA)_2(EA)_2Pb_3Br_{10}$ made following previously-published methods. [1] A simulated (Sim.) powder pattern made using the published crystal structure [1] is also shown below (calculated assuming no preferred crystallite orientation). The crystals were dropped onto quartz substrates, and seem to preferentially orient with $(0k0)$ parallel to the substrate, given the predominance of $(0k0)$ observed in the pattern. Quartz peaks are indicated with an asterisk. (b) Cross-sectional SEM of the bulk crystals, revealing thickness > 10 microns.

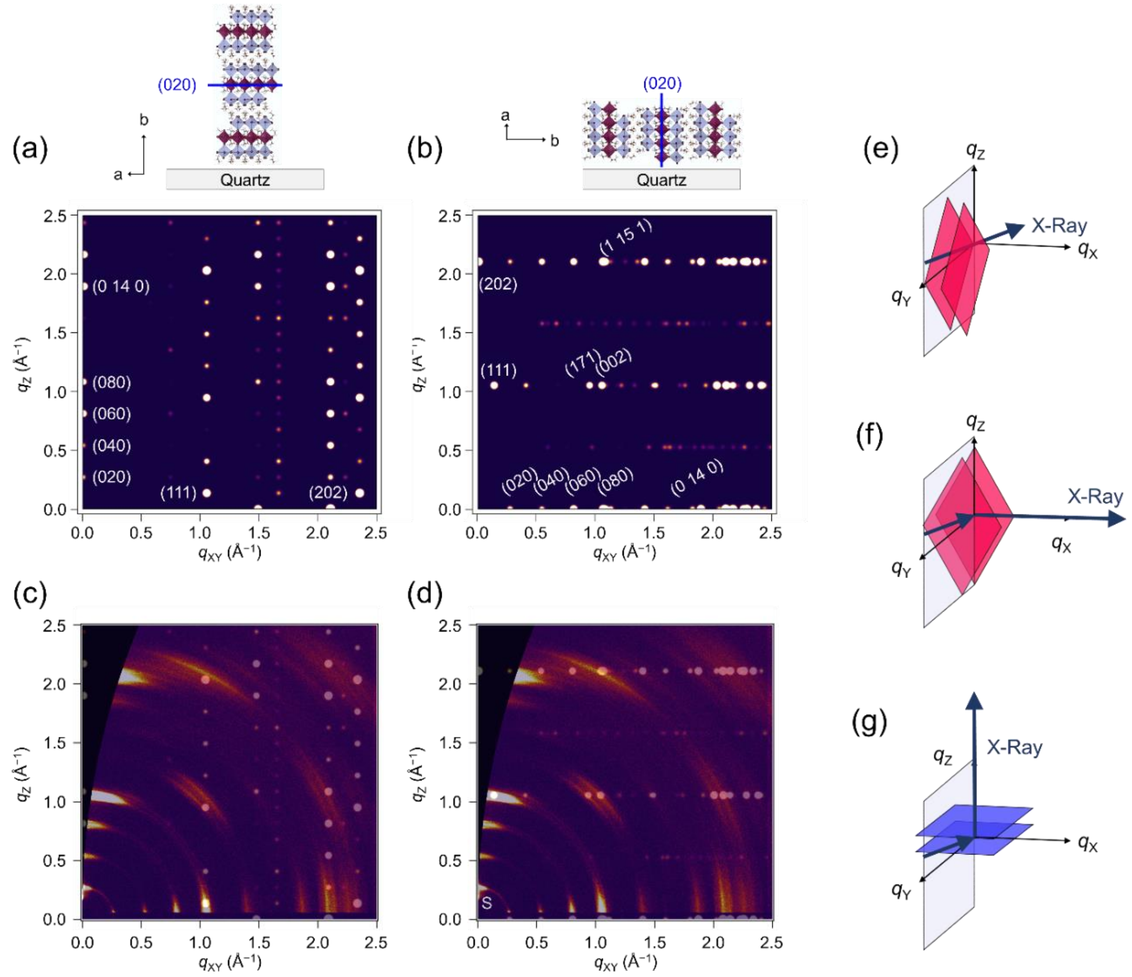

Figure 4.S3. Simulated GIWAXS pattern of (EA)$_2$(EA)$_2$Pb$_3$Br$_{10}$ assuming (a) full out-of-plane crystallite orientation and (b) full in-plane crystallite orientation. Out-of-plane- and in-plane-oriented crystallites are shown above the simulated pattern, with the (020) plane for reference. Main peaks are indexed. For simulations, the cif file from prior published work was used. [1] (c)-(d) Overlay of these simulated patterns with the experimental (EA)$_2$(EA)$_2$Pb$_3$Br$_{10}$ GIWAXS film pattern from **Figure 4.2**, with main peaks indexed. S indicates spillover from the undiffracted beam. (e)-(g) Diffraction or lack thereof for planes (e) aligned along q_Y (lack of diffraction), (f) aligned along q_X (diffraction) and (g) aligned along q_Z (diffraction). Diffraction peaks in q_{XY} are less intense than those in q_Z because a smaller fraction of planes in q_{XY} are probed; whereas all planes in q_Z are probed.

The main peaks of the experimental pattern matched with those of the simulated patterns. The (0*k*0), (111) and (202) peaks in the experimental pattern matched well with their expected locations in-plane and out-of-plane (**Figure 4.S3c-d**). This agreement confirmed the presence of the two preferred crystallite orientations. In order to assign off-axis peaks (i.e., not along q_Z, or q_{XY}), we overlaid the simulated patterns for crystallites with out-of-plane and in-plane orientation with the experimental GIWAXS pattern of **Figure 4.2**. Particularly good agreement for off-axis peaks was found when the crystallites have in-plane orientation (**Figure 4.S3d**), suggesting a greater proportion of in-plane-oriented crystallites. Geometric factors, explained in the caption and in **Figure 4.S3e-g**, cause greater probing of peaks in q_Z than in q_{XY}, which likely explains why the $(0k0)$ peaks along q_Z appear more intense than those along q_{XY}. In addition, due to the similar location of different peaks (especially near q_Z, $q_{XY} = 1$ or 2), some peaks may have several possible assignments. Some of the higher-order peaks (i.e., peaks near q_Z and $q_{XY} = 2.5$) were weaker in the experimental pattern than in the simulations. This is due to two reasons: 1) the film is both thin and disordered (strain, two crystallite orientations), so higher-order peaks are weakened and 2) the simulation took only structure factors into account, and no other factors such as Debye-Waller, which make higher-order peaks weaker. Overall, the experimental GIWAXS pattern matched well the simulated GIWAXS patterns, particularly for in-plane crystallite orientation.

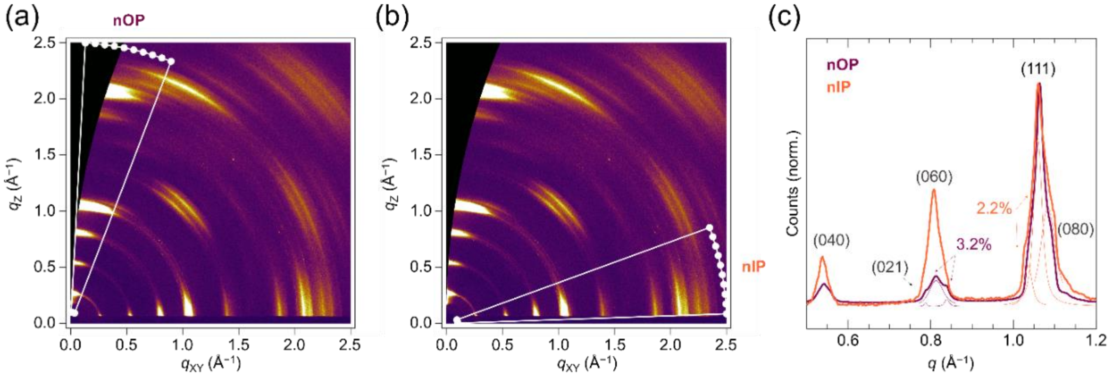

Figure 4.S4. (a) Near-out-of-plane (nOP) and (b) near-in-plane (nIP) regions used to obtain the patterns in **Figure 4.2d.** The nOP region covers angles between 3° and 21° and the nIP region covers angles between 70° and 88°. Both sections were chosen to have equal angular spread of 18°. (c) Integrated and normalized nOP and nIP patterns, with relative % strain of select peaks. Peak fits are also shown.

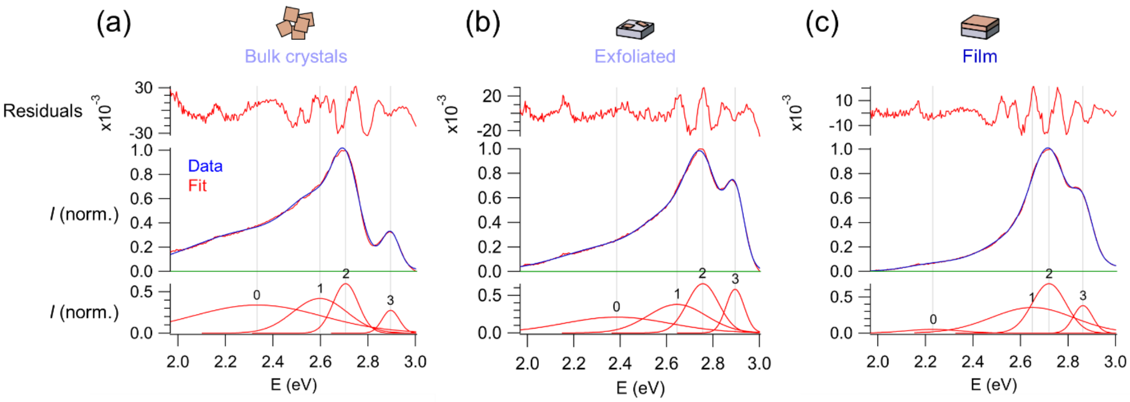

Figure 4.S5 Photoluminescence emission of bulk crystals, exfoliated flakes, film of $(EA)_4Pb_3Br_{10}$ (see **Figure 4.3** and **Figure 4.S10**). All spectra were fit to multiple Gaussians using Igor Pro 8. All measurements were performed with an excitation wavelength of 370 nm (3.35 eV - see **Experimental Section**).

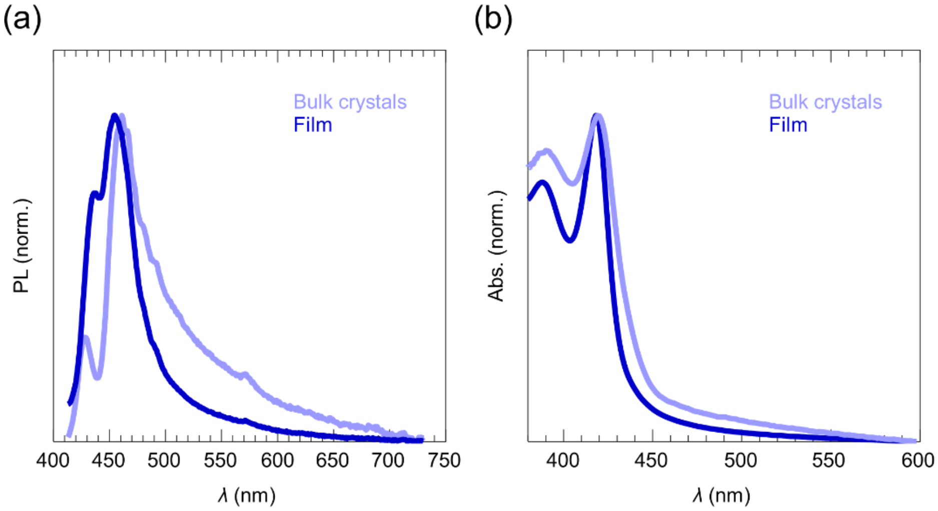

Figure 4.S6. (a) Photoluminescence emission and (b) absorbance of spin-cast films and powders of $(EA)_2(EA)_2Pb_3Br_{10}$ from **Figure 4.3**, shown here in nm (excitaiton 3.35 eV; 370 nm).

The optical data were collected in nm and converted to eV. For emission spectra, a Jacobian transformation [15] was applied to the intensities:

$$Intensity_{Converted} = \frac{1240 \times Intensity_{Collected}}{Energy^2}$$

Where $Intensity_{Converted}$ is the PL intensity of the plot in eV, $Intensity_{Collected}$ is the PL intensity of the plot in nm, and $Energy$ is 1240/wavelength.

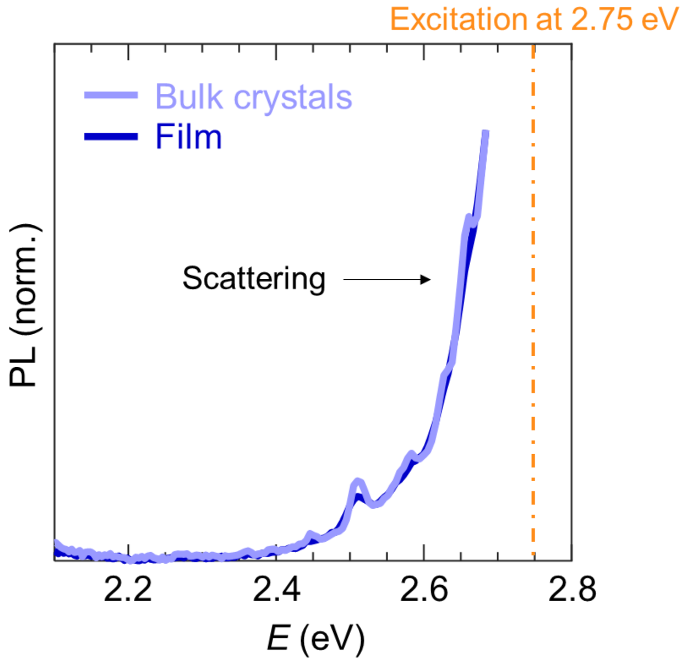

Figure 4.S7. Photoluminescence emission (75-degree collection angle) of $(EA)_2(EA)_2Pb_3Br_{10}$ bulk crystals and film. The excitation was selected to be 2.75 eV to verify that broad emission only occurs when exciting the material above the absorption edge. Despite use of a long-pass filter, some scattering was observed in all samples characterized in this study at energies closest to the excitation energy, most noticeably when no (or little) photoluminescence was present in the sample. Here, the only signal observed was this scattering, confirming that sub-onset excitation does not produce broad emission.

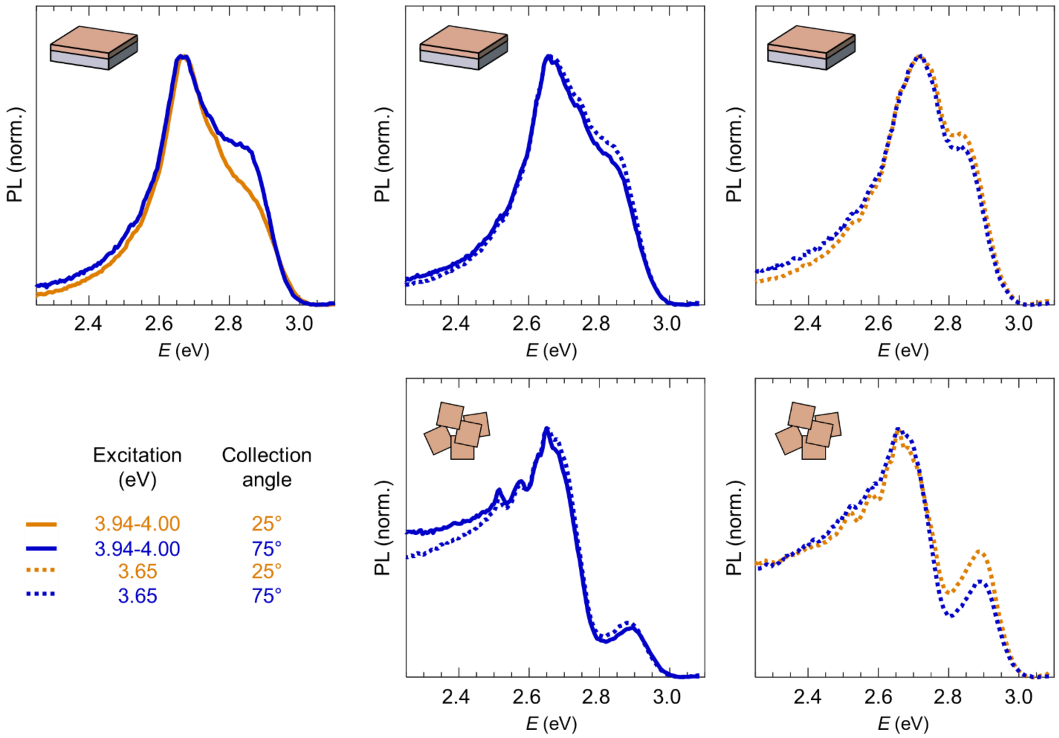

Figure 4.S8. Changes (or lack thereof) in emission in films and bulk crystals of $(EA)_2(EA)_2Pb_3Br_{10}$ with excitation energy and/or collection angle. Although some variations in the free exciton: broad emission proportions were observed when changing angle and/or excitation, the films consistently had a greater proportion of free exciton emission, and the bulk crystals consistently had a greater proportion of broad emission.

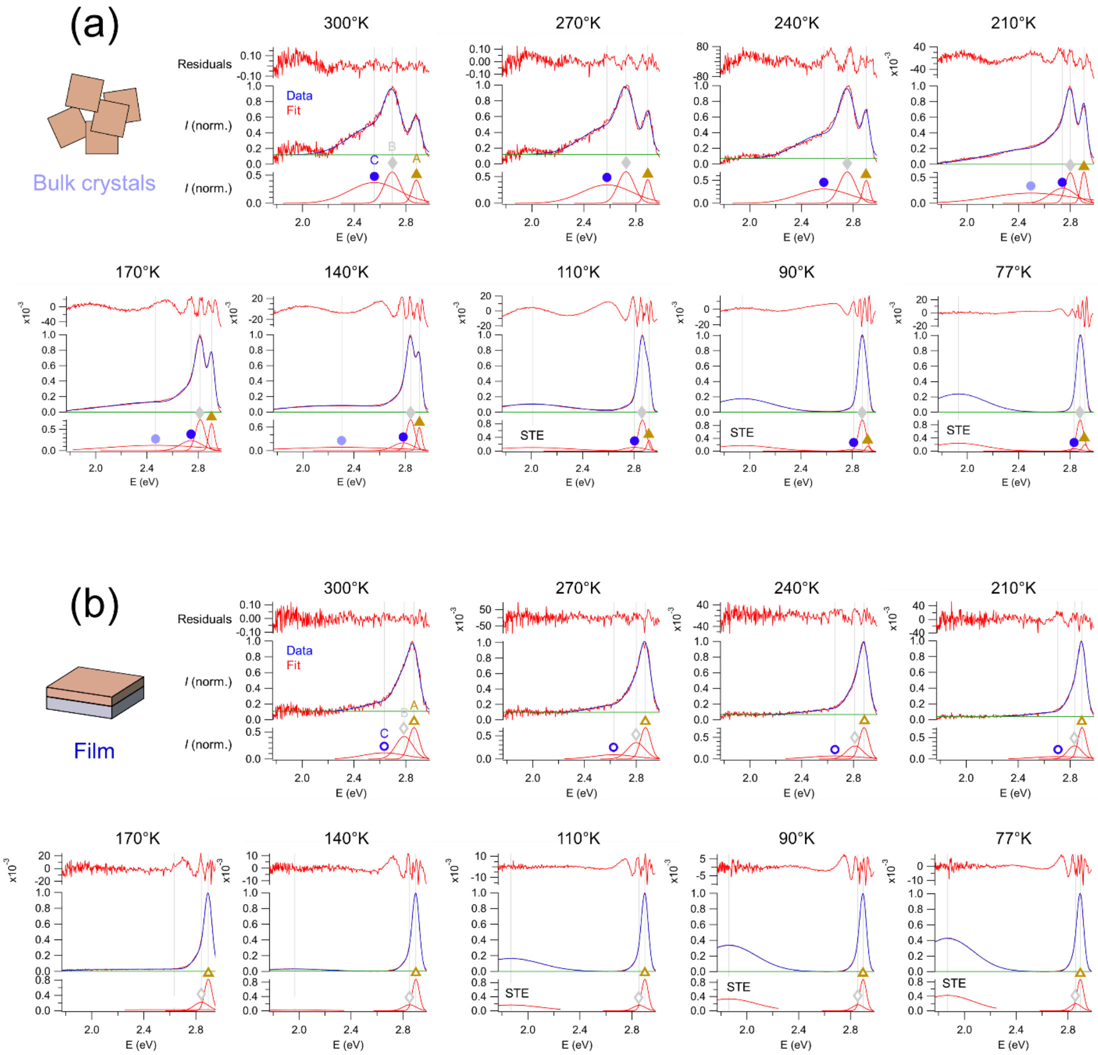

Figure 4.S9. Temperature-dependent photoluminescence emission of the (a) bulk crystals and (b) film of (EA)$_4$Pb$_3$Br$_{10}$ (see **Figure 4.4**). All spectra were fit to multiple Gaussians. Measurements were performed with an excitation wavelength of 370 nm (3.35 eV), using a pulsed laser (see **Experimental Section**).

In the low-energy region, either one or two Gaussians were needed to fit peak C, and this variation likely arose from variations in measurement conditions across different instruments (e.g., angles of 75° vs. 45° between the excitation and emission port in different instruments, different detector sensitivities in different instruments, etc.). Various fitting methods were investigated, such as increasing the number of Gaussians arbitrarily. However, the trends reported in **Figure 4.4** and **Figure 4.S9** remained the same. Because the second peak for C (lighter blue circle) broadens/flattens until disappearing, the peak position is uncertain, so it is not reported. For films, only one Gaussian was consistently needed to fit C.

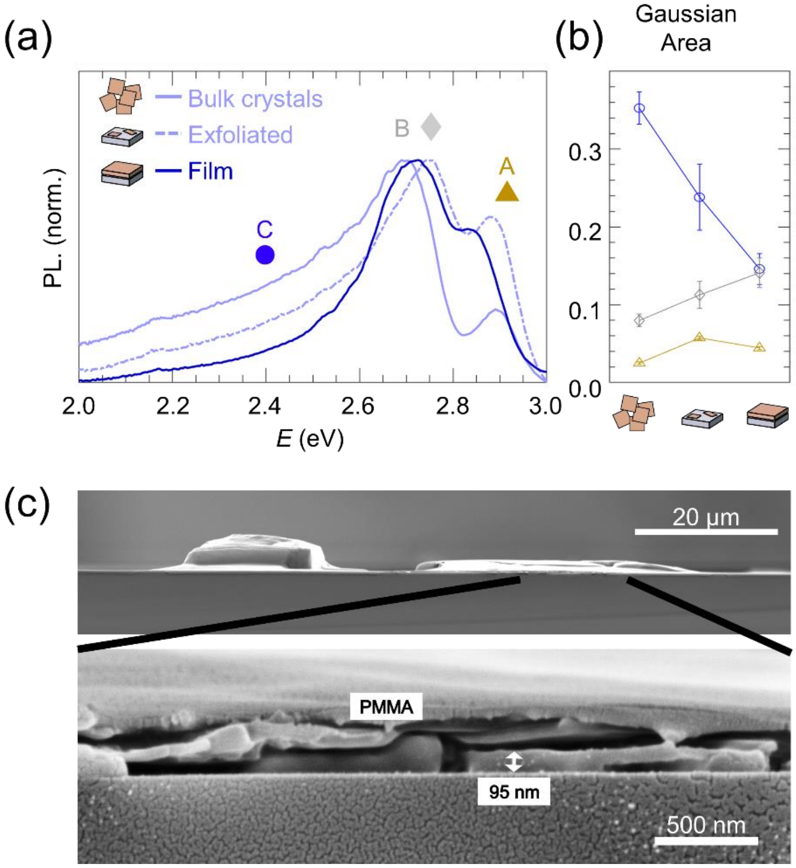

Figure 4.S10. (a) Comparison of the photoluminescence of exfoliated flakes with those of films and bulk crystals of $(EA)_4Pb_3Br_{10}$, taken under conditions identical to those for **Figure 4.3**. Exfoliated flakes of $(EA)_4Pb_3Br_{10}$ were prepared from bulk crystals via the standard scotch-tape method.[16,17] (b) Gaussian area of peaks A, B, and C. (c) Cross-sectional SEM of the exfoliated flakes on quartz, with a PMMA capping layer. The flake thickness was highly variable. The origins of differences in emission are discussed in the main text.

To examine how exfoliation may change emission from B and C, we exfoliated bulk crystals of $(EA)_4Pb_3Br_{10}$ (**Figure 4.S10**) and obtained a variety of thicknesses, with some as low as 95 nm. Photoluminescence emission of the ensemble average of these exfoliated flakes revealed that the flakes had intermediate behavior to the bulk crystals and films: the intensity of C was film < flakes < bulk, and the intensity of B was bulk < flakes < film. These differing trends suggest that B and C have different nature; i.e., one might be a phonon replica and the other, an STE. However, it is clear that the proportions of B and C both change with sample preparation. As discussed in the main text, exfoliation is not fully decoupled from strain, as mechanical exfoliation involves applying pressure to separate the sheets, and this may change the cation stacking.

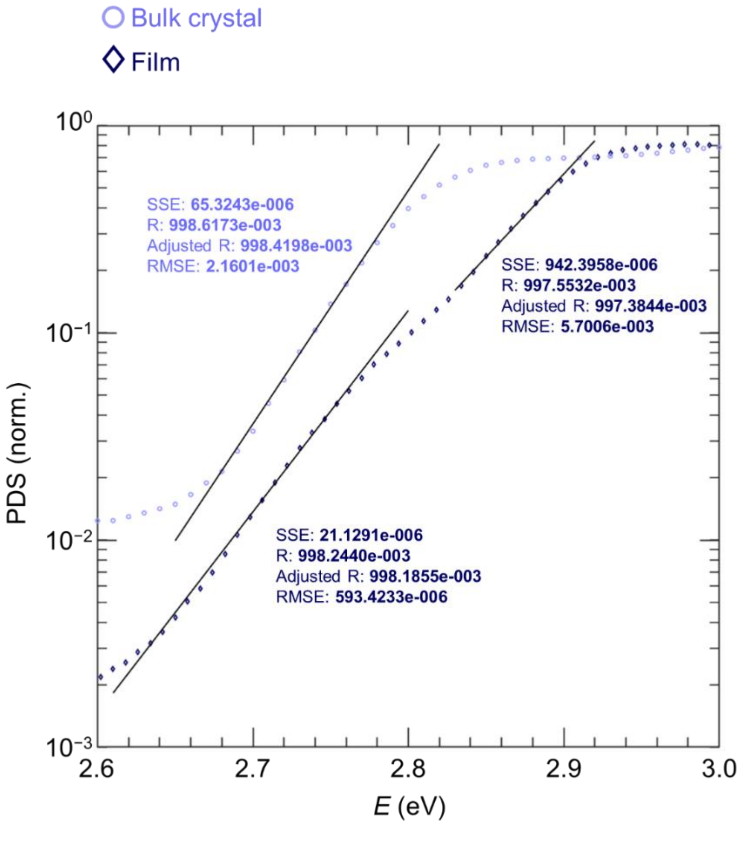

Figure 4.S11. PDS in the 2.6-3.0 eV region for the bulk crystal and film, with goodness of fit parameters from MATLAB: the sum of squares due to error (SSE), R-square (R), Adjusted R-square, and the Root mean squared error (RMSE).

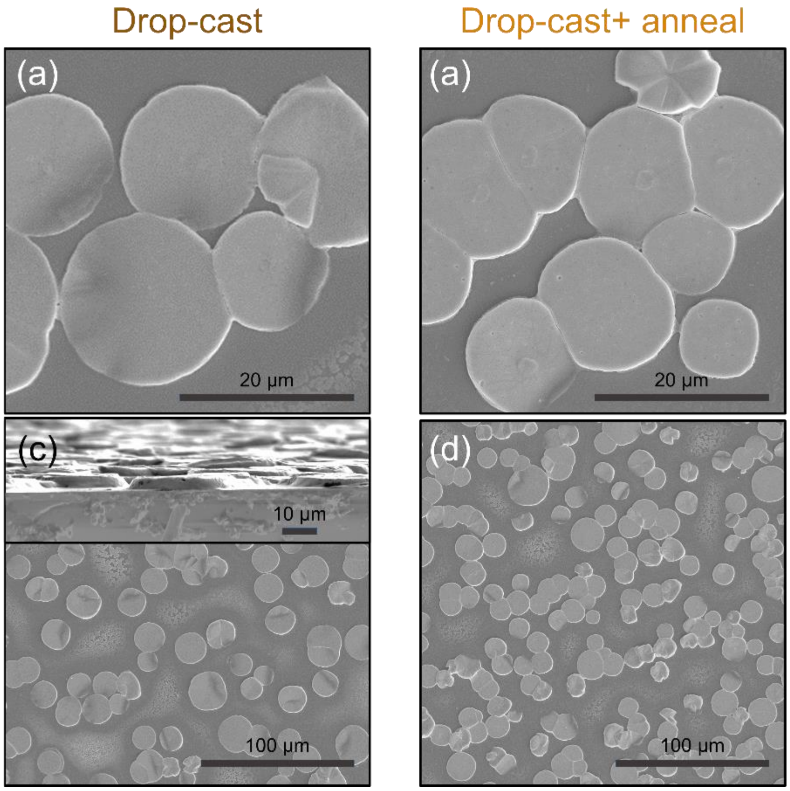

Figure 4.S12. SEM of the drop-cast films from **Figure 4.6**, with the inset of (c) showing a cross-section.

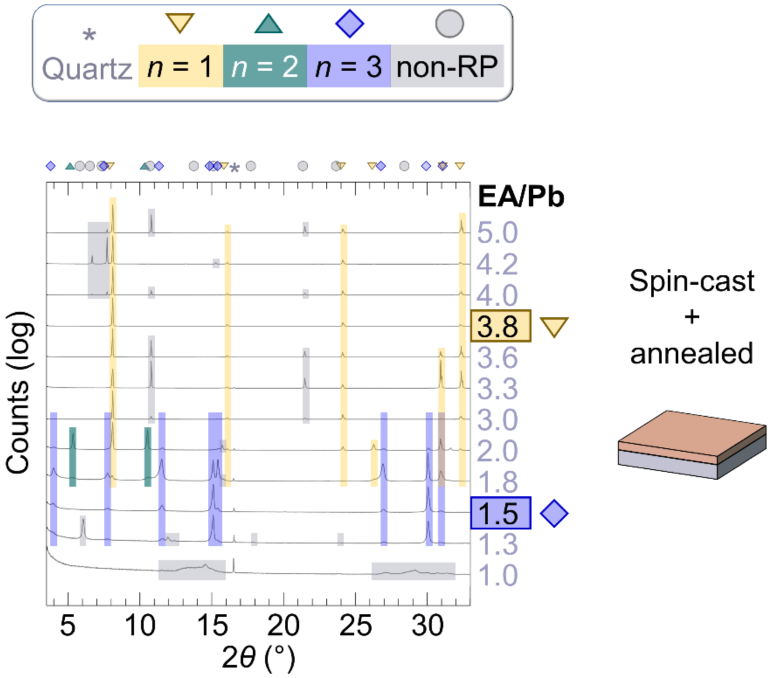

Figure 4.S13. XRD patterns of spin-cast and annealed films, for which the EA/Pb molar ratio of the precursor solutions was steadily increased. Only for EA/Pb = 1.5 and for EA/Pb = 3.8 were phase pure films obtained, and these were n = 3 and n = 1 films respectively. A slight excess of EA is thought to be needed for n = 3 film formation because Pb and Br form strong complexes with DMF. [18] However, the large excess of EA (nearly twice the stoichiometric amount) needed for the n = 1 film formation shows that n = 1 is not easily formed. No 3D film or phase was formed.

To further understand the limits of phase formation in the $(EA)_2(EA)_{n-1}Pb_nBr_{3n+1}$ family, we tried to make ethylammonium-based RP films of different n via spin-casting (**Figure 4.S13**). The molar ratio of EABr: $PbBr_2$ (EA/Pb for short) in the precursor solutions was steadily increased from 1.0 ($EAPbBr_3$ 3D stoichiometry) to 3.8 (nearly twice the n = 1 $(EA)_2PbBr_4$ stoichiometry). For EA/Pb = 1.0, which corresponds stoichiometrically to $EAPbB_3$, we obtained broad peaks, likely indicating an amorphous phase (the film was also non-emissive). In addition, no 3D-like phase was conclusively observed in any of the EA compositions tested. Despite the large range of EA/Pb molar ratios tested, only the n = 1 and n = 3 compositions could be cast as phase-pure films.

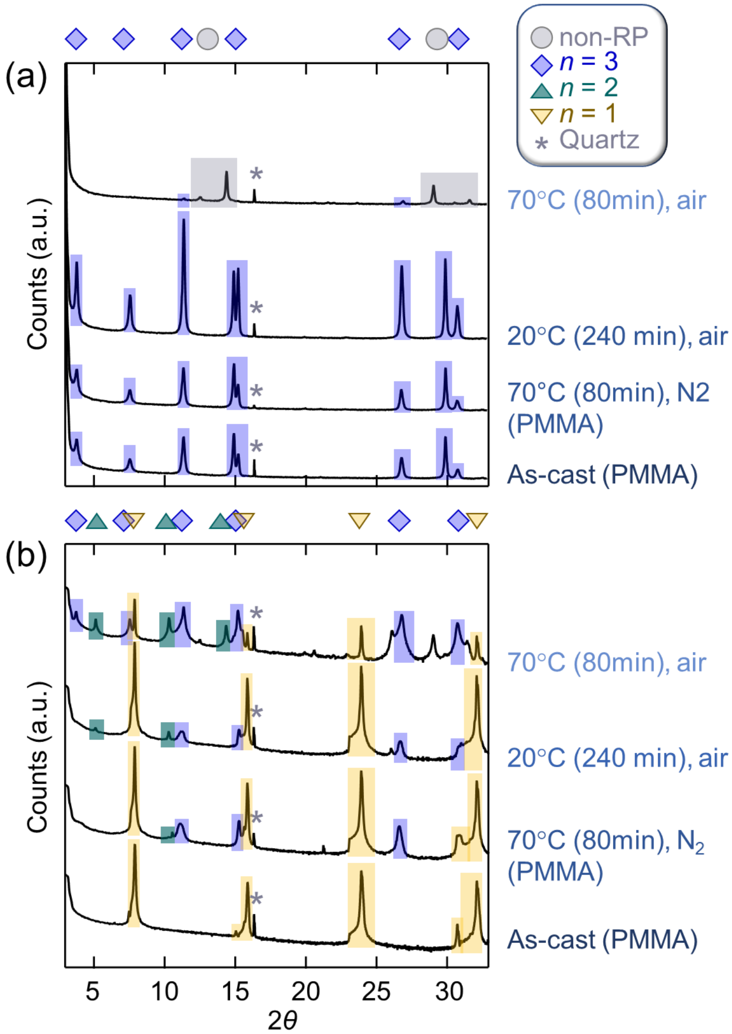

Figure 4.S14. XRD patterns under different stability testing conditions for (a) n = 3 and (b) n = 1 spin-cast films.

We examined the stability of n = 1 and n = 3 spin-cast films, in order to better understand which phases are thermodynamically favorable (**Figure 4.S14**), and summarized the results in **Scheme 4.1.** Films were spin-cast with or without the PMMA capping layer. Four testing conditions were employed, to test stability to heat and air: (1) *control*: as-cast (with PMMA capping), (2) *heat test*: heating at 70°C in the glove box (nitrogen environment) for 80 min (with PMMA capping), (3) *air test*: storage in air at 20°C for 240 min (no PMMA capping) and (4) *heat and air test*: heating at 70°C in air for 80 min (no PMMA capping).

The *n* = 3 phase proved more thermodynamically stable than the *n* = 1 (**Figure 4.S14**). Heating encapsulated *n* = 3 films in a nitrogen environment produced no change in structure, indicating that *n* = 3 is thermodynamically stable under mild conditions. In contrast, this mild heating resulted in clear phase-change in the encapsulated *n* = 1. The novel peaks were tentatively assigned to *n* = 3 and *n* = 2, although the low number of non-*n* = 1 peaks made full assignment challenging. The greater thermodynamic stability of the *n* = 3 may help explain why it formed more favorably in films.

The *n* = 3 also appeared to be much more air-stable than the *n* = 1 (**Figure 4.S14**). Short, unencapsulated storage in air resulted in retention of the *n* = 3 phase, albeit with large peak intensity increase and out-of-plane (0*k*0) stacking preference. Humidity-induced increase in grain size has been previously reported for $MAPbI_3$; [19] it is possible that humidity caused recrystallization here as well. This rearrangement is encouraging, as it suggests that post-casting treatments could control film orientation for *n* = 3. In contrast, short, unencapsulated storage in air resulted in degradation of the *n* = 1 film. Finally, heating unencapsulated *n* = 3 and *n* = 1 films in air resulted in obvious degradation of both films, indicating that encapsulation will likely be necessary for ethylammonium RP device use. The originally-*n* = 3 film contained peaks near 14 and 29 degrees, perhaps indicating a 1D degradation product. Interestingly, the originally-*n* = 1 film now very clearly contained *n* = 3 as well as some *n* = 2, indicating that *n* = 3 is a degradation product *n* = 1. The *n* = 1 to *n* = 3 phase change in heated unencapsulated films also suggests that ethylammonium desorbed. Overall, the *n* = 3 EA RP was considerably more stable than the *n* = 1.

Further Discussion on 2D and 3D phases with the EA cation

Previous work that attempted to make films of 3D $EAPbBr_3$ found that a 2D phase formed instead. [20] Given the location of the XRD peaks of this film, it is likely that the n = 3 phase formed in the film in the prior study. [20] Perhaps the use of an antisolvent in prior work helped n = 3 phase formation, which might be otherwise hindered by excess of lead in the $EAPbBr_3$ solution stoichiometry. Another report claimed formation of $EAPbBr_3$ in nanocrystals. [21] However, the optical properties of the resulting nanocrystals matched $(EA)_4Pb_3Br_{10}$, and XRD data was not collected in the range characteristic for 2D phases (below $2\theta = 10°$), [21] suggesting that the nanocrystals might instead be $(EA)_4Pb_3Br_{10}$. However, EA can be incorporated into 3D phases, provided there is a small A-site cation (e.g. MA) that it can alloy with, to form $(EA,MA)PbBr_3$. [20]

References

(1) Mao, L.; Wu, Y.; Stoumpos, C. C.; Traore, B.; Katan, C.; Even, J.; Wasielewski, M. R.; Kanatzidis, M. G. Tunable White-Light Emission in Single-Cation-Templated Three-Layered 2D Perovskites $(CH_3CH_2NH_3)_4Pb_3Br_{10-x}Cl_x$. *J. Am. Chem. Soc.* **2017**, *139* (34), 11956-11963.

(2) GIXA Calculator for Penetration Depth (and Optical Properties) for X-rays https://gixa.ati.tuwien.ac.at/tools/penetrationdepth.xhtml (accessed Nov 9, 2020).

(3) Venkatesan, N. R.; Labram, J. G.; Chabinyc, M. L. Charge-Carrier Dynamics and Crystalline Texture of Layered Ruddlesden-Popper Hybrid Lead Iodide Perovskite Thin Films. *ACS Energy Lett.* **2018**, *3* (2), 380-386.

(4) Resel, R.; Bainschab, M.; Pichler, A.; DIngemans, T.; Simbrunner, C.; Stangl, J.; Salzmann, I. Multiple Scattering in Grazing-Incidence X-Ray Diffraction: Impact on Lattice-Constant Determination in Thin Films. *J. Synchrotron Radiat.* **2016**, *23* (3), 729-734.

(5) Vandewal, K.; Albrecht, S.; Hoke, E. T.; Graham, K. R.; Widmer, J.; Douglas, J. D.; Schubert, M.; Mateker, W. R.; Bloking, J. T.; Burkhard, G. F.; et al. Efficient Charge Generation by Relaxed Charge-Transfer States at Organic Interfaces. *Nat. Mater.* **2014**, *13* (1), 63-68.

(6) Kieslich, G.; Sun, S.; Cheetham, A. K. Solid-State Principles Applied to Organic–Inorganic Perovskites: New Tricks for an Old Dog. *Chem. Sci.* **2014**, *5* (12), 4712-4715.

(7) Becker, M.; Klüner, T.; Wark, M. Formation of Hybrid ABX3 Perovskite Compounds for Solar Cell Application: First-Principles Calculations of Effective Ionic Radii and Determination of Tolerance Factors. *Dalt. Trans.* **2017**, *46* (11), 3500-3509.

(8) Goldschmidt, V. V. Die Gesetze Der Krystallochemie. *Naturwissenschaften* **1926**, *14*, 477-485.

(9) Dow, J. D.; Redfield, D. Toward a Unified Theory of Urbach's Rule and Exponential Absorption Edges. *Phys. Rev. B* **1972**, *5* (2), 594-610.

(10) Dahlman, C. J.; Decrescent, R. A.; Venkatesan, N. R.; Kennard, R. M.; Wu, G.; Everest, M. A.; Schuller, J. A.; Chabinyc, M. L. Controlling Solvate Intermediate Growth for Phase-Pure Organic Lead Iodide Ruddlesden-Popper $(C_4H_9NH_3)_2(CH_3NH_3)_{n-1}Pb_nI_{3n+1}$ Perovskite Thin Films. *Chem. Mater.* **2019**, *31* (15), 5832-5844.

(11) Ma, Z.; Li, F.; Sui, L.; Shi, Y.; Fu, R.; Yuan, K.; Xiao, G.; Zou, B. Tunable Color Temperatures and Emission Enhancement in 1D Halide Perovskites under High Pressure. *Adv. Opt. Mater.* **2020**, *8* (18), 1-7.

(12) Tu, Q.; Spanopoulos, I.; Hao, S.; Wolverton, C.; Kanatzidis, M. G.; Shekhawat, G. S.; Dravid, V. P. Out-of-Plane Mechanical Properties of 2D Hybrid Organic-Inorganic Perovskites by Nanoindentation. *ACS Appl. Mater. Interfaces* **2018**, *10* (26), 22167-22173.

(13) Feng, J. Mechanical Properties of Hybrid Organic-Inorganic CH3NH 3BX3 (B = Sn, Pb; X = Br, I) Perovskites for Solar Cell Absorbers. *APL Mater.* **2014**, *2* (8), 081801.

(14) Luo, B.; Guo, Y.; Li, X.; Xiao, Y.; Huang, X.; Zhang, J. Z. Efficient Trap-Mediated Mn^{2+} Dopant Emission in Two Dimensional Single-Layered Perovskite

$(CH_3CH_2NH_3)_2PbBr_4$. *J. Phys. Chem. C* **2019**, *123* (23), 14239-14245.

(15) Mooney, J.; Kambhampati, P. Get the Basics Right: Jacobian Conversion of Wavelength and Energy Scales for Quantitative Analysis of Emission Spectra. *J. Phys. Chem. Lett.* **2013**, *4* (19), 3316-3318.

(16) Decrescent, R. A.; Du, X.; Kennard, R. M.; Venkatesan, N. R.; Dahlman, C. J.; Chabinyc, M. L.; Schuller, J. A. Even-Parity Self-Trapped Excitons Lead to Magnetic Dipole Radiation in Two-Dimensional Lead Halide Perovskites. *ACS Nano* **2020**, *14* (7), 8958-8968.

(17) DeCrescent, R. A.; Venkatesan, N. R.; Dahlman, C. J.; Kennard, R. M.; Zhang, X.; Li, W.; Du, X.; Chabinyc, M. L.; Zia, R.; Schuller, J. A. Bright Magnetic Dipole Radiation from Two-Dimensional Lead-Halide Perovskites. *Sci. Adv.* **2020**, *6*, 1-11.

(18) Yoon, S. J.; Stamplecoskie, K. G.; Kamat, P. V. How Lead Halide Complex Chemistry Dictates the Composition of Mixed Halide Perovskites. *J. Phys. Chem. Lett.* **2016**, *7* (7), 1368-1373.

(19) Chiang, C. H.; Wu, C. G. A Method for the Preparation of Highly Oriented $MAPbI_3$ Crystallites for High-Efficiency Perovskite Solar Cells to Achieve an 86% Fill Factor. *ACS Nano* **2018**, *12*, 10355-10364.

(20) Gholipour, S.; Ali, A. M.; Correa-Baena, J. P.; Turren-Cruz, S. H.; Tajabadi, F.; Tress, W.; Taghavinia, N.; Grätzel, M.; Abate, A.; De Angelis, F.; et al. Globularity-Selected Large Molecules for a New Generation of Multication Perovskites. *Adv. Mater.* **2017**, *29* (38), 1-9.

(21) Mittal, M.; Jana, A.; Sarkar, S.; Mahadevan, P.; Sapra, S. Size of the Organic Cation Tunes the Band Gap of Colloidal Organolead Bromide Perovskite Nanocrystals. *J. Phys. Chem. Lett.* **2016**, *7* (16), 3270-3277.

Chapter 5:

Residual Solvent Removes Electronic Disorder and Low-Energy Emission in Two-Dimensional Hybrid Perovskite Films

5.1 Introduction

Two-dimension (2D) perovskites are attractive for optoelectronic applications because their emission is tunable across the visible spectrum. [1–5] Commonly-used are the Ruddlesden-Popper (RP) family of 2D perovskites, which have structure $(A')_2(A)_{n-1}M_nX_{3n+1}$, where M is a metal (typically Pb or Sn), X is a halide (I, Cl, Br), A is a small cation that sits between the M-X octahedra, and A' is a larger cation (typically organic) that acts as a spacer for the 2D semiconducting A-M-X sheets. [4–10] The emission color is changed by changing the number n of M-X octahedra in the semiconducting sheets, or by swapping the halide between I, Br and Cl. While the emission of many RP perovskites comes primarily from one narrow peak (a free exciton), [11,12] a variety of mechanisms can lead to additional low-energy, broad emission, including coupling to phonons or defects. [13–15] Increasing the proportion of lower-energy emission can broaden the emission until white. [16,17] The facile color tunability of RPs has rendered them attractive for light emitting devices, such as LEDs or lasers, and for light absorbing devices, such as solar cells or photodetectors. [3,4,18–25]

Because optoelectronic devices primarily employ polycrystalline thin films, thin film growth of RPs has been heavily investigated. Thin films are typically grown from solution-casting methods, [4] and the latter unfortunately present several challenges. The solvent and the various precursors can form different complexes in solution, some of which then precipitate into highly-emissive impurities. [26–32] In addition, orientation of the A-M-X semiconducting sheets is difficult to control, particularly for larger *n* RPs. [4,31,33] Since the orientation of the semiconducting 2D sheets determines the direction of carrier transport, control of orientation is crucial for using RPs in optoelectronic devices. [4,31,33,34] In addition, film strain stemming from spin-casting can change the proportions of narrow: broad emitting species, which changes the emission color. [35] The three challenges described here can be overcome by taking particular care with choice of precursor ions or film growth method; [35–37] however, there is still a need for enhanced understanding and control of phase composition, sheet orientation and film growth.

Here, we show that residual solvent can be incorporated into the 2D perovskite lattice in ways that greatly benefit both film growth and optoelectronic properties. The solvent is retained in between the 2D semiconducting sheets by an additive to the precursor solution. Solvent incorporation into the perovskite lattice results in a large increase in grain size of the targeted 2D phase, disappearance of pinholes, and uniform in-plane orientation of the semiconducting sheets. Interestingly, solvent incorporation removes also specific lower-energy luminescence peaks, perhaps due to reduced carrier-phonon coupling. The resulting films also have comparable electronic disorder to the single crystal. These results present new ways to control growth and emission of 2D perovskites, and extend the utility of 2D perovskites for optoelectronic devices.

5.2 Experimental section

Materials

Lead bromide ($PbBr_2$, 99.999 %), ethylammonium bromide (EABr, ≥ 98 %), lead oxide (PbO, ≥ 99.0 %), methylammonium bromide (MABr, 98 %), N-N-dimethylformamide (DMF, 99.8%, anhydrous), poly (methyl methacrylate) (PMMA, MW 350000), and hydrobromic acid (HBr, ACS reagent, 48%), deuterated DMSO (Dimethyl sulfoxide-d_6, 99.9 % atom D, in ampules of 650 μL) were purchased from Sigma Aldrich and used as received. FABr (formamidinium bromide) was made following a reported procedure. [1] Briefly, formamidine acetate (99 %, Sigma Aldrich) was dissolved in ethanol, and aqueous hydrobromic acid was added in excess with respect to FA. The mixture was left to stir in air for > 1h. The solvent was then roto-vaped off, and the resulting solids were washed multiple times with diethyl ether. The product was vacuum dried overnight. The resulting FABr was used for both film growth and bulk/single crystal syntheses. Polished z-cut quartz substrates (15 × 15 × 0.5 mm) were purchased from University Wafer.

Film casting

Quartz substrates were cleaned via ultrasonication in isopropyl alcohol for 10 min and exposed to oxygen plasma at ≈ 300 mTorr for 10 min. All subsequent solution preparation and film fabrications were performed in a nitrogen-filled glove box. Precursor solutions for films were fabricated by dissolving EABr, $PbBr_2$ FABr and MABr in DMF to make an 0.5 mM solution (based on Pb), in the molar ratio $(EA_{1-x}S_x)_{4.5}Pb_3Br_{10}$, or $MAPbBr_3$ or $FAPbBr_3$ for certain extra characterizations. A slight cation excess was found to be necessary in previous work to form the n = 3 phase, likely due to strong complexation of Pb and Br in DMF. [2] The solutions were left stirring overnight at 60°C to ensure good dissolution. Films were spin-cast at 4000 rpm for 60 seconds without antisolvent rinse, and promptly annealed at 100°C (verified by thermocouple) on a hot plate with a heat diffuser. For some experiments (XRD, PL, GIWAXS), after the films cooled, 60 μL of a PMMA solution (75 mg PMMA/3mL toluene) was spin-cast on top of the films at 2000 rpm for 30 seconds. The films were stored in a nitrogen glove box until characterization. For SEM, PDS, NMR, and FTIR, the same spin-casting procedures were employed, but PMMA was not cast on the films. Films for PDS were cast on separate amorphous quartz substates. Films for FTIR were spin-cast on thin glass slides, so that the Si-O signal wouldn't overwhelm the film signals (the quartz substrates were much thicker).

Growth of $(EA,FA)_4Pb_3Br_{10}$ bulk crystals

$(EA,FA)_4Pb_3Br_{10}$ crystals were grown similarly to the previously-published procedure. [3] Briefly, PbO, EABr and FABr in $(EA_{1-x}FA_x)_4Pb_3Br_{10}$ molar ratio were dissolved in HBr, and the solution was heated. Large crystals were formed upon cooling. Individual crystals, "single crystals", were extracted for single-crystal X-Ray analysis. Bulk crystals were drop-cast onto quartz substrates for PL measurements.

GIWAXS characterization.

Grazing Incidence Wide-Angle X-Ray Scattering (GIWAXS) experiments were performed on beamline 11-3 (12.7 keV, wiggler side-station) at the Stanford Synchrotron Radiation Lightsource (SSRL). The source-to-detector (two-dimensional Rayonix MX225 CCD) distances were calibrated using lanthanum hexaboride (LaB6). All raw images were geometrically corrected using Nika. Au nanoparticles (100 nm) drop-cast on quartz substrates were used to verify chi-q alignment post-processing. An incidence angle of 0.5° was chosen for the following reasons: (1) it is shallow enough to properly detect the nIP ($0k0$) peaks (these were cut off when large incidence angles, such as 2°, were used) and (2) it is well above the critical angle. The critical angle was calculated to be near 0.17° using GIXA; [4] this value is slightly below the measured critical angles (0.2°-0.26°) of the BA-MA RP film series. [5] It is important to be far enough above the critical angle to avoid double diffraction, which may manifest in q_Z but not q_{XY}. [6]

PDS characterization

Photothermal Deflection Spectroscopy (PDS) measurements were performed using a homebuilt instrument as previously described. [7] Briefly, monochromated light from either a 150 W Xenon or a 100 W halogen lamp is modulated at 0.5 Hz with a mechanical chopper and then split to be separately focused onto the sample and a pyroelectric detector. Degassed and filtered perfluorohexane (C6F14, 3M Fluorinert FC-72) is employed as the deflection medium. The deflection of a HeNe laser aligned perpendicularly to the pump beam to also be parallel and proximal to the sample surface is measured by a position-sensitive Si detector using a lock-in amplifier. Analysis and fitting was performed using MATLAB.). Absorbance peak positions are best determined from UV-Vis (**Figure 5.3a**), since the PDS signal is less accurate above 3 eV.

Fitting the PDS Data

Following previous work, [2,10,11] the Urbach tails were fit according to:

$$PDS = A\, exp\left(\frac{E - E_G}{E_U}\right)$$

Where PDS is the PDS signal from **Figure 5.6**, where A is a prefactor, E_G is the bandgap and E_U is the Urbach energy.

The goodness of fits are as follows (from MATLAB):

$(EA)_4Pb_3Br_{10}$ spin-cast film; E_U = 54 meV

```
sse: 942.3958e-006

rsquare: 997.5532e-003

dfe: 29.0000e+000

adjrsquare: 997.3844e-003

rmse: 5.7006e-003
```

$(EA)_4Pb_3Br_{10}$ spin-cast film; E_U = 45 meV

```
sse: 21.1291e-006

rsquare: 998.2440e-003

dfe: 60.0000e+000

adjrsquare: 998.1855e-003

rmse: 593.4233e-006
```

X_{FA} = 0.07 spin-cast film

```
sse: 1.3240e-003

rsquare: 998.2726e-003

dfe: 78.0000e+000

adjrsquare: 998.2283e-003

rmse: 4.1200e-003
```

Other Characterizations

Powder X-Ray Diffraction patterns were obtained using a Panalytical Empyrean powder diffractometer in reflection mode with a Cu-Kα source, operating with an accelerating voltage of 45 kV and beam current of 40 mA. Au nanoparticles (100 nm) drop-cast on quartz substrates were used to calibrate peak positions for strain characterization. All peak locations were obtained by Pseudo-Voigt fits using Igor Pro 8. Simulated XRD patterns were made using Vesta.

Scanning Electron Microscopy was performed using an FEI Nova Nano 650 FEG SEM operating at 7-10 keV accelerating voltage with beam currents of 0.40-0.80 nA. For SEM measurements, the samples were sputter-coated with gold to prevent charging.

Absorbance spectra were extracted from transmission measurements made on a Shimadzu UV-2600 ultraviolet-visible spectrophotometer at room temperature and in ambient conditions.

Photoluminescence spectra were acquired using a Horiba FluoroMax 4 spectrometer calibrated with Milli-Q water. Photoluminescence spectra reported in in the main text were all collected using an angle of 75° between the excitation and emission port to reduce scattering. Some PL spectra in the SI were acquired using an angle of 25° for comparison, since the proportions of different features can be angle dependent. All measurements were performed with an excitation wavelength of 370 nm (3.35 eV) and a 400 nm long-pass filter was placed in front of the mission port to reduce scattering. Spectra were fit to Gaussians using Igor Pro 8.

1H-NMR spectra were acquired using a Varian 600 MHz SB VNMRS NMR spectrometer for solutions. Drop-cast and annealed films were scraped off their quartz substrates using a razor blade, and the resulting solutions were dissolved in deuterated DMSO. XRD of drop-cast films confirmed a lack of non-n = 3 phases (**Figure 5.*S*7**). This procedure was performed in air. Several scan times were employed: 20-minute scans were performed using a 30° pulse and 5 second recycle delay, following previous work. [8] Scans with length 20 minutes and 16h were performed using a 90° pulse and 12 second recycle delay, as described previously. [9] All spectra were referenced to the residual solvent peak for DMSO at 2.50 ppm, and all processing and analysis was done using the TopSpin software package.

FTIR spectra were obtained using a Perkin-Elmer Spectrum Two spectrometer equipped with a DTGS detector and diamond windows in the range of 4000-450 cm-1 at a resolution of 4 cm-1, or in the range of 3500-1200 cm-1 at a resolution of 0.5 cm-1. For data collection, samples were placed face-down on the crystal and the pressure arm was used to force the sample into contact with the window.

5.3 Results and Discussion

We aimed to find methods to make RP films with targeted optoelectronic properties without deviating from typical fabrication procedures. We started from the $(EA)_4Pb_3Br_{10}$ composition, where EA is ethylammonium, because this phase can be spin-cast into a phase-pure RP film without taking particular care with growth procedures. [35] The structure of this n = 3 RP perovskite is shown in **Figure 5.1a**. [17] The $(EA)_4Pb_3Br_{10}$ phase is unique in that the A-site and spacer cations are identical. Solution growth of

$(EA)_4Pb_3Br_{10}$ films is thus not plagued by competing crystallizations of the $n = 3$ phase vs. emissive impurities, in contrast to the challenging growth of films of other RP perovskites, such as those belonging to the $(BA)_2(MA)_{n-1}Pb_nX_{3n+1}$ or $(PEA)_2(MA)_{n-1}Pb_nX_{3n+1}$ families. [30,31,38] The large size of EA (274 pm) [39,40] forces the outer Pb-Br octahedra to distort in both bond angle and bond length, which is thought to enhance formation of self-trapped excitons (STEs). [17,35] We previously showed that both of the low-energy emission features of $(EA)_4Pb_3Br_{10}$ are coupled to phonons, and are possibly STEs. [35] As a spin-cast film, $(EA)_4Pb_3Br_{10}$ exhibits film strain, which suppresses emission from the lowest-energy feature. [35] We wondered to what extent the $(EA)_4Pb_3Br_{10}$ composition could be modified and still retain both $n = 3$ RP structure and emission in films. We therefore sought to replace EA with other cations, such as formamidinium (FA) and methylammonium (MA). EA, MA, Pb and Br are known to form the cubic $(EA,MA)PbBr_3$ alloy for higher loadings of MA, because the small size of MA lowers the tolerance factor to be within the 3D perovskite range. [41] We also obtained the $(EA,MA)PbBr_3$ alloy at high MA loadings, and discuss the results in **Figure 5.S1**. Substitution of EA with FA, however, yielded unexpected results, and we discuss these below.

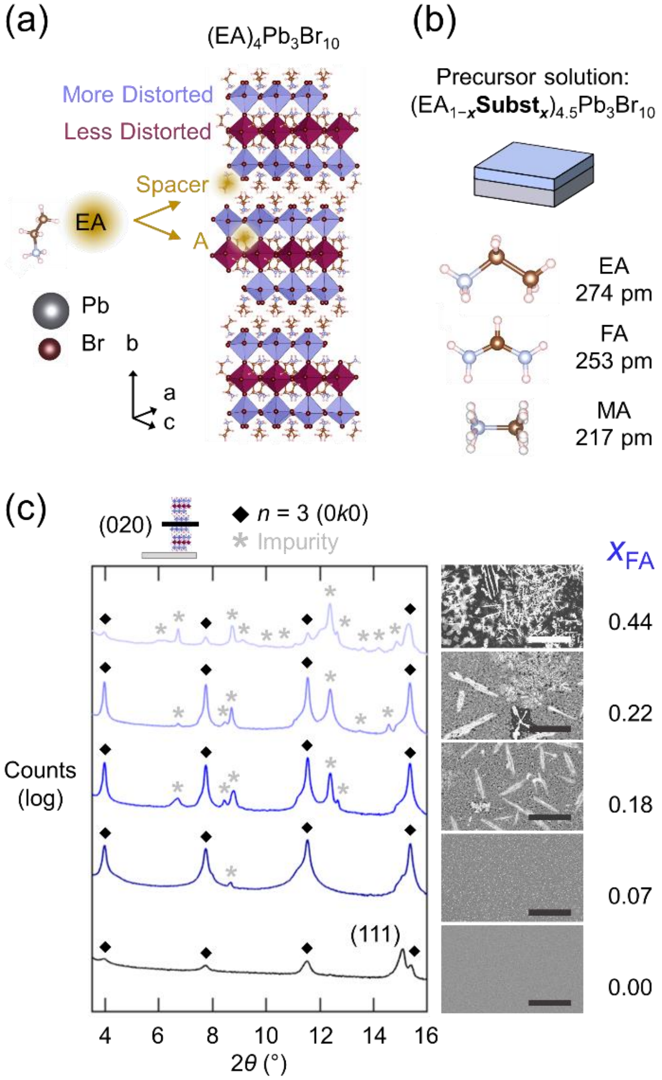

Figure 5.1. (a) Crystal structure of $(EA)_4Pb_3Br_{10}$ from reference [17] showing the more and less distorted octahedral substructures, and with ethylammonium (EA) in both A and spacer sites. (b) Schematic of a spin-cast film on a quartz substrate (films were capped with PMMA), with the precursor solution stoichiometry $(EA_{1-x}Subst._x)_{4.5}Pb_3Br_{10}$, where Subst. is the substituent formamidinium (FA) or methylammonium (MA). Cation sizes are taken from [39,40]. As discussed previously, [35] a slight excess of EA is needed to obtain the $(EA)_4Pb_3Br_{10}$ phase in films, due to strong Pb-Br-DMF complexation. [42] (c) Structure of films with precursor solution $(EA_{1-x}FA_x)_{4.5}Pb_3Br_{10}$: XRD patterns are shown on a logarithmic scale, and SEM images are shown. The n = 3 (0k0) peaks are indicated with diamonds, and the n = 3 (111) peak is also indicated. A schematic of the (020) plane is shown as an example of (0k0). The scale bar on all SEM images is 50 μm.

To prepare films, we first mixed precursor salts in dimethylformamide solvent (DMF) to form solutions with approximate stoichiometry $(EA_{1-x}Subst._x)_{4.5}Pb_3Br_{10}$, where Subst. is the substituent FA or MA (**Figure 5.1b**). We previously found that to make films with $(EA)_4Pb_3Br_{10}$ composition, a slight excess of EA was needed, such that the precursor solution had $(EA)_{4.5}Pb_3Br_{10}$ stoichiometry. [35] This slight excess of EA is likely needed to compensate for strong Pb-Br-DMF complexation. [42] For simplicity, we refer to films with precursor stoichiometry $(EA_{1-x}Subst._x)_{4.5}Pb_3Br_{10}$ by their respective x, such that x_{FA} = 0.07 films had a precursor solution with stoichiometry $(EA_{0.93}FA_{0.07})_{4.5}Pb_3Br_{10}$. Films were spin-cast and annealed, then capped with PMMA to prevent possible degradation (see **Experimental Section**) for XRD, UV-Vis absorbance, and photoluminescence emission characterizations. We also occasionally slowed growth kinetics by drop-casting the films instead of spin-coating them (see **Experimental Section**) because we previously found that slowing growth kinetics enabled recovery of the low-energy emission tail (phonon-coupled) in $(EA)_4Pb_3Br_{10}$ films. [35] To better understand the phase composition of the obtained films, we also prepared $(EA_{1-x}FA_x)_4Pb_3Br_{10}$ bulk crystals via precipitation in aqueous hydrobromic acid (see **Experimental Section**).

Spin-cast films with FA substitution exhibit the RP $n = 3$ structure, with impurities appearing for larger amounts of FA. **Figure 5.1c** shows the X-Ray Diffraction (XRD) patterns of films with $0.00 \le x_{FA} \le 0.44$. Comparison with the simulated XRD pattern of $(EA)_4Pb_3Br_{10}$ over a greater angular range can be found in **Figure 5.S2**. The initial $(0k0)$ features of $(EA)_4Pb_3Br_{10}$, which are signatures of the $n = 3$ phase, can be found in all FA-substituted films. [11,17] The (111) peak disappears, signaling a change in crystallite orientation with FA substitution. The FA-substituted films have crystallites oriented out-of-plane, such that the Pb-Br semiconducting sheets are parallel to the substrate (cartoon in **Figure 5.1c**). FA substitution also greatly improves growth of the n3 phase, which is evidenced in two ways: first, the XRD peaks increase by an order of magnitude with FA substitution, signaling high structural uniformity in the $n = 3$ crystallites. This increase is especially remarkable because the film thickness does not change much after FA substitution (**Figure 5.S3**). Second, the peak width of the compositions with FA is also considerably narrower, indicating less structural disorder (**Figure 5.*S*2**). Non-$n = 3$ peaks are clearly visible for most FA loadings, suggesting impurity formation. To better understand $n = 3$ and impurity growth, we examined the structure of the films using Scanning Electron Microscopy (SEM). The $x_{\mathrm{FA}} = 0.07$ film appears homogeneous via SEM, consistent with $n = 3$ being the predominant phase seen in XRD. In contrast, the $x_{\mathrm{FA}} = 0.18$ film exhibits large, needle-like impurities, consistent with impurity peaks readily appearing in XRD. The needle-like shape of the impurities suggests that they are 1-D phases. More impurities appeared for $x_{\mathrm{FA}} = 0.22$ and $x_{\mathrm{FA}} = 0.44$, with different crystal habit, suggesting impurities of different phases. The obvious presence of these impurities in XRD and SEM contrasts with the behavior of impurities in $(\mathrm{BA})_2(\mathrm{MA})_{n-1}\mathrm{Pb}_n\mathrm{I}_{3n+1}$ RP films. Impurities in $(\mathrm{BA})_2(\mathrm{MA})_{n-1}\mathrm{Pb}_n\mathrm{I}_{3n+1}$ RP films are often off-target n RP phases, and they form intergrown into the same grain as the RP of targeted n, [27,28] and as such are indistinguishable in SEM. In contrast, the $(\mathrm{EA})_2(\mathrm{EA})_{n-1}\mathrm{Pb}_n\mathrm{Br}_{3n+1}$ family can form very few n phases, so impurities are likely not other RP phases, and do not intergrow with $n = 3$. [35] Overall, FA substitution in the precursor solution improves growth of the $n = 3$ RP phase in bulk, with uniform in-plane orientation of the semiconducting sheets, but with non-$n = 3$ impurities readily appearing for larger amounts of FA.

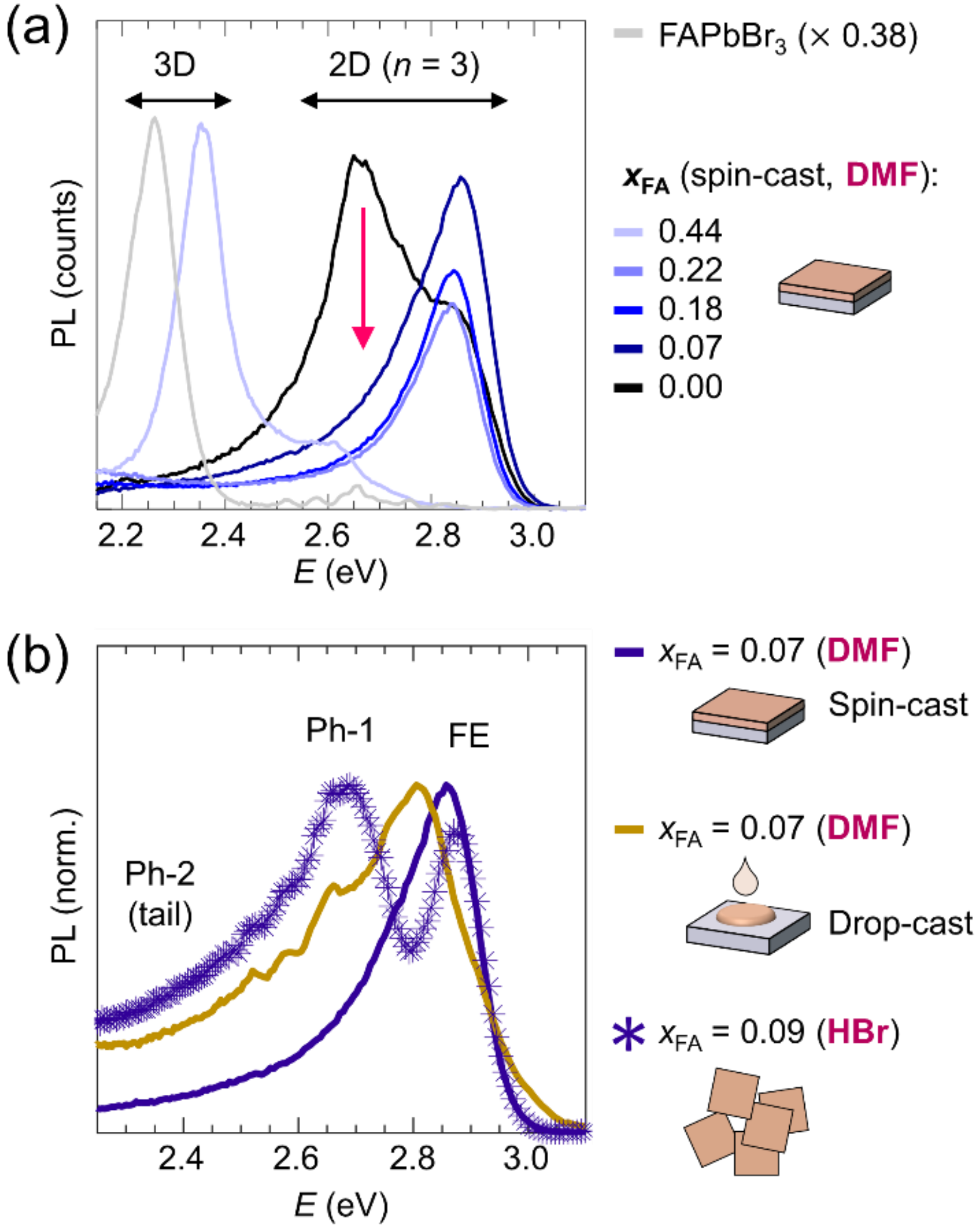

Figure 5.2. Photoluminescence emission of films with FA substitution ($(EA_{1-x}FA_x)_{4.5}Pb_3Br_{10}$ precursor stoichiometry in DMF), for 3.94 eV excitation. 2D (n = 3) emission is retained until $x_{FA} = 0.22$, with $x_{FA} = 0.44$ having emission from the 3D (EA,FA)$PbBr_3$ phase. The intensity of an $FAPbBr_3$ film, made for comparison, is multiplied by 0.38. (b) Photoluminescence emission of spin-cast and drop-cast films (with annealing) of $x_{FA} = 0.07$, and of bulk crystals grown from precipitation in aqueous HBr with $(EA_{0.91}FA_{0.09})_4Pb_3Br_{10}$ precursor stoichiometry. For films, the solvent (DMF) is labelled. Assignments of different emission features to excitons (FE) and phonon-coupled emission (Ph) are labelled, following the analysis in prior work. [35]

The photoluminescence emission of most FA-substituted films exhibit emission from only the n = 3 phase, despite containing impurities. **Figure 5.2a** shows the photoluminescence emission of the films with $0.00 \leq x_{FA} \leq 0.44$, as well as of an $FAPbBr_3$ film for comparison. Prior work on $(EA)_4Pb_3Br_{10}$ (x_{FA} = 0.00) identified the emission peak at 2.9 eV to be a free exciton (FE), and found that the 2.7 eV peak and the low-energy tail are phonon-coupled. [35] The free exciton emission of the n = 3 phase at 2.9 eV is retained for all $0.00 \leq x_{FA} \leq 0.22$. Thus, emission coming from the n = 3 phase is retained until very high FA substitution despite obvious non-n = 3 phases appearing in both XRD and SEM (**Figure 5.1c**). This suggests that these non-n = 3 phases are emissively silent below 3.1 eV, similarly to how PbI_2 or $PbBr_2$ are emissively silent in $MAPbX_3$ films. This interpretation is confirmed by UV-Vis absorbance measurements, which reveal a peak near 4 eV that gets stronger with increasing FA content (**Figure 5.S4**). The absence of emissive impurities contrasts with the behavior of $(BA)_2(MA)_{n-1}Pb_nI_{3n+1}$ RP films, in which off-target n RP phases with smaller bandgap dominate the emission. [27,28,30,31,36] Indeed, the $(EA)_2(EA)_{n-1}Pb_nBr_{3n+1}$ family can form very few RP n phases, and substitution with FA for $x_{FA} \leq 0.22$ does not seem to perturb this property. [35] The x_{FA} = 0.44 film exhibits emission similar in location and peak shape to $FAPbBr_3$, and has absorbance onset near 2.2 eV (**Figure 5.S4**) suggesting that the emission from the x_{FA} = 0.44 film comes from the $(EA,FA)PbBr_3$ alloy (see also **Figure 5.S5** [43]). The $(EA,FA)PbBr_3$ alloy has blue-shifted emission from $FAPbBr_3$, likely because EA widens the gap, consistent with prior work showing that the $(EA,MA)PbBr_3$ alloy has larger gap than $MAPbBr_3$. [41] Overall, most films with FA substitution exhibit emission from the n = 3 phase.

Surprisingly, substitution with even very small amounts of FA turns off the phonon-coupled emission at 2.7 eV. We verified that this is not an effect of measurement conditions that may change emission proportions, such as photoluminescence collection angle (**Figure 5.S6**). The 2.7 eV feature is not turned off for MA-substituted films that retained *n* = 3 emission (**Figure 5.S1**), suggesting that something particular to FA substitution causes extinction of the 2.7 eV feature. To better understand this, we changed the growth conditions of FA-containing *n* = 3 phases (**Figure 5.2b**). We first checked the role of film casting kinetics by drop-casting the x_{FA} = 0.07 precursor and annealing the resulting films, and obtain large, unconstrained grains of the *n* = 3 phase, and observe only one crystal habit via SEM (**Figure 5.S7**). The photoluminescence of the drop-cast x_{FA} = 0.07 film contains the *n* = 3 free exciton (**Figure 5.2, Figure 5.S7**). In agreement with the behavior of drop-cast $(EA)_4Pb_3Br_{10}$, [35] the drop-cast x_{FA} = 0.07 contains a greater proportion of low-energy phonon-coupled tail than the spin-cast film does, but the 2.7 eV feature is still missing. Thus, casting conditions are not responsible for removing the 2.7 eV peak. We also prepared bulk crystals of $(EA,FA)_4Pb_3Br_{10}$ from aqueous hydrobromic acid, and examined their structure and emission (**Figure 5.2b**). Individual bulk crystals ("single crystals") were selected for single crystal XRD analysis, which reveals that FA can go either in the A-site (*in* the Pb-Br sheets) or in the spacer site (*between* the Pb-Br sheets - **Figure 5.S8**). The FA-substituted bulk crystals grown from aqueous acid retain the 2.7 eV feature, so FA substitution alone does not extinguish this feature. One big difference in the preparation of bulk crystals vs. films was the solvent: the crystals were prepared from aqueous hydrobromic acid, while the films were prepared from DMF. Thus, FA substitution in combination with DMF is likely key to extinguishing the 2.7 eV emission.

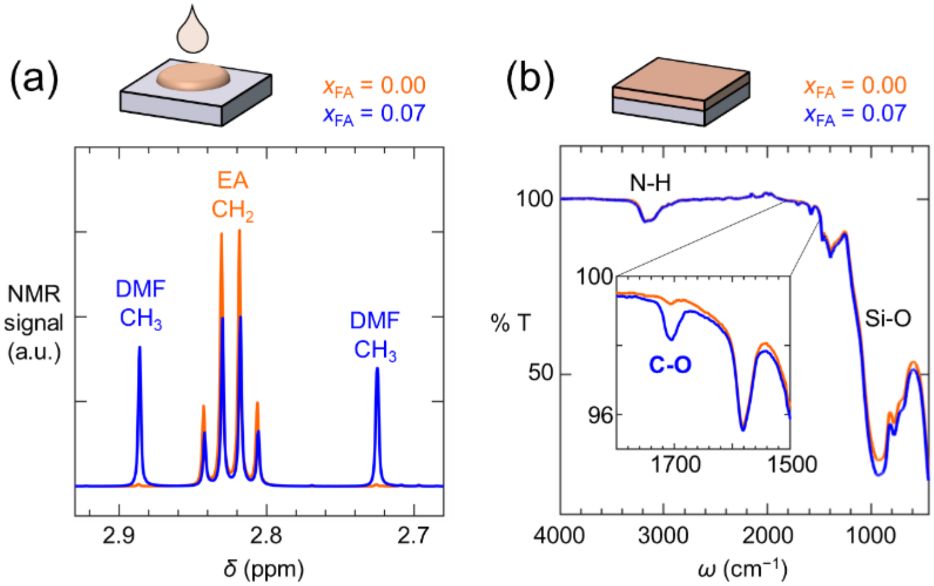

Figure 5.3. Retention of DMF when FA is present. (a) 1H-NMR of drop-cast and annealed films with x_{FA} = 0.07 and x_{FA} = 0.00 compositions prepared from DMF (no PMMA capping layer), that were then scraped off the substrates and dissolved in deuterated DMSO. (b) Transmission (%T) FTIR of spin-cast and annealed films with x_{FA} = 0.07 and x_{FA} = 0.00 compositions prepared from DMF (no PMMA capping layer).

Spectroscopic analyses reveal that when FA is present, DMF is retained in the *n* = 3 perovskite structure (**Figure 5.3**). Drop-cast and annealed films of x_{FA} = 0.00 and x_{FA} = 0.07 (**Figure 5.S7**) were prepared and scraped off their substrates. The scraped films were then dissolved in deuterated DMSO, and proton NMR was run on the resulting solutions (**Figure 5.3a** – for discussion of 1H-NMR on spin-cast films see the **Appendix to Chapter 5**). Notably, while both solutions contain NH_3 peaks from EA, the drop-cast x_{FA} = 0.07 sample additionally contains large DMF peaks. Very weak FA peaks are also visible in the drop-cast x_{FA} = 0.07 sample, and peak integration revealed that FA and EA are present in the proportions weighed out (**Figure 5.S9**). **Figure 5.3b** shows Fourier Transform Infrared Spectroscopy (FTIR) of spin-cast x_{FA} = 0.00 and x_{FA} = 0.07 films. A weak carbonyl peak is present for x_{FA} = 0.07, but not for x_{FA} = 0.00. This weak carbonyl is likely from DMF, since DMF has a carbonyl and since FA, EA, and $PbBr_2$ do not contain carbonyls. Thus, it seems that the x_{FA} = 0.07 films, independently of preparation, retain DMF. Since the only difference between x_{FA} = 0.00 and x_{FA} = 0.07 is the presence of FA, it is likely that FA is causing the DMF retention.

FA is likely retaining DMF in between the Pb-Br sheets. From the analysis of the bulk crystals discussed above (see also **Figure 5.S8**), we know that FA can go in the spacer site. DMF (≈ 300 pm) [44] is too large to go in the A-site, so it can only reside in between the Pb-Br sheets. It is likely that the amino groups of FA are encouraging retention of the carbonyl group of the DMF via hydrogen bonding. H-bonding of DMF has previously been reported in 1D perovskite-like structures, $(MA)[PbI_3]\cdot DMF$ and $(BA)[PbI_3]\cdot DMF$, where the ammonium groups of methylammonium or butylammonium hydrogen bond with the carbonyl of DMF. [30] A 1D needle structures with FA and DMF has also been reported, $(FA)_2Pb_3I_8\cdot 4DMF$. [45] This structure contains twice as much DMF as the corresponding MA analogue ($(MA)_2Pb_3I_8\cdot 2DMF$) because FA forms more hydrogen bonds with DMF than MA. [45] In addition, incorporation of non-spacer molecules between M-X sheets via electrostatic interactions has previously been reported, whereby benzene was incorporated into an n = 1 RP via fluoroaryl-aryl interactions with the fluorinated aromatic spacer. [46] Thus, small amounts of FA can encourage DMF retention in the interlayer.

The presence of DMF likely removes conditions necessary for emission at 2.7 eV. Prior work showed that the 2.7 eV feature is likely phonon-coupled, [35] and phonon-coupled emission can be sensitive to cation stacking, [47] the dynamics of which may depend on the spacer cation. [48] DMF in the interlayer would certainly modify how the spacer cations are arranged; perhaps to such an extent that the 2.7 eV feature is extinguished. It is remarkable that the 2.7 eV phonon-coupled feature is turned off, but that the low-energy phonon-coupled tail is retained (**Figure 5.2b**). This suggests that the 2.7 eV feature is coupled to one phonon mode, while the low-energy may be coupled to a separate phonon mode, which would be less perturbed by DMF incorporation. The unusual behavior of the solvent is remarkable: while residual solvent can be a hindrance to obtaining desired emission color, [30] here the presence of residual solvent can be used to turn on or off different emission peaks, thus further tuning the color emitted by (EA,A')Pb_3Br_{10} perovskites.

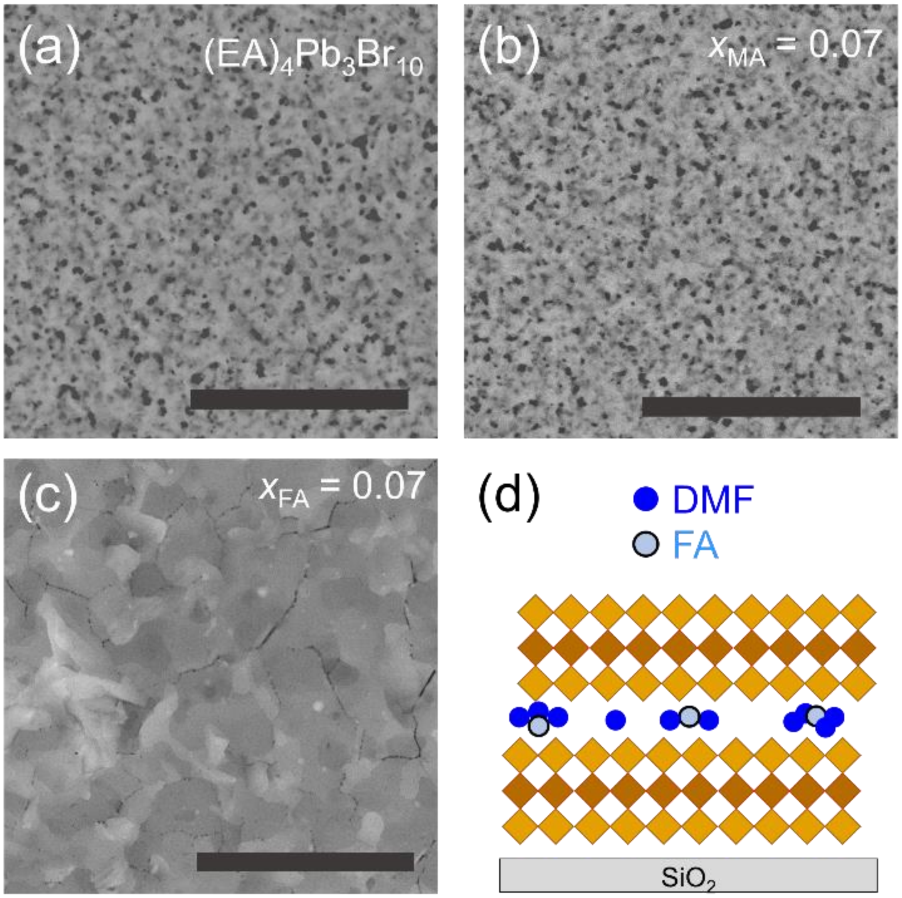

Figure 5.4. SEM images of spin-cast films with composition (a) $(EA)_4Pb_3Br_{10}$, (b) $x_{MA} = 0.07$ and (c) $x_{FA} = 0.07$. The scale bar on all images is 5 μm. (d) Schematic of how DMF-FA is thought to help large lateral grain growth.

DMF retention in the interlayer explains improvements to film growth. **Figure 5.4** shows SEM images of spin-cast films with $(EA)_4Pb_3Br_{10}$, $x_{FA} = 0.07$ and $x_{MA} = 0.07$ compositions. For $(EA)_4Pb_3Br_{10}$ and $x_{MA} = 0.07$, the films have small, < 200 nm-sized grains and many pinholes. In contrast, FA substitution yields an order-of-magnitude increase in lateral grain size, with grains ~ 5 μm, and disappearance of the pinholes. The increase in grain size is preserved for all FA substitutions (**Figure 5.S10**) and is lateral only, as FA-DMF incorporation does not make the films thicker (**Figure 5.S3**). To better understand this improvement to lateral grain size, we employed Grazing Incidence Wide-

Angle X-Ray Scattering (GIWAXS – **Figure 5.5**). A simulated GIWAXS pattern of $(EA)_4Pb_3Br_{10}$ with full out-of-plane crystallite orientation is shown in **Figure 5.5a**, with the n = 3 signature (0k0) peaks labelled. The pattern of the x_{FA} = 0.07 film matches this simulation very closely, revealing full out-of-plane orientation of the 2D sheets. The peaks are sharp and small, further indicating good orientational uniformity, consistent with the XRD analysis above (**Figure 5.1** and **Figure 5.S2**). The amount of FA-DMF that can incorporate in the n = 3 structure seems to saturate, as evidenced by two observations: first, the appearance of non-n = 3 impurities for $x_{FA} \geq 0.18$ (**Figure 5.1c**), and second, by the lack of contraction of the 2D sheets for $x_{FA} \geq 0.07$ (**Figure 5.S2**). Thus, since DMF does not need to leave the interlayer, 2D sheets can grow more easily. The easiest growth direction for the 2D sheets is parallel to the substrate, so large grains are formed with uniform 2D sheet orientation parallel to the substrate.

The contrast in the morphology and structure of the different compositions tested reveals that cation chemistry is key to controlling growth. In contrast to the behavior of FA films, rings are observed in the GIWAXS pattern of the x_{MA} = 0.07 film, indicating that the 2D sheets have no preferred orientation. In addition, 2D sheets in the $(EA)_4Pb_3Br_{10}$ film have two preferred orientations, with semiconducting sheets being both in-plane and out-of-plane, evidenced by (0k0) peaks along both q_{XY} and q_Z (**Figure 5.5b**). [35] Most MA compositions, as well as $(EA)_4Pb_3Br_{10}$, have very small grains, in contrast to the large grain size of the FA compositions (**Figure 5.4, Figure 5.S1, Figure 5.S10**). In addition, DMF incorporation into the n = 3 structure is likely what frustrates solvate formation in x_{FA} = 0.07 films, as solvate formation requires available solvent. This is confirmed by examining drop-cast films without annealing: the n = 3 phase is formed, and one crystal habit is seen via SEM (**Figure 5.S7**). Overall, controlling the orientation and growth of the semiconducting sheets is closely tied to the chemistry of the A/A'-site cations. Such improvements are crucial to the development of optoelectronic devices.

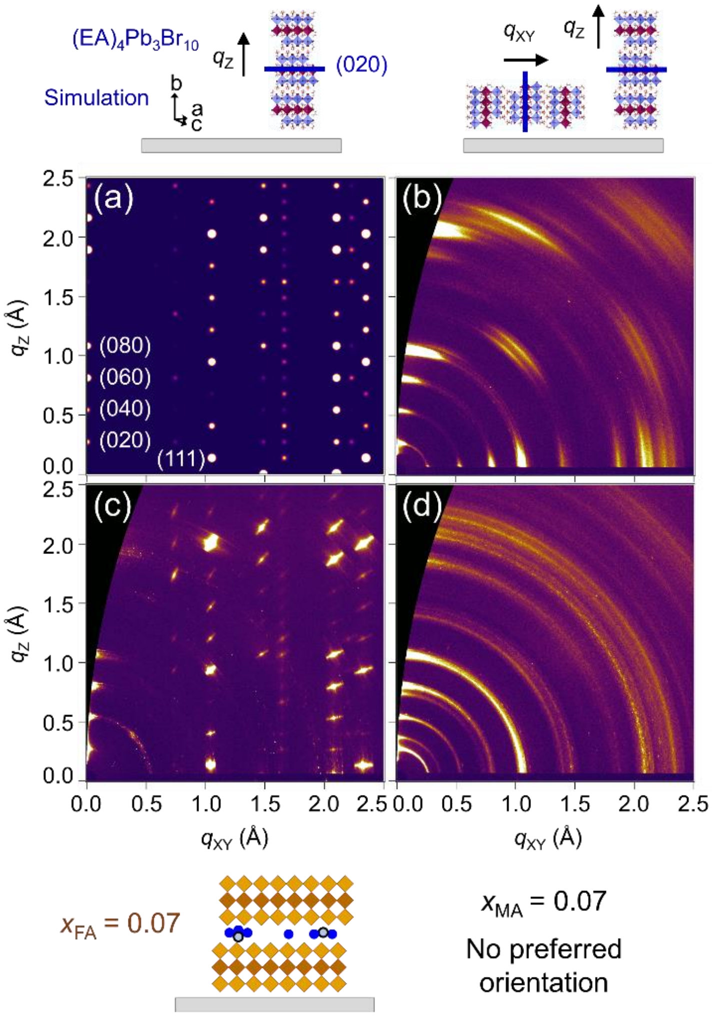

Figure 5.5. Grazing Incidence Wide-Angle X-Ray Scattering (GIWAXS) analysis of FA and MA-substituted spin-cast films. (a) Simulation of the GIWAXS pattern for $(EA)_4Pb_3Br_{10}$, assuming full out-of-plane crystallite orientation (made using the cif file from prior work [17]). The main (0*k*0) peaks are indexed, as well as the (111). (b) GIWAXS pattern of an $(EA)_4Pb_3Br_{10}$ spin-cast film, showing the two preferred crystallite orientations. (c) GIWAXS pattern of an x_{FA} = 0.07 spin-cast film, showing the sole preferred out-of-plane orientation, and (d) GIWAXS pattern of an x_{MA} = 0.07 spin-cast film, showing no preferred orientation.

Finally, FA-DMF incorporation greatly reduces electronic disorder. **Figure 5.6** shows Photothermal Deflection Spectroscopy (PDS) analysis of the absorbance onsets of thin films of $(EA)_4Pb_3Br_{10}$ and $x_{FA} = 0.07$, throughout the < 200 nm film thickness (**Figure 5.S3**). Onsets were fit in order to extract the Urbach energies E_U, which represents the degree electronic disorder near the absorption edge. As discussed previously, the $(EA)_4Pb_3Br_{10}$ film has two absorbance onsets that likely correspond to the two crystallite types in the film, those with in-plane orientation and those with out-of-plane orientation. Both have high Urbach energies, of 45 meV and 54 meV. In contrast, the $x_{FA} = 0.07$ film has a single absorbance onset, with much lower Urbach energy of 37 meV. This is on the order of bulk crystals of $(EA)_4Pb_3Br_{10}$, which have Urbach energy of 38 meV. [35] The increase in sharpness in absorbance onset is also visible via UV-Vis (**Figure 5.S4**), and quantitatively confirmed here with PDS. The reduction in electronic disorder may originate from the larger grain size and uniform sheet orientation. In addition, DMF in the interlayer may be removing strains by lowering mechanical interactions between top and bottom 2D sheets, such that there is less strain-induced disorder. Such sharp onset in a film is highly desirable for absorption-based optoelectronic devices such as photovoltaics or photodetectors. [49]

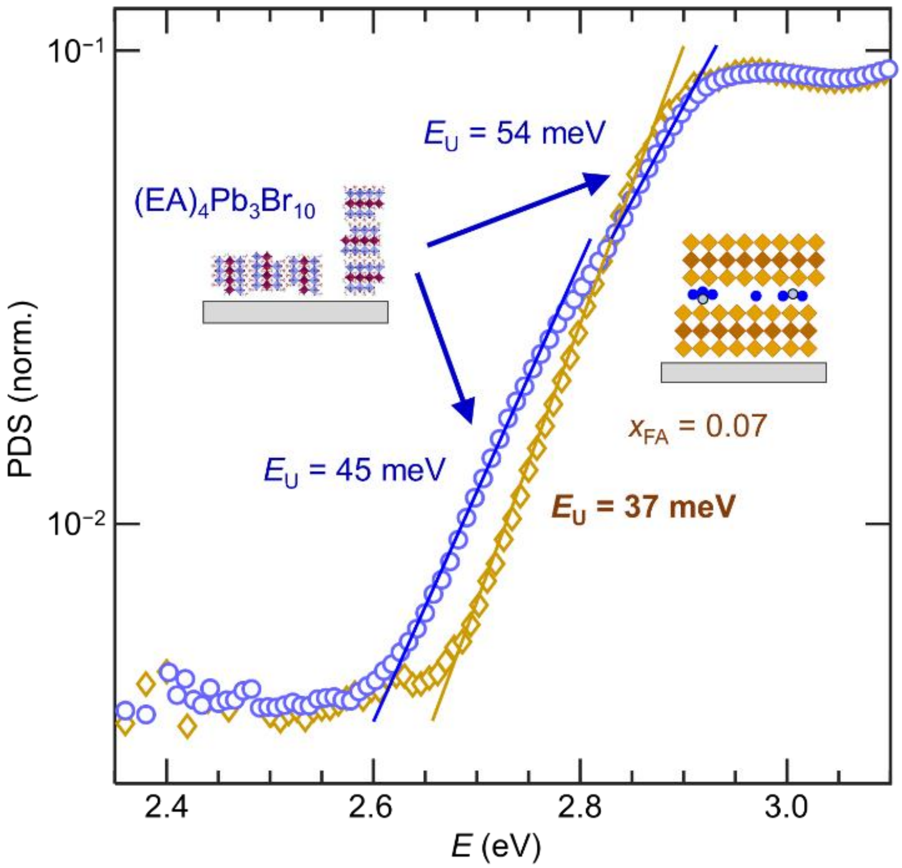

Figure 5.6. PDS spectra of a spin-cast films of $(EA)_4Pb_3Br_{10}$ and x_{FA} = 0.07, showing fits of different absorption onsets and their respective Urbach energies E_U. For goodness of fits see **Experimental Section**.

5.4 Conclusions

Overall, we have shown that solvent incorporation into the 2D perovskite lattice can be can be highly beneficial for both film growth and the resulting optoelectronic properties of the film. The solvent is retained between the semiconducting sheets by an additive to the precursor solution. This is unusual, as residual solvent usually forms separate and highly-emissive phases. The resulting films have narrow emission from the targeted 2D phase, electronic disorder comparable to that of bulk crystals, uniform orientation of the semiconducting sheets, and order-of-magnitude increase in lateral grains size. Notably, solvent anchoring turns off specific phonon-coupled emission features, which provides an additional knob with which to tune the emission color of 2D perovskites. These results present new ways to control growth and emission of 2D perovskites, and extend the utility of 2D perovskites for optoelectronic devices.

5.5 Acknowledgments

Growth and structural characterization were supported by the U.S. Department of Energy, Office of Science, Basic Energy Sciences, under Award Number DE-SC-0012541. Support of optical characterization was provided by the U.S. Department of Energy (DOE), Office of Science, Basic Energy Sciences (BES), under Award Number DE-SC0019273, as well as from Quantum Materials for Energy Efficient Neuromorphic Computing, an Energy Frontier Research Center funded by the U.S. Department of Energy (DOE), Office of Science, Basic Energy Sciences, (BES), under Award Number DE-SC0019273. Time-resolved spectroscopy capabilities were supported by DURIP ARO grant 66886LSRIP. Use of the Stanford Synchrotron Radiation Lightsource, SLAC National Accelerator Laboratory, is supported by the U.S. Department of Energy, Office of Science, Office of Basic Energy Sciences under Contract No. DE-AC02-76SF00515. The research reported here also made use the shared facilities of the UCSB MRSEC (National Science Foundation DMR 1720256), a member of the Materials Research Facilities Network (www.mrfn.org). R.M.K. gratefully acknowledges the National Defense Science and Engineering Graduate fellowship for financial support.

5.6 References

(1) Zhou, Y.; Chen, J.; Bakr, O. M.; Mohammed, O. F. Metal Halide Perovskites for X - Ray Imaging Scintillators and Detectors. *ACS Energy Lett.* **2021**, *6*, 739–768.

(2) Saparov, B.; Mitzi, D. B. Organic-Inorganic Perovskites: Structural Versatility for Functional Materials Design. *Chem. Rev.* **2016**, *116* (7), 4558–4596.

(3) Ge, C.; Xue, Y. Z. B.; Li, L.; Tang, B.; Hu, H. Recent Progress in 2D/3D Multidimensional Metal Halide Perovskites Solar Cells. *Front. Mater.* **2020**, *7* (October).

(4) Li, X.; Hoffman, J. M.; Kanatzidis, M. G. The 2D Halide Perovskite Rulebook: How the Spacer Influences Everything from the Structure to Optoelectronic Device Efficiency. *Chem. Rev.* **2021**.

(5) Smith, M. D.; Crace, E. J.; Jaffe, A.; Karunadasa, H. I. The Diversity of Layered Halide Perovskites. *Annu. Rev. Mater. Res.* **2018**, *48*, 111–136.

(6) Ruddlesden, S. N.; Popper, P. The Compound Sr 3 Ti 2 O 7 and Its Structure . *Acta Crystallogr.* **1958**, *11* (1), 54–55.

(7) Ruddlesden, S. N.; Popper, P. New Compounds of the K 2 NIF 4 Type . *Acta Crystallogr.* **1957**, *10* (8), 538–539.

(8) Smith, I. C.; Hoke, E. T.; Solis-Ibarra, D.; McGehee, M. D.; Karunadasa, H. I. A Layered Hybrid Perovskite Solar-Cell Absorber with Enhanced Moisture Stability. *Angew. Chemie* **2014**, *126* (42), 11414–11417.

(9) Stoumpos, C. C.; Cao, D. H.; Clark, D. J.; Young, J.; Rondinelli, J. M.; Jang, J. I.; Hupp, J. T.; Kanatzidis, M. G. Ruddlesden-Popper Hybrid Lead Iodide Perovskite 2D Homologous Semiconductors. *Chem. Mater.* **2016**, *28* (8), 2852–2867.

(10) Mao, L.; Stoumpos, C. C.; Kanatzidis, M. G. Two-Dimensional Hybrid Halide Perovskites: Principles and Promises. *J. Am. Chem. Soc.* **2019**, *141* (3), 1171–1190.

(11) Stoumpos, C. C.; Cao, D. H.; Clark, D. J.; Young, J.; Rondinelli, J. M.; Jang, J. I.; Hupp, J. T.; Kanatzidis, M. G. Ruddlesden-Popper Hybrid Lead Iodide Perovskite 2D Homologous Semiconductors. *Chem. Mater.* **2016**, *28* (8), 2852–2867.

(12) Blancon, J. C.; Stier, A. V.; Tsai, H.; Nie, W.; Stoumpos, C. C.; Traoré, B.; Pedesseau, L.; Kepenekian, M.; Katsutani, F.; Noe, G. T.; et al. Scaling Law for Excitons in 2D Perovskite Quantum Wells. *Nat. Commun.* **2018**, *9* (1), 1–10.

(13) Moral, R. F.; Germino, J. C.; Bonato, L. G.; Almeida, D. B.; Therézio, E. M.; Atvars, T. D. Z.; Stranks, S. D.; Nome, R. A.; Nogueira, A. F. Influence of the Vibrational Modes from the Organic Moieties in 2D Lead Halides on Excitonic Recombination and Phase Transition. *Adv. Opt. Mater.* **2020**, *8* (24), 1–8.

(14) Decrescent, R. A.; Du, X.; Kennard, R. M.; Venkatesan, N. R.; Dahlman, C. J.; Chabinyc, M. L.; Schuller, J. A. Even-Parity Self-Trapped Excitons Lead to Magnetic Dipole Radiation in Two-Dimensional Lead Halide Perovskites. *ACS Nano* **2020**, *14* (7), 8958–8968.

(15) Cortecchia, D.; Neutzner, S.; Kandada, A. R. S.; Mosconi, E.; Meggiolaro, D.; De Angelis, F.; Soci, C.; Petrozza, A. Broadband Emission in Two-Dimensional Hybrid Perovskites: The Role of Structural Deformation. *J. Am. Chem. Soc.* **2017**, *139* (1), 39–42.

(16) Dohner, E. R.; Hoke, E. T.; Karunadasa, H. I. Self-Assembly of Broadband White-

Light Emitters. *J. Am. Chem. Soc.* **2014**, *136* (5), 1718–1721.

(17) Mao, L.; Wu, Y.; Stoumpos, C. C.; Traore, B.; Katan, C.; Even, J.; Wasielewski, M. R.; Kanatzidis, M. G. Tunable White-Light Emission in Single-Cation-Templated Three-Layered 2D Perovskites (CH3CH2NH3)4Pb3Br10-XClx. *J. Am. Chem. Soc.* **2017**, *139* (34), 11956–11963.

(18) Gharibzadeh, S.; Hossain, I. M.; Fassl, P.; Nejand, B. A.; Abzieher, T.; Schultes, M.; Ahlswede, E.; Jackson, P.; Powalla, M.; Schäfer, S.; et al. 2D/3D Heterostructure for Semitransparent Perovskite Solar Cells with Engineered Bandgap Enables Efficiencies Exceeding 25% in Four-Terminal Tandems with Silicon and CIGS. *Adv. Funct. Mater.* **2020**, *30* (19).

(19) Gharibzadeh, S.; Abdollahi Nejand, B.; Jakoby, M.; Abzieher, T.; Hauschild, D.; Moghadamzadeh, S.; Schwenzer, J. A.; Brenner, P.; Schmager, R.; Haghighirad, A. A.; et al. Record Open-Circuit Voltage Wide-Bandgap Perovskite Solar Cells Utilizing 2D/3D Perovskite Heterostructure. *Adv. Energy Mater.* **2019**, *9* (21).

(20) Sutanto, A. A.; Szostak, R.; Drigo, N.; Queloz, V. I. E.; Marchezi, P. E.; Germino, J. C.; Tolentino, H. C. N.; Nazeeruddin, M. K.; Nogueira, A. F.; Grancini, G. In Situ Analysis Reveals the Role of 2D Perovskite in Preventing Thermal-Induced Degradation in 2D/3D Perovskite Interfaces. *Nano Lett.* **2020**, *20* (5), 3992–3998.

(21) Grancini, G.; Roldán-Carmona, C.; Zimmermann, I.; Mosconi, E.; Lee, X.; Martineau, D.; Narbey, S.; Oswald, F.; De Angelis, F.; Graetzel, M.; et al. One-Year Stable Perovskite Solar Cells by 2D/3D Interface Engineering. *Nat. Commun.* **2017**, *8*, 1–8.

(22) Schlipf, J.; Hu, Y.; Pratap, S.; Bießmann, L.; Hohn, N.; Porcar, L.; Bein, T.; Docampo, P.; Müller-Buschbaum, P. Shedding Light on the Moisture Stability of 3D/2D Hybrid Perovskite Heterojunction Thin Films. *ACS Appl. Energy Mater.* **2019**, *2* (2), 1011–1018.

(23) Yantara, N.; Bruno, A.; Iqbal, A.; Jamaludin, N. F.; Soci, C.; Mhaisalkar, S.; Mathews, N. Designing Efficient Energy Funneling Kinetics in Ruddlesden–Popper Perovskites for High-Performance Light-Emitting Diodes. *Adv. Mater.* **2018**, *30* (33), 1–7.

(24) Xu, Z.; Li, Y.; Liu, X.; Ji, C.; Chen, H.; Li, L.; Han, S.; Hong, M.; Luo, J.; Sun, Z. Highly Sensitive and Ultrafast Responding Array Photodetector Based on a Newly Tailored 2D Lead Iodide Perovskite Crystal. *Adv. Opt. Mater.* **2019**, *1900308*, 1–7.

(25) Wang, J.; Zhang, J.; Li, J.; Tan, Q.; Li, L.; Zhang, J.; Zang, J.; Tan, P.; Li, D. Controllable Synthesis of Two-Dimensional Ruddlesden-Popper-Type Perovskite Heterostructures. *J. Phys. Chem. Lett.* **2017**, *8* (24), 6211–6219.

(26) Zhou, M.; Fei, C.; Sarmiento, J. S.; Wang, H. Manipulating the Phase Distributions and Carrier Transfers in Hybrid Quasi-Two-Dimensional Perovskite Films. *Sol. RRL* **2019**, *3* (4), 1–9.

(27) Venkatesan, N. R.; Kennard, R. M.; DeCrescent, R. A.; Nakayama, H.; Dahlman, C. J.; Perry, E. E.; Schuller, J.; Chabinyc, M. L. Phase Intergrowth and Structural Defects in Organic Metal Halide Ruddlesden–Popper Thin Films. *Chem. Mater.* **2018**, *30*, 8615–8623.

(28) Tan, W. L.; Cheng, Y. B.; McNeill, C. R. Direct Assessment of Structural Order and Evidence for Stacking Faults in Layered Hybrid Perovskite Films from X-Ray Scattering Measurements. *J. Mater. Chem. A* **2020**, *8* (25), 12790–12798.

(29) Blancon, J. C.; Tsai, H.; Nie, W.; Stoumpos, C. C.; Pedesseau, L.; Katan, C.; Kepenekian, M.; Soe, C. M. M.; Appavoo, K.; Sfeir, M. Y.; et al. Extremely Efficient Internal Exciton Dissociation through Edge States in Layered 2D Perovskites. *Science (80-.).* **2017**, *355* (6331), 1288–1292.

(30) Dahlman, C. J.; Decrescent, R. A.; Venkatesan, N. R.; Kennard, R. M.; Wu, G.; Everest, M. A.; Schuller, J. A.; Chabinyc, M. L. Controlling Solvate Intermediate Growth for Phase-Pure Organic Lead Iodide Ruddlesden-Popper (C4H9NH3)2(CH3NH3)n-1Pb NI3 N+1 Perovskite Thin Films. *Chem. Mater.* **2019**, *31* (15), 5832–5844.

(31) Quintero-Bermudez, R.; Gold-Parker, A.; Proppe, A. H.; Munir, R.; Yang, Z.; Kelley, S. O.; Amassian, A.; Toney, M. F.; Sargent, E. H. Compositional and Orientational Control in Metal Halide Perovskites of Reduced Dimensionality. *Nat. Mater.* **2018**, *17* (10), 900–907.

(32) Hoffman, J. M.; Strzalka, J.; Flanders, N. C.; Hadar, I.; Cuthriell, S. A.; Zhang, Q.; Schaller, R. D.; Dichtel, W. R.; Chen, L. X.; Kanatzidis, M. G. In Situ Grazing-Incidence Wide-Angle Scattering Reveals Mechanisms for Phase Distribution and Disorientation in 2D Halide Perovskite Films. *Adv. Mater.* **2020**, *32* (33), 1–8.

(33) Venkatesan, N. R.; Labram, J. G.; Chabinyc, M. L. Charge-Carrier Dynamics and Crystalline Texture of Layered Ruddlesden-Popper Hybrid Lead Iodide Perovskite Thin Films. *ACS Energy Lett.* **2018**, *3* (2), 380–386.

(34) Liao, K.; Li, C.; Xie, L.; Yuan, Y.; Wang, S.; Cao, Z.; Ding, L.; Hao, F. Hot-Casting Large-Grain Perovskite Film for Efficient Solar Cells: Film Formation and Device Performance. *Nano-Micro Lett.* **2020**, *12* (1), 1–22.

(35) Al, K. et. Placeholder for EA Paper.

(36) Liang, C.; Gu, H.; Xia, Y.; Wang, Z.; Liu, X.; Xia, J.; Zuo, S.; Hu, Y.; Gao, X.; Hui, W.; et al. Two-Dimensional Ruddlesden–Popper Layered Perovskite Solar Cells Based on Phase-Pure Thin Films. *Nat. Energy* **2020**.

(37) Luo, S. Q.; Wang, J. F.; Yang, B.; Yuan, Y. B. Recent Advances in Controlling the Crystallization of Two-Dimensional Perovskites for Optoelectronic Device. *Front. Phys.* **2019**, *14* (5).

(38) Yuan, M.; Quan, L. N.; Comin, R.; Walters, G.; Sabatini, R.; Voznyy, O.; Hoogland, S.; Zhao, Y.; Beauregard, E. M.; Kanjanaboos, P.; et al. Perovskite Energy Funnels for Efficient Light-Emitting Diodes. *Nat. Nanotechnol.* **2016**, *11* (10), 872–877.

(39) Kieslich, G.; Sun, S.; Cheetham, A. K. An Extended Tolerance Factor Approach for Organic-Inorganic Perovskites. *Chem. Sci.* **2015**, *6* (6), 3430–3433.

(40) Becker, M.; Klüner, T.; Wark, M. Formation of Hybrid ABX3 Perovskite Compounds for Solar Cell Application: First-Principles Calculations of Effective Ionic Radii and Determination of Tolerance Factors. *Dalt. Trans.* **2017**, *46* (11), 3500–3509.

(41) Gholipour, S.; Ali, A. M.; Correa-Baena, J. P.; Turren-Cruz, S. H.; Tajabadi, F.; Tress, W.; Taghavinia, N.; Grätzel, M.; Abate, A.; De Angelis, F.; et al. Globularity-Selected Large Molecules for a New Generation of Multication Perovskites. *Adv. Mater.* **2017**, *29* (38), 1–9.

(42) Yoon, S. J.; Stamplecoskie, K. G.; Kamat, P. V. How Lead Halide Complex Chemistry Dictates the Composition of Mixed Halide Perovskites. *J. Phys. Chem. Lett.* **2016**, *7* (7), 1368–1373.

(43) Spanopoulos, I.; Hadar, I.; Ke, W.; Guo, P.; Mozur, E. M.; Morgan, E.; Wang, S.; Zheng, D.; Padgaonkar, S.; Reddy, G. N. M.; et al. Tunable Broad Light Emission from 3D “

Hollow ” Bromide Perovskites through Defect Engineering. **2021**.

(44) Benassi, E.; Fan, H. Determination of the Molecular Size from Measurements of Vapour Pressure of Binary Liquid Mixtures. Theory, Experiments and Quantum Chemical Calculations. *J. Mol. Liq.* **2020**, *313*, 113202.

(45) Petrov, A. A.; Fateev, S. A.; Khrustalev, V. N.; Li, Y.; Dorovatovskii, P. V.; Zubavichus, Y. V.; Goodilin, E. A.; Tarasov, A. B. Formamidinium Haloplumbate Intermediates: The Missing Link in a Chain of Hybrid Perovskites Crystallization. *Chem. Mater.* **2020**, *32* (18), 7739–7745.

(46) Mitzi, D. B.; Medeiros, D. R.; Malenfant, P. R. L.; Watson, I. B. M. T. J.; Box, P. O.; Heights, Y.; York, N. Intercalated Organic − Inorganic Perovskites Stabilized by Fluoroaryl − Aryl Interactions. **2002**, *41* (8), 2134–2145.

(47) Du, Q.; Zhu, C.; Yin, Z.; Na, G.; Cheng, C.; Han, Y.; Liu, N.; Niu, X.; Zhou, H.; Chen, H.; et al. Stacking Effects on Electron-Phonon Coupling in Layered Hybrid Perovskites via Microstrain Manipulation. *ACS Nano* **2020**, *14* (5), 5806–5817.

(48) Dahlman, C. J.; Kennard, R. M.; Paluch, P.; Venkatesan, N. R.; Chabinyc, M. L.; Manjunatha Reddy, G. N. Dynamic Motion of Organic Spacer Cations in Ruddlesden-Popper Lead Iodide Perovskites Probed by Solid-State NMR Spectroscopy. *Chem. Mater.* **2021**, *33* (2), 642–656.

(49) De Wolf, S.; Holovsky, J.; Moon, S. J.; Löper, P.; Niesen, B.; Ledinsky, M.; Haug, F. J.; Yum, J. H.; Ballif, C. Organometallic Halide Perovskites: Sharp Optical Absorption Edge and Its Relation to Photovoltaic Performance. *J. Phys. Chem. Lett.* **2014**, *5* (6), 1035–1039.

5.7 Appendix to Chapter 5

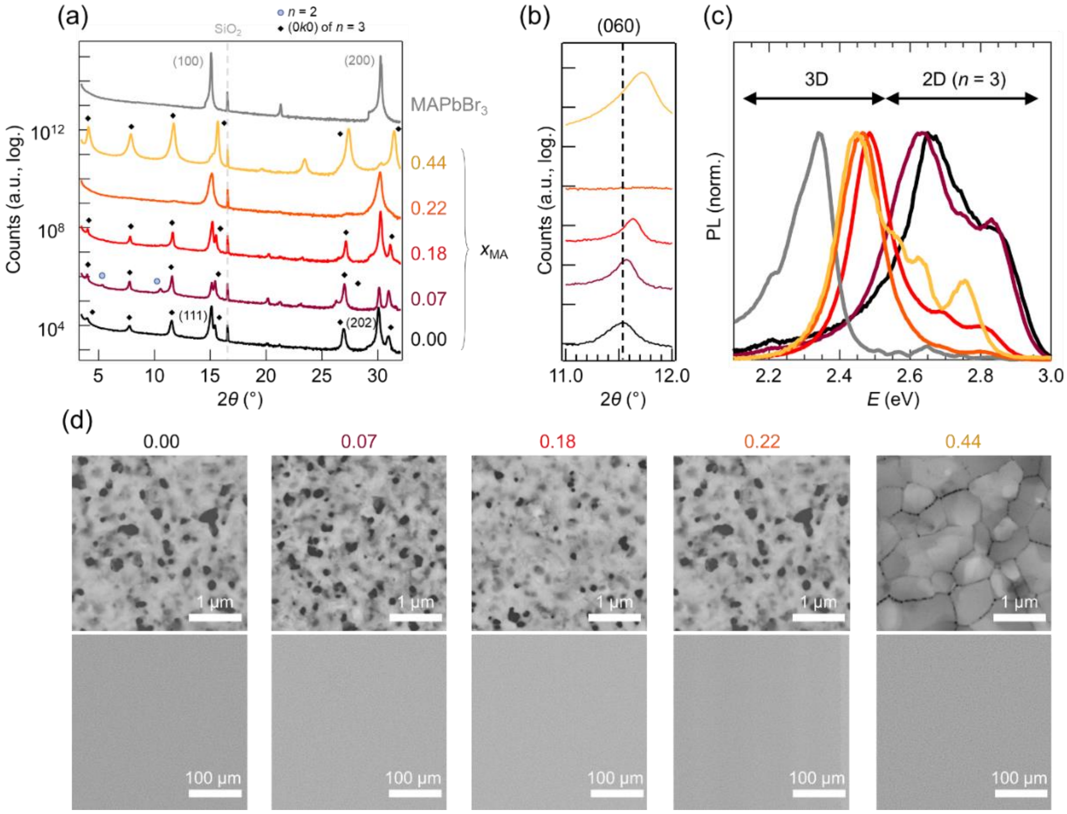

Figure 5.S1. Structural and optical characterizations of spin-cast films with precursor solution stoichiometry $(EA_{1-x}MA_x)_{4.5}Pb_3Br_{10}$, as well as $MAPbBr_3$. (a) XRD patterns. The $n = 3$ peaks are indexed and visible for most patterns, with some that we assign to $n = 2$, by analogy with the $(BA)_2(MA)_{n-1}Pb_nI_{3n+1}$ RP films. [12] (b) Closer look at the (060) peak from the $n = 3$ phase. (c) Photoluminescence emission (3.94 eV excitation). (d) SEM images.

Overall, the MA compositions retain the $n = 3$ phase, but can also form $(EA,MA)PbBr_3$, which dominates the emission. The growth and sheet orientation are not improved for most MA compositions, in contrast to those with FA. Notably, MA substitution does not turn off the emission at 2.7 eV, in contrast with FA substitution.

We explain here these conclusions in more detail. The XRD peaks of $n = 3$ are retained for most MA compositions (**Figure 5.S1a**). A closer look at the (060) peak, which corresponds to stacking of the $n = 3$ semiconducting sheets, reveals contraction of the semiconducting sheets (**Figure 5.S1b**). Since MA is small (217 pm) and typically an A-site cation, it is likely that MA is being incorporated into the n = 3 structure in the A-site. However, most x_{MA} compositions have emission from both the n = 3 phase as well as the 3D (EA,MA)$PbBr_3$ phase (**Figure 5.S1c**), [13] suggesting a coexistence of n = 3 and (EA,MA)$PbBr_3$ in the films. For x_{MA} = 0.22, only the (EA,MA)$PbBr_3$ phase is observed via XRD and PL. Notably, substitution with MA did *not* extinguish the 2.7 eV emission: x_{MA} = 0.07 retained both the 2.9 eV and 2.7 eV emission peaks, although the 2.7 eV peak seemed slightly red-shifted. This behavior contrasts strongly with the behavior of the FA compositions, for which the 2.7 eV feature disappears with x_{FA} = 0.07. Indeed, MA, with its sole ammonium group and position in the A-site, is not anchoring DMF in the spacer site.

SEM (**Figure 5.S1d**) revealed that the grain size and film morphology stayed the same for most MA substitutions. The intensities of the n = 3 XRD peaks also did not change much for most MA substitutions, and the relative proportions of the (0k0) and (111) were similar (**Figure 5.S1a**). Thus, MA substitution does not improve growth for most compositions in the way that FA substitution does, likely because MA isn't retaining DMF. The x_{MA} = 0.44 composition had very strong (0k0) in XRD, indicating uniform in-plane orientation of the n = 3 semiconducting sheets, and correspondingly very large grains (**Figure 5.S1d**). This composition is close to the stoichiometry of $(EA)_2(MA)_2Pb_3Br_{10}$, and it is possible that full MA substitution in the A-site relieves octahedral distortions to a point that large growth is made much easier. However, the emission of this film was still mostly from 3D phases. A 3D phase was not strongly apparent in XRD, so 3D crystallites in the x_{MA} = 0.44 film are likely very small, and contained in grains that mostly have the n = 3 phase.

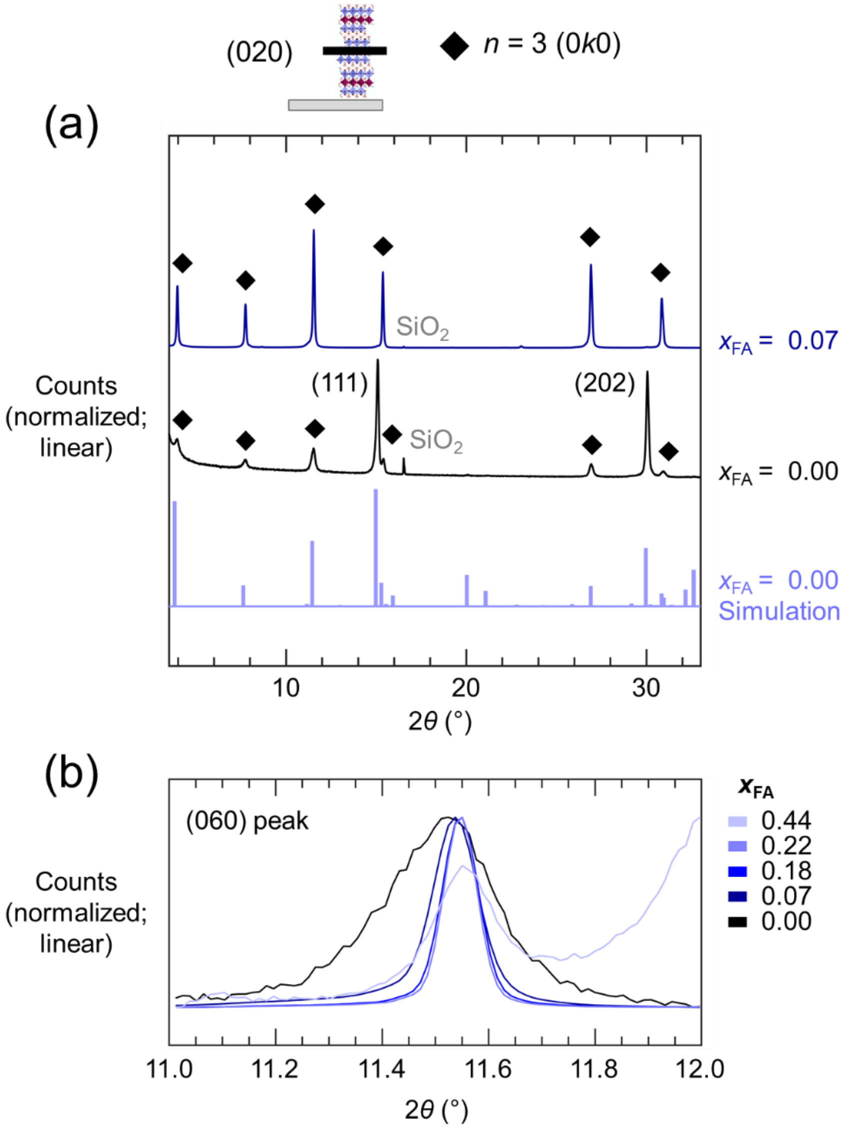

Figure 5.S2. (a) XRD patterns of x_{FA} = 0.07 and x_{FA} = 0.00, compared with the simulated pattern for x_{FA} = 0.00. The patterns are shown on a linear scale; with (0*k*0) peaks marked by the black diamonds; (111) and (202) peaks as labelled, and SiO_2 peaks from the substrate labelled as well. The simulation was performed with the cif file from the reported structure, [3] using Vesta. (b) Closer examination of the (060) peak. In contrast with the MA compositions, there is (1) strong narrowing and (2) a lack of peak shift past x_{FA} = 0.07. These are consistent with FA-DMF improving growth of the n = 3 phase, and with the amount of FA-DMF in the n = 3 structure saturating.

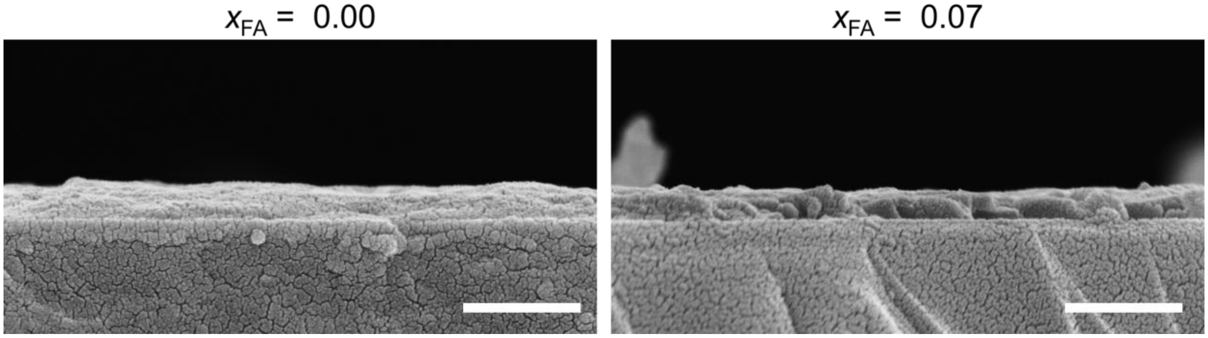

Figure 5.S3. Cross-sectional SEM of x_{FA} = 0.00 and 0.07 spin-cast films (no PMMA). The scale bar is 500 nm. The substrate is quartz. Spin-cast films were cut in half with a diamond scribe, which likely induced some fracturing. However, even in cross-sectional SEM, the x_{FA} = 0.07 film appears to have more defined grains than the x_{FA} = 0.00.

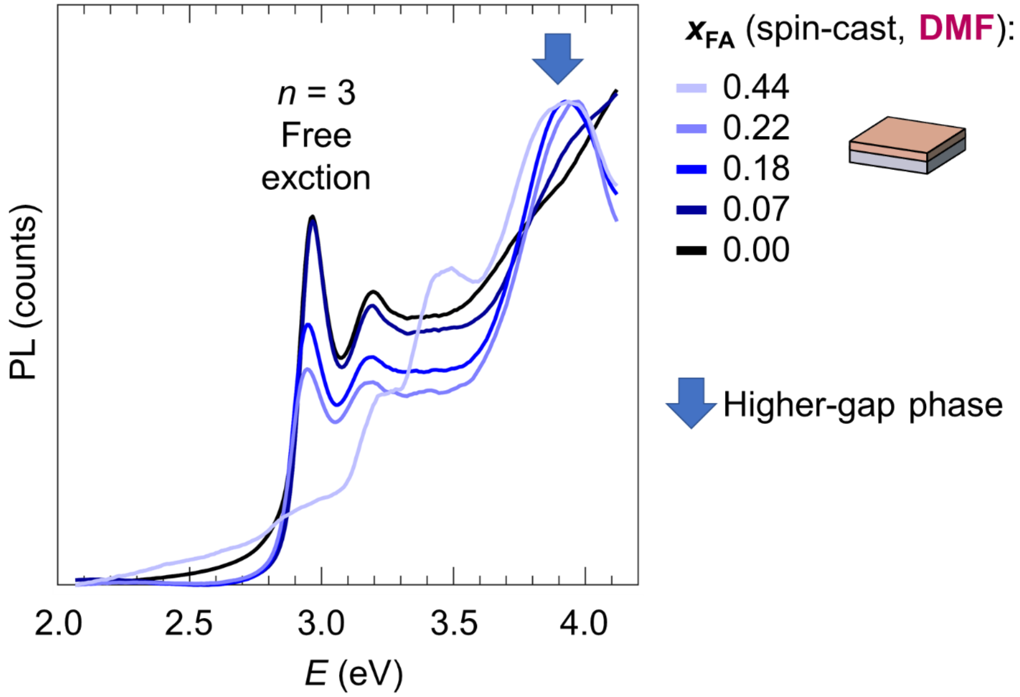

Figure 5.S4. UV-Vis absorbance of the x_{FA} spin-cast films, with PMMA covering. A higher-gap phase appears with more FA substituted. The $n = 3$ free exction is visible for most samples, and very weak for $x_{FA} = 0.44$, which starts absorbing near the onset of $FAPbBr_3$ and has a very shallow slope. All the other x_{FA}, in contrast, have very sharp onset at the $n = 3$ free exciton. Most FA films have sharper sub-gap slope than the EA-only film; this is explored more greatly with the PDS experiment (**Figure 5.6**).

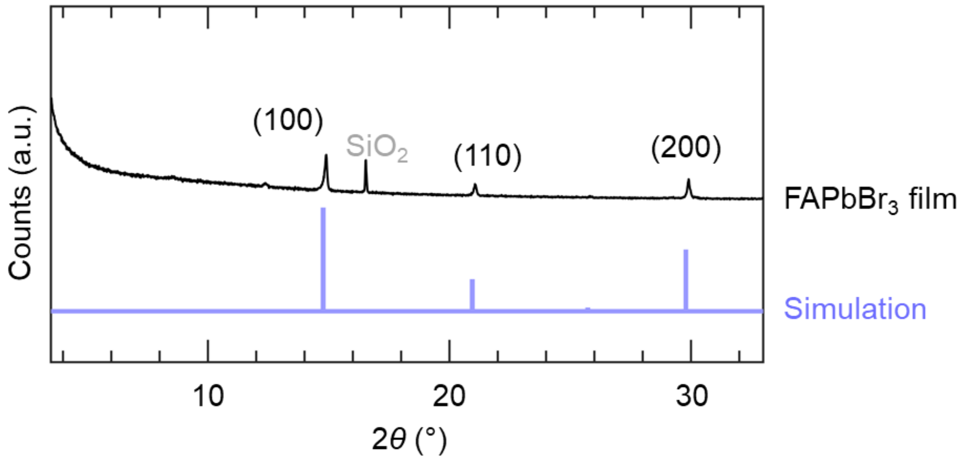

Figure 5.S5. XRD pattern of the FAPbBr$_3$ film, with peaks indicated. The simulation made using the cif file from reference. [14] The pattern was well-matched with the simulation. The 3D cubic phase contains no peaks at low angle.

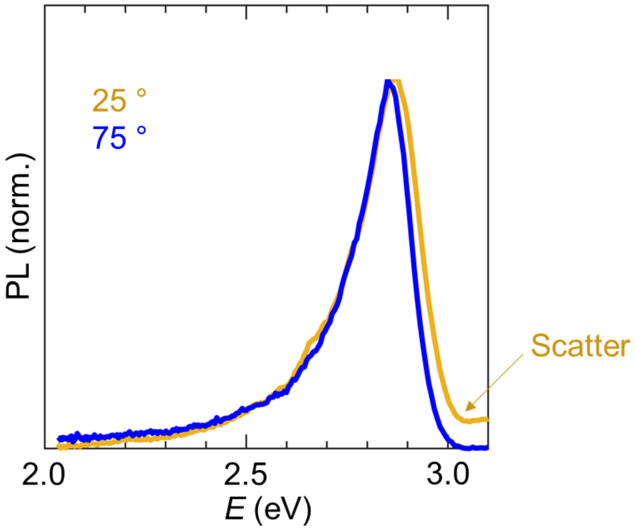

Figure 5.S6. PL emission of an x_{FA} = 0.07 film, taken by varying the angle the sample makes with the excitation and emission ports.

The relative emissive proportions of free excitons vs. lower-energy features can sometimes depend on the angle of the 2D semiconducting sheets with respect to the PL collection ("emission port" on fluorimeters). [15,16] For this reason, we varied the collection angle on the x_{FA} = 0.07 film, to see if the 2.7 eV feature would reappear. Traditionally, PL measurements are collected with films making a 45° angle with the emission port; here we used 25° and 75° to better probe the angle dependence of emission from the oriented 2D sheets (**Figures 5.1,5.5**). As shown in **Figure 5.S6**, the emission does not change when rotating the film. A small extra amount of scattering appears when the sample is practically facing the excitation port (25°). We previously also verified that the relative proportions of different features do not change for $(EA)_4Pb_3Br_{10}$ films. [2]

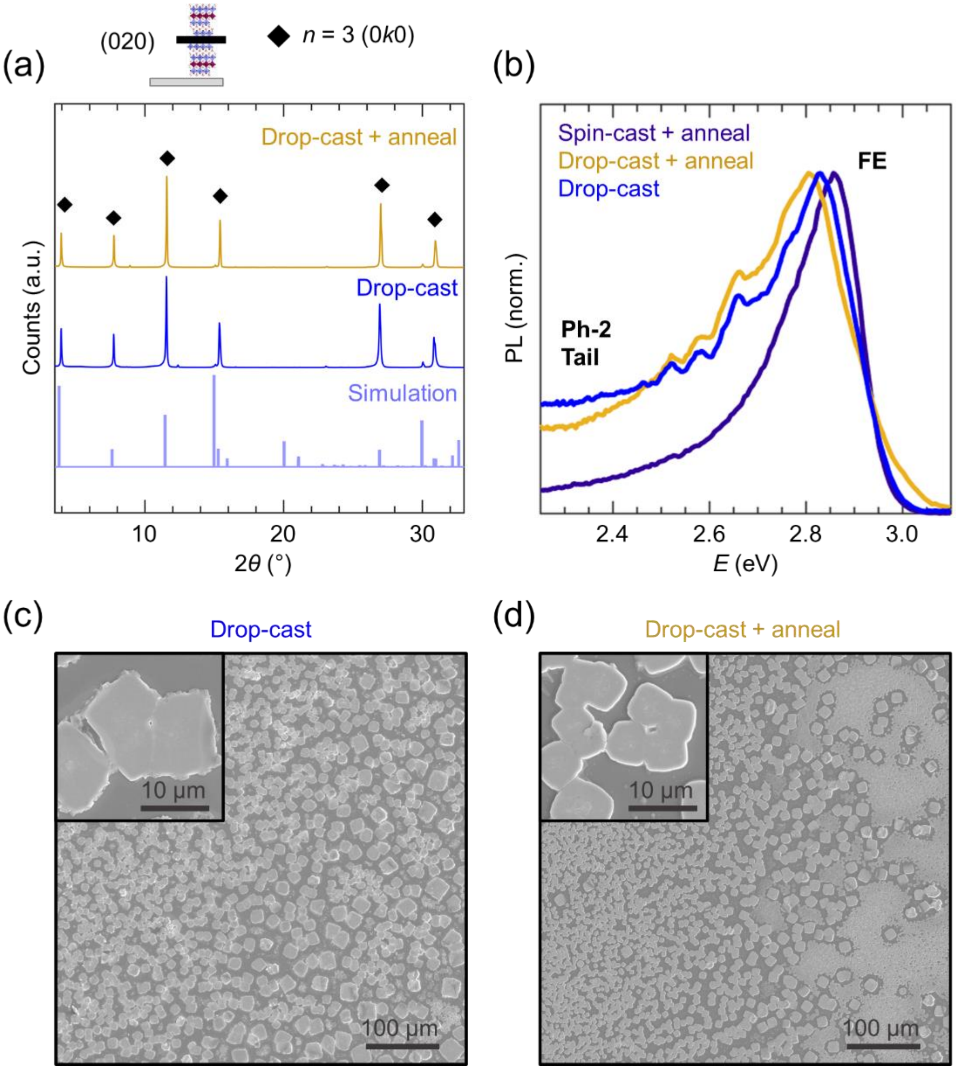

Figure 5.S7. Structural and optical properties of drop-cast films of x_{FA} = 0.07. (a) XRD of drop-cast films, with and without annealing, of x_{FA} = 0.07. The simulated pattern of $(EA)_4Pb_3Br_{10}$ is also shown, and was made using the published structure. [3] (b) PL emission of these films and of the spin-cast film of x_{FA} = 0.07 film, with 3.95 eV excitation and 75 ° collection angle. FE stands for free exciton, and Ph-2 stands for phonon-coupled emission (the 2nd phonon-coupled peak; the 1st one is at 2.7 eV and is not present in FA films). (c) SEM of drop-cast films, with and without annealing.

The drop-cast films contain primarily the n = 3 phase, and are oriented uniformly with the semiconducting sheets parallel to the substrate. The grains are micron-scale, and many are unconstrained. The phonon-coupled emission tail at low energy is more pronounced when making the films via drop-casting, than it is using spin-casting. Similar results were found for drop-cast films of $(EA)_4Pb_3Br_{10}$. [2] Notably, the drop-cast films do not have the 2.7 eV emission, despite the low-energy tail being present. This verifies that growth conditions are not responsible for turning off the 2.7 eV peak.

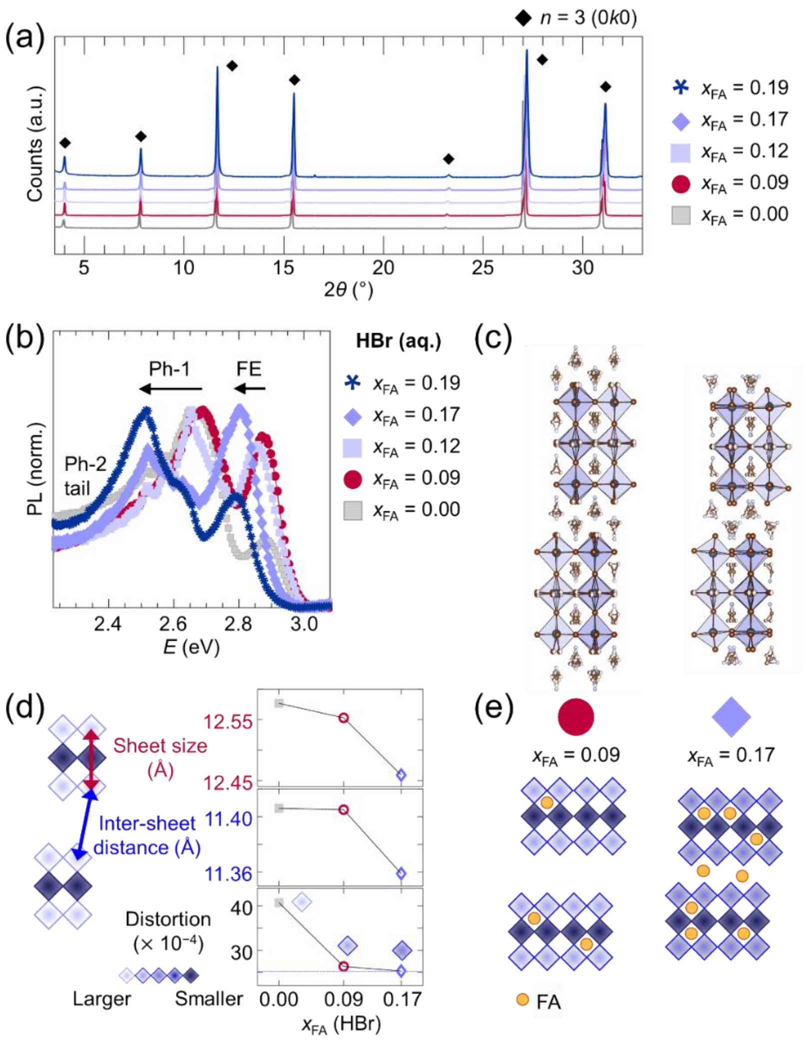

Figure 5.S8. Structural and optical properties of bulk crystals made from aqueous HBr. (a) Powder XRD patterns of bulk crystals dropped onto quartz substrates, where the $(HBr)_{aq}$ solution had concentration $(EA_{1-x}FA_x)_4Pb_3Br_{10}$. Characteristic $n = 3$ peaks are visible for all samples. (b) PL emission of these crystals (excitation 3.95 eV). The free exciton (FE), and phonon-coupled features (Ph-1 and Ph-2) remain present in all samples, even if Ph-1 strongly red-shifts. (c) Structures of single crystals of $x_{FA} = 0.09$ and $x_{FA} = 0.17$. (d) Evolution of sheet size, inter-sheet distance and distortion for $x_{FA} = 0.00$, 0.09 and 0.17. All distances were from Pb ion to Pb ion of the designated octahedra. Values for $x_{FA} = 0.00$ were taken from published work. [3] (e) Schematic of where FA goes and what happens to the octahedra distortions for the $x_{FA} = 0.09$ and 0.17 single crystals.

Overall, analysis of bulk crystals grown in aqueous HBr shows that the 2.7 eV emission, Ph-1, is retained when FA alone is incorporated into the *n* = 3 RP structure (see below).

Figure 5.S8a shows powder XRD patterns of bulk crystals dropped onto quartz substrates. The crystals preferentially orient with the semiconducting sheets parallel to the substrate, consistent with prior work. [2] The n = 3 (0k0) peaks are retained with FA loading, and the lattice contracts slightly (peaks shift to larger angle) with increasing FA, consistent with FA being smaller than EA.

Figure 5.S8b shows that Ph-1 red-shifts with increasing FA, but does not disappear. The free exciton also red-shifts, and the phonon-coupled tail (Ph-2) is also retained.

Crystals of the x_{FA} = 0.09 and 0.17 compositions were selected to be "single" crystals, and single-crystal XRD was used to generate the structures in **Figure 5.S8c**. Because FA and EA are difficult to resolve via XRD, we did not rely on XRD to see where FA was going, and instead measured the Pb-Pb ion distances (**Figure 5.S8d**). We looked at two distances: the top-bottom Pb-Pb distance to get the sheet size, and the Pb-Pb of the top and bottom sheets to get the inter-sheet distance. For x_{FA} = 0.09, the sheet size decreases slightly and the inter-sheet distance remains the same, so FA is going in the in the A-site only (**Figure 5.S8d-e**). For x_{FA} = 0.17, both the sheet size and inter-sheet distance decrease, so FA is going in both the A-site and the spacer site. The distortion is calculated using:

$$\Delta d = \frac{1}{6}\sum\left(\frac{d_n - d}{d}\right)^2$$

where d_n are the six individual Pb-Br bond lengths and d is the mean Pb−Br bond length. The distortion of the outer octahedra is shown in **Figure 5.S8c**. The outer octahedra exhibit a sharp decrease in distortion with FA increase, but the distortions are still quite high (≈ 25×10^{-4}). For comparison, the distortions of the outer layer of $(BA)_2(MA)_2Pb_3I_{10}$ are 5×10^{-4} (calculated using cif file from [12]) and most of the emission of this compound comes from its free exciton. The high distortions to the outer octahedra of $x_{FA} = 0.09$ and 0.17 are in agreement with the retention of the phonon-coupled features, as distortions can favor phonon-coupled emission such as self-trapped exciton emission. [3,16]

The next page shows refinement data for the single crystals of the $x_{FA} = 0.09$ and $x_{FA} = 0.17$ compositions.

Table 5.S1. Crystal data and structure refinement for x_{FA} = 0.09 and x_{FA} = 0.17.

Crystal	**x_{FA} = 0.09**	**x_{FA} = 0.17**
Empirical formula	$(C_{7.90}H_{31.70}N_{4.10})Pb_3Br_{10}$	$(C_{7.68}H_{30.08}N_{4.32})Pb_3Br_{10}$
Formula weight	1604.94	1603.74
Temperature	296(2) K	293(2) K
Wavelength	0.71073 Å	0.71073 Å
Crystal system	Orthorhombic	Orthorhombic
Space group	Ccca	Ccca
Unit cell dimensions	a = 8.4199(11) Å α= 90°	a = 8.4199(11) Å α = 90°
	b = 46.305(6) Å β= 90°	b = 46.305(6) Å β = 90°
	c = 8.4216(10) Å γ = 90°	c = 8.4216(10) Å γ = 90°
Volume	3283.4(7) Å^3	3283.4(7) Å^3
Z	4	4
Density (calculated)	3.247 mg/m^3	3.244 mg/m^3
Absorption coefficient	27.519 mm^{-1}	27.519 mm^{-1}
F(000)	2815	2810
Crystal size	0.150 x 0.100 x 0.100 mm^3	0.150 x 0.100 x 0.100 mm^3
Θ range	3.450 to 30.546°	3.450 to 27.163°
Index ranges	−11<=h<=10, −64<=k<=64, −11<=l<=11	−10<=h<=10, −42<=k<=58, −10<=l<=10
Reflections collected	13809	10255
Independent reflections	2442 [R(int) = 0.0997]	1826 [R(int) = 0.1153]
Completeness to Θ = 25.242°	99.7 %	99.7 %
Refinement method	Full-matrix least-squares on F^2	Full-matrix least-squares on F2
Data/restrains/parameters	2442 / 14 / 63	1826 / 11 / 62
Goodness of fit on F^2	1.140	1.115
Final R indices [I>2sigma(I)]	R1 = 0.1637, wR2 = 0.3262	R1 = 0.1514, wR2 = 0.290
R indices	R1 = 0.2275, wR2 = 0.3527	R1 = 0.2122, wR2 = 0.3193
Largest diff. peak and hole	4.094 and −9.843 e.Å^{-3}	3.326 and -8.281 e.Å^{-3}

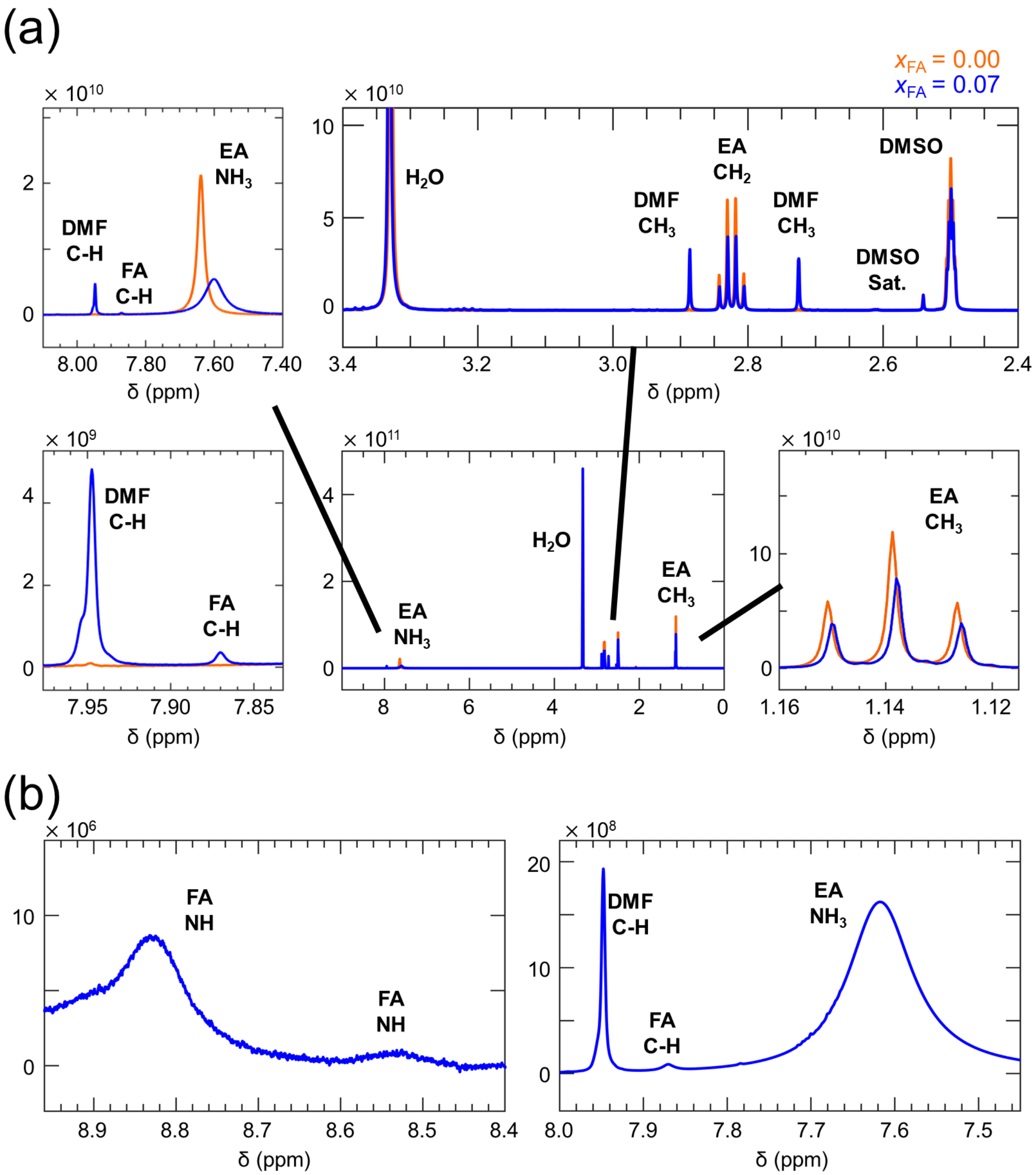

Figure 5.S9. 1H-NMR spectra of drop-cast and annealed films with x_{FA} = 0.07 and x_{FA} = 0.00 compositions prepared from DMF (no PMMA capping layer), that were then scraped off the substrates and dissolved in deuterated DMSO. (a) shows the full spectra, and select regions, of spectra taken with 20-minute integration time. The region near 2.8 ppm is shown in more detail in the main text. (b) shows a 16h scan of the x_{FA} = 0.07 sample in the region of the FA peaks, to better resolve them.

NMR analysis confirmed that the x_{FA} = 0.07 composition (drop-cast and annealed; see **Figure 5.S7 for XRD**) had both FA and DMF. Peak assignments were made using the

NIST spectrum for DMF, and using prior work for EA and FA. [9,17] Peak integration yielded EA: DMF of 0.998: 0.002 for the x_{FA} = 0.00 sample and EA: DMF: FA of 0.79: 0.19: 0.02 for the x_{FA} = 0.07 sample. The proportion of DMF relative to FA is perhaps over-estimated in the x_{FA} = 0.07 sample; however, it is clear that the presence of FA also results in the presence of a large amount of DMF. FA and EA are approximately in the proportions expected from weighing out the powders; as 0.02 / (0.79 + 0.02) ≈ 0.02, which is not very far off from 0.07. All relative ratios were obtained using:

$$\frac{Moles\ EA}{Moles\ DMF} = \frac{Integration\ for\ EA}{Integration\ for\ DMF} \times \frac{Number\ of\ H\ in\ DMF\ signal}{Number\ of\ H\ in\ EA\ signal}$$

and

$$\frac{Moles\ EA}{Moles\ FA} = \frac{Integration\ for\ EA}{Integration\ for\ FA} \times \frac{Number\ of\ H\ in\ FA\ signal}{Number\ of\ H\ in\ EA\ signal}$$

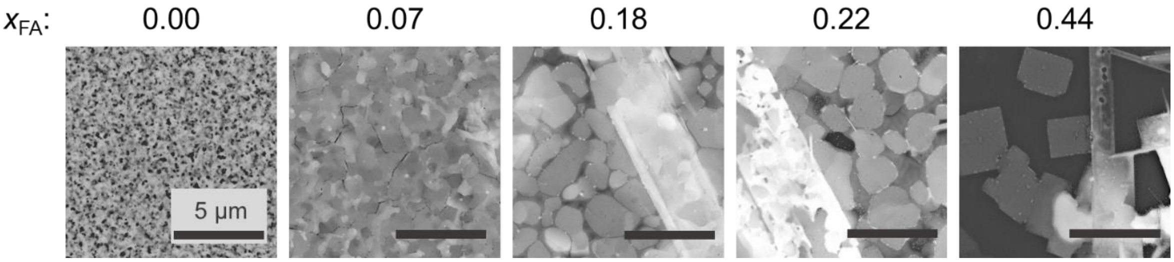

Figure 5.S10. SEM of different x_{FA} compositions (spin-cast films). Although obvious impurities appear for x_{FA} = 0.18 and above, the grain size of all phases present, including n = 3, remains quite large.

References

(1) Carnie, M. J.; Charbonneau, C.; Davies, M. L.; Troughton, J.; Watson, T. M.; Wojciechowski, K.; Snaith, H.; Worsley, D. A. A One-Step Low Temperature Processing Route for Organolead Halide Perovskite Solar Cells. *Chem. Commun.* **2013**, *49* (72), 7893–7895.

(2) Al, K. et. Placeholder for EA Paper.

(3) Mao, L.; Wu, Y.; Stoumpos, C. C.; Traore, B.; Katan, C.; Even, J.; Wasielewski, M. R.; Kanatzidis, M. G. Tunable White-Light Emission in Single-Cation-Templated Three-Layered 2D Perovskites (CH3CH2NH3)4Pb3Br10-XClx. *J. Am. Chem. Soc.* **2017**, *139* (34), 11956–11963.

(4) GIXA Calculator for Penetration Depth (and Optical Properties) for X-rays https://gixa.ati.tuwien.ac.at/tools/penetrationdepth.xhtml (accessed Nov 9, 2020).

(5) Venkatesan, N. R.; Labram, J. G.; Chabinyc, M. L. Charge-Carrier Dynamics and Crystalline Texture of Layered Ruddlesden-Popper Hybrid Lead Iodide Perovskite Thin Films. *ACS Energy Lett.* **2018**, *3* (2), 380–386.

(6) Resel, R.; Bainschab, M.; Pichler, A.; DIngemans, T.; Simbrunner, C.; Stangl, J.; Salzmann, I. Multiple Scattering in Grazing-Incidence X-Ray Diffraction: Impact on Lattice-Constant Determination in Thin Films. *J. Synchrotron Radiat.* **2016**, *23* (3), 729–734.

(7) Vandewal, K.; Albrecht, S.; Hoke, E. T.; Graham, K. R.; Widmer, J.; Douglas, J. D.; Schubert, M.; Mateker, W. R.; Bloking, J. T.; Burkhard, G. F.; et al. Efficient Charge Generation by Relaxed Charge-Transfer States at Organic Interfaces. *Nat. Mater.* **2014**, *13* (1), 63–68.

(8) Venkatesan, N. R.; Kennard, R. M.; DeCrescent, R. A.; Nakayama, H.; Dahlman, C. J.; Perry, E. E.; Schuller, J.; Chabinyc, M. L. Phase Intergrowth and Structural Defects in Organic Metal Halide Ruddlesden–Popper Thin Films. *Chem. Mater.* **2018**, *30*, 8615–8623.

(9) Van Gompel, W. T. M.; Herckens, R.; Reekmans, G.; Ruttens, B.; D'Haen, J.; Adriaensens, P.; Lutsen, L.; Vanderzande, D. Degradation of the Formamidinium Cation and the Quantification of the Formamidinium-Methylammonium Ratio in Lead Iodide Hybrid Perovskites by Nuclear Magnetic Resonance Spectroscopy. *J. Phys. Chem. C* **2018**, *122* (8), 4117–4124.

(10) Dow, J. D.; Redfield, D. Toward a Unified Theory of Urbach's Rule and Exponential Absorption Edges. *Phys. Rev. B* **1972**, *5* (2), 594–610.

(11) Dahlman, C. J.; Decrescent, R. A.; Venkatesan, N. R.; Kennard, R. M.; Wu, G.; Everest, M. A.; Schuller, J. A.; Chabinyc, M. L. Controlling Solvate Intermediate Growth for Phase-Pure Organic Lead Iodide Ruddlesden-Popper (C4H9NH3)2(CH3NH3)n-1Pb NI3 N+1 Perovskite Thin Films. *Chem. Mater.* **2019**, *31* (15), 5832–5844.

(12) Stoumpos, C. C.; Cao, D. H.; Clark, D. J.; Young, J.; Rondinelli, J. M.; Jang, J. I.; Hupp, J. T.; Kanatzidis, M. G. Ruddlesden-Popper Hybrid Lead Iodide Perovskite 2D Homologous Semiconductors. *Chem. Mater.* **2016**, *28* (8), 2852–2867.

(13) Gholipour, S.; Ali, A. M.; Correa-Baena, J. P.; Turren-Cruz, S. H.; Tajabadi, F.; Tress, W.; Taghavinia, N.; Grätzel, M.; Abate, A.; De Angelis, F.; et al. Globularity-Selected

Large Molecules for a New Generation of Multication Perovskites. *Adv. Mater.* **2017**, *29* (38), 1–9.

(14) Spanopoulos, I.; Hadar, I.; Ke, W.; Guo, P.; Mozur, E. M.; Morgan, E.; Wang, S.; Zheng, D.; Padgaonkar, S.; Reddy, G. N. M.; et al. Tunable Broad Light Emission from 3D " Hollow " Bromide Perovskites through Defect Engineering. **2021**.

(15) DeCrescent, R. A.; Venkatesan, N. R.; Dahlman, C. J.; Kennard, R. M.; Zhang, X.; Li, W.; Du, X.; Chabinyc, M. L.; Zia, R.; Schuller, J. A. Bright Magnetic Dipole Radiation from Two-Dimensional Lead-Halide Perovskites. *Sci. Adv.* **2020**, No. February, 1–11.

(16) Decrescent, R. A.; Du, X.; Kennard, R. M.; Venkatesan, N. R.; Dahlman, C. J.; Chabinyc, M. L.; Schuller, J. A. Even-Parity Self-Trapped Excitons Lead to Magnetic Dipole Radiation in Two-Dimensional Lead Halide Perovskites. *ACS Nano* **2020**, *14* (7), 8958–8968.

(17) Wu, C.; Chen, K.; Guo, D. Y.; Wang, S. L.; Li, P. G. Cations Substitution Tuning Phase Stability in Hybrid Perovskite Single Crystals by Strain Relaxation. *RSC Adv.* **2018**, *8* (6), 2900–2905.

Chapter 6:
Summary and Outlook

This dissertation explored the fundamental properties of hybrid perovskite films, which are attractive for a variety of optoelectronic devices. Chapter 2 showed how bending films can change the proportions of different sub-grain structures, and how the formation of such structures is directly linked to film degradation. Chapter 3 set upper bounds for halide interdiffusion coefficients for the iodide-bromide perovskites, which are the most widely-used 3D perovskites. Chapters 4 and 5 showed how to grow phase-pure 2D films, and how strain and solvent incorporation can change the proportions of different emissive features.

The findings of this dissertation open new questions regarding film properties. Twinning seems to have the opposite impacts on the optical properties of films vs. bulk crystals of $MAPbI_3$; the impacts of twinning on the optical properties of films with large grains is unclear. In addition, the effects of solvent anchoring in the interlayer of 2D perovskites merits more exploration. In this dissertation, it was shown that solvent anchoring can turn off select phonon-coupled emission features; this effect may be tunable by using bulkier solvents, or solvents with different polarity. The ability to make phase-pure 2D films is highly useful, both for studies of fundamental properties and for device fabrication.

With the commercialization of perovskite solar cells already underway, we can expect attempts at commercializing perovskites for other applications as well, such as light emitting devices or photodetectors. The tunable structure and resulting wealth of optical and ionic properties will continue to put hybrid halide perovskites at the forefront of optoelectronics research.